frontiers | Research Topics

Mechanobiology at multiple scales

Edited by
Yuhui Li and Guang-Kui Xu

Published in
Frontiers in Bioengineering and Biotechnology

ISSN 1664-8714
ISBN 978-2-8325-2842-6
DOI 10.3389/978-2-8325-2842-6

About Frontiers

Frontiers is more than just an open access publisher of scholarly articles: it is a pioneering approach to the world of academia, radically improving the way scholarly research is managed. The grand vision of Frontiers is a world where all people have an equal opportunity to seek, share and generate knowledge. Frontiers provides immediate and permanent online open access to all its publications, but this alone is not enough to realize our grand goals.

Frontiers journal series

The Frontiers journal series is a multi-tier and interdisciplinary set of open-access, online journals, promising a paradigm shift from the current review, selection and dissemination processes in academic publishing. All Frontiers journals are driven by researchers for researchers; therefore, they constitute a service to the scholarly community. At the same time, the *Frontiers journal series* operates on a revolutionary invention, the tiered publishing system, initially addressing specific communities of scholars, and gradually climbing up to broader public understanding, thus serving the interests of the lay society, too.

Dedication to quality

Each Frontiers article is a landmark of the highest quality, thanks to genuinely collaborative interactions between authors and review editors, who include some of the world's best academicians. Research must be certified by peers before entering a stream of knowledge that may eventually reach the public - and shape society; therefore, Frontiers only applies the most rigorous and unbiased reviews. Frontiers revolutionizes research publishing by freely delivering the most outstanding research, evaluated with no bias from both the academic and social point of view. By applying the most advanced information technologies, Frontiers is catapulting scholarly publishing into a new generation.

What are Frontiers Research Topics?

Frontiers Research Topics are very popular trademarks of the *Frontiers journals series*: they are collections of at least ten articles, all centered on a particular subject. With their unique mix of varied contributions from Original Research to Review Articles, Frontiers Research Topics unify the most influential researchers, the latest key findings and historical advances in a hot research area.

Find out more on how to host your own Frontiers Research Topic or contribute to one as an author by contacting the Frontiers editorial office: frontiersin.org/about/contact

Mechanobiology at multiple scales

Topic editors

Yuhui Li — Commissariat à l'Energie Atomique et aux Energies Alternatives (CEA), France

Guang-Kui Xu — Xi'an Jiaotong University, China

Citation

Li, Y., Xu, G.-K., eds. (2023). *Mechanobiology at multiple scales*. Lausanne: Frontiers Media SA. doi: 10.3389/978-2-8325-2842-6

Table of contents

frontiers | Frontiers in Bioengineering and Biotechnology

TYPE Editorial
PUBLISHED 14 June 2023
DOI 10.3389/fbioe.2023.1226198

OPEN ACCESS

EDITED AND REVIEWED BY
Markus O. Heller,
University of Southampton,
United Kingdom

*CORRESPONDENCE
Yuhui Li,
yuhui.li@u-paris.fr
Guang-Kui Xu,
guangkuixu@mail.xjtu.edu.cn

RECEIVED 20 May 2023
ACCEPTED 06 June 2023
PUBLISHED 14 June 2023

CITATION
Li Y and Xu G-K (2023), Editorial: Mechanobiology at multiple scales. *Front. Bioeng. Biotechnol.* 11:1226198. doi: 10.3389/fbioe.2023.1226198

Editorial: Mechanobiology at multiple scales

Yuhui Li[1]* and Guang-Kui Xu[2]*

[1]Université PSL, Commissariat à l'énergie atomique et aux énergies alternatives (CEA), Institut Pierre-Gilles De Gennes, CytoMorpho Lab, Paris, France, [2]Laboratory for Multiscale Mechanics and Medical Science, Department of Engineering Mechanics, SVL, School of Aerospace Engineering, Xi'an Jiaotong University, Xi'an, China

KEYWORDS

mechanobiology, scaling, cells, proteins, organs

Editorial on the Research Topic
Mechanobiology at multiple scales

The significance of mechanical forces across multiple scales in biological systems cannot be understated. Understanding the impact of these forces on biological systems is essential for unraveling the complex interplay between mechanical stimuli and cellular responses. In addition, exploring the effects of mechanical forces at various scales provides valuable insights into either physiological or pathological conditions. Here, the aim of this Research Topic is dedicated to two points: 1) Highlighting the significance of mechanical forces across different scales of biological components. 2) Emphasizing the importance of recognizing the impact of mechanical forces not only in physiological conditions but also in pathological contexts, offering potential avenues for diagnostic and clinical advancements.

At the nanoscale, the interaction between receptors and ligands is influenced by mechanical forces, dictating cellular signaling and behavior. One typical example is the cell-cell communication process, representing a quintessential example of a phenomenon encompassing multiple receptors and ligands at the nanoscale that are anchored to adjacent membranes. These processes are mediated by the specific binding of receptors and ligands that are anchored to adjacent membranes. Li's laboratory has made noteworthy progress in studying mechanotransduction in this domain, focusing on three aspects: 1) protein-membrane interactions, 2) single-molecule forces, and 3) bioelectrical microenvironments (An et al.). They reviewed recent progressive achievements in the field and concluded that the binding kinetics of proteins constitute a crucial parameter that guides intercellular and cell-cell communication. Furthermore, the influence of multi-scale coupling effects on binding affinity is expected to emerge as an important area of research in the future.

At the microscale level, mechanical forces play a critical role in cell mechanics and motility. For example, Yang's laboratory has introduced an innovative experimental technique complemented by a corresponding computational fluid dynamics (CFD) model intended to investigate cell mechanics under dynamic loading conditions (Xu et al.). By applying Water-Hammer theories, they successfully evaluate and simulate the exerted stress on individual cells. This pioneering approach harmoniously merges microfluidic chips with a projectile pump, yielding insightful outcomes. This microfluidic-based methodology establishes a novel instrument for probing the dynamic mechanical properties of cells, presenting a fresh perspective for further exploration in this field. In another case, Zhou's laboratory has presented a noteworthy investigation detailing

an optical-tweezer-based platform that facilitates the assessment of both the chirality and frequency of human sperm rotation. These measurements can potentially serve as indicators of sperm motility and quality (Zhong et al.). To streamline the measurement system's complexity, the research team opted to determine the orientation of the sperm head along the optical axis within the optical trap, utilizing the intensity distribution patterns of micron-sized particles positioned off-focus. This study not only unveils promising avenues for future research on sperm rolling but also underscores the significance of integrating artificial intelligence imaging analysis within intracytoplasmic sperm injection treatment.

Exploring the effects of mechanical forces at various scales provides valuable insights into either physiological or pathological conditions. In physiological contexts, understanding the mechanical cues that regulate cell behavior and tissue homeostasis can aid in designing biomaterials, tissue engineering strategies, and regenerative medicine approaches. On the other hand, in pathological conditions such as cancer, cardiovascular diseases, and musculoskeletal disorders, aberrant mechanical forces can drive disease progression and tissue dysfunction. Thus, comprehending the mechanobiological mechanisms across multiple scales holds great potential for developing diagnostics, therapeutics, and interventions targeting various diseases. The Research Topic also presents the related results from Qiao's laboratory. They conducted a quantitative examination to explore the correlation between stent malapposition (SM) distance and stent thrombosis (Qu et al.). The findings reveal a notable rise in thrombus formation as the gap distance increases when the SM distance measures less than 150 μm. However, the thrombogenicity progression weakens once the gap distance exceeds 150 μm. Consequently, heightened attention is warranted when SM manifests with a 150 μm gap distance. Meanwhile, Long's laboratory undertook a comprehensive review encompassing the hemodynamic changes induced by partial hepatectomy during liver regeneration and the decoupling of mechanical forces within hepatic sinusoids (Wu et al.). This exploration encompassed factors such as shear stress, mechanical stretch, blood pressure, and tissue stiffness. The study delved into potential mechanosensor and the associated signaling pathways. Additionally, Xu's laboratory compiled a comprehensive summary elucidating the necessary biochemical signatures observed during cardiac fibrosis (Liu et al.). These signatures were classified into two distinct categories, static and dynamic, with a specific focus on the unique attributes of the heart. Researchers aim to pave the way for effective anti-fibrosis strategies in clinical therapy by comprehending these dynamic and static biomechanical characteristics.

In a separate investigation, Gong's laboratory examined the biomechanical properties of articular cartilage and subchondral bone in guinea pigs with spontaneous hip osteoarthritis (Gao et al.). Their report highlights the occurrence of morphological degeneration in cartilage preceding the degeneration of mechanical properties. These findings provide novel insights into the structural and micromechanical interplay underlying hip osteoarthritis, serving as a theoretical foundation for comprehending its formation and progression. Furthermore, Panzetta's laboratory expounded upon the effects of radiation on the expression ratio of YAP in the nucleus and cytoplasm, observing an increase in healthy cells and a decrease in breast cancer cells (La Verde et al.). These findings deepen our comprehension of the extracellular matrix's role and shed light on the impact of X-rays on YAP and lamin A/C expression. Such insights can inform radiation therapy optimization through refined dosage and timing.

By investigating the mechanical forces at different scales, we can unravel the hierarchy and interconnectivity inherent to mechanobiology. This knowledge enables us to decipher the fundamental principles governing mechanotransduction, mechanoresponses, and mechanosensing in biological systems. Moreover, it provides a foundation for developing innovative technologies and methodologies that can detect, quantify, and manipulate mechanical forces at the microscale, nanoscale, and beyond. Recognizing the importance of mechanical forces across multiple scales is crucial for advancing our understanding of fundamental biological processes and their implications in health and disease. Integrating multidisciplinary approaches, including engineering, biology, and physics, can provide comprehensive insights into the mechanobiological complexities and pave the way for transformative advancements in various fields, ranging from regenerative medicine to drug discovery. While our Research Topic merely scratches the surface of the mechanobiology field, we anticipate these findings will contribute to the broader comprehension of the intricate dynamics involved when mechanical forces propagate within multi-scale biological systems.

Author contributions

YL and G-KX wrote the editorial. All authors contributed to the article and approved the submitted version.

Funding

This study was supported by the Fundamental Research Funds for the Central Universities of China.

Conflict of interest

The authors declare that the research was conducted in the absence of any commercial or financial relationships that could be construed as a potential conflict of interest.

Publisher's note

frontiers | Frontiers in Bioengineering and Biotechnology

REVIEW
published: 28 June 2022
doi: 10.3389/fbioe.2022.953353

Insights into intercellular receptor-ligand binding kinetics in cell communication

Chenyi An[1,2], *Xiaohuan Wang*[3], *Fan Song*[4,5], *Jinglei Hu*[6]* and *Long Li*[4]*

[1]School of Biology and Engineering, Guizhou Medical University, Guiyang, China, [2]Department of Cell Biology and Department of Cardiology of the Second Affiliated Hospital, Zhejiang University School of Medicine, Zhejiang University, Hangzhou, China, [3]Department of Rehabilitation Medicine, Peking University Third Hospital, Beijing, China, [4]State Key Laboratory of Nonlinear Mechanics and Beijing Key Laboratory of Engineered Construction and Mechanobiology, Institute of Mechanics, Chinese Academy of Sciences, Beijing, China, [5]School of Engineering Science, University of Chinese Academy of Sciences, Beijing, China, [6]Kuang Yaming Honors School and Institute for Brain Sciences, Nanjing University, Nanjing, China

Cell-cell communication is crucial for cells to sense, respond and adapt to environmental cues and stimuli. The intercellular communication process, which involves multiple length scales, is mediated by the specific binding of membrane-anchored receptors and ligands. Gaining insight into two-dimensional receptor-ligand binding kinetics is of great significance for understanding numerous physiological and pathological processes, and stimulating new strategies in drug design and discovery. To this end, extensive studies have been performed to illuminate the underlying mechanisms that control intercellular receptor-ligand binding kinetics *via* experiment, theoretical analysis and numerical simulation. It has been well established that the cellular microenvironment where the receptor-ligand interaction occurs plays a vital role. In this review, we focus on the advances regarding the regulatory effects of three factors including 1) protein-membrane interaction, 2) biomechanical force, and 3) bioelectric microenvironment to summarize the relevant experimental observations, underlying mechanisms, as well as their biomedical significances and applications. Meanwhile, we introduce modeling methods together with experiment technologies developed for dealing with issues at different scales. We also outline future directions to advance the field and highlight that building up systematic understandings for the coupling effects of these regulatory factors can greatly help pharmaceutical development.

Keywords: cell communication, intercellular receptor-ligand binding kinetics, protein-membrane interaction, biomechanical force, bioelectric microenvironment

OPEN ACCESS

Edited by:
Guang-Kui Xu,
Xi'an Jiaotong University, China

Reviewed by:
Yunfeng Chen,
University of Texas Medical Branch at Galveston, United States
Li-Tang Yan,
Tsinghua University, China

***Correspondence:**
Jinglei Hu
hujinglei@nju.edu.cn
Long Li
lilong@lnm.imech.ac.cn

Specialty section:
This article was submitted to Biomechanics, a section of the journal Frontiers in Bioengineering and Biotechnology

Received: *26 May 2022*
Accepted: *09 June 2022*
Published: *28 June 2022*

Citation:
An C, Wang X, Song F, Hu J and Li L (2022) Insights into intercellular receptor-ligand binding kinetics in cell communication. Front. Bioeng. Biotechnol. 10:953353. doi: 10.3389/fbioe.2022.953353

INTRODUCTION

Cells communicate with their neighbors to sense, respond and adapt to outside world, and transduce crucial signals to shape their functions and determine their fate. The cell-cell communication process, which involves multiple length scales ranging from angstroms (specific binding of receptors and ligands), to tens of nanometers (length of receptor-ligand complex) to micrometers (lateral size of a typical adhesion zone), is mediated by the specific binding of receptor and ligand anchored in apposing membranes (Liu et al., 2014; Ju et al., 2016; Sudhof, 2018; Zhu et al., 2019a; Zhu et al., 2019b; Chen et al., 2019). The key parameters characterizing the intercellular binding of receptors and ligands are their binding kinetics that involve kinetic rates (on-rate, k_{on} and off-rate, k_{off}, defining

the velocities of bond formation and dissociation, respectively) and binding affinity ($K_a = k_{on} / k_{off} = [RL] / ([R][L])$, quantifying the strength of receptor-ligand interactions) (Hu et al., 2013; Liu et al., 2015). Here, [R], [L] and [RL] are densities of unbound receptors, unbound ligands and bound receptor-ligand complexes in equilibrium state, respectively. The binding kinetics of intercellular receptor-ligand interactions determine the extent of membrane receptors' transmembrane signaling during cell communication and thereby affect physiological and pathological cellular activities, such as immune responses, cell locomotion and cancer metastasis (Burdick et al., 2001; Huang et al., 2010; Chen and Zhu, 2013; Liu et al., 2014; Liu et al., 2015). For example, the binding kinetics of interactions between T cell receptor (TCR) and peptide major histocompatibility complex (pMHC) determine the recognition of T cells to different antigens and the processes of target cell killing, with accumulated receptor-ligand binding duration as a threshold for triggering T cells activation (Huang et al., 2010; Liu et al., 2014; Wu et al., 2019). Mutations in von Willebrand factor (VWF) and/or platelet glycoprotein Ib (GPIb), which alter their binding kinetics, induce hemostatic defects, such as von Willebrand disease (Ju et al., 2013). Considering the vital role of intercellular receptor-ligand binding kinetics in processing extracellular stimuli to direct cellular activities and their promising potential for biomedical applications, such as immunotherapies including monoclonal antibodies, chimeric antigen receptor T (CART) cells and TCR-T cells, the regulatory mechanisms responsible for the receptor-ligand binding kinetics and their transmembrane signaling have been hotspots in the fields of mechanobiology (Fagerberg et al., 2010; An et al., 2020; Li R. et al., 2020b; He et al., 2022).

Much of our early understanding of receptor-ligand binding kinetics came from *in vitro* three-dimensional (3D) measurements by surface plasmon resonance (SPR) for purified variants of the receptors and ligands that are removed from their cellular environment (Huang et al., 2012). The kinetics parameters are derived by SPR angle shifts when the mass of the surface layer changes due to receptor-ligand binding (Su and Wang, 2018). However, there are significant limitations for SPR in faithfully investigating receptor-ligand interactions due to the lack of physiological-mimicking conditions (Huang et al., 2010). For example, compared to *in vitro* 3D measurements in solution, the *in situ* receptor-ligand binding occurs in two dimensions (2D) with both proteins anchored in apposing membranes, resulting in different units for on-rate k_{on} (M^{-1} s^{-1} in 3D and μm^2 s^{-1} in 2D) and binding affinity K_a (M^{-1} in 3D and μm^2 in 2D) in different dimensions (Dustin et al., 2001). Thus, the binding kinetics measured by SPR cannot be used to derive reliable information on 2D binding. With the development of technology, various experimental techniques have been exploited to study the intercellular receptor-ligand binding kinetics, including fluorescence spectroscopy, micropipette aspiration, atomic force microscopy, and flow chamber (Krobath et al., 2009; Weikl et al., 2016). It has been well established that the *in situ* kinetics of receptor-ligand interactions depend not only on the receptor-ligand binding strength, but also on the cellular microenvironment. For example, utilizing live-cell based single-molecule biomechanical assay, Fan et al. showed that the bond lifetimes ($1 / k_{off}$) of stimulatory immune receptor NKG2D interacting with its ligands (e.g., MICA and MICB) are prolonged in the presence of mechanical force (Fan et al., 2022). The force-dependent bond lifetime and binding affinity are attributed to the conformational changes of ligands, enabling NKG2D to precisely discriminate ligands to differentially activate natural killer cell or T cell functions and fulfill proper immune responses (Fan et al., 2022). Chen et al. used a fluorescence dual biomembrane force probe to identify an intermediate state of integrin $\alpha IIb\beta_3$ with intermediate affinity and bond lifetimes by applying precisely controlled mechanical stimulations to platelets (Chen et al., 2019). They found that this intermediate state of integrin $\alpha IIb\beta_3$ regulates biomechanical platelet aggregation, which is responsible for the thrombus formation and growth. These studies provide new insights into the intercellular receptor-ligand binding kinetics in cell communication, and promising therapeutic strategies for the disease treatment. In this review, we summarize recent advances regarding the regulation of intercellular receptor-ligand binding kinetics by three *in situ* membrane-associated factors, including 1) protein-membrane interaction, 2) biomechanical force, and 3) bioelectric microenvironment, wherein modeling approaches and experiment technologies used to deal with issues at different scales are introduced. Further, we outline directions for dissecting functional mechanisms of intercellular receptor-ligand binding and indicate optimization strategies for biomedical applications.

PROTEIN-MEMBRANE INTERACTION

In contrast to the interactions of soluble proteins in solution, the interactions of membrane-anchored receptors and ligands during cell-cell communication are restricted to two-dimensional membrane environment, since the proteins can only diffuse laterally along the membranes (Krobath et al., 2009; Hu et al., 2013; Weikl et al., 2016). Central questions involve how the binding kinetics of membrane-anchored receptor and ligand are affected by protein-membrane interaction, which will be discussed in this section.

Membrane fluctuations

A membrane-anchored receptor can bind to a ligand anchored in apposing membrane only if the local membrane separation at the protein site is within binding range. Therefore, the binding of receptor and ligand molecules depends strongly on the local separation of the two membranes, which varies in time and space due to the thermal shape fluctuations of flexible membranes (Li and Song, 2016; Li and Song, 2018). As mentioned above, the intercellular communication process involves multiple length scales ranging from angstroms to micrometers. To deal with such complexity, coarse-grained mechanical models have been developed with suitable simplification and approximations (Krobath et al., 2009; Rozycki et al., 2010; Hu et al., 2013; Xu et al., 2015; Weikl et al., 2016). In the Monte Carlo (MC) simulation model, both adhering membranes are discretized

into small patches (Krobath et al., 2009; Xu et al., 2015). Then the membrane conformations can be described by the local intermembrane separation. By analogy to lattice-gas-type models, a membrane patch can only accommodate one receptor or ligand protein. The spatial distribution of receptor and ligand is then described by the composition field with values 0 or 1 indicating the absence or presence of protein at discretized patch. The membrane anchoring of receptor and ligand, which can rotate around their anchoring points, is regulated by the protein-membrane anchoring strength. To reflect the protein flexibility, the bead-spring model for polymer chains can be adopted. The specific binding of receptor and ligand shows a distance- and angle-dependent behavior. The configurational energy of the adhesion system then consists of membrane bending energy, receptor-ligand binding energy, as well as anchoring energy. This MC model basically captures the key events that occur in the adhesion zone. Another coarse-grained model is based on molecular dynamics (MD) technique (Hu et al., 2013; Hu et al., 2015). In the coarse-grained MD simulation model, several molecule groups are clustered into a single bead. This coarse graining procedure leads to a significant computational speed-up. Each lipid molecule, receptor and ligand proteins are represented by a set of beads connected *via* spring potential. A lipid molecule consists of hydrophilic and hydrophobic parts. Both lipid-anchored and transmembrane receptor and ligand proteins can be modeled. The thermodynamic properties of the adhesion system are determined by the conservative force. In comparison, the coarse-grained MC method has advantages in both computing scale and efficiency. Results from statistic mechanics theory and coarse-grained simulations indicate that the binding affinity and on-rate can be obtained from the relations: $K_a = \int K_a(l)P(l)dl$, $k_{on} = \int k_{on}(l)P(l)dl$, where $K_a(l)$ and $k_{on}(l)$ are the binding affinity and on-rate of receptor and ligand anchored to two planar and parallel membranes with fixed separation l, respectively (Hu et al., 2015; Weikl, 2018). The probability distribution of the local membrane separation $P(l)$ reflects the temporal and spatial variation of local membrane separation l and is associated with the membrane elasticity. For adhering membranes with a single type of receptor-ligand complex, this probability distribution $P(l)$ is usually assumed to be Gaussian with mean $\bar{l} = l$ and standard deviation $\xi_\perp = \sqrt{(l-\bar{l})^2}$ (Hu et al., 2015). $\xi_\perp$ is the relative roughness from thermally excited shape fluctuations and measures how strong the fluctuations of the two membranes are (Hu et al., 2013; Li et al., 2018b). The larger the roughness $\xi_\perp$, the stronger the membrane fluctuations and the more configurations the membranes can adopt. The formation of receptor-ligand complexes constrains the membrane thermal fluctuation, thus affecting the relative roughness. The relative roughness is proportional to the average distance between neighboring receptor-ligand complex $\xi_\perp \sim 1/\sqrt{[RL]}$ (Hu et al., 2013; Weikl, 2018).

At the optimal average membrane separation for receptor-ligand binding, theoretical and computational results consistently reveal that the binding affinity roughly scales as: $K_a \sim 1/\xi_\perp$ (Hu et al., 2013). Such an inverse proportionality results from the entropy loss of the flexible membranes upon the receptor-ligand binding. Coarse-grained MD simulations show that the on-rate k_{on} and off-rate k_{off} decrease and increase with increasing relative roughness, respectively, indicating that both k_{on} and k_{off} contribute to the roughness-dependence of K_a. Given the scaling relation $\xi_\perp \sim 1/\sqrt{[RL]}$, a modified law of mass action $[RL] \sim [R]^2[L]^2$ appears (Krobath et al., 2009; Hu et al., 2013). This quadratic dependence indicates cooperative binding of membrane adhesion proteins. The physical picture is that the formation of the receptor-ligand complexes suppresses membrane shape fluctuations which, in turn, facilitates the formation of additional receptor-ligand complexes. The feedback between the suppression of membrane fluctuations and the formation of receptor-ligand complexes gives rise to cooperativity in the process of receptor-ligand binding (Li et al., 2021b). Recently, Steinkühler et al. confirmed the binding cooperativity of 'marker of self' protein CD47 with the macrophage checkpoint receptor SIRPα using fluorescent recovery after bleaching (FRAP) assays, and found that membrane stiffening by regulating acidosis condition enhances the binding affinity (Steinkühler et al., 2019).

Different experimental methods for measuring the binding affinity have led to values differing by several orders of magnitude (Krobath et al., 2009). Note that mechanical methods measure the receptor-ligand binding kinetics during initial contacts. In contrast, fluorescence methods probe the binding kinetics in equilibrated zones (Weikl et al., 2016). Considering the fact that both the average membrane separation $\bar{l}$ and relative membrane roughness $\xi_\perp$ during initial membrane contacts are larger than that in equilibrated adhesion zones, the dependence of K_a on $\bar{l}$ and $\xi_\perp$ helps to understand why the values of K_a measured by mechanical and fluorescence methods differ by several orders of magnitude.

Protein-Lipid Interaction

The membrane proteins associate with cell membranes *via* transmembrane domains (e.g. integrins, cadherins) or glycosylphosphatidyl-inositol anchors (e.g. CD48). The anchoring to membranes is of particular importance for intercellular receptor-ligand interaction and protein function (**Figure 1A**). For example, an I232T mutation in Fcγ receptor, which is clinically relevant to systemic lupus erythematosus, alters the interaction between transmembrane helix of Fcγ receptor and membrane. As a result, the mutated Fcγ receptor allosterically tilts its ectodomain to a bent conformation, which attenuates its accessibility by ligands and thereby reduces its ligand-binding affinity (Hu et al., 2019). Meanwhile, the anchoring strength, characterizing the tilting of binding protein relative to the membrane, also plays an important role in the binding kinetics of receptor and ligand molecules, since it affects the loss in the rotational free energy upon the formation of a receptor-ligand complex. Therefore, soft anchoring of binding proteins decreases binding affinity and slower on-rate (Hu et al., 2015; Xu et al., 2015).

The interaction of protein and membrane may very likely generate local membrane curvature and accordingly affect the intercellular receptor-ligand interactions. Extensive studies have

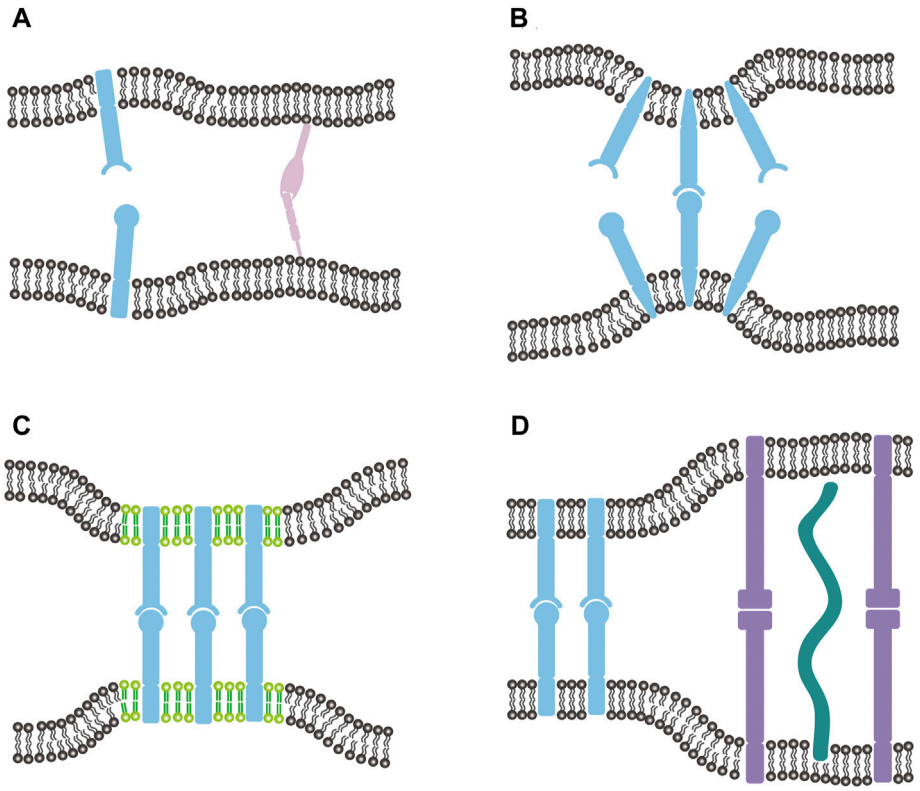

FIGURE 1 | (A) Two fluctuating membranes adhering *via* specific binding of transmembrane (light blue) and lipid-anchored (light purple) receptor and ligand proteins. Both the thermal shape fluctuations of membranes, which change the average membrane separation and relative membrane roughness, and the anchoring energy affect the receptor-ligand binding kinetics. **(B)** Wedge-shaped transmembrane proteins bend their associated membranes to induce membrane curvature. The local curvatures induced by receptor and ligand affect their binding kinetics by 1) altering the local separation and relative roughness of the two apposing membranes and 2) causing protein-protein *cis*-repulsion on each membrane. **(C)** Preferential partitioning of membrane-anchored receptors and ligands in the lipid rafts (light green) enhances the binding affinity of those proteins, which can be partially attributed to the entropy gain of the membranes resulting from raft-induced protein aggregation. **(D)** Adhering membranes linked *via* two types of membrane-anchored receptors and ligands with different lengths in the presence of glycocalyx (dark green). The difference in lengths between the shorter and longer receptor-ligand complexes, on the one hand, forms a steric barrier for the complex formation, on the other hand, facilitates protein aggregation to enhance binding. These two competing effects are additionally regulated by the presence of glycocalyx.

shown that transmembrane proteins of wedge shape, and peripheral proteins either inserting asymmetric amphipathic or hydrophobic structures into the bilayer or binding to the surface of one membrane monolayer are efficient ways to induce local membrane curvature (**Figure 1B**) (McMahon and Gallop, 2005; Ramakrishnan et al., 2014; McMahon and Boucrot, 2015). Crowding of monomeric hydrophilic protein domains bound to the membrane surface has also been shown to induce curvature (Stachowiak et al., 2012). MC simulations revealed that the local membrane curvatures induced by receptors and ligands affect their binding by 1) altering the local separation and relative roughness of the two adhering membranes, and 2) causing protein-protein *cis*-repulsion on each membrane (Li et al., 2019). Depending on the signs of the curvatures, the binding affinity increases or decreases with the curvatures. It suggests that the ability to induce membrane curvatures represents a molecular property of the adhesion proteins and should be carefully considered in experimental characterization of the binding affinity.

Local aggregation or clustering of the protein molecules also affects their binding kinetics. Cumulative evidence indicates that the membranes are not structurally homogeneous, but rather consist of microdomains enriched in saturated phospholipids and cholesterol (Lingwood and Simons, 2010; Sezgin et al., 2017). These microdomains, termed as lipid rafts, exist as distinct liquid-ordered phases that float freely as stable entities in the liquid-disordered matrix of the plasma membrane. Lipid rafts can lead to a heterogeneous distribution of proteins in the membranes by recruiting them to variable extents (**Figure 1C**) (Li L. et al., 2020a; Li et al., 2021c). The surface area and length of protein transmembrane domains as well as protein palmitoylation are the major factors determining the affinity of membrane proteins for lipid rafts (Lorent et al., 2017). It is generally believed that lipid rafts, serving as signaling platforms, can facilitate protein-protein interactions on the same membrane by virtue of spatial proximity of participating components. For intercellular receptor-ligand binding, *in situ* experimental studies have reported that lipid rafts help the binding of TCR to pMHC anchored to antigen-presenting cell membranes (Anderson and Roche, 2015). Disrupting the rafts in T cell membrane *via* cholesterol depletion with methyl-beta-cyclodextrin (MβCD) directly

reduces the binding affinity K_a, but increases the off-rate k_{off} of TCR-pMHC interaction (Huang et al., 2010). To further uncover the mechanism underlying the effect of lipid rafts on the intercellular receptor-ligand binding kinetics, these microdomains are incorporated into the coarse-grained MC model described above (Li et al., 2021b; Li et al., 2021c). The lipid rafts are modeled as dynamic patches experiencing the contact energy with their nearest neighbors. Similarly, the spatial distribution of lipid rafts is also described by the composition field. The association of receptor and ligand with lipid rafts is taken into account by introducing the coupling energy, i.e., the raft affinity to adhesion proteins. Simulation results from this multicomponent membrane system with biologically relevant parameters consistently show that the preferential partitioning of membrane-anchored receptor and ligand proteins in the lipid rafts significantly increases the binding affinity of those proteins, depending strongly on the properties of lipid rafts such as area fraction, size and the affinity of rafts to the proteins (Li et al., 2017b; Li et al., 2017c; Li et al., 2018a; Li et al., 2021d). This enhancement is traced back to the entropy gain of the membranes resulting from raft-induced protein aggregation. Contrary to the case of homogeneous membranes where the binding of the anchored receptor and ligand molecules is weakened by the shape fluctuations of the membranes, the membrane roughness actually functions as a positive regulator for the binding in collaboration with lipid rafts. The bending rigidity contrast between the lipid rafts and liquid-disordered domains further helps the aggregation of proteins and therefore facilitates the binding (Li et al., 2017b; Li et al., 2021b). These studies suggest that cells might regulate the binding kinetics of membrane-anchored receptors and ligands by modulating raft characteristics under physiological conditions.

Length Difference of Proteins

Length difference of proteins imposes a steric barrier for the bond formation and affects protein distribution, thus affecting the intercellular receptor-ligand binding kinetics. There are a variety of membrane-anchored receptor and ligand molecules with different lengths in adhesion zone (**Figure 1D**). For example, important receptor-ligand complexes in the T cell adhesion to antigen-presenting cells include the TCR-pMHC complex with a length of about 15 nm, the CD2-CD48 complex with approximately the same length as TCR-pMHC complex, and the LFA1-ICAM1 complex with a length of about 40 nm (Li et al., 2021a). The difference in lengths between the shorter and longer receptor-ligand complexes forms a steric barrier for the formation of the two types of protein complexes, thus affecting their binding kinetics. Milstein et al. utilized the planar bilayer system to examine the effect of difference in complex lengths by increasing the size of ligand CD48, and found that nanoscale increase in the length of CD2-CD48 complexes increases the average intermembrane spacing and decreases the adhesion strength of the receptor-ligand interaction (Milstein et al., 2008). Meanwhile, the difference in lengths between the shorter and longer receptor-ligand complexes can lead to a membrane-mediated repulsion between them because the lipid membranes have to be bent to compensate for the length mismatch, which costs elastic energy (Li et al., 2021a). Milstein et al. observed that both CD2-CD48 variant complexes with elongated ligand segregate from the CD2-CD48 wildtype complexes for specific protein densities (Milstein et al., 2008). Experimental studies of a T cell adhering to supported bilayer with pMHC and ICAM1 have also showed that intercellular protein complexes with different lengths segregate and form characteristic special patterns with a central domain of TCR-pMHC complexes surrounded by a ring-shaped domain of LFA1-ICAM1 complexes for a range of protein densities and affinities (Grakoui et al., 1999; Hammer et al., 2019). Of note, several other mechanisms based on the active transport by actin cytoskeleton, signaling, pre-clustering of TCRs have also been proposed for the formation of the bull's-eye pattern during T-cell adhesion (Dustin and Cooper, 2000; Choudhuri and Dustin, 2010; Lillemeier et al., 2010; Hammer et al., 2019; Li et al., 2021a). These mechanisms certainly do not need to be mutually exclusive, but instead work together to contribute to the pattern formation. MC simulations and statistical-mechanical calculations for two types of anchored ligands binding to different cell receptors showed that coexistence of domains enriched in the shorter and longer receptor-ligand complexes requires equal effective binding strengths (Rozycki et al., 2010). This length difference-induced protein aggregation will locally affect the binding kinetics of each type of receptor and ligand (e.g., increase the on-rate constant) due to cooperative binding discussed above.

In addition to specific binders, the cells are also covered with anchored polymers or glycoprotein (**Figure 1D**). These repulsive repellers protruding from both membranes form a protective barrier, the glycocalyx, and can impose an additional steric barrier for the formation of receptor-ligand complexes with a length shorter than that of repellers. Interestingly, the composition and expression level of glycocalyx change markedly with cell fate transitions and cell type. Mulivor and Lipowsky (2002) experimentally observed that removal of the glycocalyx with heparinase increases leukocyte-endothelial cell adhesion, leading to the conclusion that the glycocalyx presents a physical barrier to adhesion and that the shedding of glycocalyx during natural activation of endothelial cells may be an essential part of the inflammatory response. Lorz et al. (2007) analyzed the adhesion of giant vesicles decorated with sialyl-Lewis^X ligands and lipopolymers to E-selectin-functionalized substrate by means of reflection interference contrast microscopy and found that the lipopolymers decrease the affinity of receptor-ligand binding. Paszek et al. (2014) found that the overall rate of integrin bond formation reduces in the presence of the glycocalyx. Recent simulation and theoretical studies investigate the binding kinetics of a few and a large number of bonds in the presence of the glycocalyx, representing the cases of initial and mature stages of cell adhesion, respectively (Xu et al., 2016). It is found that the glycocalyx affects the binding kinetics differently for the two cases in the force loading case. More specifically, increasing thickness and stiffness of the glycocalyx decreases the binding affinity for a few bonds, but has negligible effect on the affinity for a large number of bonds. Meanwhile, the thicker glycocalyx is shown to facilitate the clustering of receptors,

consistent with the experimental results by Paszek et al. (2014), showing the cancer glycocalyx enhances integrin clustering into focal adhesions and promotes cell growth and survival. These results suggest that the glycocalyx are attractive targets for therapeutic interventions that aim at mediating receptor-ligand interaction.

Studies on the effects of protein-membrane interaction on the receptor-ligand binding kinetics have provided routes and strategies for novel therapies. Extensive studies have revealed that the lipid rafts are involved in a variety of diseases, such as cancer, viral infection, neurodegenerative diseases (e.g., Alzheimer, Parkinson and Prion diseases), immunological diseases (e.g., systemic lupus erythematosus) (Simons and Ehehalt, 2002; Vona et al., 2021). In view of the critical role of lipid raft in cell adhesion and migration by regulating intercellular receptor-ligand binding, therapeutic strategies targeting lipid raft by modulating cholesterol have opened exciting new avenues for cancer prevention and treatment (Vona et al., 2021). Lipid rafts also contribute to the binding and entry of different viruses to host cells, including human immunodeficiency virus (HIV) and coronaviruses. Take the syndrome coronavirus-2 (SARS-CoV-2) for example, it reveals that lipid rafts provide a functional platform able to concentrate angiotensin-converting enzyme-2 (ACE-2), the main receptor for SARS-CoV-2, on the host cell membrane, which facilitates the interaction of ACE-2 with the spike protein on viral envelope (Sorice et al., 2021). Lipid raft disruption by drugs (e.g., stains and cyclodextrins) can lead to reduced SARS-CoV-2 infectivity. The effect of lipid rafts targeting drugs on the infectious process of coronavirus introduces a new potential task in the pharmacological approach against coronavirus that currently ravages the world. Glycocalyx has also been an attractive target for therapeutic interventions due to its implication in the platelet and leucocyte adhesion, inflammatory processes by affecting intercellular receptor-ligand binding. Therapeutic strategies designed to restore the glycocalyx have led to promising results both in the treatment of chronic vascular disease and in an acute critical care setting (Becker et al., 2010). In addition, editing the cancer cell glycocalyx with an antibody-enzyme conjugate to intervene the intercellular receptor-ligand binding between natural killer cell and cancer cell is shown to enhance tumor cell susceptibility to antibody-dependent cell-mediated cytotoxicity (ADCC), thus providing a promising approach to cancer immune therapy (Xiao et al., 2016). Together, an in-depth study regarding the effect of protein-membrane interaction on the receptor-ligand binding kinetics will further provide potential therapeutic strategies and targets for disease prevention and treatment.

BIOMECHANICAL FORCES

Benefitting from the development of biomechanical techniques, researches on mechanobiology have leaped ahead in the past decades (Su and Ju, 2018; Zhu et al., 2019a; Wang et al., 2022). Biomechanical tools, such as traction force microscopy, micropillar array and DNA force probe, have definitely confirmed the existence of biomechanical forces actively exerted by single cells to their binding partners through receptor-ligand interactions (Wang and Ha, 2013; Bashour et al., 2014; Liu et al., 2016; Colin-York et al., 2019; Ma et al., 2019). Further, single-molecule force spectroscopy (SMFS) techniques, mainly including atomic force microscopy (AFM), optical tweezers (OT), magnetic tweezers (MT) and biomembrane force probe (BFP), resolve biomechanical regulatory mechanisms of intercellular receptor-ligand binding kinetics in single-molecule level (Neuman and Nagy, 2008; Brenner et al., 2011; Liu et al., 2015). These novel techniques have revealed crucial biomechanical regulatory effects on intercellular receptor-ligand binding kinetics, which is an unachievable task for ensemble protein based biochemical methods, such as SPR (Liu et al., 2015; Zhu et al., 2019a). Force-dependent binding kinetics were firstly proposed by Bell in 1978, demonstrating that mechanical force exponentially accelerates molecular bond dissociation (slip bond) (Bell, 1978). Along with the development of SMFS techniques, a series of catch bonds, whose dissociation rates are conversely slowed down by mechanical forces, are found to play essential roles in cellular activities, such as trafficking, adhesion and antigen recognition (Marshall et al., 2003; Chen et al., 2010; Wu et al., 2019). For example, catch bond is directly observed by AFM measurement of P-selectin/P-selectin glycoprotein ligand-1 (PSGL-1) interaction, correlating with leukocyte adhesion to vascular surfaces under dynamic shear stress applied by blood flow (**Figure 2A**) (Marshall et al., 2003). The average lifetime ($1/k_{off}$) ranking of different TCR-pMHCs bonds at zero force is completely reversed by 10 pN force due to catch bond behavior of agonist pMHCs, and the lifetime ranking under 10 pN force perfectly matches peptide potency, suggesting a crucial role of biomechanical force during TCR-based antigen recognition process (Liu et al., 2014). In addition, "ideal bonds", whose dissociation rates are insensitive to the sustaining forces, are also found in cadherin adhesion (Rakshit et al., 2012). Noting that these crucial regulatory mechanisms are undetectable by conventional biochemical methods, which measure receptor-ligand binding kinetics in force-free manners (Liu et al., 2014; Wu et al., 2019).

Moreover, in contrast to purified protein based biochemical methods, live cell based SMFS techniques detect membrane receptor-ligand binding kinetics in a more physiological-relevant cellular microenvironment and provide opportunities for dissecting the biomechanical-chemical coupling signal transduction circuits (An and Chen, 2021). As a representative example, integrins can adopt three kinds of conformational states: bent-closed, extended-closed and extended-open conformations, which are strongly associated with their ligand binding strength (Chen et al., 2010; Chen et al., 2019). The equilibrium of the three states can be altered by biomechanical forces induced by ligand binding (outside-in), as well as chemical inside-out signaling events (**Figure 2B**) (Chen et al., 2010; Chen et al., 2012; Springer and Dustin, 2012; Li J. et al., 2017a; Chen et al., 2019). The interaction between VWF and GPIb under biomechanical tension induces platelet integrin conformational shifts from bent-closed (low-affinity) state to extended-closed (intermediate-affinity) state, as an inside-out signaling pathway

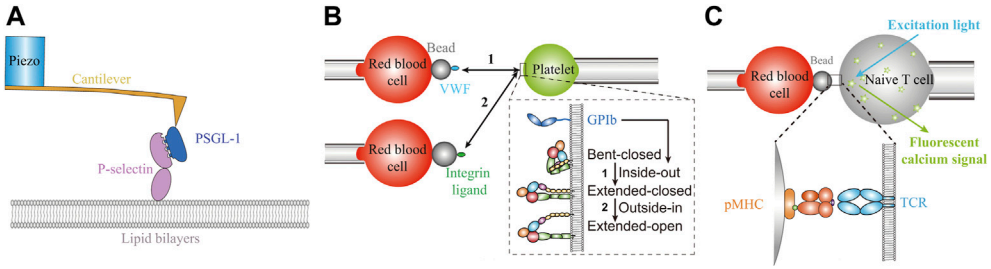

FIGURE 2 | Biomechanical regulations of membrane receptors' functions revealed by SMFS techniques. **(A)** AFM dissecting biomechanical regulations on the interaction of P-selectin and PSGL-1 [Adapted from Ref. (An et al., 2017)]. **(B)** Dual BFP system revealing biomechanical-chemical coupling signal transduction circuits on platelet. **(C)** Fluorescent imaging integrated BFP system digitalizing the triggering threshold of TCR [Adapted from Ref. (An et al., 2017)].

for integrin activation (**Figure 2B**) (Ju et al., 2016; Chen et al., 2019). Further mechanical affinity maturation of the intermediate integrins demands outside-in signaling, with ligand binding under biomechanical tension as a requirement (**Figure 2B**) (Chen et al., 2019). Based on this biomechanical signal transduction circuit, integrin functions as a mechanosensor to mediate platelet adhesion and aggregation processes (Chen et al., 2019). In this regard, live cell based SMFS techniques outperform conventional biochemical methods in revealing the mechano-chemistry of membrane receptor-ligand binding and dissecting their functional mechanisms (Chen et al., 2010; Chen et al., 2012; Chen et al., 2019).

The incorporation of fluorescent spectroscopy into SMFS techniques further allows correlating intercellular receptor-ligand binding kinetics with intracellular signaling cascades, thereby resolving the transmembrane signaling transduction mechanisms of membrane receptors (Kim et al., 2009; He et al., 2012; Liu et al., 2014; Hu and Butte, 2016; Ju et al., 2016; Feng et al., 2017; Brazin et al., 2018). For example, fluorescent imaging integrated BFP successfully quantified the relationship between force-regulated bond lifetimes of intercellular receptor-ligand interactions and intracellular C_a^{2+} signaling, revealing the triggering mechanisms of crucial membrane receptors on T cells and platelets (Liu et al., 2014; Ju et al., 2016). For TCR-pMHC interactions, catch bonds potentiate their bond lifetimes and reach maximum at ~10 pN, where C_a^{2+} responses are also strongest (Liu et al., 2014). Detailed analyses of the series binding-dissociation dynamics with the concurrent fluorescent C_a^{2+} signals suggest that T cells exhibit C_a^{2+} signals only when accumulated bond lifetime exceeds 10 s during the first 60 s, digitalizing the threshold for TCR triggering (**Figure 2C**) (Liu et al., 2014). Similarly on platelet, GPIb-VWF interactions under stretching forces induce cooperative unfolding processes of two separate domains in GPIb, determining the intensity and type of C_a^{2+} signals in platelets and transducing extracellular biomechanical stimuli into intracellular biochemical signaling cascades (Ju et al., 2016). More comprehensive biomechanical regulations on membrane receptor-ligand binding kinetics have been summarized in published review articles (Liu et al., 2015; Zhu et al., 2019a; Zhu et al., 2019b; An and Chen, 2021).

In most of the aforementioned single-molecule researches, receptor-ligand bond lifetimes are collected under constant forces (known as force-clamp assay) to reveal biomechanical regulatory mechanisms of intercellular receptor-ligand binding kinetics. However, biomechanical forces sustained by intercellular receptor-ligand bonds are dynamic *in situ*, rather than constant. Experimentally, cytoskeletal forces transducing to and exerting on intercellular receptor-ligand bonds are revealed to be dynamic by traction force microscopy (Colin-York et al., 2019). Moreover, a "motor-clutch" model has been proposed to theoretically characterize the dynamic traction forces induced by myosin movements (Chan and Odde, 2008). The cyclic traction forces sustained by the membrane receptor-ligand molecular bonds depend on substrate stiffness, where softer substrates give rise to larger traction forces (Chan and Odde, 2008; Elosegui-Artola et al., 2016). It has been found that the dynamic force waveforms with different force application histories experienced by the receptor-ligand bonds would affect their dissociation rates and determine membrane receptors' functions (Kong et al., 2013; Zhu et al., 2019b). For example, cyclic forces applied to integrin-ligand bond result in bond lifetime reinforcement, manifesting a "cyclic mechanical reinforcement" effect (Kong et al., 2013). In this way, the physiologically relevant dynamic forces on intercellular receptor-ligand bonds would potentially enforces more delicate regulations on membrane receptors' functions. Nevertheless, how to accurately and efficiently investigate the biomechanical force dynamics sustained by *in situ* intercellular receptor-ligand bonds are still problems unresolved.

Complementary to the experiments, all-atom MD simulations have been extensively used to uncover the mechanisms underlying the regulation of biomechanical forces in the receptor-ligand binding kinetics by providing high temporal resolution and atomic details (Hu et al., 2019; Wu et al., 2019; Fan et al., 2022). In contrast to the coarse-grained MD model, all-atom MD simulation method models the native structure of a protein at atomic detail, and all-atom force fields are used for every type of atoms in the receptor-ligand binding system, including hydrogen. Atomic trajectories are then calculated by

solving Newton's Laws of motion. Compared to the coarse-grained simulation method, the computational expense of explicitly modeling every atom limits the atomistic MD simulation to a timescale up to tens of nanoseconds. Fan et al. performed atomistic MD simulation to study the force-strengthened binding affinity and bond lifetimes of NKG2D and MICA. They found that additional hydrogen bond forms at the NKG2D-MICA binding interface in response to the mechanical force. The force-induced ligand conformational changes impede MICA dissociation under force, thus illuminating the molecular basis for this force-strengthened NKG2D-MICA binding (Fan et al., 2022). Similarly, the force-induce formation of additional hydrogen bonds also occurs at the TCR and pMHC binding interface, which contribute to TCR-pMHC catch bonds and T cell activation (Wu et al., 2019). This force-induced conformational changes in pMHCs help to explain why the T cell-based immunotherapies do not work for some cancer patients (Wu et al., 2019). These atomistic molecular dynamics studies definitely provide insights into the detailed molecular mechanisms of receptor-ligand binding, potentially aiding the design of pharmaceuticals.

Resolving the biomechanical regulatory mechanisms of intercellular receptor-ligand binding kinetics would further contribute to biomedical applications. Immunotherapies, such as monoclonal antibodies, bi-/tri-specific antibodies, CAR-T cells, and TCR-T cells, have efficiently revolutionized cancer treatment (Melero et al., 2007; Rapoport et al., 2015; Garber, 2018; Brinkmann and Kontermann, 2021; Seung et al., 2022). The binding affinity of these reagents versus their respective targets is one of the most instructive parameters in their screening and optimization processes (Labrijn et al., 2019; Staflin et al., 2020; Choe et al., 2021). Although current methodologies, such as SPR, yeast display etc., have efficiently filtered low-affinity candidates, the effects of physiological-relevant biomechanical forces on the expected interactions have been neglected (Malmqvist, 1993; Hoogenboom, 2005; Yang et al., 2016; An et al., 2020; Li R. et al., 2020b). Immune checkpoint blockade monoclonal antibodies are assumed to block inhibitory immune receptors in a soluble (force-free) state. However, *in vivo* imaging assay suggests that myeloid cells capture programmed cell death protein-1 (PD-1) antibody through Fcγ receptor-Fc interactions soon after injection, linking PD-1 expressing T cells to another cell and thereby sustaining biomechanical forces similar to membrane-anchored receptor-ligand interactions (Arlauckas et al., 2017). Thus, the blocking effects of the monoclonal antibodies would rely on not only their force-free affinity but the off-rate under biomechanical forces (An et al., 2020). In this regard, BFP-based force-dependent k_{off} measurements of three approved PD-1 antibodies versus PD-1 have been found to outperforms SPR measurements in correlating with their clinical responses (An et al., 2020). The scenarios are similar in bi-/tri-specific antibodies, CAR-T cells, and TCR-T cells, where the expected effective molecular bonds also sustain biomechanical forces. As aforementioned, the average TCR-pMHC bond lifetime ranking can even be reversed by biomechanical forces (Liu et al., 2014). Therefore, taking into account the regulatory effects of biomechanical forces is promising in further optimizing the screening process and improving clinical responses of the immunotherapeutic candidates. Moreover, pathological stiffness alterations have been reported in many diseases, not restricted to cancer (Wuerfel et al., 2010; Tian et al., 2015; Liu et al., 2017). The stiffness alterations affect the biomechanical forces exerting on membrane receptor-ligand bonds (Chan and Odde, 2008; Lei et al., 2021). The stiffness of cancer cells can even affect the response of immunotherapies (Lei et al., 2021; Tello-Lafoz et al., 2021; Tello-Lafoz et al., 2022). Therefore, investigating the biomechanical regulations on intercellular receptor-ligand binding kinetics in depth would provide new strategies for biomedical applications in the near future.

BIOELECTRIC MICROENVIRONMENT

Bioelectric cues surrounding membrane receptors, mainly including membrane potential, charged lipid components, ion flux, etc. (**Figure 3**), are also crucial biophysical regulators for cells throughout cell lifespan, e.g., modulating key cellular activities including proliferation, differentiation and morphological alterations (Yang and Brackenbury, 2013; Chang and Minc, 2014; Zhou et al., 2015; Boedtkjer and Pedersen, 2020). Especially for neurons, their neuronal activities including neuronal synapse formation, plasticity, maturation, elimination and neuronal excitability are all controlled by dynamic action potential and spontaneous neurotransmitter release (Chubykin et al., 2007; Flavell and Greenberg, 2008; Catterall, 2010; Epsztein et al., 2011; Kwon et al., 2012; Lee et al., 2012; Peixoto et al., 2012; Bian et al., 2015; Sudhof, 2018). The investigations on molecular mechanisms underlying these bioelectrical regulations are mostly confined to ion channels and intracellular signaling cascades (Flavell and Greenberg, 2008; Catterall, 2010; Zhou et al., 2015). Among these studies, the structural and functional mechanisms of voltage-gated ion channels have been thoroughly resolved, where the transmembrane helices in the ion channels perform allosteric alterations in response to membrane potential changes, known as 'helix-sliding' (Catterall, 2010). However, whether and how non-ion-channel membrane receptors, as the sensors of cells to collect outside stimuli by interacting with ligands anchored in apposing membrane, response to bioelectric alterations and then adjust their binding kinetics with ligands remain largely unknown.

There are indications that membrane potential directly regulates receptor-ligand binding kinetics. Take for example the G-protein coupled receptors (GPCRs), which have been widely investigated due to their prevalent expression patterns and paramount biomedical significance (Hopkins and Groom, 2002; Mahaut-Smith et al., 2008; Vickery et al., 2016). Similar to aforementioned voltage-gated ion channels, a number of GPCRs have been shown to be membrane potential-sensitive, and the binding kinetics of soluble ligand to GPCRs are demonstrated to be membrane potential-dependent (Ben-Chaim et al., 2006; Mahaut-Smith et al., 2008). All-atom MD studies revealed that membrane potential changes induce conformational alterations inside the transmembrane domains of GPCRs, which constructs

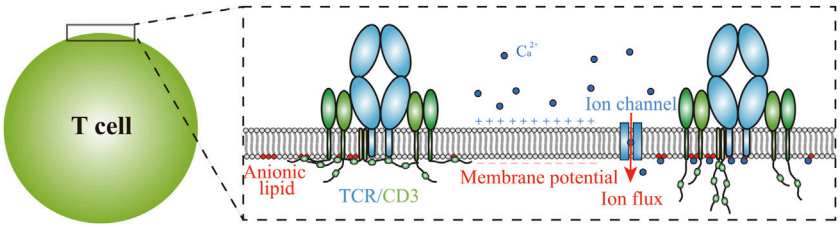

FIGURE 3 | Bioelectric cues surrounding TCRs on T cell membranes. The bioelectric cues that potentially affect TCR functions include membrane potential, ion flux and anionic lipids in the inner cell membranes. Ca^{2+} flux induced by TCR triggering impedes the electrostatic interaction between anionic lipids and the basic rich regions in CD3 tails.

the ligand binding site and the intracellular effector binding site, accordingly altering their ligand binding affinity, as well as the signaling cascades (Ben-Chaim et al., 2006; Rinne et al., 2015; Vickery et al., 2016). In addition, the effects of membrane potential on GPCRs binding are GPCR-specific and ligand-dependent, indicating delicate modulations of GPCRs to cellular activities (Ben-Chaim et al., 2006; Navarro-Polanco et al., 2011; Rinne et al., 2015). More importantly, the membrane potential-induced conformational change that underlies receptor binding ability would potentially be utilized as a general principle to regulate the intercellular binding kinetics of adhesion GPCRs to ligands anchored in apposing membrane (Vizurraga et al., 2020).

It should be noted that bioelectric cues surrounding membrane receptors are actually interconnected. One of the representative examples is that membrane potential modulates the distribution of anionic lipids, such as phosphatidylserine (PS) and phosphatidylinositol 4,5-biphosphate (PIP2) (Zhou et al., 2015). These anionic lipids not only affect the localization of cytosolic proteins, such as K-Ras and synaptotagmin-1, but potentially lead to the aggregation of membrane receptors with positively charged regions in their cytoplasmic domains (Shi et al., 2013; Park et al., 2015; Zhou et al., 2015). These distributional alterations can affect intercellular receptor-ligand binding affinity through cooperative binding and accordingly modulate receptor triggering (van der Merwe and Dushek, 2011; Hu et al., 2013). Besides, the electrostatic interactions between anionic lipids and positively charged cytoplasmic tails of membrane receptors are further modulated by ion fluxes (Shi et al., 2013). For example, local C_a^{2+} concentration enhancement induced by TCR triggering shields the anionic lipids and releases CD3 tails from membrane to facilitate its tyrosine phosphorylation (**Figure 3**) (Shi et al., 2013). Although these conformational changes occur mainly in the intracellular domain of membrane receptors, the possibility that the intercellular receptor-ligand binding kinetics undergoes allosteric modulations cannot be excluded (Hong et al., 2018). The reasonable scenario is that membrane receptors orchestrate different bioelectric cues to finely tune their ligand binding kinetics and thereby modulate downstream signaling cascades transduced across cell membranes, needs to be further verified.

Although studies regarding bioelectric regulations on intercellular receptor-ligand binding kinetics are still limited due to the lacking of efficient tools, the aforementioned researches provide promising pathways to achieve a significant breakthrough in biomedical applications. For GPCR-targeting medicines, valuable information on voltage-induced conformational changes in GPCRs can be exploited to study novel therapeutic pathways and contributes to biomedical treatments, such as cardiovascular drug development (Navarro-Polanco et al., 2011; Vickery et al., 2016). In view of the aforementioned bioelectric modulation that positively charged CD3 tails are shielded by anionic lipids in the inner cell membranes of T cells in resting states, new strategies for potentiating CAR-T cell persistence have been proposed, where the basic rich sequence of CD3 tail is incorporated into CAR-T design (Shi et al., 2013; Wu et al., 2020). Research on the effect of bioelectric microenvironment on the intercellular receptor-ligand binding is just unfolding. Further resolving the bioelectric regulatory mechanisms of intercellular receptor-ligand binding kinetics would undoubtedly inspire new strategies for biomedical applications.

CONCLUSION AND PERSPECTIVE

Cells communicate with their immediate neighbors by intercellular interactions of membrane-anchored receptors and ligands to govern numerous biological processes, such as signal transduction, tissue formation, immune responses, as well as cancer invasion and metastasis (Krobath et al., 2009; Briquez et al., 2020; Cho et al., 2021; Li et al., 2021d; Li Y. et al., 2021e). The two-dimensional receptor-ligand interactions have attracted extensive attention in the past decades, due to their great potential to stimulate new strategies in drug design and improve disease prevention and treatment. The key parameters quantifying the intercellular receptor-ligand interactions are their binding kinetics. In sharp contrast to the binding in solution, the intercellular binding kinetics appear to depend strongly on the cellular microenvironment, requiring more in-depth investigation to elucidate the regulatory mechanisms. This review summarizes the advances regarding the regulatory effects on the intercellular receptor-ligand binding kinetics mainly from three aspects: 1) protein-membrane interaction, 2) biomechanical force, and 3) bioelectric microenvironment. We introduce modeling methods and experiment technologies

developed for dealing with issues at different scales and provide insights into the underlying mechanisms. Meanwhile, we outline future directions to advance the fields of intercellular receptor-ligand binding kinetics and drug discovery. For example, the dynamic nature of biomechanical forces sustained by the intercellular receptor-ligand bonds under physiological conditions needs to be accurately quantified, and how the dynamic forces affect the intercellular binding kinetics also needs to be further illuminated. In addition, the role of bioelectric microenvironment in intercellular interactions has become a pressing issue to be solved. These prospective studies would contribute to identifying potential new strategies for drug development and disease therapy.

In fact, these regulatory factors for the intercellular receptor-ligand binding kinetics, which are investigated separately in general, are not mutually exclusive but instead are closely interrelated. For example, mechanical tension within the axons contributes to clustering of neurotransmitter vesicles at presynaptic terminals, which is implicated in neurotransmission efficiency and electrical activity at the synapse (Siechen et al., 2009). In addition, the bioelectric microenvironment surrounding membranes can change their mechanical property (e.g., bending rigidity) (Faizi et al., 2019), which in turn affects the thermal shape fluctuations of flexible membranes, thus leading to the alternation of intermembrane local separation and dynamic force sustained by the intercellular receptor-ligand bonds. To obtain a comprehensive understanding of intercellular receptor-ligand binding kinetics under physiological conditions for the discovery of more effective drugs, further studies on coupling effect of regulatory factors on the intercellular binding kinetics based on more complicated multiparameter systems are needed. Coupled with innovations in technology, the results of future studies will keep contributing to the rational design of clinically effective drug and promoting the transition from a promising field of intercellular receptor-ligand binding kinetics to medical application.

AUTHOR CONTRIBUTIONS

LL and JH contributed to conception and design of the study. CA, XW, LL, and JH wrote the first draft of the manuscript. All authors contributed to manuscript revision, read, and approved the submitted version.

FUNDING

LL, JH, CA, and FS acknowledge support from the National Natural Science Foundation of China (Grant Nos. 11902327, 11972041, 12102389, 22161132012, 21973040), Youth Innovation Promotion Association CAS, China Postdoctoral Science Foundation (Grant No. 2020M681834).

REFERENCES

An, C., and Chen, W. (2021). Multiplexed single-molecule force spectroscopy for dissecting biophysical regulation of membrane receptors functions on live cells. *Biophys. Rep.* 7, 377–383.

An, C., Hu, W., Gao, J., Ju, B.-F., Obeidy, P., Zhao, Y. C., Tu, X., Fang, W., Ju, L. A., and Chen, W. (2020). Ultra-stable biomembrane force probe for accurately determining slow dissociation kinetics of PD-1 blockade antibodies on single living cells. *Nano Lett.* 20, 5133–5140. doi:10.1021/acs.nanolett.0c01360

An, C.Y., Fei, P.Y., and Chen, W. (2017). Power of one: Investigating protein dynamic functions using single-molecule force spectroscopy (in Chinese). *Chin J Biochem Mol Biol* 33, 965–978. doi:10.13865/j.cnki.cjbmb.2017.10.01

Anderson, H. A., and Roche, P. A. (2015). MHC class II association with lipid rafts on the antigen presenting cell surface. *Biochimica et Biophysica Acta (BBA) - Molecular Cell Research* 1853, 775–780. doi:10.1016/j.bbamcr.2014.09.019

Arlauckas, S. P., Garris, C. S., Kohler, R. H., Kitaoka, M., Cuccarese, M. F., Yang, K. S., Miller, M. A., Carlson, J. C., Freeman, G. J., Anthony, R. M., Weissleder, R., and Pittet, M. J. (2017). *In Vivo*v imaging reveals a tumor-associated macrophage-mediated resistance pathway in anti-PD-1 therapy. *Sci. Transl. Med.* 9, eaal3604. doi:10.1126/scitranslmed.aal3604

Bashour, K. T., Gondarenko, A., Chen, H., Shen, K., Liu, X., Huse, M., Hone, J. C., and Kam, L. C. (2014). CD28 and CD3 have complementary roles in T-cell traction forces. *Proc. Natl. Acad. Sci. U.S.A.* 111, 2241–2246. doi:10.1073/pnas.1315606111

Becker, B. F., Chappell, D., Bruegger, D., Annecke, T., and Jacob, M. (2010). Therapeutic strategies targeting the endothelial glycocalyx: acute deficits, but great potential. *Cardiovascular Research* 87, 300–310. doi:10.1093/cvr/cvq137

Bell, G. I. (1978). Models for the Specific Adhesion of Cells to Cells. *Science* 200, 618–627. doi:10.1126/science.347575

Ben-Chaim, Y., Chanda, B., Dascal, N., Bezanilla, F., Parnas, I., and Parnas, H. (2006). Movement of 'gating charge' is coupled to ligand binding in a G-protein-coupled receptor. *Nature* 444, 106–109. doi:10.1038/nature05259

Bian, W.-J., Miao, W.-Y., He, S.-J., Qiu, Z., and Yu, X. (2015). Coordinated spine pruning and maturation mediated by inter-spine competition for cadherin/catenin complexes. *Cell* 162, 808–822. doi:10.1016/j.cell.2015.07.018

Boedtkjer, E., and Pedersen, S. F. (2020). The acidic tumor microenvironment as a driver of cancer. *Annu. Rev. Physiol.* 82, 103–126. doi:10.1146/annurev-physiol-021119-034627

Brazin, K. N., Mallis, R. J., Boeszoermenyi, A., Feng, Y., Yoshizawa, A., Reche, P. A., Kaur, P., Bi, K., Hussey, R. E., Duke-Cohan, J. S., Song, L., Wagner, G., Arthanari, H., Lang, M. J., and Reinherz, E. L. (2018). The T Cell Antigen Receptor α Transmembrane Domain Coordinates Triggering through Regulation of Bilayer Immersion and CD3 Subunit Associations. *Immunity* 49, 829–841. doi:10.1016/j.immuni.2018.09.007

Brenner, M. D., Zhou, R., and Ha, T. (2011). Forcing a connection: impacts of single-molecule force spectroscopy on *In Vivo*in v tension sensing. *Biopolymers* 95, 332–344. doi:10.1002/bip.21587

Brinkmann, U., and Kontermann, R. E. (2021). Bispecific antibodies. *Science* 372, 916–917. doi:10.1126/science.abg1209

Briquez, P. S., Hauert, S., de Titta, A., Gray, L. T., Alpar, A. T., Swartz, M. A., and Hubbell, J. A. (2020). Engineering targeting materials for therapeutic cancer vaccines. *Front. Bioeng. Biotechnol.* 8, 19. doi:10.3389/fbioe.2020.00019

Burdick, M. M., McCarty, O. J. T., Jadhav, S., and Konstantopoulos, K. (2001). Cell-cell interactions in inflammation and cancer metastasis. *IEEE Eng. Med. Biol. Mag.* 20, 86–91. doi:10.1109/51.932731

Catterall, W. A. (2010). Ion channel voltage sensors: Structure, function, and pathophysiology. *Neuron* 67, 915–928. doi:10.1016/j.neuron.2010.08.021

Chan, C. E., and Odde, D. J. (2008). Traction dynamics of filopodia on compliant substrates. *Science* 322, 1687–1691. doi:10.1126/science.1163595

Chang, F., and Minc, N. (2014). Electrochemical control of cell and tissue polarity. *Annu. Rev. Cell Dev. Biol.* 30, 317–336. doi:10.1146/annurev-cellbio-100913-013357

Chen, W., Lou, J., Evans, E. A., and Zhu, C. (2012). Observing force-regulated conformational changes and ligand dissociation from a single integrin on cells. *J. Cell Biol.* 199, 497–512. doi:10.1083/jcb.201201091

Chen, W., Lou, J., and Zhu, C. (2010). Forcing Switch from Short- to Intermediate- and Long-lived States of the αA Domain Generates LFA-1/ICAM-1 Catch

Bonds. *Journal of Biological Chemistry* 285, 35967–35978. doi:10.1074/jbc.M110.155770

Chen, W., and Zhu, C. (2013). Mechanical regulation of T-cell functions. *Immunol. Rev.* 256, 160–176. doi:10.1111/imr.12122

Chen, Y., Ju, L. A., Zhou, F., Liao, J., Xue, L., Su, Q. P., Jin, D., Yuan, Y., Lu, H., Jackson, S. P., and Zhu, C. (2019). An integrin αIIbβ3 intermediate affinity state mediates biomechanical platelet aggregation. *Nat. Mater.* 18, 760–769. doi:10.1038/s41563-019-0323-6

Cho, H.-Y., Choi, J.-H., Kim, K.-J., Shin, M., and Choi, J.-W. (2021). Microfluidic system to analyze the effects of interleukin 6 on lymphatic breast cancer metastasis. *Front. Bioeng. Biotechnol.* 8, 611802. doi:10.3389/fbioe.2020.611802

Choe, J. H., Watchmaker, P. B., Simic, M. S., Gilbert, R. D., Li, A. W., Krasnow, N. A., Downey, K. M., Yu, W., Carrera, D. A., Celli, A., Cho, J., Briones, J. D., Duecker, J. M., Goretsky, Y. E., Dannenfelser, R., Cardarelli, L., Troyanskaya, O., Sidhu, S. S., Roybal, K. T., Okada, H., and Lim, W. A. (2021). SynNotch-CAR T cells overcome challenges of specificity, heterogeneity, and persistence in treating glioblastoma. *Sci. Transl. Med.* 13, eabe7378. doi:10.1126/scitranslmed.abe7378

Choudhuri, K., and Dustin, M. L. (2010). Signaling microdomains in T cells. *FEBS Lett* 584, 4823–4831. doi:10.1016/j.febslet.2010.10.015

Chubykin, A. A., Atasoy, D., Etherton, M. R., Brose, N., Kavalali, E. T., Gibson, J. R., and Südhof, T. C. (2007). Activity-dependent validation of excitatory versus inhibitory synapses by neuroligin-1 versus neuroligin-2. *Neuron* 54, 919–931. doi:10.1016/j.neuron.2007.05.029

Colin-York, H., Javanmardi, Y., Skamrahl, M., Kumari, S., Chang, V. T., Khuon, S., Taylor, A., Chew, T.-L., Betzig, E., Moeendarbary, E., Cerundolo, V., Eggeling, C., and Fritzsche, M. (2019). Cytoskeletal control of antigen-dependent T cell activation. *Cell Reports* 26, 3369–3379. doi:10.1016/j.celrep.2019.02.074

Dustin, M. L., Bromley, S. K., Davis, M. M., and Zhu, C. (2001). Identification of self through two-dimensional chemistry and synapses. *Annu. Rev. Cell Dev. Biol.* 17, 133–157. doi:10.1146/annurev.cellbio.17.1.133

Dustin, M. L., and Cooper, J. A. (2000). The immunological synapse and the actin cytoskeleton: molecular hardware for T cell signaling. *Nat. Immunol.* 1, 23–29. doi:10.1038/76877

Elosegui-Artola, A., Oria, R., Chen, Y., Kosmalska, A., Pérez-González, C., Castro, N., Zhu, C., Trepat, X., and Roca-Cusachs, P. (2016). Mechanical regulation of a molecular clutch defines force transmission and transduction in response to matrix rigidity. *Nat. Cell Biol.* 18, 540–548. doi:10.1038/ncb3336

Epsztein, J., Brecht, M., and Lee, A. K. (2011). Intracellular determinants of hippocampal CA1 place and silent cell activity in a novel environment. *Neuron* 70, 109–120. doi:10.1016/j.neuron.2011.03.006

Fagerberg, L., Jonasson, K., von Heijne, G., Uhlén, M., and Berglund, L. (2010). Prediction of the human membrane proteome. *Proteomics* 10, 1141–1149. doi:10.1002/pmic.200900258

Faizi, H. A., Frey, S. L., Steinkühler, J., Dimova, R., and Vlahovska, P. M. (2019). Bending rigidity of charged lipid bilayer membranes. *Soft Matter* 15, 6006–6013. doi:10.1039/c9sm00772e

Fan, J., Shi, J., Zhang, Y., Liu, J., An, C., Zhu, H., Wu, P., Hu, W., Qin, R., Yao, D., Shou, X., Xu, Y., Tong, Z., Wen, X., Xu, J., Zhang, J., Fang, W., Lou, J., Yin, W., and Chen, W. (2022). NKG2D discriminates diverse ligands through selectively mechano-regulated ligand conformational changes. *The EMBO Journal* 41, e107739. doi:10.15252/embj.2021107739

Feng, Y., Brazin, K. N., Kobayashi, E., Mallis, R. J., Reinherz, E. L., and Lang, M. J. (2017). Mechanosensing drives acuity of αβ T-cell recognition. *Proc. Natl. Acad. Sci. U.S.A.* 114, E8204–E8213. doi:10.1073/pnas.1703559114

Flavell, S. W., and Greenberg, M. E. (2008). Signaling mechanisms linking neuronal activity to gene expression and plasticity of the nervous system. *Annu. Rev. Neurosci.* 31, 563–590. doi:10.1146/annurev.neuro.31.060407.125631

Garber, K. (2018). Driving T-cell immunotherapy to solid tumors. *Nat. Biotechnol.* 36, 215–219. doi:10.1038/nbt.4090

Grakoui, A., Bromley, S. K., Sumen, C., Davis, M. M., Shaw, A. S., Allen, P. M., and Dustin, M. L. (1999). The immunological synapse: A molecular machine controlling T cell activation. *Science* 285, 221–227. doi:10.1126/science.285.5425.221

Hammer, J. A., Wang, J. C., Saeed, M., and Pedrosa, A. T. (2019). Origin, organization, dynamics, and function of actin and actomyosin networks at the T cell immunological synapse. *Annu. Rev. Immunol.* 37, 201–224. doi:10.1146/annurev-immunol-042718-041341

He, J., Xiong, X., Yang, H., Li, D., Liu, X., Li, S., Liao, S., Chen, S., Wen, X., Yu, K., Fu, L., Dong, X., Zhu, K., Xia, X., Kang, T., Bian, C., Li, X., Liu, H., Ding, P., Zhang, X., Liu, Z., Li, W., Zuo, Z., and Zhou, P. (2022). Defined tumor antigen-specific T cells potentiate personalized TCR-T cell therapy and prediction of immunotherapy response. *Cell Res* 32, 530–542. doi:10.1038/s41422-022-00627-9

He, Y., Lu, M., Cao, J., and Lu, H. P. (2012). Manipulating protein conformations by single-molecule AFM-FRET nanoscopy. *ACS Nano* 6, 1221–1229. doi:10.1021/nn2038669

Hong, J., Ge, C., Jothikumar, P., Yuan, Z., Liu, B., Bai, K., Li, K., Rittase, W., Shinzawa, M., Zhang, Y., Palin, A., Love, P., Yu, X., Salaita, K., Evavold, B. D., Singer, A., and Zhu, C. (2018). A TCR mechanotransduction signaling loop induces negative selection in the thymus. *Nat. Immunol.* 19, 1379–1390. doi:10.1038/s41590-018-0259-z

Hoogenboom, H. R. (2005). Selecting and screening recombinant antibody libraries. *Nat. Biotechnol.* 23, 1105–1116. doi:10.1038/nbt1126

Hopkins, A. L., and Groom, C. R. (2002). The druggable genome. *Nat. Rev. Drug Discov.* 1, 727–730. doi:10.1038/nrd892

Hu, J., Lipowsky, R., and Weikl, T. R. (2013). Binding constants of membrane-anchored receptors and ligands depend strongly on the nanoscale roughness of membranes. *Proc. Natl. Acad. Sci. U.S.A.* 110, 15283–15288. doi:10.1073/pnas.1305766110

Hu, J., Xu, G.-K., Lipowsky, R., and Weikl, T. R. (2015). Binding kinetics of membrane-anchored receptors and ligands: Molecular dynamics simulations and theory. *The Journal of Chemical Physics* 143, 243137. doi:10.1063/1.4936135

Hu, K. H., and Butte, M. J. (2016). T cell activation requires force generation. *J. Cell Biol.* 213, 535–542. doi:10.1083/jcb.201511053

Hu, W., Zhang, Y., Sun, X., Zhang, T., Xu, L., Xie, H., Li, Z., Liu, W., Lou, J., and Chen, W. (2019). FcγRIIB-I232T polymorphic change allosterically suppresses ligand binding. *Elife* 8, e46689. doi:10.7554/eLife.46689

Huang, J., Meyer, C., and Zhu, C. (2012). T cell antigen recognition at the cell membrane. *Molecular Immunology* 52, 155–164. doi:10.1016/j.molimm.2012.05.004

Huang, J., Zarnitsyna, V. I., Liu, B., Edwards, L. J., Jiang, N., Evavold, B. D., and Zhu, C. (2010). The kinetics of two-dimensional TCR and pMHC interactions determine T-cell responsiveness. *Nature* 464, 932–936. doi:10.1038/nature08944

Ju, L., Chen, Y., Xue, L., Du, X., and Zhu, C. (2016). Cooperative unfolding of distinctive mechanoreceptor domains transduces force into signals. *Elife* 5, e15447. doi:10.7554/eLife.15447

Ju, L., Dong, J.-f., Cruz, M. A., and Zhu, C. (2013). The N-terminal Flanking Region of the A1 Domain Regulates the Force-dependent Binding of von Willebrand Factor to Platelet Glycoprotein Ibα. *Journal of Biological Chemistry* 288, 32289–32301. doi:10.1074/jbc.M113.504001

Kim, S. T., Takeuchi, K., Sun, Z.-Y. J., Touma, M., Castro, C. E., Fahmy, A., Lang, M. J., Wagner, G., and Reinherz, E. L. (2009). The αβ T Cell Receptor Is an Anisotropic Mechanosensor. *Journal of Biological Chemistry* 284, 31028–31037. doi:10.1074/jbc.M109.052712

Kong, F., Li, Z., Parks, W. M., Dumbauld, D. W., García, A. J., Mould, A. P., Humphries, M. J., and Zhu, C. (2013). Cyclic mechanical reinforcement of integrin-ligand interactions. *Molecular Cell* 49, 1060–1068. doi:10.1016/j.molcel.2013.01.015

Krobath, H., Różycki, B., Lipowsky, R., and Weikl, T. R. (2009). Binding cooperativity of membrane adhesion receptors. *Soft Matter* 5, 3354–3361. doi:10.1039/b902036e

Kwon, H.-B., Kozorovitskiy, Y., Oh, W.-J., Peixoto, R. T., Akhtar, N., Saulnier, J. L., Gu, C., and Sabatini, B. L. (2012). Neuroligin-1-dependent competition regulates cortical synaptogenesis and synapse number. *Nat. Neurosci.* 15, 1667–1674. doi:10.1038/nn.3256

Labrijn, A. F., Janmaat, M. L., Reichert, J. M., and Parren, P. W. H. I. (2019). Bispecific antibodies: a mechanistic review of the pipeline. *Nat. Rev. Drug Discov.* 18, 585–608. doi:10.1038/s41573-019-0028-1

Lee, D., Lin, B.-J., and Lee, A. K. (2012). Hippocampal place fields emerge upon single-cell manipulation of excitability during behavior. *Science* 337, 849–853. doi:10.1126/science.1221489

Lei, K., Kurum, A., Kaynak, M., Bonati, L., Han, Y., Cencen, V., Gao, M., Xie, Y.-Q., Guo, Y., Hannebelle, M. T. M., Wu, Y., Zhou, G., Guo, M., Fantner, G. E., Sakar,

M. S., and Tang, L. (2021). Cancer-cell stiffening via cholesterol depletion enhances adoptive T-cell immunotherapy. *Nat. Biomed. Eng.* 5, 1411–1425. doi:10.1038/s41551-021-00826-6

Li, J., Su, Y., Xia, W., Qin, Y., Humphries, M. J., Vestweber, D., Cabañas, C., Lu, C., and Springer, T. A. (2017a). Conformational equilibria and intrinsic affinities define integrin activation. *Embo J* 36, 629–645. doi:10.15252/embj.201695803

Li, L., Hu, J., Li, L., and Song, F. (2019). Binding constant of membrane-anchored receptors and ligands that induce membrane curvatures. *Soft Matter* 15, 3507–3514. doi:10.1039/c8sm02504e

Li, L., Hu, J., Różycki, B., and Song, F. (2020a). Intercellular receptor-ligand binding and thermal fluctuations facilitate receptor aggregation in adhering membranes. *Nano Lett.* 20, 722–728. doi:10.1021/acs.nanolett.9b04596

Li, L., Hu, J., Różycki, B., Wang, X., Wu, H., and Song, F. (2021a). Influence of lipid rafts on pattern formation during T-cell adhesion. *New J. Phys.* 23, 043052. doi:10.1088/1367-2630/abeacb

Li, L., Hu, J., Shi, X., Różycki, B., and Song, F. (2021b). Interplay between cooperativity of intercellular receptor-ligand binding and coalescence of nanoscale lipid clusters in adhering membranes. *Soft Matter* 17, 1912–1920. doi:10.1039/d0sm01904f

Li, L., Hu, J., Shi, X., Shao, Y., and Song, F. (2017b). Lipid rafts enhance the binding constant of membrane-anchored receptors and ligands. *Soft Matter* 13, 4294–4304. doi:10.1039/c7sm00572e

Li, L., Hu, J., Wu, H., and Song, F. (2021c). Cis-interaction of ligands on a supported lipid bilayer affects their binding to cell adhesion receptors. *Sci. China Phys. Mech. Astron.* 64, 108712. doi:10.1007/s11433-021-1752-0

Li, L., Hu, J., Xu, G., and Song, F. (2018a). Binding constant of cell adhesion receptors and substrate-immobilized ligands depends on the distribution of ligands. *Phys. Rev. E* 97, 012405. doi:10.1103/PhysRevE.97.012405

Li, L., and Song, F. (2016). Entropic force between biomembranes. *Acta Mech. Sin.* 32, 970–975. doi:10.1007/s10409-016-0588-9

Li, L., and Song, F. (2018). Undulation force between membranes. *Adv. Mech.* 48, 438–460.

Li, L., Wang, X., Shao, Y., Li, W., and Song, F. (2018b). Entropic pressure between fluctuating membranes in multilayer systems. *Sci. China Phys. Mech. Astron.* 61, 128711. doi:10.1007/s11433-018-9264-x

Li, L., Wang, X., Wu, H., Shao, Y., Wu, H., and Song, F. (2021d). Interplay between receptor-ligand binding and lipid domain formation depends on the mobility of ligands in cell-substrate adhesion. *Front. Mol. Biosci.* 8, 655662. doi:10.3389/fmolb.2021.655662

Li, L., Xu, G.-K., and Song, F. (2017c). Impact of lipid rafts on theT-cell-receptor and peptide-major-histocompatibility-complex interactions under different measurement conditions. *Phys. Rev. E* 95, 012403. doi:10.1103/PhysRevE.95.012403

Li, R., Ma, C., Cai, H., and Chen, W. (2020b). The CAR T-Cell Mechanoimmunology at a Glance. *Adv. Sci.* 7, 2002628. doi:10.1002/advs.202002628

Li, Y., Miao, W., He, D., Wang, S., Lou, J., Jiang, Y., and Wang, S. (2021e). Recent progress on immunotherapy for breast cancer: tumor microenvironment, nanotechnology and more. *Front. Bioeng. Biotechnol.* 9, 680315. doi:10.3389/fbioe.2021.680315

Lillemeier, B. F., Mörtelmaier, M. A., Forstner, M. B., Huppa, J. B., Groves, J. T., and Davis, M. M. (2010). TCR and Lat are expressed on separate protein islands on T cell membranes and concatenate during activation. *Nat. Immunol.* 11, 90–96. doi:10.1038/ni.1832

Lingwood, D., and Simons, K. (2010). Lipid rafts as a membrane-organizing principle. *Science* 327, 46–50. doi:10.1126/science.1174621

Liu, B., Chen, W., Evavold, B. D., and Zhu, C. (2014). Accumulation of dynamic catch bonds between TCR and agonist peptide-MHC triggers T cell signaling. *Cell* 157, 357–368. doi:10.1016/j.cell.2014.02.053

Liu, B., Chen, W., and Zhu, C. (2015). Molecular force spectroscopy on cells. *Annu. Rev. Phys. Chem.* 66, 427–451. doi:10.1146/annurev-physchem-040214-121742

Liu, L., You, Z., Yu, H., Zhou, L., Zhao, H., Yan, X., Li, D., Wang, B., Zhu, L., Xu, Y., Xia, T., Shi, Y., Huang, C., Hou, W., and Du, Y. (2017). Mechanotransduction-modulated fibrotic microniches reveal the contribution of angiogenesis in liver fibrosis. *Nature Mater* 16, 1252–1261. doi:10.1038/nmat5024

Liu, Y., Blanchfield, L., Ma, V. P.-Y., Andargachew, R., Galior, K., Liu, Z., Evavold, B., and Salaita, K. (2016). DNA-based nanoparticle tension sensors reveal that T-cell receptors transmit defined pN forces to their antigens for enhanced fidelity. *Proc. Natl. Acad. Sci. U.S.A.* 113, 5610–5615. doi:10.1073/pnas.1600163113

Lorent, J. H., Diaz-Rohrer, B., Lin, X., Spring, K., Gorfe, A. A., Levental, K. R., and Levental, I. (2017). Structural determinants and functional consequences of protein affinity for membrane rafts. *Nat. Commun.* 8, 1219. doi:10.1038/s41467-017-01328-3

Lorz, B. G., Smith, A.-S., Gege, C., and Sackmann, E. (2007). Adhesion of Giant Vesicles Mediated by Weak Binding of Sialyl-LewisX to E-Selectin in the Presence of Repelling Poly(ethylene glycol) Molecules. *Langmuir* 23, 12293–12300. doi:10.1021/la701824q

Ma, R., Kellner, A. V., Ma, V. P.-Y., Su, H., Deal, B. R., Brockman, J. M., and Salaita, K. (2019). DNA probes that store mechanical information reveal transient piconewton forces applied by T cells. *Proc. Natl. Acad. Sci. U.S.A.* 116, 16949–16954. doi:10.1073/pnas.1904034116

Mahaut-Smith, M. P., Martinez-Pinna, J., and Gurung, I. S. (2008). A role for membrane potential in regulating GPCRs? *Trends in Pharmacological Sciences* 29, 421–429. doi:10.1016/j.tips.2008.05.007

Malmqvist, M. (1993). Surface plasmon resonance for detection and measurement of antibody-antigen affinity and kinetics. *Current Opinion in Immunology* 5, 282–286. doi:10.1016/0952-7915(93)90019-o

Marshall, B. T., Long, M., Piper, J. W., Yago, T., McEver, R. P., and Zhu, C. (2003). Direct observation of catch bonds involving cell-adhesion molecules. *Nature* 423, 190–193. doi:10.1038/nature01605

McMahon, H. T., and Boucrot, E. (2015). Membrane curvature at a glance. *J. Cell Sci.* 128, 1065–1070. doi:10.1242/jcs.114454

McMahon, H. T., and Gallop, J. L. (2005). Membrane curvature and mechanisms of dynamic cell membrane remodelling. *Nature* 438, 590–596. doi:10.1038/nature04396

Melero, I., Hervas-Stubbs, S., Glennie, M., Pardoll, D. M., and Chen, L. (2007). Immunostimulatory monoclonal antibodies for cancer therapy. *Nat. Rev. Cancer.* 7, 95–106. doi:10.1038/nrc2051

Milstein, O., Tseng, S.-Y., Starr, T., Llodra, J., Nans, A., Liu, M., Wild, M. K., van der Merwe, P. A., Stokes, D. L., Reisner, Y., and Dustin, M. L. (2008). Nanoscale increases in CD2-CD48-mediated intermembrane spacing decrease adhesion and reorganize the immunological synapse. *Journal of Biological Chemistry* 283, 34414–34422. doi:10.1074/jbc.M804756200

Mulivor, A. W., and Lipowsky, H. H. (2002). Role of glycocalyx in leukocyte-endothelial cell adhesion. *American Journal of Physiology-Heart and Circulatory Physiology* 283, H1282–H1291. doi:10.1152/ajpheart.00117.2002

Navarro-Polanco, R. A., Galindo, E. G. M., Ferrer-Villada, T., Arias, M., Rigby, J. R., Sánchez-Chapula, J. A., and Tristani-Firouzi, M. (2011). Conformational changes in the M2 muscarinic receptor induced by membrane voltage and agonist binding. *J. Physiol.-London.* 589, 1741–1753. doi:10.1113/jphysiol.2010.204107

Neuman, K. C., and Nagy, A. (2008). Single-molecule force spectroscopy: optical tweezers, magnetic tweezers and atomic force microscopy. *Nat. Methods.* 5, 491–505. doi:10.1038/nmeth.1218

Park, Y., Seo, J. B., Fraind, A., Pérez-Lara, A., Yavuz, H., Han, K., Jung, S.-R., Kattan, I., Walla, P. J., Choi, M., Cafiso, D. S., Koh, D.-S., and Jahn, R. (2015). Synaptotagmin-1 binds to PIP2-containing membrane but not to SNAREs at physiological ionic strength. *Nat. Struct. Mol. Biol.* 22, 815–823. doi:10.1038/nsmb.3097

Paszek, M. J., DuFort, C. C., Rossier, O., Bainer, R., Mouw, J. K., Godula, K., Hudak, J. E., Lakins, J. N., Wijekoon, A. C., Cassereau, L., Rubashkin, M. G., Magbanua, M. J., Thorn, K. S., Davidson, M. W., Rugo, H. S., Park, J. W., Hammer, D. A., Giannone, G., Bertozzi, C. R., and Weaver, V. M. (2014). The cancer glycocalyx mechanically primes integrin-mediated growth and survival. *Nature* 511, 319–325. doi:10.1038/nature13535

Peixoto, R. T., Kunz, P. A., Kwon, H., Mabb, A. M., Sabatini, B. L., Philpot, B. D., and Ehlers, M. D. (2012). Transsynaptic signaling by activity-dependent cleavage of neuroligin-1. *Neuron* 76, 396–409. doi:10.1016/j.neuron.2012.07.006

Rakshit, S., Zhang, Y., Manibog, K., Shafraz, O., and Sivasankar, S. (2012). Ideal, catch, and slip bonds in cadherin adhesion. *Proc. Natl. Acad. Sci. U.S.A.* 109, 18815–18820. doi:10.1073/pnas.1208349109

Ramakrishnan, N., Sunil Kumar, P. B., and Radhakrishnan, R. (2014). Mesoscale computational studies of membrane bilayer remodeling by curvature-inducing proteins. *Physics Reports* 543, 1–60. doi:10.1016/j.physrep.2014.05.001

Rapoport, A. P., Stadtmauer, E. A., Binder-Scholl, G. K., Goloubeva, O., Vogl, D. T., Lacey, S. F., Badros, A. Z., Garfall, A., Weiss, B., Finklestein, J., Kulikovskaya, I., Sinha, S. K., Kronsberg, S., Gupta, M., Bond, S., Melchiori, L., Brewer, J. E., Bennett, A. D., Gerry, A. B., Pumphrey, N. J., Williams, D., Tayton- Martin, H. K., Ribeiro, L., Holdich, T., Yanovich, S., Hardy, N., Yared, J., Kerr, N., Philip, S., Westphal, S., Siegel, D. L., Levine, B. L., Jakobsen, B. K., Kalos, M., and June, C. H. (2015). NY-ESO-1-specific TCR-engineered T cells mediate sustained antigen-specific antitumor effects in myeloma. *Nat. Med.* 21, 914–921. doi:10.1038/nm.3910

Rinne, A., Mobarec, J. C., Mahaut-Smith, M., Kolb, P., and Bünemann, M. (2015). The mode of agonist binding to a G protein-coupled receptor switches the effect that voltage changes have on signaling. *Sci. Signal.* 8, ra110. doi:10.1126/scisignal.aac7419

Różycki, B., Lipowsky, R., and Weikl, T. R. (2010). Segregation of receptor-ligand complexes in cell adhesion zones: phase diagrams and the role of thermal membrane roughness. *New J. Phys.* 12, 095003. doi:10.1088/1367-2630/12/9/095003

Seung, E., Xing, Z., Wu, L., Rao, E., Cortez-Retamozo, V., Ospina, B., Chen, L., Beil, C., Song, Z., Zhang, B., Levit, M., Deng, G., Hebert, A., Kirby, P., Li, A., Poulton, E.-J., Vicente, R., Garrigou, A., Piepenhagen, P., Ulinski, G., Sanicola-Nadel, M., Bangari, D. S., Qiu, H., Pao, L., Wiederschain, D., Wei, R., Yang, Z.-y., and Nabel, G. J. (2022). A trispecific antibody targeting HER2 and T cells inhibits breast cancer growth via CD4 cells. *Nature* 603, 328–334. doi:10.1038/s41586-022-04439-0

Sezgin, E., Levental, I., Mayor, S., and Eggeling, C. (2017). The mystery of membrane organization: composition, regulation and roles of lipid rafts. *Nat. Rev. Mol. Cell Biol.* 18, 361–374. doi:10.1038/nrm.2017.16

Shi, X., Bi, Y., Yang, W., Guo, X., Jiang, Y., Wan, C., Li, L., Bai, Y., Guo, J., Wang, Y., Chen, X., Wu, B., Sun, H., Liu, W., Wang, J., and Xu, C. (2013). Ca2+ regulates T-cell receptor activation by modulating the charge property of lipids. *Nature* 493, 111–115. doi:10.1038/nature11699

Siechen, S., Yang, S., Chiba, A., and Saif, T. (2009). Mechanical tension contributes to clustering of neurotransmitter vesicles at presynaptic terminals. *Proc. Natl. Acad. Sci. U.S.A.* 106, 12611–12616. doi:10.1073/pnas.0901867106

Simons, K., and Ehehalt, R. (2002). Cholesterol, lipid rafts, and disease. *J. Clin. Invest.* 110, 597–603. doi:10.1172/JCI16390

Sorice, M., Misasi, R., Riitano, G., Manganelli, V., Martellucci, S., Longo, A., Garofalo, T., and Mattei, V. (2021). Targeting lipid rafts as a strategy against coronavirus. *Front. Cell Dev. Biol.* 8, 618296. doi:10.3389/fcell.2020.618296

Springer, T. A., and Dustin, M. L. (2012). Integrin inside-out signaling and the immunological synapse. *Current Opinion in Cell Biology* 24, 107–115. doi:10.1016/j.ceb.2011.10.004

Stachowiak, J. C., Schmid, E. M., Ryan, C. J., Ann, H. S., Sasaki, D. Y., Sherman, M. B., Geissler, P. L., Fletcher, D. A., and Hayden, C. C. (2012). Membrane bending by protein-protein crowding. *Nat. Cell Biol.* 14, 944–949. doi:10.1038/ncb2561

Staflin, K., Zuch de Zafra, C. L., Schutt, L. K., Clark, V., Zhong, F., Hristopoulos, M., Clark, R., Li, J., Mathieu, M., Chen, X., Johnston, J., Low, J., Ybarra, R., Slaga, D., Yang, J., Ovacik, M., Dybdal, N. O., Totpal, K., Junttila, M. R., Ellerman, D., Lee, G., Dennis, M. S., Prell, R., and Junttila, T. T. (2020). Target arm affinities determine preclinical efficacy and safety of anti-HER2/CD3 bispecific antibody. *JCI Insight* 5, e133757. doi:10.1172/jci.insight.133757

Steinkühler, J., Różycki, B., Alvey, C., Lipowsky, R., Weikl, T. R., Dimova, R., and Discher, D. E. (2019). Membrane fluctuations and acidosis regulate cooperative binding of "marker of self" CD47 with macrophage checkpoint receptor SIRPα. *J. Cell Sci.* 132, jcs216770. doi:10.1242/jcs.216770

Su, Q. P., and Ju, L. A. (2018). Biophysical nanotools for single-molecule dynamics. *Biophys. Rev.* 10, 1349–1357. doi:10.1007/s12551-018-0447-y

Su, Y.-w., and Wang, W. (2018). Surface plasmon resonance sensing: from purified biomolecules to intact cells. *Anal. Bioanal. Chem.* 410, 3943–3951. doi:10.1007/s00216-018-1008-8

Südhof, T. C. (2018). Towards an understanding of synapse formation. *Neuron* 100, 276–293. doi:10.1016/j.neuron.2018.09.040

Tello-Lafoz, M., de Jesus, M. M., and Huse, M. (2022). Harder, better, faster, stronger: Biochemistry and biophysics in the immunosurveillance concert. *Trends in Immunology* 43, 96–105. doi:10.1016/j.it.2021.12.003

Tello-Lafoz, M., Srpan, K., Sanchez, E. E., Hu, J., Remsik, J., Romin, Y., Calò, A., Hoen, D., Bhanot, U., Morris, L., Boire, A., Hsu, K. C., Massagué, J., Huse, M., and Er, E. E. (2021). Cytotoxic lymphocytes target characteristic biophysical vulnerabilities in cancer. *Immunity* 54, 1037–1054. doi:10.1016/j.immuni.2021.02.020

Tian, M., Li, Y., Liu, W., Jin, L., Jiang, X., Wang, X., Ding, Z., Peng, Y., Zhou, J., Fan, J., Cao, Y., Wang, W., and Shi, Y. (2015). The nanomechanical signature of liver cancer tissues and its molecular origin. *Nanoscale* 7, 12998–13010. doi:10.1039/c5nr02192h

van der Merwe, P. A., and Dushek, O. (2011). Mechanisms for T cell receptor triggering. *Nat. Rev. Immunol.* 11, 47–55. doi:10.1038/nri2887

Vickery, O. N., Machtens, J.-P., and Zachariae, U. (2016). Membrane potentials regulating GPCRs: insights from experiments and molecular dynamics simulations. *Current Opinion in Pharmacology* 30, 44–50. doi:10.1016/j.coph.2016.06.011

Vizurraga, A., Adhikari, R., Yeung, J., Yu, M., and Tall, G. G. (2020). Mechanisms of adhesion G protein-coupled receptor activation. *Journal of Biological Chemistry* 295, 14065–14083. doi:10.1074/jbc.REV120.007423

Vona, R., Iessi, E., and Matarrese, P. (2021). Role of cholesterol and lipid rafts in cancer signaling: a promising therapeutic opportunity? *Front. Cell Dev. Biol.* 9, 622908. doi:10.3389/fcell.2021.622908

Wang, H., Zhou, F., Guo, Y., and Ju, L. A. (2022). Micropipette-based biomechanical nanotools on living cells. *Eur Biophys J* 51, 119–133. doi:10.1007/s00249-021-01587-5

Wang, X., and Ha, T. (2013). Defining single molecular forces required to activate integrin and notch signaling. *Science* 340, 991–994. doi:10.1126/science.1231041

Weikl, T. R., Hu, J., Xu, G.-K., and Lipowsky, R. (2016). Binding equilibrium and kinetics of membrane-anchored receptors and ligands in cell adhesion: Insights from computational model systems and theory. *Cell Adhesion & Migration* 10, 576–589. doi:10.1080/19336918.2016.1180487

Weikl, T. R. (2018). Membrane-mediated cooperativity of proteins. *Annu. Rev. Phys. Chem.* 69, 521–539. doi:10.1146/annurev-physchem-052516-050637

Wu, P., Zhang, T., Liu, B., Fei, P., Cui, L., Qin, R., Zhu, H., Yao, D., Martinez, R. J., Hu, W., An, C., Zhang, Y., Liu, J., Shi, J., Fan, J., Yin, W., Sun, J., Zhou, C., Zeng, X., Xu, C., Wang, J., Evavold, B. D., Zhu, C., Chen, W., and Lou, J. (2019). Mechano-regulation of peptide-MHC Class I conformations determines TCR antigen recognition. *Molecular Cell* 73, 1015–1027. doi:10.1016/j.molcel.2018.12.018

Wu, W., Zhou, Q., Masubuchi, T., Shi, X., Li, H., Xu, X., Huang, M., Meng, L., He, X., Zhu, H., Gao, S., Zhang, N., Jing, R., Sun, J., Wang, H., Hui, E., Wong, C. C., and Xu, C. (2020). Multiple Signaling Roles of CD3ε and Its Application in CAR-T Cell Therapy. *Cell* 182, 855–871. doi:10.1016/j.cell.2020.07.018

Wuerfel, J., Paul, F., Beierbach, B., Hamhaber, U., Klatt, D., Papazoglou, S., Zipp, F., Martus, P., Braun, J., and Sack, I. (2010). MR-elastography reveals degradation of tissue integrity in multiple sclerosis. *Neuroimage* 49, 2520–2525. doi:10.1016/j.neuroimage.2009.06.018

Xiao, H., Woods, E. C., Vukojicic, P., and Bertozzi, C. R. (2016). Precision glycocalyx editing as a strategy for cancer immunotherapy. *Proc. Natl. Acad. Sci. U.S.A.* 113, 10304–10309. doi:10.1073/pnas.1608069113

Xu, G.-K., Hu, J., Lipowsky, R., and Weikl, T. R. (2015). Binding constants of membrane-anchored receptors and ligands: A general theory corroborated by Monte Carlo simulations. *The Journal of Chemical Physics* 143, 243136. doi:10.1063/1.4936134

Xu, G.-K., Qian, J., and Hu, J. (2016). The glycocalyx promotes cooperative binding and clustering of adhesion receptors. *Soft Matter* 12, 4572–4583. doi:10.1039/c5sm03139g

Yang, D., Singh, A., Wu, H., and Kroe-Barrett, R. (2016). Comparison of biosensor platforms in the evaluation of high affinity antibody-antigen binding kinetics. *Analytical Biochemistry* 508, 78–96. doi:10.1016/j.ab.2016.06.024

Yang, M., and Brackenbury, W. J. (2013). Membrane potential and cancer progression. *Front. Physiol.* 4, 185. doi:10.3389/fphys.2013.00185

Zhou, Y., Wong, C.-O., Cho, K.-j., van der Hoeven, D., Liang, H., Thakur, D. P., Luo, J., Babic, M., Zinsmaier, K. E., Zhu, M. X., Hu, H., Venkatachalam, K., and Hancock, J. F. (2015). Membrane potential modulates plasma membrane phospholipid dynamics and K-Ras signaling. *Science* 349, 873–876. doi:10.1126/science.aaa5619

Zhu, C., Chen, W., Lou, J., Rittase, W., and Li, K. (2019a). Mechanosensing through immunoreceptors. *Nat. Immunol.* 20, 1269–1278. doi:10.1038/s41590-019-0491-1

Zhu, C., Chen, Y., and Ju, L. A. (2019b). Dynamic bonds and their roles in mechanosensing. *Current Opinion in Chemical Biology* 53, 88–97. doi:10.1016/j.cbpa.2019.08.005

Conflict of Interest: The authors declare that the research was conducted in the absence of any commercial or financial relationships that could be construed as a potential conflict of interest.

Publisher's Note: All claims expressed in this article are solely those of the authors and do not necessarily represent those of their affiliated organizations, or those of the publisher, the editors and the reviewers. Any product that may be evaluated in this article, or claim that may be made by its manufacturer, is not guaranteed or endorsed by the publisher.

frontiers | Frontiers in Bioengineering and Biotechnology

TYPE Original Research
PUBLISHED 24 August 2022
DOI 10.3389/fbioe.2022.969004

OPEN ACCESS

EDITED BY
Guang-Kui Xu,
Xi'an Jiaotong University, China

REVIEWED BY
Maria Jose Gomez-Benito,
University of Zaragoza, Spain
Dechang Li,
Zhejiang University, China

*CORRESPONDENCE
Sabato Fusco,
sabato.fusco@unimol.it

SPECIALTY SECTION
This article was submitted to Biomechanics, a section of the journal Frontiers in Bioengineering and Biotechnology

RECEIVED 14 June 2022
ACCEPTED 28 July 2022
PUBLISHED 24 August 2022

CITATION
La Verde G, Artiola V, Pugliese M, La Commara M, Arrichiello C, Muto P, Netti PA, Fusco S and Panzetta V (2022), Radiation therapy affects YAP expression and intracellular localization by modulating lamin A/C levels in breast cancer.
Front. Bioeng. Biotechnol. 10:969004.
doi: 10.3389/fbioe.2022.969004

Radiation therapy affects YAP expression and intracellular localization by modulating lamin A/C levels in breast cancer

Giuseppe La Verde[1,2], Valeria Artiola[3], Mariagabriella Pugliese[1,3], Marco La Commara[1,2], Cecilia Arrichiello[4], Paolo Muto[4], Paolo A. Netti[5,6], Sabato Fusco[7]* and Valeria Panzetta[5,6]

[1]Istituto Nazionale di Fisica Nucleare, INFN Sezione di Napoli, Naples, Italy, [2]Dipartimento di Farmacia, Università Degli Studi di Napoli Federico II, Naples, Italy, [3]Dipartimento di Fisica "Ettore Pancini", Università Degli Studi di Napoli Federico II, Naples, Italy, [4]Radiotherapy Unit, Istituto Nazionale Tumori-IRCCS-Fondazione "G. Pascale", Naples, Italy, [5]Interdisciplinary Research Centre on Biomaterials (CRIB) and Dipartimento di Ingegneria Chimica, Dei Materiali e Della Produzione Industriale, Università Degli Studi di Napoli Federico II, Naples, Italy, [6]Center for Advanced Biomaterials for Healthcare@CRIB, Istituto Italiano di Tecnologia, Naples, Italy, [7]Department of Medicine and Health Sciences "V. Tiberio", University of Molise, Campobasso, Italy

The microenvironment of breast cancer actively participates in tumorigenesis and cancer progression. The changes observed in the architecture of the extracellular matrix initiate an oncogene-mediated cell reprogramming, that leads to a massive triggering of YAP nuclear entry, and, therefore, to cancer cell proliferation, invasion and probably to increased radiation-resistance. However, it is not yet fully understood how radiotherapy regulates the expression and subcellular localization of YAP in breast cancer cells experiencing different microenvironmental stiffnesses. To elucidate the role of extracellular matrix stiffness and ionizing radiations on YAP regulation, we explored the behaviour of two different mammary cell lines, a normal epithelial cell line (MCF10A) and a highly aggressive and invasive adenocarcinoma cell line (MDA-MB-231) interacting with polyacrylamide substrates mimicking the mechanics of both normal and tumour tissues (~1 and ~13 kPa). We report that X-ray radiation affected in a significant way the levels of YAP expression, density, and localization in both cell lines. After 24 h, MCF10A and MDA-MB-231 increased the expression level of YAP in both nucleus and cytoplasm in a dose dependent manner and particularly on the stiffer substrates. After 72 h, MCF10A reduced mostly the YAP expression in the cytoplasm, whereas it remained high in the nucleus of cells on stiffer substrates. Tumour cells continued to exhibit higher levels of YAP expression, especially in the cytoplasmic compartment, as indicated by the reduction of nuclear/cytoplasmic ratio of total YAP. Then, we investigated the existence of a correlation between YAP localization and the expression of the nuclear envelope protein lamin A/C, considering its key role in modulating nuclear deformability and changes in YAP shuttling phenomena. As supposed, we found that the effects of radiation on YAP nucleus/cytoplasmic expression ratio, increasing in healthy cells and decreasing in tumour ones, were accompanied by lower and higher lamin A/C levels in MCF10A and MDA-MB-231 cells, respectively. These findings point to obtain a deeper knowledge

of the role of the extracellular matrix and the effects of X-rays on YAP and lamin A/C expression that can be used in the design of doses and timing of radiation therapy.

KEYWORDS

breast cancer, mechanobiology, extracellular matrix stiffness, YAP, lamin A/C, radiotherapy

1 Introduction

Breast cancer is one of the most diagnosed diseases in women (Ferlay et al., 2018; DeSantis et al., 2019), which incidence increases together with age and other factors, such as ethnicity and family history of cancer (Coughlin, 2019). Therefore, together with prevention, enhancement and optimization of conventional treatments are fundamental for the reduction of its mortality. From several decades one of the most widely used treatment for breast tumours is radiotherapy since that the X-rays, produced by the linear accelerator (LINAC), can severely damage the DNA of the cells, through the formation of double-stranded breaks (Iliakis et al., 2003). The effect of ionizing radiations on the cell is well known in the literature: many studies have proven how radiation can provoke almost half of the DNA lesions leading to a plethora of consequences, such as carcinogenesis, cell death, or mutation (Elkind, 1984; Sinclair and Fry, 1987; Smith, 1987; Ward, 1988). On the other hand, yet a small number of investigations have focused on the mechanobiology of irradiated cell and tissues. It is nowadays well established a direct connection between the development of cancer and the alteration in the components of the cytoskeleton (CSK) (Hall, 2009; Panzetta et al., 2017), a structure that regulates several biological processes (Krieg et al., 2019; Ladoux and Mège, 2017). Specifically, during cancer transformation, the CSK is subjected to modifications in its arrangement and composition, generally accompanied by a lowering of the cell mechanical properties (Yilmaz and Christofori, 2009; La Verde et al., 2021). The reorganization of the CSK in tumour cells may results in epithelial-mesenchymal transition (EMT), which can promote cell migration and tumour invasiveness. Another biological structure essential to the correct functioning of cells and tissues is the extracellular matrix (ECM), which, in the transformation process of a healthy tissue into a tumoral one, stiffens, increasing its mechanical properties (Panzetta et al., 2017). In this regard, a massive effort is underway to elucidate the precise relationship existing between ECM mechanics and cell oncogenic reprogramming. And, even if not everything has been understood, a growing body of evidence indicates that the ECM stiffening (typical of ageing, inflammation, fibrosis, diabetes and smoking) (Panciera et al., 2017) can instruct normal cells to undergo a profound reprogramming and to acquire a tumour malignant phenotype. It has been demonstrated, in fact, that matrices recapitulating the stiffnesses of fibrotic tissues can promote some elements of this process, by inducing changes in cell shape, reduction in E-cadherin, followed by increase of N-cadherin, nuclear localization of β-catenin (Wei et al., 2015; Fattet et al., 2020), an increase in cell proliferation and a more active invasion process (Panzetta et al., 2017; Stowers et al., 2017; Panciera et al., 2020), particularly for breast cancer (Li et al., 2008; Baker et al., 2010; Nikkhah et al., 2010; Plodinec et al., 2012). Taken together these facts demonstrate how the loss of tissue homeostasis and diseases onset are strictly correlated to the point that some traditional and novel cancer treatments are targeting these structures (Karahalil et al., 2019). Indeed, going deeper, another fundamental function of the CSK is the conversion of mechanical signal into biochemical responses. With the mechanotransduction process, the CSK can pick mechanical stimuli and send them to the cell through the activation of mechanosensors, like Yes-associated protein (YAP)/ Transcriptional coactivator with PDZ-binding motif (TAZ) complex (Low et al., 2014a). YAP is a transcriptional coactivators protein that, together with TAZ is strictly associated to mechanical and structural changes in the cell microenvironment. These proteins can move from the cytoplasm to the nucleus, where they interact with the TEA domain (TEAD) (Piccolo et al., 2014), association considered fundamental to promote their transcriptional abilities (Zhao et al., 2008; Chan et al., 2009; Zanconato et al., 2015). In healthy tissues, YAP moves from the nucleus to the cytoplasm (Dupont et al., 2011), where they can be degraded or inactivated, whereas in tumoral tissues YAP moves in the other direction where its transcriptional activity can be activated (Nukuda et al., 2015; Pocaterra et al., 2020). Additionally, it was reported that these proteins are usually stimulated during the development of most solid tumours, inducing cell proliferation, and increasing cells' ability to create metastases (Camargo et al., 2007; Dong et al., 2007; Zhao et al., 2007; Chan et al., 2008; Zanconato et al., 2016a). YAP/TAZ complex is becoming a target in some cancer therapies since it has been proved that there is an increased expression of YAP and TAZ in the cell's nucleus in KRAS-mutated cells, such as the invasive adenocarcinoma cell line MDA-MB-231. Conversely, the normal epithelial cell line MCF10A shows high concentrations of YAP in the cytoplasm (Panciera et al., 2020). Some recent studies have also reported a direct correlation between YAP and cell resistance to radiation. To high levels of YAP activation is associated a low response to X-rays, while YAP silencing increases sensitivity to radiation and the cell DNA damage (Fernandez-L et al., 2012; Akervall et al.,

2014; Xu et al., 2019). Thus, all this indicates the necessity to implement new therapeutical approaches that consider the different and complex mechanisms underlying tumoral treatment. In this frame, we here investigated how the combination of different X-ray doses and ECM stiffness regulates the expression of YAP in two different mammary cell lines. The healthy cell line, MCF10A, and its tumoral counterpart, MDA-MB-231 were seeded on type I collagen functionalized polyacrylamide substrates, characterised by a Young's Modulus of 1.3 and 13 kPa to recapitulate some characteristics of the healthy and cancerous tissue respectively. In fact, breast cancer with its characteristic highly fibrotic collagen content shows an increased stiffness (5–10 kPa) in comparison with healthy breast tissue characterized by a stiffness of 1 kPa (Levental et al., 2009; Plodinec et al., 2012). Once interacting with mechanically different substrates, cells were exposed to two doses of X-rays: 2 and 10 Gy, corresponding the former to the daily dose delivered in conventional radiotherapy and the latter to the maximum dose employed in metastases treatment. Specifically, here we report a first attempt to study the role that the substrate stiffness plays in mediating the cellular response to X-ray radiation in terms of YAP expression, density, and localization. Then, we investigated the existence of a correlation between YAP localization and the expression of the nuclear envelope protein lamin A/C, considering its key role in modulating nuclear deformability and changes in YAP shuttling phenomena. Importantly, we found that X-ray radiation affected YAP localization, increased in nuclei of healthy cells, and decreased in those of tumour ones, concurrently with the reduction and the enhancement of lamin A/C levels in MCF10A and MDA-MB-231 cells. These findings underscore the necessity to further examine the effects that X-rays induce on YAP and lamin A/C expression, in relation to the mechanical microenvironment, on subsequent cell behaviour (i.e., radiation sensitization or induction of radiation resistance). Such knowledge could be useful in tailoring therapeutic procedures and especially in the design of doses and timing of radiation therapy.

2 Materials and methods

2.1 Polyacrylamide substrate preparation

Polyacrylamide substrates were prepared and functionalized as previously reported (Panzetta et al., 2020). Specifically, 2 different formulations were prepared: 4% acrylamide/0.15% methylene-bis-acrylamide and 10% acrylamide/0.1% methylene-bis-acrylamide corresponding to 1.3 and 13 kPa (Young's modulus), respectively. The substrates were functionalized with a solution of bovine type I collagen (50 μg/ml) using a bifunctional photoreactive crosslinker (sulfosuccinimidyl 6-(4′-azido-2′-nitrophenylamino) hexanoate, sulfo-SANPAH; Fischer Scientific, Loughborough, United Kingdom). Mechanical measurements substrates were performed by a stress-controlled shear rheometer (Anton Paar MCR 502) equipped with 25 mm stainless steel parallel plate geometry tool and a Peltier heating system to control the temperature at 37°C. Dynamic frequency sweeps were performed with frequency ranging from 10^{-2} to 10 Hz in the linear regime (strain of 0.1%, Supplementary Figure S1).

2.2 Cell culture

The cell lines analysed in this study were the healthy MCF10A cell line, and the triple-negative cancerous one, MDA-MB-231. The former was cultured in Lonza Dulbecco's Modified Eagle Medium (DMEM/F-12) supplemented with 0.4% Bovine Pituitary Extract (BPE), 0.1% Human Epidermal Growth Factor (hEGF), 0.1% insulin, 0.1% hydrocortisone, 1% penicillin-streptomycin. MDA-MB-231 cells were cultured in the same basal medium supplemented with 10% foetal bovine serum (FBS), 1% L-Glutamine, and 1% penicillin-streptomycin. ~10^6 cells were seeded per polyacrylamide substrates (~$12.5{\cdot}10^3$ cells/cm^2), obtaining the cell confluence condition.

2.3 X-ray irradiation

Cells were irradiated using the Synergy Agility LINAC produced by ELEKTA company, characterised by a field size of 20 × 20 cm^2. The samples were irradiated at the National Cancer Institute "Pascale" of Naples with a 6 MV photon beam, usually employed in the conventional treatment. The cell plates were placed between two plexiglass plaques, the one on top thinner than the other, to attenuate the radiations and emulate the skin sparing effect.

2.4 Immunofluorescence

To analyse the samples, 24 and 72 h after irradiation, cells were fixed using 4% paraformaldehyde, heated to 37 °C, for 15 min. Afterwards, the samples were washed with Phosphate Buffered Saline (PBS). The immunofluorescence procedure can be divided into three phases: permeabilization, blocking, and immunostaining. For the permeabilization process, cell plates were covered with 250 μl of Triton-X 100, diluted at 0.1%, for 10 min. Afterwards, for the blocking phase, the samples were incubated with 250 μl of Bovine Serum Albumin (BSA) at 1% for 1 h at room temperature. Then, lamin A/C was localized by mouse monoclonal lamin A/C antibody (Santacruz, SC-376248) and Alexa488 goat anti-mouse secondary antibodies (Life Technologies, A11008).

YAP was localized by YAP1 polyclonal rabbit antibody (PA1-46189, ThermoFisher Scientific) and Alexa546 mouse anti-rabbit secondary antibody.

2.5 Confocal acquisition

To quantify YAP concentration and lamin A/C level in cells, the samples were observed with Olympus confocal microscope with a 63× objective. 10 z-stack images (12-bit color), averaging 4 frames each acquisition, were acquired for each sample. Each image was characterized by a size of 13.8 μm × 13.8 μm with a pixel size of 0.13 μm.

2.6 YAP analysis

Total YAP expression in both cell's nucleus, Y_N, and cytoplasm, Y_C, was investigated employing ImageJ Fiji software (NIH, Bethesda, MD, United States). Briefly, the z-stacks for the red channel (YAP) were projected into a single image using the "sum projection" function in ImageJ. YAP and lamin A/C images were used to extract individual cellular and nuclear outlines using ImageJ ROI manager tool and YAP expression at each condition was evaluated in terms of integrated fluorescence intensity within individual cellular and nuclear boundaries, Y_{Cell} and Y_N, respectively. The total YAP expression in the cytoplasm was calculated as difference between Y_{Cell} and Y_N. Then, the following parameters were evaluated:

$$Y_{N/C} = \frac{Y_N}{Y_C} \tag{1}$$

representing nuclear to cytoplasmic ratio of total YAP. Values lower or higher than 1 indicate prevalent localization of YAP in the cytoplasm or the nucleus, respectively.

$$Y_N^d = \frac{Y_N}{A_N} \tag{2}$$

$$Y_C^d = \frac{Y_C}{A_{Cell} - A_N} \tag{3}$$

where A_N and A_C are the nucleus and the cytoplasm area, whereas Y_N^d and Y_C^d represent the nuclear and cytoplasmic density/concentration of YAP, respectively.

Finally, the nuclear to cytoplasmic ratio of YAP density was calculated:

$$Y_{N/C}^d = \frac{Y_N^d}{Y_C^d} \tag{4}$$

This parameter is the most used to study the effects of translocation processes from nucleus to cytoplasm and vice versa and indicates if YAP is more concentrated into the cytoplasm ($Y_{N/C}^d \ll 1$) or in the nucleus ($Y_{N/C}^d \gg 1$).

All the analyses were carried out for both cell lines, doses, and times.

Considering that the analysis of the YAP fluorescence from the slices on the top and on the bottom of the nucleus may give a signal classified as belonging to the nucleus instead of to the cytoplasmic compartment, the analysis of all the parameters above introduced was performed by following a different procedure for a set of randomly selected cells in different conditions (13 cells). For the analysis of YAP in the nucleus, the slices where the nucleus is present were extracted and projected into a single image using again the 'sum projection' function in ImageJ. Then, Y_N was evaluated in terms of integrated fluorescence intensity within the nuclear boundaries and used as real YAP expression in the nucleus (Y_N^R). The analysis of all the other parameters was performed as previously described (Y_C^R and $Y_{N/C}^R$). The error committed for Y_N, Y_C and $Y_{N/C}$ was evaluated as: $\varepsilon\% = \frac{Y-Y^R}{Y}\%$ (Supplementary Figure S2).

2.6 Lamin A/C analysis

To quantify lamin A/C level, the z-stacks for the green channel (lamin A/C) were projected into a single image using the "maximum projection" function in ImageJ. Then, lamin A/C expression at each condition was evaluated in terms of integrated fluorescence intensity within individual nuclear boundaries.

2.7 Statistical analysis

Statistical comparisons were performed with a nonparametric Kruskal-Wallis test followed by Dunn-Bonferroni post-hoc method with p-values < 0.05 considered statistically significant.

3 Results and discussion

3.1 Radiation effects on nuclear to cytoplasmic YAP ratio density

The Hippo-YAP/TAZ pathway is an evolutionary conserved mechano-signalling pathway that has a crucial role in regulating organ size and tumorigenesis by moderating the balance between cellular proliferation and apoptosis. Inhibition of the Hippo-YAP/TAZ signalling pathway promotes the translocation of YAP/TAZ into the nucleus, thereby allowing the activation of the downstream genes. It has also been demonstrated that overexpression of YAP enhances tumorigenesis and metastasis also *in vivo* by inducing the EMT process and then, the upregulation of N-cadherin followed by the downregulation of E-cadherin. Furthermore, the role of YAP in mediating

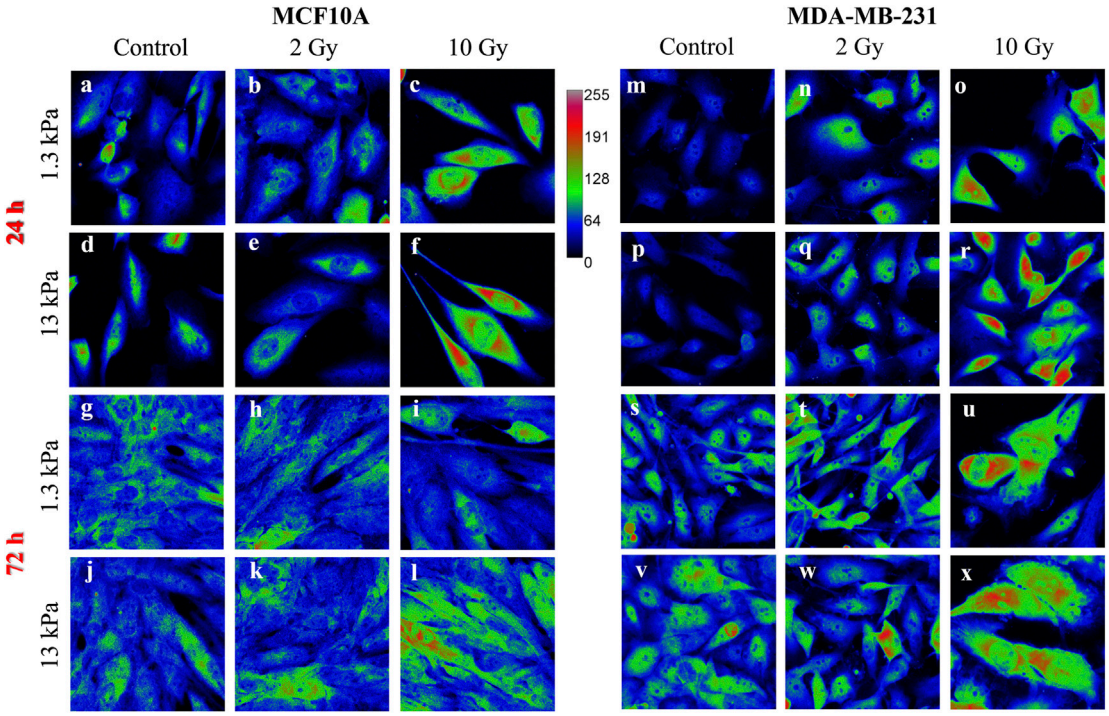

FIGURE 1
Sum intensity projections of z-stack images taken from YAP immunofluorescence in MCF10A **(A–L)** and MDA-MB-231 **(M–X)**, shown as rainbow RGB look-up table. Colour bar: YAP intensity **(A–U)**. Scale bar, 50 μm.

radiotherapy and chemotherapy resistance has been the subject of many studies that have indicated that high levels of YAP expression correlate with poor cell response to radiation therapy (Fernandez-L et al., 2012; Akervall et al., 2014). Further, YAP nuclear expression levels were demonstrated be correlated with poor prognosis of patients and with low sensitivity to radiation (Tsujiura et al., 2014).

Nevertheless, little is known about the effects of radiation on YAP expression and localization in breast cells interacting with physio-pathological microenvironments. In particular, the effects of radiation on the localization of YAP were evaluated using Eq. 4, where YAP concentration of both the nucleus and the cytoplasm was calculated measuring the integrated fluorescence with the ImageJ software (Figure 1).

This ratio was calculated for both cell lines and the used time points were 24 and 72 h after irradiation. The obtained values are shown in Figure 2, where the box plots show the mean value, the median, the interquartile range, and the outliers. The healthy cell line was characterised by a YAP ratio close to 1 on both substrates, indicating an evenly distributed signal into the cytoplasmic and nuclear compartments. A slight but significant increase of this ratio was found passing from 1.3 to 13 Young's modulus, indicating that MCF10A cells can perceive the different mechanical properties of their microenvironment. However, the high confluence cooperates to prevent a massive translocation into the nucleus also in those mechanical conditions where YAP activity is generally promoted ($Y^{d}_{N/C} >> 1$) (Dupont et al., 2011). Then, we investigated the effects of irradiation after 24 h and found a dose-dependent increase of the ratio on the soft substrate (Figure 2). On the stiffer substrate, YAP concentration of MCF10A cells showed higher values than the control condition after being irradiated with a dose of 2 Gy, while the higher dose did not affect the YAP ratio.

MDA-MB-231 cells showed a YAP ratio strongly higher than 1, indicating a substantial accumulation of YAP into the nucleus. Interestingly, the value of the ratio was not significantly varied passing from 1.3 to 13 kPa Young's modulus. This phenomenon was already confirmed by other studies (Harvey et al., 2013; Piccolo et al., 2014) since it is proven that YAP is highly active in almost all tumour cells (Zanconato et al., 2016b). In fact, in both sparse and confluent conditions, the loss of E-cadherin-β-catenin complexes directly controls the nuclear localization of YAP in tumour cells, and specifically in MDA-MB-231 (Kim et al., 2011). After irradiation, YAP concentration decreased in a dose-related manner in both conditions, supporting the idea of a repression effect of radiation exposure on the activation of YAP signalling, as previously observed also in glioma cells (Xu et al., 2019). The values obtained from the analyses carried out

10.3389/fbioe.2022.969004

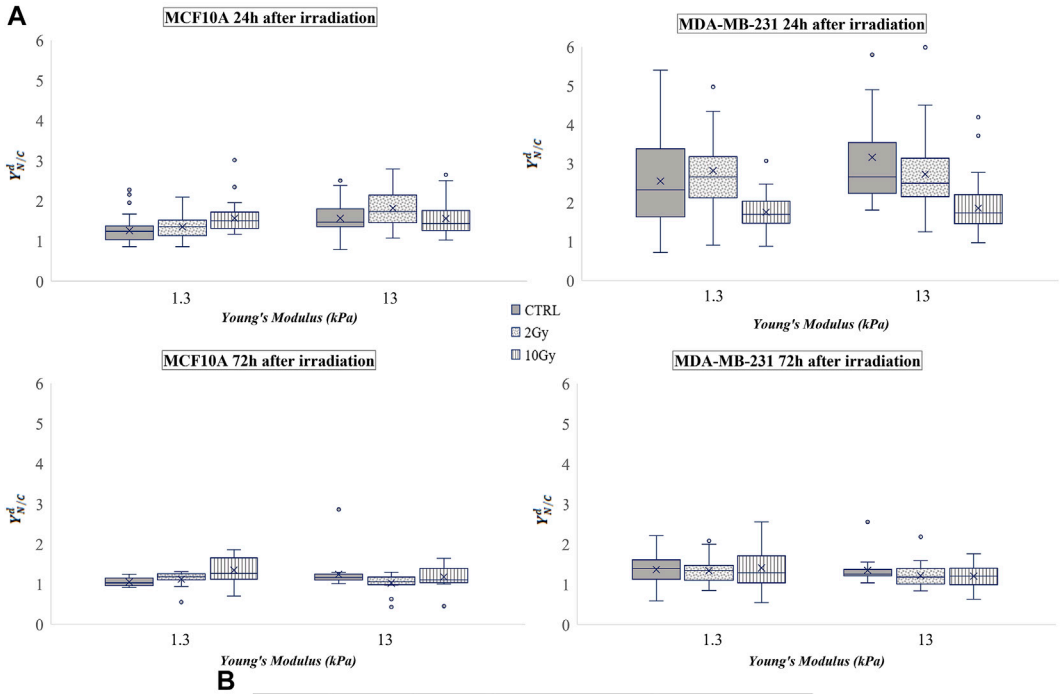

B

		Control	2 Gy		10 Gy	
		13 kPa	1.3 kPa	13 kPa	1.3 kPa	13 kPa
Control	1.3 kPa	***,NS NS,NS	NS,* NS, NS	***,NS NS, NS	***,*** ###, NS	*,NS ##, NS
	13 kPa	-	NS,NS NS, NS	NS, NS NS, NS	NS, NS ###, NS	NS, NS ###, NS
2 Gy	1.3 kPa	-	-	***, NS NS, NS	NS, NS ###, NS	NS, NS ###, NS
	13 kPa	-	-	-	NS,** ###, NS	NS, NS ###, NS
10 Gy	1.3 kPa	-	-	-	-	NS, NS NS, NS

FIGURE 2
(A) Box plots in which the mean value, the median, the interquartile, and the outliers of the normalized YAP nucleus to cytoplasm ratio, $Y^d_{N/C}$, are shown. The values have been estimated for both cell lines 24 (top) and 72 h (bottom) after irradiation. MCF10A on: 1.3 kPa substrate at 24 h n = 50, 39,and 40 for control, 2 Gy, 10 Gy, respectively; 1.3 kPa substrate at 72 h n = 20 for control, 2 Gy, 10 Gy; 13 kPa at 24 h n = 48, 33, and 23 for control, 2 Gy, 10 Gy, respectively; 13 kPa at 72 h n = 20 for control, 2 Gy, 10 Gy; MDA-MB-231 on: 1.3 kPa substrate at 24 h n= 43, 35, and 41 for control, 2 Gy, 10 Gy, respectively; 1.3 kPa substrate at 72 h n = 51, 54, 36 for control, 2 Gy, 10 Gy, respectively; 13 kPa at 24 h n = 33, 46, and 60 for control, 2 Gy, 10 Gy, respectively; 13 kPa at 72 h n = 18, 53, and 35 for control, 2 Gy, 10 Gy, respectively. **(B)** Statistical analysis: asterisks (*) refer to $Y^d_{N/C}$ at 24 h (blue) and 72 h (black) of MCF10A cell. Hash signs (#) to those of MDA-MB-231 cells. ***, $^{###}P< 0.001$. **, $^{##}P< 0.01$. *$P< 0.05$. NS not significant.

72 h after irradiation show that MDA-MB-231 cells reduced the values of $Y^d_{N/C}$ in all conditions, exhibiting identical ratios on both substrates and in both control and irradiated conditions.

3.2 Radiation effects on expression levels and activation status of YAP

The analysis of $Y^d_{N/C}$ gives information about the subcellular YAP concentration (predominantly nuclear or cytoplasmic) but does not provide details about nuclear and cytoplasmic YAP expression intensity. Then, the quantitative evaluation of both nuclear and cytoplasmic YAP density (Y^d_N, Y^d_C) and the overall expression of nuclear and cytoplasmic YAP (Y_N, Y_C), as indicated in the subsection 2.5, was performed.

If no dramatic effects were observed in the normalized values of N/C ratio ($Y^d_{N/C}$), the analysis of both Y^d_N and Y_N indicates that the radiation exposure affected sensitively the healthy cells. In particular, 24 h after irradiation a slight reduction with the lower dose and a significant enhancement of Y^d_N with the higher one (Supplementary Figure S3) were found, whereas Y_N increased with both doses (Figure 3). However, all these effects were reversed or completely recovered after 72 h on the soft substrates, indicating a probable defensive role of the healthy tissue mechanical condition, as previously reported (Panzetta

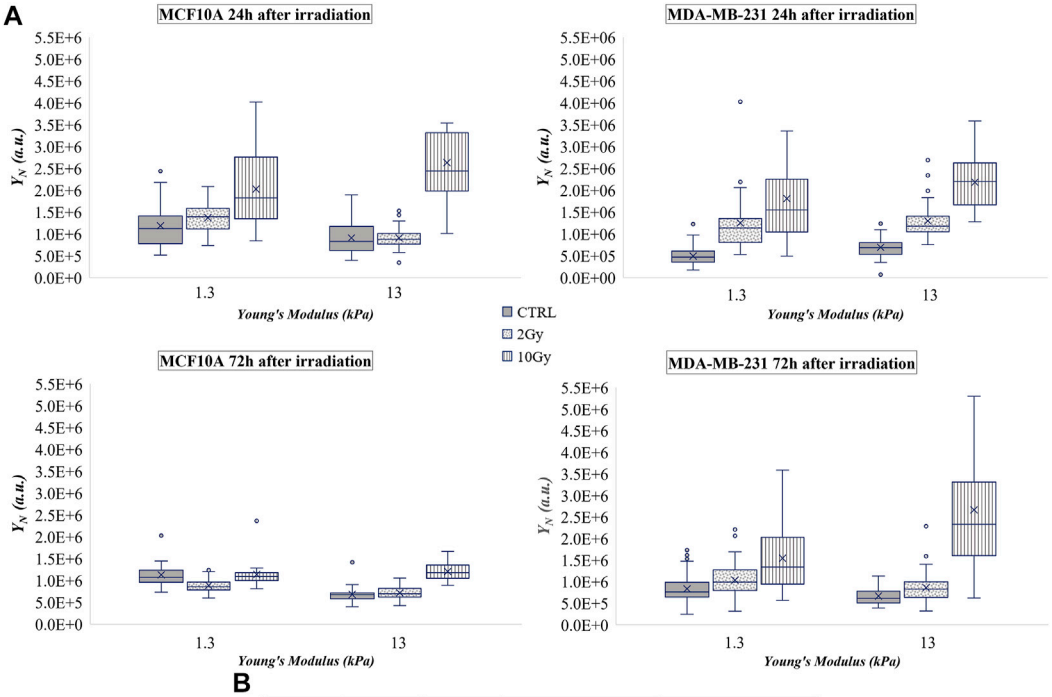

B

		Control	2 Gy		10 Gy	
		13 kPa	1.3 kPa	13 kPa	1.3 kPa	13 kPa
Control	1.3 kPa	NS,*** NS,NS	NS,NS ###,NS	NS,*** ###,NS	***,NS ###,###	***,NS ###,###
	13 kPa	-	***,NS ##,###	NS,NS ###,NS	***,*** ###,###	***,*** ###,###
2 Gy	1.3 kPa	-	-	***,NS NS,NS	NS,NS NS,NS	**,*** ###,###
	13 kPa	-	-	-	***,*** NS,###	***,*** ###,###
10 Gy	1.3 kPa	-	-	-	-	NS,NS NS,NS

FIGURE 3
(A) Box plots in which the mean value, the median, the interquartile, and the outliers of the YAP expression into the nucleus, Y_N, are shown. The values have been estimated for both cell lines 24 (top) and 72 h (bottom) after irradiation. MCF10A on: 1.3 kPa substrate at 24 h n = 50, 39, and 40 for control, 2 Gy, 10 Gy, respectively; 1.3 kPa substrate at 72 h n = 20 for control, 2 Gy, 10 Gy; 13 kPa at 24 h n = 48, 33, and 23 for control, 2 Gy, 10 Gy, respectively; 13 kPa at 72 h n = 20 for control, 2 Gy, 10 Gy; MDA-MB-231 on: 1.3 kPa substrate at 24 h n= 43, 35, 41 for control, 2 Gy, 10 Gy, respectively; 1.3 kPa substrate at 72 h n = 51, 54, 36 for control, 2 Gy, 10 Gy, respectively; 13 kPa at 24 h n = 33, 46, and 60 for control, 2 Gy, 10 Gy, respectively; 13 kPa at 72 h n = 18, 53, and 35 for control, 2 Gy, 10 Gy, respectively. **(B)** Statistical analysis: Asterisks (*) refer to Y_N at 24 h (blue) and 72 h (black) of MCF10A cell. Hash signs (#) to those of MDA-MB-231 cells. ***, $^{\#\#\#}P < 0.001$. **, $^{\#\#}P < 0.01$. NS not significant.

et al., 2020). On the other hand, cells seeded on the substrate that mimics the tumoral tissue mechanics were not affected by the lower radiation dose, while the booster dose continued to promote an accumulation process of YAP in the nucleus, even if a partial recovery was found.

The tumoral cell line showed a substantial increase of Y_N^d after the delivery of both doses on both polyacrylamide substrates. If the results discussed in the previous section suggest a translocation process of YAP from the nucleus to the cytoplasm in the tumour cells, the data reported in Figure 3 and Supplementary Figure 3 clearly indicate that the analysis of the only $Y_{N/C}^d$ could be partial and, eventually, misleading. The enhancement of Y_N^d and Y_N observed for both doses and both stiffnesses supports, in fact, previous results indicating that the radiation exposure promotes YAP activation on various tumour cells, by impairing and increasing nuclear localization (Fernandez-L et al., 2012; Zhang et al., 2019; Zhang et al., 2021).

At the same time, the analyses 24 h after the treatment, showed that X-rays radiation did not affect YAP concentration in the cell cytoplasm (Y_C^d) when MCF10A cells are seeded on the softer substrate (Supplementary Figure S4), even if the overall expression of cytoplasmic YAP (Y_C) increased in a manner (Figure 4). A different trend can be observed for cells seeded on the 13 kPa substrate. In fact, the delivery of the lower dose led to a significant decrease of Y_C, while the dose of 10 Gy affected cells by increasing both Y_C^d and Y_C (Figure 4, and Supplementary Figure S4). 3 days after radiation, the healthy cell

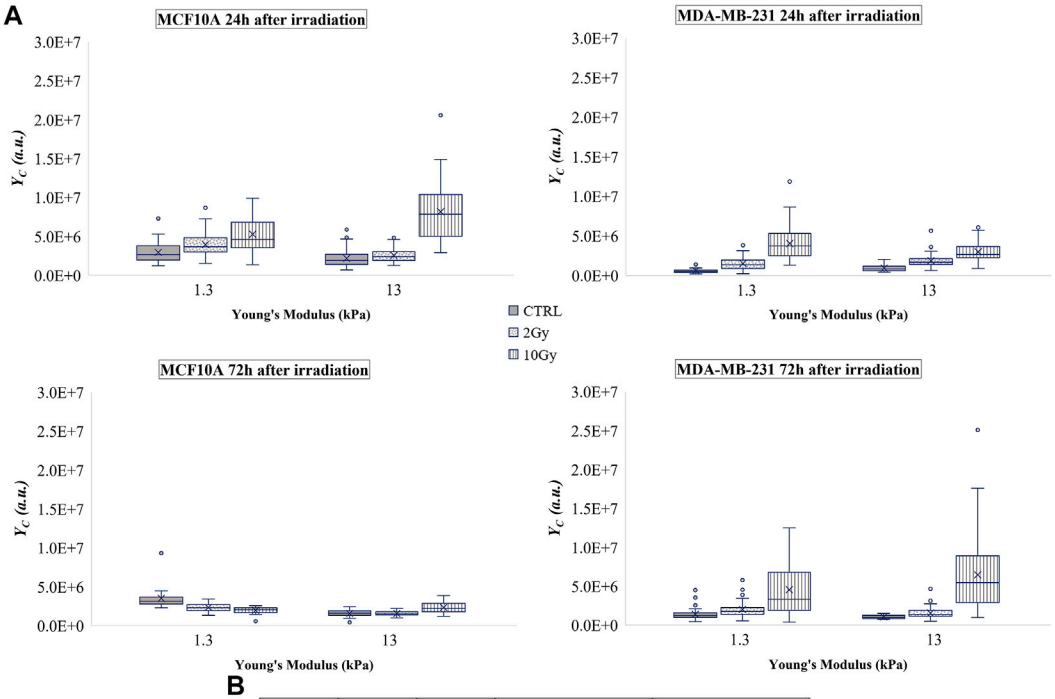

B

		Control	2 Gy		10 Gy	
		13 kPa	1.3 kPa	13 kPa	1.3 kPa	13 kPa
Control	1.3 kPa	NS,*** NS, NS	NS,* ###, #	NS,*** ###,NS	***,*** ###, ###	***,* ###, ###
	13 kPa	-	***,*** NS, ###	NS,NS ###,NS	***,NS ###, ###	***,*** ###, ###
2 Gy	1.3 kPa	-	-	**, *** NS,NS	NS,NS ###, #	*,NS ###, ###
	13 kPa	-	-	-	***,NS ###, ###	***,*** ###, ###
10 Gy	1.3 kPa	-	-	-	-	NS,NS NS,NS

FIGURE 4
(A) Box plots in which the mean value, the median, the interquartile, and the outliers of the YAP expression into the cytoplasm, Y_C, are shown. The values have been estimated for both cell lines 24 (top) and 72 h (bottom) after irradiation. MCF10A on: 1.3 kPa substrate at 24 h n = 50, 39, and 40 for control, 2 Gy, 10 Gy, respectively; 1.3 kPa substrate at 72 h n = 20 for control, 2 Gy, 10 Gy; 13 kPa at 24 h n = 48, 33, and 23 for control, 2 Gy, 10 Gy, respectively; 13 kPa at 72 h n = 20 for control, 2 Gy, 10 Gy; MDA-MB-231 on: 1.3 kPa substrate at 24 h n= 43, 35, and 41 for control, 2 Gy, 10 Gy, respectively; 1.3 kPa substrate at 72 h n = 51, 54, and 36 for control, 2 Gy, 10 Gy, respectively; 13 kPa at 24 h n = 33, 46, and 60 for control, 2 Gy, 10 Gy, respectively; 13 kPa at 72 h n = 18, 53, and 35 for control, 2 Gy, 10 Gy, respectively.**(B)** Statistical analysis: Asterisks (*) refer to Y_C at 24 h (blue) and 72 h (black) of MCF10A cell. Hash signs (#) to those of MDA-MB-231 cells. ***, $^{###}P < 0.001$. **$P < 0.01$. *, $^{\#}P < 0.05$. NS not significant. Subcellular YAP expression correlates with lamin A/C level.

line showed a significant decrease of Y_C^d, while on the 13 kPa substrate an opposite trend, with a dose-dependent increase in Y_C was found.

On the other side, X-rays radiation affected tumour cells by increasing Y_C^d and Y_C on both substrates. The values resulted particularly augmented when cells were treated with the dose of 10 Gy for both time periods.

Taken together, these results indicate that, after the irradiation, the tumour cell line exhibits a profound and dose-dependent augmentation of both quote of phosphorylated (Y_C) and dephosphorylated YAP (Y_N). In general, it has been demonstrated that YAP silencing potentiates sensitivity of breast cancer cells to radiation therapy (Andrade et al., 2017) and that, on the contrary, the overall overexpression of YAP (here found particularly in cells irradiated with the booster dose and cultured on stiff substrates) might upregulate the expression levels of some anti-apoptosis genes, such as BCL2L1 and BIRC5, then decreasing progressively the apoptotic sensitivity of tumour cells (Lee and Yonehara 2012; Rosenbluh et al., 2012). However, as already reported, more than the whole expression level of YAP, its nucleo-cytoplasmic distribution effectively describes YAP activity regulated by upstream core components of the Hippo pathway (Piccolo et al., 2014). The coactivating transcriptional function of YAP, in fact, is restrained when the activation of the Hippo pathway produces its serine phosphorylation and the consequent cytoplasmic sequestration (Hansen et al., 2015).

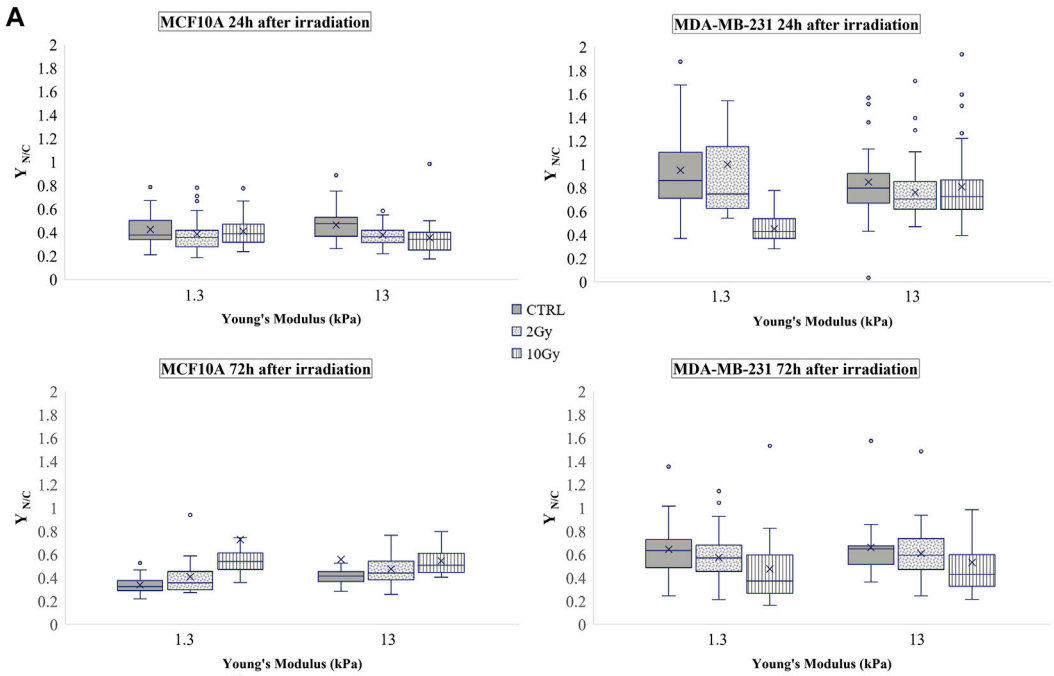

B

		Control	2 Gy		10 Gy	
		13 kPa	1.3 kPa	13 kPa	1.3 kPa	13 kPa
Control	1.3 kPa	NS,NS NS,NS	NS,NS NS,NS	NS,*** NS,NS	NS,*** ###,###	NS,*** NS,##
	13 kPa	-	*,NS NS,NS	NS,NS NS,NS	NS,* ###,###	***,* NS,NS
2 Gy	1.3 kPa	-	-	NS,NS NS,NS	NS,*** ###,#	NS,*** NS,NS
	13 kPa	-	-	-	NS,NS ###,###	NS,NS NS,NS
10 Gy	1.3 kPa	-	-	-		NS,NS ###,NS

FIGURE 5
(A) Box plots in which the mean value, the median, the interquartile, and the outliers of the nuclear to cytoplasmic ratio of total YAP, $Y_{N/C}$, are shown. The values have been estimated for both cell lines 24 (top) and 72 h (bottom) after irradiation. MCF10A on: 1.3 kPa substrate at 24 h n = 50, 39, and 40 for control, 2 Gy, 10 Gy, respectively; 1.3 kPa substrate at 72 h n = 20 for control, 2 Gy, 10 Gy; 13 kPa at 24 h n = 48, 33, and 23 for control, 2 Gy, 10 Gy, respectively; 13 kPa at 72 h n = 20 for control, 2 Gy, 10 Gy; MDA-MB-231 on: 1.3 kPa substrate at 24 h n= 43, 35, 41 for control, 2 Gy, 10 Gy, respectively; 1.3 kPa substrate at 72 h n = 51, 54, 36 for control, 2 Gy, 10 Gy, respectively; 13 kPa at 24 h n = 33, 46, and 60 for control, 2 Gy, 10 Gy, respectively; 13 kPa at 72 h n = 18, 53, and 35 for control, 2 Gy, 10 Gy, respectively. **(B)** Statistical analysis: Asterisks (*) refer to $Y_{N/C}$ at 24 h (blue) and 72 h (black) of MCF10A cell. Hash signs (#) to those of MDA-MB-231 cells. ***, $^{###}P < 0.001$. $^{##}P < 0.01$. *, $^{#}P < 0.05$. NS not significant.

Taking this into account, the localization of YAP was quantified in terms of $Y_{N/C}$ in order to better define the effects of radiation on its activation status. On one hand, MDA-MB-231 maintained at 24 h the global Y_C and Y_N at similar values, as indicated by the unaltered value of $Y_{N/C}$, except on the soft substrate where the higher dose induced its significant reduction (Figure 5). On the other hand, the booster dose induced a global reduction of the same parameter after 72 h, even if not in a significant way on the stiffer substrate. Similarly, the healthy cell line manifested a substantial reduction of $Y_{N/C}$ on the stiff substrate after 24 h when irradiated with the higher dose, whereas at longer time this response was completely reversed with a dose-dependent increase of the same parameter on both substrates (Figure 5).

In late response to irradiation, the process of YAP sequestering in the nucleus of MCF10A or in the cytoplasm of MDA-MB-231 could be a mechanism by which cell growth or apoptosis are regulated. Dephosphorylation of YAP, that associates with its transportation in the nucleus, has been shown to reduce p73 binding and the consequent cell apoptosis downstream in breast cancer cells (Matallanas et al., 2007). However, other researches have revealed that phosphorylation of YAP in response to ionizing radiation might impede YAP functioning as co-activator of p73 to enhance proapoptotic genes, thereby contributing to cell protection (Strano et al., 2005; Levy et al., 2008) (Lapi et al., 2008).

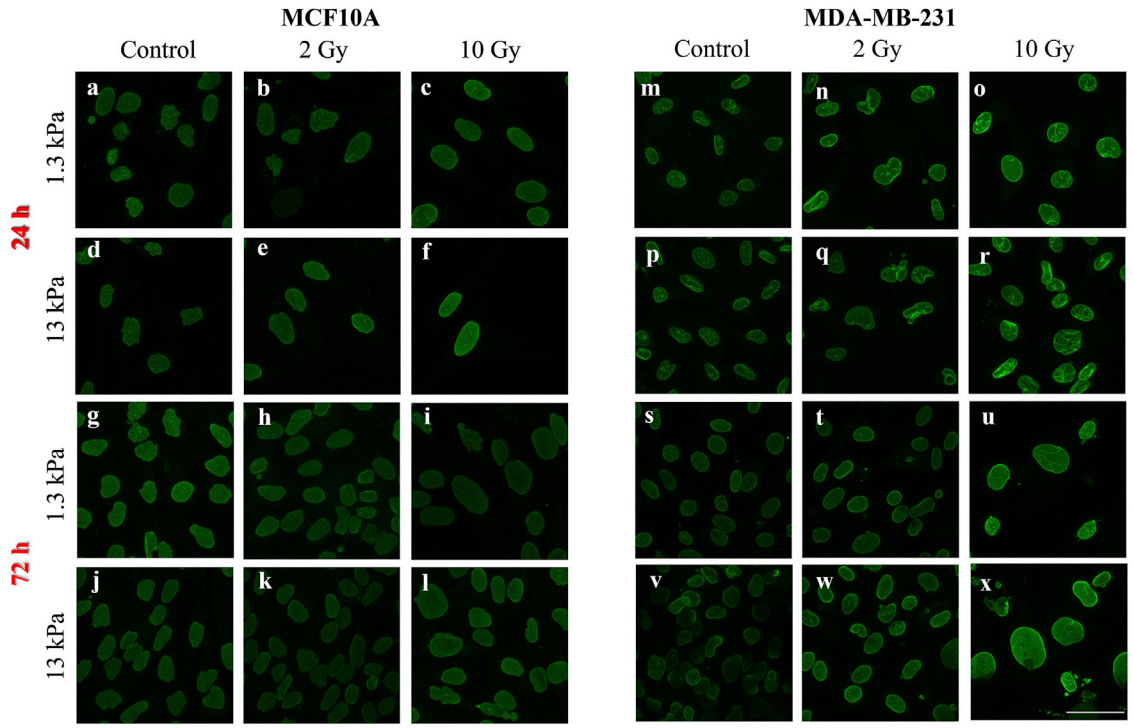

FIGURE 6
Representative images of lamin A/C immunofluorescence in MCF10A **(A–L)** and MDA-MB-231 **(M–X)** are shown. Scale bar, 50 μm.

3.3 Subcellular YAP expression correlates with lamin A/C level

A vast literature indicates the key role of nuclear deformability in mediating changes in YAP localization (Elosegui-Artola et al., 2017; Kalukula et al., 2022; Maremonti et al., 2022). It has been demonstrated, in fact, that cells with stiffer nuclei require greater contractile forces from the cytoskeleton to compress the nucleus and to evoke YAP shuttling from the cytoplasm to the nucleus (Koushki et al., 2020). On the other side, the key role of lamin A/C in regulating nuclear stiffness (Koushki et al., 2020) led us to question if the changes in YAP localization after irradiation can be correlated to variations in lamin A/C expression level (Figure 6). As shown in Figure 7, at short time the irradiation increased in a dose-dependent manner the lamin A/C expression in both cell lines and on both stiffnesses. At longer time, this response was completely reversed in the healthy cells and accompanied by the nuclear translocation of YAP. On the contrary, the higher levels of lamin A/C, together with the reduction of the nuclear localization of YAP (Figure 5), persisted in the tumour cells, when irradiated with the booster dose. These findings suggest that the variations of YAP n/c expression ratio could be ascribed to the effects that the irradiation can have on lamin A/C levels and, consequently, on the nuclear deformability.

4 Conclusion

In this study, two mammary cell lines, the healthy MCF10A and the cancerous MDA-MB-231, were employed to investigate the changes in the expression of the YAP protein before and after radiation treatment. Cells were irradiated with doses used in the conventional radiotherapy treatment, 2 and 10 Gy, and analysed 24 and 72 h after the treatment. Additionally, cells were seeded on polyacrylamide substrates with two different Young's modulus, 1.3 and 13 kPa, that emulate the healthy and tumour tissue respectively, to evaluate the role of the ECM in this process.

Our results showed that X-ray irradiation affected in a significant way the levels of YAP expression, density, and localization in both cell lines. The early short time response (24 h) results to be transient in the healthy cells; in fact, MCF10A, after an overall increase of YAP level in both the nucleus and cytoplasm and on both substrates, reduced mostly the YAP expression in the cytoplasm by inducing a translocation process into the nucleus, dependent on both substrate stiffness and X-ray dose. Tumour cells responded similarly to the healthy ones at short time, but the effects of X-ray were completely reversed at 72 h in terms of subcellular localization, as indicated by the reduction of $Y_{N/C}$.

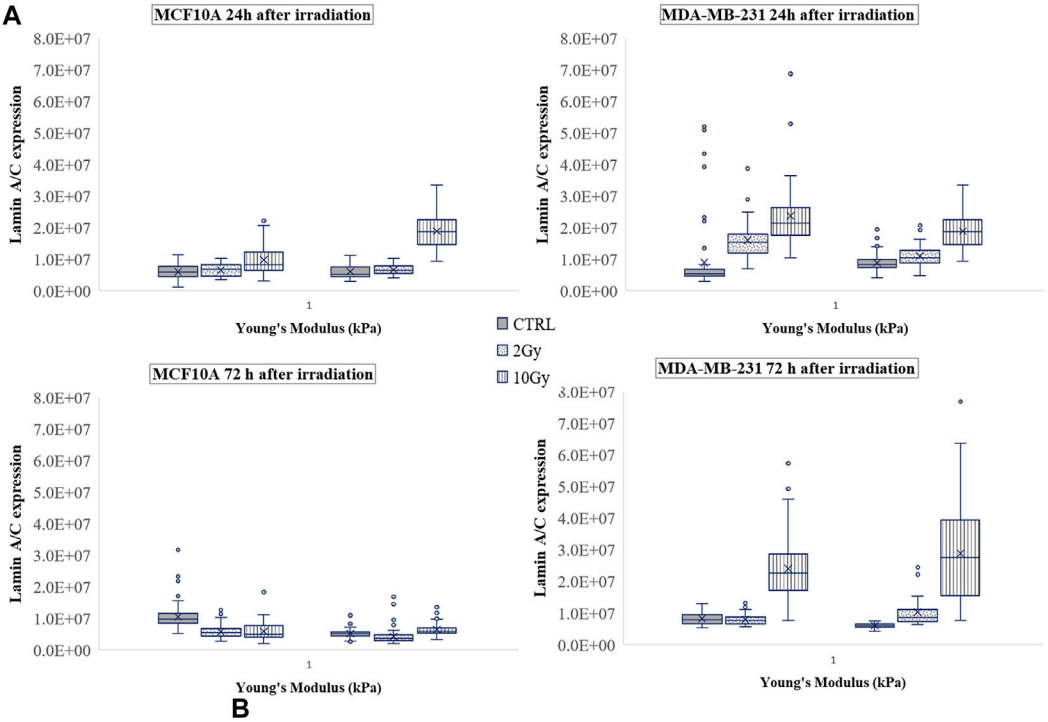

B

		Control	2 Gy		10 Gy	
		13 kPa	1.3 kPa	13 kPa	1.3 kPa	13 kPa
Control	1.3 kPa	NS,*** ###, NS	NS,*** ###, NS	NS,*** ###, NS	***,*** ###,###	***,*** ###,###
	13 kPa	-	NS,NS ###, NS	NS,*** NS,###	***,NS ###,###	***,* ###,###
2 Gy	1.3 kPa	-	-	NS,*** NS,NS	NS,NS NS,###	***,NS NS,###
	13 kPa	-	-	-	NS,*** ###,###	***,*** NS,###
10 Gy	1.3 kPa	-	-	-	-	***,NS NS,NS

FIGURE 7
(A) Box plots in which the mean value, the median, the interquartile, and the outliers of the levels of lamin A/C expression are shown. The values have been estimated for both cell lines 24 (top) and 72 h (bottom) after irradiation. MCF10A on: 1.3 kPa substrate at 24 h n = 50, 40, and 42 for control, 2 Gy, 10 Gy, respectively; 1.3 kPa substrate at 72 h n = 89, 78, and 70 for control, 2 Gy, 10 Gy, respectively; 13 kPa at 24 h n = 43, 41, 23 for control, 2 Gy, 10 Gy, respectively; 13 kPa at 72 h n = 75, 83, and 63 for control, 2 Gy, 10 Gy, respectively; MDA-MB-231 on: 1.3 kPa substrate at 24 h n = 99, 42, and 33 for control, 2 Gy, 10 Gy, respectively; 1.3 kPa substrate at 72 h n = 22, 25, and 37 for control, 2 Gy, 10 Gy, respectively; 13 kPa at 24 h n = 108, 40, and 37 for control, 2 Gy, 10 Gy, respectively; 13 kPa at 72 h n = 22, 39, and 35 for control, 2 Gy, 10 Gy, respectively. **(B)** Statistical analysis: Asterisks (*) refer to lamin A/C at 24 h (blue) and 72 h (black) of MCF10A cell. Hash signs (#) to those of MDA-MB-231 cells. ***, $^{###}P < 0.001$. *$P < 0.05$. NS not significant.

Since YAP works as a transcriptional co-activator, its localization into the nucleus before and after irradiation could have a different impact on subsequent cell behaviour. In particular, the reduced expression of YAP and its translocation into the nucleus could be a mechanism by which healthy cells protect themselves from apoptosis (Zhang et al., 2012) and control their growth (increased $Y_{N/C}$ associates also with growth process). On the other side, the YAP nuclear exclusion/reduction can result in a temporary confined inhibition of cell proliferation and invasion, as supported by previous findings (Panzetta et al., 2020; La Verde et al., 2021), but more importantly in a modulation of cell sensitivity to radiation (Tsujiura et al., 2014) that can be used in the design of doses and timing of subsequent radiation therapy.

These results can aid in obtaining a deeper knowledge of the role of the ECM and the effect of radiotherapy on both healthy and cancerous cells and in developing the diagnostic and therapeutical aspects of radiation therapy.

Data availability statement

The raw data supporting the conclusion of this article will be made available by the authors, without undue reservation.

Author contributions

Conceptualization, VP and SF; methodology, GL, VA, and VP; validation, VP and SF; formal analysis, GL and VA; investigation, GL and VA; data curation, VP, GL, and VA; writing—original draft preparation, GL, VA, and VP; writing—review and editing, GL, VA, MP, CA, ML, PN, SF, and VP; supervision, SF and VP; funding acquisition, MP, ML, and PN. All authors have read and agreed to the published version of the manuscript.

Conflict of interest

The authors declare that the research was conducted in the absence of any commercial or financial relationships that could be construed as a potential conflict of interest.

Publisher's note

Supplementary material

The Supplementary Material for this article can be found online at: https://www.frontiersin.org/articles/10.3389/fbioe.2022.969004/full#supplementary-material

References

Akervall, J., Nandalur, S., Zhang, J., Qian, C. N., Goldstein, N., Gyllerup, P., et al. (2014). A novel panel of biomarkers predicts radioresistance in patients with squamous cell carcinoma of the head and neck. *Eur. J. Cancer* 50 (3), 570–581. doi:10.1016/j.ejca.2013.11.007

Andrade, D., Mehta, M., Griffith, J., Panneerselvam, J., Srivastava, A., Kim, T. D., et al. (2017). YAP1 inhibition radiosensitizes triple negative breast cancer cells by targeting the DNA damage response and cell survival pathways. *Oncotarget* 8 (58), 98495–98508. doi:10.18632/oncotarget.21913

Baker, E. L., Lu, J., Yu, D., Bonnecaze, R. T., and Zaman, M. H. (2010). Cancer cell stiffness: Integrated roles of three-dimensional matrix stiffness and transforming potential. *Biophys. J.* 99, 2048–2057. doi:10.1016/j.bpj.2010.07.051

Camargo, F. D., Gokhale, S., Johnnidis, J. B., Fu, D., Bell, G. W., Jaenisch, R., et al. (2007). YAP1 increases organ size and expands undifferentiated progenitor cells. *Curr. Biol.* 17, 2054–2060. doi:10.1016/j.cub.2007.10.039

Chan, S. W., Lim, C. J., Guo, K., Ng, C. P., Lee, I., Hunziker, W., et al. (2008). A role for TAZ in migration, invasion, and tumorigenesis of breast cancer cells. *Cancer Res.* 68, 2592–2598. doi:10.1158/0008-5472.CAN-07-2696

Chan, S. W., Lim, C. J., Loo, L. S., Chong, Y. F., Huang, C., and Hong, W. (2009). TEADs mediate nuclear retention of TAZ to promote oncogenic transformation. *J. Biol. Chem.* 284, 14347–14358. doi:10.1074/jbc.M901568200

Coughlin, S. S. (2019). Epidemiology of breast cancer in women. *Adv. Exp. Med. Biol.* 1152, 9–29. doi:10.1007/978-3-030-20301-6_2

DeSantis, C. E., Ma, J., Gaudet, M. M., Newman, L. A., Miller, K. D., Goding Sauer, A., et al. (2019). Breast cancer statistics, 2019. *Ca. A Cancer J. Clin.* 69 (6), 438–451. doi:10.3322/caac.21583

Dong, J., Feldmann, G., Huang, J., Wu, S., Zhang, N., Comerford, S. A., et al. (2007). Elucidation of a universal size-control mechanism in Drosophila and mammals. *Cell.* 130, 1120–1133. doi:10.1016/j.cell.2007.07.019

Dupont, S., Morsut, L., Aragona, M., Enzo, E., Giulitti, S., Cordenonsi, M., et al. (2011). Role of YAP/TAZ in mechanotransduction. *Nature* 474, 179–183. doi:10.1038/nature10137

Elkind, M. M. (1984). Repair processes in radiation biology. *Radiat. Res.* 100, 425–449. doi:10.2307/3576409

Elosegui-Artola, A., Andreu, I., Beedle, A. E., Lezamiz, A., Uroz, M., Kosmalska, A. J., et al. (2017). Force triggers YAP nuclear entry by regulating transport across nuclear pores. *Cell.* 171 (6), 1397–1410.e14. doi:10.1016/j.cell.2017.10.008

Fattet, L., Jung, H. Y., Matsumoto, M. W., Aubol, B. E., Kumar, A., Adams, J. A., et al. (2020). Matrix rigidity controls epithelial-mesenchymal plasticity and tumor metastasis via a mechanoresponsive EPHA2/LYN complex. *Dev. Cell.* 54 (3), 302–316.e7. doi:10.1016/j.devcel.2020.05.031

Ferlay, J., Colombet, M., Soerjomataram, I., Dyba, T., Randi, G., Bettio, M., et al. (2018). Cancer incidence and mortality patterns in Europe: Estimates for 40 countries and 25 major cancers in 2018. *Eur. J. Cancer* 103, 356–387. doi:10.1016/j.ejca.2018.07.005

Fernandez-L, A., Squatrito, M., Northcott, P., Awan, A., Holland, E. C., Taylor, M. D., et al. (2012). Oncogenic YAP promotes radioresistance and genomic instability in medulloblastoma through IGF2-mediated Akt activation. *Oncogene* 31 (15), 1923–1937. doi:10.1038/onc.2011.379

Hall, A. (2009). The cytoskeleton and cancer. *Cancer Metastasis Rev.* 28, 5–14. doi:10.1007/s10555-008-9166-3

Hansen, C. G., Moroishi, T., and Guan, K. L. (2015). YAP and TAZ: A nexus for hippo signaling and beyond. *Trends Cell. Biol.* 25 (9), 499–513. doi:10.1016/j.tcb.2015.05.002

Harvey, K., Zhang, X., and Thomas, D. (2013). The Hippo pathway and human cancer. *Nat. Rev. Cancer* 13, 246–257. doi:10.1038/nrc3458

Iliakis, G., Wang, Y. A., Guan, J., and Wang, H. (2003). DNA damage checkpoint control in cells exposed to ionizing radiation. *Oncogene* 22, 5834–5847. doi:10.1038/sj.onc.1206682

Kalukula, Y., Stephens, A. D., Lammerding, J., and Gabriele, S. (2022). Mechanics and functional consequences of nuclear deformations. *Nat. Rev. Mol. Cell. Biol.*, 1–20. doi:10.1038/s41580-022-00480-z

Karahalil, B., Yardım-Akaydin, S., and Nacak Baytas, S. (2019). An overview of microtubule targeting agents for cancer therapy. *Arh. Hig. Rada. Toksikol.* 70, 160–172. doi:10.2478/aiht-2019-70-3258

Kim, N.-G., Koh, E., Chen, X., and Gumbiner, B. M. (2011). E-cadherin mediates contact inhibition of proliferation through hippo signaling-pathway components. *Proc. Natl. Acad. Sci. U. S. A.* 108, 11930–11935. doi:10.1073/pnas.1103345108

Koushki, N., Ghagre, A., Srivastava, L. K., Sitaras, C., Yoshie, H., Molter, C., et al. (2020). Lamin A redistribution mediated by nuclear deformation determines dynamic localization of YAP. *Biophysical J.* 118, 3 252a. doi:10.1101/2020.03.19.998708

Krieg, M., Fläschner, G., Alsteens, D., Gaub, B. M., Roos, W. H., Wuite, G. J. L., et al. (2019). Atomic force microscopy-based mechanobiology. *Nat. Rev. Phys.* 1, 41–57. doi:10.1038/s42254-018-0001-7

La Verde, G., Artiola, V., Panzetta, V., Pugliese, M., Netti, P. A., and Fusco, S. (2021). Cytoskeleton response to ionizing radiation: A brief review on adhesion and migration effects. *Biomedicines* 9 (9), 1102. doi:10.3390/biomedicines9091102

Ladoux, B., and Mège, R. M. (2017). Mechanobiology of collective cell behaviours. *Nat. Rev. Mol. Cell. Biol.* 18, 743–757. doi:10.1038/nrm.2017.98

Lapi, E., Di Agostino, S., Donzelli, S., Gal, H., Domany, E., Rechavi, G., et al. (2008). PML, YAP, and p73 are components of a proapoptotic autoregulatory feedback loop. *Mol. Cell.* 32 (6), 803–814. doi:10.1016/j.molcel.2008.11.019

Lee, K. K., and Yonehara, S. (2012). Identification of mechanism that couples multisite phosphorylation of yes-associated protein (YAP) with transcriptional coactivation and regulation of apoptosis. *J. Biol. Chem.J Biol. Chem.* 291287 (912), 9568–9578. doi:10.1074/jbc.M111.296954

Levental, Kandice R., Yu, H., Kass, L., Lakins, J. N., Egeblad, M., Erler, J. T., et al. (2009). Matrix crosslinking forces tumor progression by enhancing integrin signaling. *Cell.* 1395, 891–906. doi:10.1016/j.cell.2009.10.027

Levy, D., Adamovich, Y., Reuven, N., and Shaul, Y. (2008). Yap1 phosphorylation by c-Abl is a critical step in selective activation of proapoptotic genes in response to DNA damage. *Mol. Cell.* 29 (3), 350–361. doi:10.1016/j.molcel.2007.12.022

Li, Q. S., Lee, G. Y., Ong, C. N., and Lim, C. T. (2008). AFM indentation study of breast cancer cells. *Biochem. Biophys. Res. Commun.* 374, 609–613. doi:10.1016/j.bbrc.2008.07.078

Low, B. C., Pan, C. Q., Shivashankar, G. V., Bershadsky, A., Sudol, M., and Sheetz, M. (2014a). YAP/TAZ as mechanosensors and mechanotransducers in regulating organ size and tumor growth. *FEBS Lett.* 588, 2663–2670. doi:10.1016/j.febslet.2014.04.012

Low, B. C., Pan, C. Q., Shivashankar, G. V., Bershadsky, A., Sudol, M., and Sheetz, M. (2014b). YAP/TAZ as mechanosensors and mechanotransducers in regulating organ size and tumor growth. *FEBS Lett.* 588 (16), 2663–2670. doi:10.1016/j.febslet.2014.04.012

Maremonti, M. I., Panzetta, V., Dannhauser, D., Netti, P. A., and Causa, F. (2022). Wide-range viscoelastic compression forces in microfluidics to probe cell-dependent nuclear structural and mechanobiological responses. *J. R. Soc. Interface* 19 (189), 20210880. doi:10.1098/rsif.2021.0880

Matallanas, D., Romano, D., Yee, K., Meissl, K., Kucerova, L., Piazzolla, D., et al. (2007). RASSF1A elicits apoptosis through an MST2 pathway directing proapoptotic transcription by the p73 tumor suppressor protein. *Mol. Cell.* 27 (6), 962–975. doi:10.1016/j.molcel.2007.08.008

Nikkhah, M., Strobl, J. S., De Vita, R., and Agah, M. (2010). The cytoskeletal organization of breast carcinoma and fibroblast cells inside three dimensional (3-D) isotropic silicon microstructures. *Biomaterials* 31, 4552–4561. doi:10.1016/j.biomaterials.2010.02.034

Nukuda, A., Sasaki, C., Ishihara, S., Mizutani, T., Nakamura, K., Ayabe, T., et al. (2015). Stiff substrates increase YAP-signaling-mediated matrix metalloproteinase-7 expression. *Oncogenesis* 4, e165. doi:10.1038/oncsis.2015.24

Panciera, T., Azzolin, L., Cordenonsi, M., and Piccolo, S. (2017). Mechanobiology of YAP and TAZ in physiology and disease. *Nat. Rev. Mol. Cell. Biol.* 18 (12), 758–770. doi:10.1038/nrm.2017.87

Panciera, T., Citron, A., Di Biagio, D., Battilana, G., Gandin, A., Giulitti, S., et al. (2020). Reprogramming normal cells into tumour precursors requires ECM stiffness and oncogene-mediated changes of cell mechanical properties. *Nat. Mat.* 19, 797–806. doi:10.1038/s41563-020-0615-x

Panzetta, V., La Verde, G., Pugliese, M., Artiola, V., Arrichiello, C., Muto, P., et al. (2020). Adhesion and migration response to radiation therapy of mammary epithelial and adenocarcinoma cells interacting with different stiffness substrates. *Cancers* 12 (5), 1170. doi:10.3390/cancers12051170

Panzetta, V., Musella, I., Rapa, I., Volante, M., Netti, P. A., and Fusco, S. (2017). Mechanical phenotyping of cells and extracellular matrix as grade and stage markers of lung tumor tissues. *Acta Biomater.* 57, 334–341. doi:10.1016/j.actbio.2017.05.002

Piccolo, S., Dupont, S., and Cordenonsi, M. (2014). The biology of YAP/TAZ: Hippo signaling and beyond. *Physiol. Rev.* 94, 1287–1312. doi:10.1152/physrev.00005.2014

Plodinec, M., Loparic, M., Monnier, C. A., Obermann, E. C., Zanetti-Dallenbach, R., Oertle, P., et al. (2012). The nanomechanical signature of breast cancer. *Nat. Nanotechnol.* 7, 757–765. doi:10.1038/nnano.2012.167

Pocaterra, A., Romani, P., and Dupont, S. (2020). YAP/TAZ functions and their regulation at a glance. *J. Cell. Sci.* 133 (2), jcs230425. doi:10.1242/jcs.230425

Rosenbluh, J., Nijhawan, D., Cox, A. G., Li, X., Neal, J., Schafer, E., et al. (2012). β-Catenin-Driven cancers require a YAP1 transcriptional complex for survival and tumorigenesis. *Cell.* 151 (7), 1457–1473. doi:10.1016/j.cell.2012.11.026

Sinclair, W. K., and Fry, R. J. M. (1987). Mechanisms of radiation interaction with DNA: Potential implications for radiation protection. *Radiat. Res.* 112, 407–417. doi:10.2307/3577094

Smith, C. A. (1987). DNA repair in specific sequences in mammalian cells. *J. Cell. Sci.* 6, 225–241. doi:10.1242/jcs.1984.supplement_6.16

Stowers, R. S., Allen, S. C., Sanchez, K., Davis, C. L., Ebelt, N. D., Van Den Berg, C., et al. (2017). Extracellular matrix stiffening induces a malignant phenotypic transition in breast epithelial cells. *Cell. Mol. Bioeng.* 10, 114–123. doi:10.1007/s12195-016-0468-1

Strano, S., Monti, O., Pediconi, N., Baccarini, A., Fontemaggi, G., Lapi, E., et al. (2005). The transcriptional coactivator yes-associated protein drives p73 gene-target specificity in response to DNA damage. *Mol. Cell.* 18 (4), 447–459. 429. doi:10.1016/j.molcel.2005.04.008

Tsujiura, M., Mazack, V., Sudol, M., Kaspar, H. G., Nash, J., Carey, D. J., et al. (2014). Yes-associated protein (YAP) modulates oncogenic features and radiation sensitivity in endometrial cancer. *PloS one* 9 (6), e100974. doi:10.1371/journal.pone.0100974

Ward, J. F. (1988). DNA damage produced by ionizing radiation in mammalian cells: Identities, mechanisms of formation and reparability. *Prog. Nucleic Acid. Res. Mol. Biol.* 35, 95–125. doi:10.1016/s0079-6603(08)60611-x

Wei, S. C., Fattet, L., Tsai, J. H., Guo, Y., Pai, V. H., Majeski, H. E., et al. (2015). Matrix stiffness drives epithelial-mesenchymal transition and tumour metastasis through a TWIST1-G3BP2 mechanotransduction pathway. *Nat. Cell. Biol.* 17 (5), 678–688. doi:10.1038/ncb3157

Xu, X., Chen, Y., Wang, X., and Mu, X. (2019). Role of Hippo/YAP signaling in irradiation-induced glioma cell apoptosis. *Cancer Manag. Res.* 11, 7577–7585. doi:10.2147/CMAR.S210825

Yilmaz, M., and Christofori, G. (2009). EMT, the cytoskeleton, and cancer cell invasion. *Cancer Metastasis Rev.* 28, 15–33. doi:10.1007/s10555-008-9169-0

Zanconato, F., Battilana, G., Cordenonsi, M., and Piccolo, S. (2016a). YAP/TAZ as therapeutic targets in cancer. *Curr. Opin. Pharmacol.* 29, 26–33. doi:10.1016/j.coph.2016.05.002

Zanconato, F., Cordenonsi, M., and Piccolo, S. (2016b). YAP/TAZ at the roots of cancer. *Cancer Cell.* 29 (6), 783–803. doi:10.1016/j.ccell.2016.05.005

Zanconato, F., Forcato, M., Battilana, G., Azzolin, L., Quaranta, E., Bodega, B., et al. (2015). Genome-wide association between YAP/TAZ/TEAD and AP-1 at enhancers drives oncogenic growth. *Nat. Cell. Biol.* 17, 1218–1227. doi:10.1038/ncb3216

Zhang, H., Wu, S., and Xing, D. (2012). Inhibition of Aβ(25-35)-induced cell apoptosis by low-power-laser-irradiation (LPLI) through promoting Akt-dependent YAP cytoplasmic translocation. *Cell. Signal.* 24 (1), 224–232. doi:10.1016/j.cellsig.2011.09.004

Zhang, L., Shi, H., Chen, H., Gong, A., Liu, Y., Song, L., et al. (2019). Dedifferentiation process driven by radiotherapy-induced HMGB1/TLR2/YAP/HIF-1α signaling enhances pancreatic cancer stemness. *Cell. Death Dis.* 10, 724. doi:10.1038/s41419-019-1956-8

Zhang, Y., Wang, Y., Zhou, D., Wang, K., Wang, X., Wang, X., et al. (2021). Radiation-induced YAP activation confers glioma radioresistance via promoting FGF2 transcription and DNA damage repair. *Oncogene* 40 (27), 4580–4591. doi:10.1038/s41388-021-01878-3

Zhao, B., Wei, X., Li, W., Udan, R. S., Yang, Q., Kim, J., et al. (2007). Inactivation of YAP oncoprotein by the Hippo pathway is involved in cell contact inhibition and tissue growth control. *Genes. Dev.* 21, 2747–2761. doi:10.1101/gad.1602907

Zhao, B., Ye, X., Yu, J., Li, L., Li, W., Li, S., et al. (2008). TEAD mediates YAP-dependent gene induction and growth control. *Genes. Dev.* 22, 1962–1971. doi:10.1101/gad.1664408

frontiers | Frontiers in Bioengineering and Biotechnology

TYPE Original Research
PUBLISHED 21 September 2022
DOI 10.3389/fbioe.2022.1002661

OPEN ACCESS

EDITED BY
Guang-Kui Xu,
Xi'an Jiaotong University, China

REVIEWED BY
Lihai Zhang,
The University of Melbourne, Australia
Bo Li,
Tsinghua University, China

*CORRESPONDENCE
Yulong Li,
liyulong@nwpu.edu.cn
Hui Yang,
kittyyh@nwpu.edu.cn

†These authors have contributed equally to this work

SPECIALTY SECTION
This article was submitted to Biomechanics, a section of the journal Frontiers in Bioengineering and Biotechnology

RECEIVED 25 July 2022
ACCEPTED 24 August 2022
PUBLISHED 21 September 2022

CITATION
Xu D, Zhang N, Wang S, Zhang P, Li Y and Yang H (2022), A method for generating dynamic compression shear coupled stress loading on living cells. *Front. Bioeng. Biotechnol.* 10:1002661. doi: 10.3389/fbioe.2022.1002661

A method for generating dynamic compression shear coupled stress loading on living cells

Dasen Xu[1,2†], Nu Zhang[2,3†], Sijie Wang[2,3], Pan Zhang[2,3], Yulong Li[2,4,5*] and Hui Yang[2,3*]

[1]School of Aeronautics, Northwestern Polytechnical University, Xi'an, China, [2]Center of Special Environmental Biomechanics; Biomedical Engineering, Northwestern Polytechnical University, Xi'an, China, [3]School of Life Science, Northwestern Polytechnical University, Xi'an, China, [4]School of Civil Aviation, Northwestern Polytechnical University, Xi'an, China, [5]Joint International Research Laboratory of Impact Dynamic and Its Engineering Application, Xi'an, China

Changes in the mechanical properties of single cells are related to the physiological state and fate of cells. The construction of cell constitutive equations is essential for understanding the material characteristics of single cells. With the help of atomic force microscopy, bio-image processing algorithms, and other technologies, research investigating the mechanical properties of cells during static/quasi-static processes has developed rapidly. A series of equivalent models, such as viscoelastic models, have been proposed to describe the constitutive behaviors of cells. The stress-strain relations under dynamic processes are essential to completing the constitutive equations of living cells. To explore the dynamic mechanical properties of cells, we propose a novel method to generate a controllable dynamical compression shear coupling stress on living cells. A CFD model was established to visualize this method and display the theories, as well as assess the scope of the application. As the requirements or limitations are met, researchers can adjust the details of this model according to their lab environment or experimental demands. This micro-flow channel-based method is a new tool for approaching the dynamic mechanical properties of cells.

KEYWORDS

dynamic compression-shear coupling stress, Device development, cell mechanics, CFD model, weak shock wave

Introduction

During the processes of cell development, differentiation, physiology, and disease, cells receive not only chemical signals but also mechanical signals from the extracellular matrix and surrounding environment (Hamed, 2020). Mechanical forces are experienced by cells and may be interpreted as a signal to induce phenotypic and functional responses or pathways, such as gene expression cascades, protein synthesis, proliferation, and movement; these responses can temporarily or even permanently change the cellular state

(Desprat et al., 2005; Patterson et al., 2019). Moreover, the mechanobiological responses of biological cells had been extensively studied also, e.g., the responses of mesenchymal stem cells and chondrocytes to mechanical stimuli (Zhang et al., 2008; Zhang et al., 2012; Ganadhiepan et al., 2019). From a mechanical perspective, cells present a special material that is far more complex than ordinary materials, such as metal and glass. It is worth noting that the mechanical properties of cells remain unstable in most pathological processes, such as metastasis, asthma, sickle cell anemia, and apoptosis (Alberts et al., 2002; Desprat et al., 2005; Hao et al., 2020). Thus, understanding the mechanical behaviors of cells can provide a useful perspective on describing disease progression and revealing the fundamental mechanisms of the working of biomaterials (Bao and Suresh, 2003; Moeendarbary and Harris, 2014).

In exploring the mechanical behaviors of cells and establishing stress-strain relationships in them, it is a challenge to properly apply a controllable force on the tissue/monolayer/cell and capture its real-time strain at a single cell scale (i.e., 10^{-5} m) (Patterson, 2020). In this regard, various reasonable assumptions have been proposed, which present a research-scale perspective on mechanical methods, including the mechanical and biological methods (Moeendarbary and Harris, 2014; Hao et al., 2020).

In conjunction with atomic force microscopy (AFM), the bio-image processing algorithm (Dudani et al., 2013), micropipette aspiration (MA) (Evans and Yeung, 1989), and microfluidic platforms (Urbanska et al., 2020) are the most common and effective mechanical tools to apply compression/tensile or shear stress on cells. In addition, to improve accuracy and collect more information, some modified techniques and methods have been designed, such as magnetic twisting cytometry (MTC) (Trepat et al., 2004) and uniaxial stretching rheometer (USR) (Desprat et al., 2005). Through these static or quasi-static mechanical experiments, it is believed that the mechanical behavior of cells is likely to resemble that of viscoelastic material (Katti et al., 2019). However, experiments exploring the stress-strain relationship of isolated living cells did not reach dynamic conditions or higher strain rates ($\dot{\epsilon} > 10^{-1}$ s^{-1}). Commonly, the dynamic loading process of materials, including living cells, differs significantly from the static or quasi-static situations. For instance, a quasi-static deformation situation comprises a sequence of equilibrium states, where the well-known equations describing the mechanics of materials work (i.e., $\sum F = 0$; $\sum M = 0$). On the contrary, the dynamic loading process can be treated as a stress wave traveling through the body at an acoustic speed (Meyers, 1994). When an external deformation is imparted at a very high rate, it induces stress on one portion of the body, while other portions remain unaffected. As cells can sense mechanical behaviors, they react rapidly to adapt to them (Pelham and Wang, 1997). Cells subjected to dynamic loading processes exhibit distinct mechanical behaviors rather than viscoelastic material. Moreover, the stress-strain relations under dynamic processes are an important part of the single-cells constitutive equations. Therefore, developing methods to apply dynamic stress on cells will significantly promote the understanding of the mechanical behaviors of cells under dynamic conditions (Bao and Suresh, 2003).

In the present work, we propose a novel method to apply combined dynamic compression-shear loading on isolated living cells under normal conditions; in addition, we extend the range of stiffness tensor of single biological cell piecewise function to higher strain rates ($\dot{\epsilon} > 10^{0}$ s^{-1}). The basis of this new method is the theory of transient flow, or in detail, the theory of the weak shock wave (where "weak" signifies that the thermal energy generated by impact compression is smaller compared to the total internal energy of the fluid (Smith, 1973)) propagation in a viscous fluid, which would suddenly induce both the compression and shear stresses in the boundary layer. In addition, the water hammer theory asserts that we can repeatedly apply disturbance with the amplitude of the weak shock wave, which is precisely controllable by changing the speed of the projectile. Briefly, this method includes two parts: the stress loading part accelerates a projectile to impact a fluid-fulfilled microchannel seeded with living cells on the bottom, while the strain acquisition part is equipped with a high-speed camera to assist with an image processing algorithm. Once the assumptions and requirements are fulfilled, the details of the design remain readily changeable. The proposed methods can be used to explore the stress-strain relations under dynamic processes and clarify the constitutive behavior of single cells to dynamic loadings.

Methods

To illustrate the dynamic and coupled compression-shear loading method, a simple schematic diagram of the model is presented in Figures 1A,B. The model exhibits a gas gun, projectile, and a microfluidic chip with a rectangular conduit channel, where cells can be seeded on the bottom wall. In this mode, a projectile was accelerated to an initial velocity (u_p) to impact the buffer; a pressure surge was then generated, which traveled through the fluid matter. As this stress wave propagated at the acoustic velocity, the cells cultured on the bottom wall experienced the compression stress by the stress wave directly, as well as shear stress due to the viscosity of the fluid (Figure 1C).

Navier-Stokes equations

To allow the pressure waves to propagate, the fluid used in this experiment was compressible with constant viscosity. Therefore, the equations of continuity and momentum (Navier-Stokes equations) used to describe the motion of the fluid are written as:

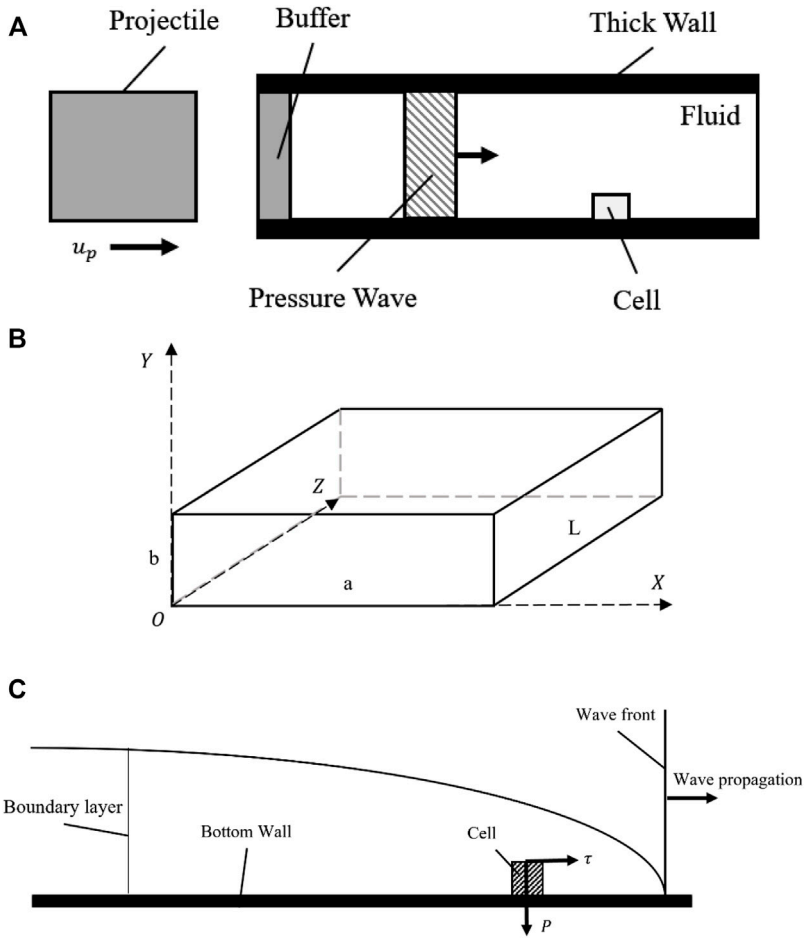

FIGURE 1
A schematic diagram showing the basics of the proposed model. **(A)** The schematic diagram of the geometry of the model; **(B)** The sketch of the rectangular channel; **(C)** The stress analysis of cells during wave propagation.

$$\frac{\partial \rho}{\partial t} + \nabla \cdot (\rho u) = 0 \tag{1}$$

$$\frac{\partial (\rho u)}{\partial t} + \nabla \cdot (\rho u \cdot u) = -\nabla P + \mu \nabla^2 u + \frac{\mu}{3} \nabla (\nabla \cdot u) \tag{2}$$

Where ρ is the fluid density; μ is the dynamic viscosity; u is the fluid velocity; $''\nabla''$ is the gradient operator; $''\nabla \cdot ''$ is the divergence operator; $''\nabla^2''$ is the Laplace operator which means $''\nabla \cdot \nabla''$; t is time, and P is the total pressure in the fluid. For isotropic and homogeneous newton fluid, the stress tensor can be expressed as:

$$\sigma_{ii} = -P + 2\mu \frac{\partial u_i}{\partial x_i} - \frac{2}{3}\mu \nabla \cdot u \tag{3}$$

$$\tau_{ij} = \mu \left(\frac{\partial u_i}{\partial x_j} + \frac{\partial u_j}{\partial x_i} \right) \tag{4}$$

Where u_i is the fluid velocity, and x_i is the spatial coordinate ($i = 1, 2, 3$). σ_{ii} is the pressure components of stress tensor, and τ_{ij} is the shear components of stress tensor. In the channel flow with non-slip wall condition, the wall shear stress (τ_i^w) could be calculated using:

$$\tau_i^w = \mu \left(\frac{\partial u_i}{\partial n_w} \right) \tag{5}$$

Where n_w is the distance normal to the wall.

Wave propagation celerity in a rectangular conduit channel

A general solution for the celerity of pressure wave propagating in the fluid has been derived by Hutarew and can be applied for a conduit of any cross-section (Hutarew, 1973). The form is:

$$c_f = 1 \Big/ \left(\rho \left(\frac{1}{K} + \frac{1}{\mathcal{A}} \frac{\delta \mathcal{A}}{\delta p} \right) \right) \tag{6}$$

Where K is the fluid bulk modulus, $\mathcal{A}$ is the cross-section area of the channel, and c_f is the wave propagation celerity. δ is a small change sign. Eq. 6 shows the effect of fluid-structure interaction on the propagation speed of the pressure surge. This means that despite the fluid in the Computational Fluid Dynamics (CFD) model being considered compressible, the deformation of channel walls should be taken into account. However, in this study, a rigid-walled boundary condition was preferred, which could make the measurement and calculation of the cell strain field much more concise. Hence, a corrected fluid bulk modulus (K_{mod}) was proposed to incorporate structural behavior in he CFD model. For the propagation of pressure surge in liquids traveling through thick-walled pipes and ducts of rectangular cross-section, the theoretical wave celerity equation was given by Thorley (Thorley and Guymer, 1976):

$$c_f = 1\Big/\left(\rho\left(\frac{1}{K}+\frac{\Phi(a,b)}{abEe^2}\right)\right) \tag{7}$$

$$\Phi(a,b) = \frac{a^3+b^3}{2(a+b)}\left(\frac{a^3}{6}+\frac{a^2b}{2}-\frac{b^3}{3}\right) - \frac{a^5}{20}-\frac{a^2a^3}{4}+\frac{b^5}{5}+\frac{Ee^2}{4G}\left(a^3+b^3\right)+\frac{abe^2}{2}(a+b) \tag{8}$$

Where a and b are the lengths of the long and short sides of the rectangular cross-section; e is the wall thickness; E and G are the elastic and shear moduli of the wall material, respectively. $\Phi(a,b)$ was solved using Eq. 8. According to the equation defining wave propagation velocity, the corrected fluid bulk modulus K_{mod} equation is:

$$c_f = \left(\frac{K_{mod}}{\rho_0}\right)^{\frac{1}{2}} \tag{9}$$

Nevertheless, the properties of solids involved played an important role in wave propagation as per the wave celerity equation. An evaluation of the fluid-solid coupling effect was needed to examine the limitations when the motion of the channel was rigid. A dimensional parameter "β", named "fluid loading", was proposed by Pinnington to evaluate the fluid-solid coupling; it corresponded to the Korteweg wave speed equation (Korteweg, 1878; Pinnington, 1997; Shepherd and Inaba, 2009).

$$\beta = \left(c_0/c_f\right) \tag{10}$$

$$\beta = \left(\frac{c_f^2}{c_s^2}\right)\left(\frac{\rho_f}{\rho_s}\right)\left(\frac{2R}{e}\right) \tag{11}$$

Where c_0 is the acoustic speed in fluid; R is the mean radius of the channel; the subscript, "s", denotes a structure, and the subscript, "f", means fluid. Moreover, according to the limiting cases of fluid-structure interaction (FSI) discussed by Shepherd and Inaba, the case, where $\ll 1$, indicated that the channel could be regarded as rigid (Shepherd and Inaba, 2009). Substituting the wave celerity and acoustic speed in Eq. 10 to get the parameter β helped us design the details of the channel.

Pressure wave generation by projectile impact

To describe the fluid suitable here with equations, the Tait and Tammann equations of state, which apply to a wide range of liquids, were used (Dymond and Malhotra, 1988; Hoang et al., 2015). The Tait equation can be written as a function of pressure (p) and density (ρ)

$$p = B\left(\frac{\rho}{\rho_0}\right)^{\gamma} - B \tag{12}$$

Where B is a weak function of entropy, which is usually treated as a pressure constant of 3.35×10^8 Pa. γ is the adiabatic exponent that equals 7.15 (Nagayama et al., 2002). The Tait equation was rewritten as a partial differential equation form.

$$\ln(p+B) = \ln(B) + \gamma\ln\left(\frac{\rho}{\rho_0}\right)$$
$$\frac{\partial p}{\partial \rho} = \frac{\gamma(p+B)}{\rho} \tag{13}$$

As the whole process was assumed to be isentropic, the adiabatic exponent γ was:

$$\gamma = -\frac{\gamma}{p}\frac{dp}{d\gamma}\Big|_s \tag{14}$$

Where γ is the volume Upon substituting volume γ by density ρ, we obtained:

$$\frac{p}{p_0} = \left(\frac{\rho}{\rho_0}\right)^{-\gamma} \tag{15}$$

The definition of acoustic velocity is:

$$c^2 = \left(\frac{\partial p}{\partial \rho}\right) \tag{16}$$

Upon integration of Eq. 16, a function of pressure and wave speed describing the fluid density was obtained, which could be used to correct the density in CFD, as the fluid was considered compressible.

$$\rho = \rho_0 + c^{-2}p \tag{17}$$

The acoustic velocity is derived from Eq. 15.

$$\left(\frac{\partial p}{\partial \rho}\right)_s = \gamma\left(\frac{p_0}{\rho_0}\right)\left(\frac{\rho}{\rho_0}\right)^{\gamma-1} = c^2 \tag{18}$$

As the compressibility of the fluid was limited, an approximation of the acoustic velocity under normal conditions could be written as:

$$\lim_{\rho \longrightarrow \rho_0}\left(\frac{\partial p}{\partial \rho}\right)_s = \frac{\gamma p_0}{\rho_0} = c_0^2 \tag{19}$$

The local acoustic velocity could be written as:

$$c = \left(\frac{\partial p}{\partial \rho}\right)^{\frac{1}{2}} = c_0\left(\frac{p}{p_0}\right)^{\frac{\gamma-1}{2\gamma}} = c_0\left(\frac{\rho}{\rho_0}\right)^{\frac{\gamma-1}{2\gamma}} \tag{20}$$

Figure 2A displays the shock wave jumps conditions with a coordinate fixed at the shock wave front. The equations of conservation (mass; momentum; energy) could be written as:

$$\rho_0(u_0 - c_s) = \rho_1(u_1 - c_s) \tag{21}$$

$$\rho_0(u_0 - c_s)u_0 dt = \rho_1(u_1 - c_s)u_1 dt \tag{22}$$

$$\frac{1}{2}u_0^2 + \frac{\gamma}{\gamma-1}\frac{p_0}{\rho_0} = \frac{1}{2}u_1^2 + \frac{\gamma}{\gamma-1}\frac{p_1}{2} \tag{23}$$

These equations are usually known as the Rankine-Hugoniot equations (Smith, 1973). Here, we neglected the thickness of the shock front, and thus, the particle velocity, u and shock velocity, c_s behind the shock front could be solved. For very weak shock waves, the jump process could be treated as an isentropic process, yielding the following equation:

$$c_s = \left(\left(\frac{\rho}{\rho_0}\right)\left(\frac{p - p_0}{\rho - \rho_0}\right)\right)^{\frac{1}{2}} \tag{24}$$

$$u = \frac{(\rho - \rho_0)}{\rho} c_s \tag{25}$$

$$\frac{\rho_1}{\rho_0} = \frac{(\gamma+1)p_1 + (\gamma-1)p_0}{(\gamma+1)p_0 + (\gamma-1)p_1} = \frac{u_0}{u_1} \tag{26}$$

The particle velocity could then be rewritten with Eq. 19.

$$u = \frac{p - p_0}{\rho_0 c_0} = \frac{c_0}{\gamma p_0}(p - p_0) \tag{27}$$

or

$$\frac{p}{p_0} = 1 + \frac{\gamma u}{c_0} \tag{28}$$

Substituting by Eq. 20, gave:

$$c_s = c_0\left(1 + \frac{\gamma u}{c_0}\right)^{\frac{\gamma-1}{2\gamma}} \tag{29}$$

The Taylor expanded form of Eq. 29 thus obtained is:

$$\begin{aligned} c_s &= c_0\left(1 + \frac{\gamma-1}{2c_0}u + \mathcal{O}(u^2) + \ldots\right) \\ &\cong c_0\left(1 + \frac{\gamma-1}{2c_0}u\right) \cong c_o + \left(\frac{\gamma-1}{2}\right)u \end{aligned} \tag{30}$$

As the relationship between acoustic velocity and particle velocity was obtained, the differential form was:

$$du_p = du = \frac{2}{\gamma-1} dc_S \tag{31}$$

As no cavitation or fluid column separation occurred and no cross-section changes were recorded along the channel, the Joukowsky equation was a perfect approximation to predict the maximum pressure in a water-hammer impact situation (Joukowsky, 1900; Walters and Leishear, 2018). This impact occurs at $(x, t) = (0, 0)$, and an equation, $p(t)$, describes the dynamic pressure of the fluid at the interface of the fluid and projectile. This initial impact would create a weak shock wave with an amplitude that can be determined by the pressure-velocity matching method (Meyers, 1994; Deshpande et al., 2006; Shepherd and Inaba, 2009)

$$\Delta p = p(0) = \frac{(\rho c)_f (\rho c)_p}{(\rho c)_f + (\rho c)_p} u_p \tag{32}$$

Where $(\rho c)_f$ is the fluid impedance; $(\rho c)_p$ is the projectile impedance. The impedance of a projectile is much higher than that of the fluid in most cases, and Eq. 12 can reduce it to an approximated expression:

$$p(0) \approx (\rho c)_f u_p \tag{33}$$

After the conditions of the fluid were solved, the impact condition obtained is shown in Figure 2B. The shock wave generation due to the projectile impact was a discrete process. In this study, since the buffer was assumed to be as thin as possible, it could be neglected given that it had the same impendence as the projectile. This model could be simplified to a projectile impacting the fluid column directly. Analysis of the projectile motion was performed according to Newton's second law.

$$p_i \mathcal{A}_p = m_p \frac{du_p}{dt} \tag{34}$$

Where p_i is the pressure by every discrete impact; u_p is the interface velocity of projectile and fluid; $\mathcal{A}_p$ is the cross area of the projectile, and m_p is the mass of the projectile. Substituting Eq. 34 with Eq. 31, the result was:

$$p = \frac{2}{\gamma-1}\frac{m_p}{\mathcal{A}_p}\frac{dc_s}{dt} \tag{35}$$

Meanwhile, Eq. 12 was rewritten in terms of local acoustic velocity c_s to obtain the following:

$$p = B\left(\frac{\rho_0 c^2}{nB}\right)^{\frac{\gamma}{\gamma-1}} - B \tag{36}$$

The partial differential form of Eq. 33 is:

$$\frac{\partial p}{\partial c} = \frac{2\gamma}{\gamma-1}\frac{P + B}{c} \tag{37}$$

In our model, the pressure was too small as compared with the pressure constant, which is 3.35×10^8 Pa (Nagayama et al., 2002). A linear approximation treatment (Lennon, 1994) was used with normal condition parameters (p_0, c_0) to calculate Eq. 34, which could be rewritten as:

$$\left(\frac{\partial p}{\partial c}\right)_s = \frac{2\gamma}{\gamma-1}\frac{P_0 + B}{c_0} \tag{38}$$

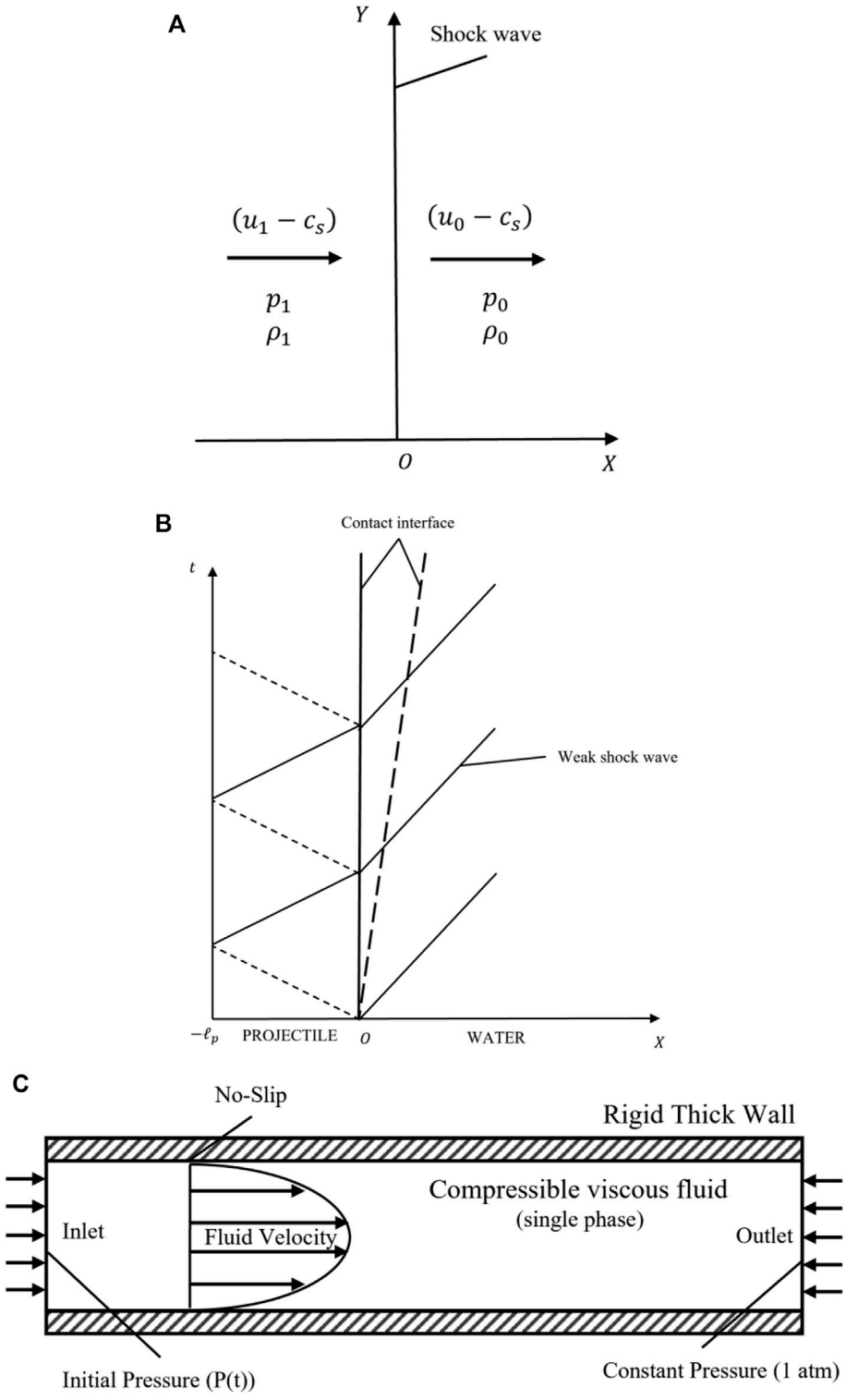

FIGURE 2
The isolation of boundary conditions and analysis of the model. **(A)** The weak shock wave jumps conditions under a coordinate fixed with the shock wave front; **(B)** The weak shock wave generated by projectile impact analysis; **(C)** A schematic diagram illustrating the micro-channel boundary conditions in CFD modeling.

The normal conditions here were $p_0 = 101325\,Pa$, $\rho_0 = 999.8$ kg/m^3, and $c_0 = 1439$ m/s. Eq. 33 was then rewritten as follows:

$$p = \frac{2}{\gamma - 1}\frac{m_p}{\mathcal{A}_p}\frac{dc_s}{dt} = \frac{2}{\gamma - 1}\frac{m_p}{\mathcal{A}_p}\left(\frac{\partial c}{\partial p}\right)_s\frac{dp}{dt} \tag{39}$$

Upon integration of Eq. 36, a simplified function of pressure was gained.

$$p(t) = p(0)\exp(-\lambda t) \tag{40}$$

Where the time constant was as follows:

$$\lambda = \frac{\gamma - 1}{2}\frac{\mathcal{A}_p}{m_p}\left(\frac{\partial p}{\partial c}\right)_s \tag{41}$$

Boundary layer induced by a very weak shock wave

Once a weak shock wave enters a static fluid boundary through the wall, a boundary layer begins to appear at the interaction point of the weak shock wave and the wall (Ackroyd, 1967; Davies and Bernstein, 1969). A study of the laminar compressible boundary layer induced by this weak shock wave was solved by H. Mirels' in 1955, who provided theoretical evidence to prove that the weak shock waves generated by projectile impact indeed induce a boundary layer (Mirels, 1955).

Considering a possible turbulent boundary layer, R. E Melnik and B. Grossman developed an asymptotic theory within the limit of weak shock waves (Melnik and Grossman, 1974). Their three-layer description of the boundary layer was a natural extension of the asymptotic theories of Mellor (Mellor, 1972), Yajnik (Yajnik, 1970), Bush and Fendell (Bush and Fendell, 1972; Bush and Fendell, 1973) for incompressible boundary layers, as well as the theory by Afzal (Afzal, 1973) for compressible non-interacting turbulent boundary layers. FLUENT is a reliable and acceptable CFD software employed for relevant numerical simulations. To simulate our model, the k-ε model was utilized to analyze turbulent flow (Versteeg and Malalasekera, 2007; Nikpour et al., 2014).

Geometry definition

In the present work, the geometry definition consisted of a volume occupied by the flow with a specified shape of the physical boundaries. Here are several important criteria to limit the size of the channel, although, in the beginning, we planned to put the 'lab' into just one small chip to make this as convenient as possible. A fundamental restriction applied was the continuous flow in the fluid domain to ensure that the theories being considered were effective. A dimensionless parameter, the Knudsen number, was used to describe this problem (Guo et al., 2013); this number is defined as

$$K_n = \lambda\!\!\!^{-}/\ell_{char} \tag{42}$$

Where $\lambda\!\!\!^{-}$ is the mean free path of the particle, and ℓ_{char} is the characteristic length scale. The fluid domain was described as a continuum and solved by Navier-Stokes (N-S) equations with no-slip boundary conditions, therefore, the K_n was generally considered to be less than 0.001 (Ben-Dor et al., 2000; Kandlikar et al., 2005; Rapp, 2016).

According to the requirements above, we established a simple CFD model to describe our method. The Cartesian coordinates system was created as shown in Figure 1B, and a 3 × 3 × 60 mm rectangular conduit channel was drawn in ANSYS. The details of size were kept adjustable to adapt to various laboratory environments for other researchers. An example size is proposed here to describe dynamic stress loading methods.

Mesh generation and solver settings

Transient simulation is strongly dependent on the quality of the mesh. For most water-hammer models to accurately capture the near-wall velocity, the mesh density near the wall should be concentrated. During the cross-section meshing process, the boundary layer neighboring the wall was divided into 20 layers with the first layer having a thickness of 1×10^{-6} m (1.1 growth rate); this design was based on the mesh independence analysis of 3D pressurized pipe flow with CFD modeling previously described by Martins et al. (Martins et al., 2018). Given the axial direction, a sweep method was applied. The Courant-Friedrichs-Lewy (CFL) criterion was used to maintain stability during the movement of the acoustic wave across the discrete elements in CFD, which determined the element size in the axial direction. The non-dimensional Courant number was calculated using the following equation:

$$C_{\text{courant}} = c_f\frac{\Delta t}{\Delta z} \tag{43}$$

Where Δz is the element size in the axial direction, and Δt is the calculation time step. There were two main considerations for the determination of $C_{courant}$: one was to capture the wave velocity in the fluid; and the other was to calculate the stress on an arbitrary cell at the channel wall. The $C_{courant}$ was ideally expected to be ≤ 1. Moreover, to maintain the meshing quality, i.e., to keep the aspect ratio of all mesh elements < 10^3, the axial element size was $\Delta z = 0.1$ mm with a time step of $t = 0.7 \times 10^{-7}$ s. The total time was assumed to be 4.2×10^{-5} s, i.e., 600 steps in total, to ensure that the entire compression wave could travel completely from inlet to outlet. The total mesh count was 1.98 million elements (Martins et al., 2014; Mandair, 2020).

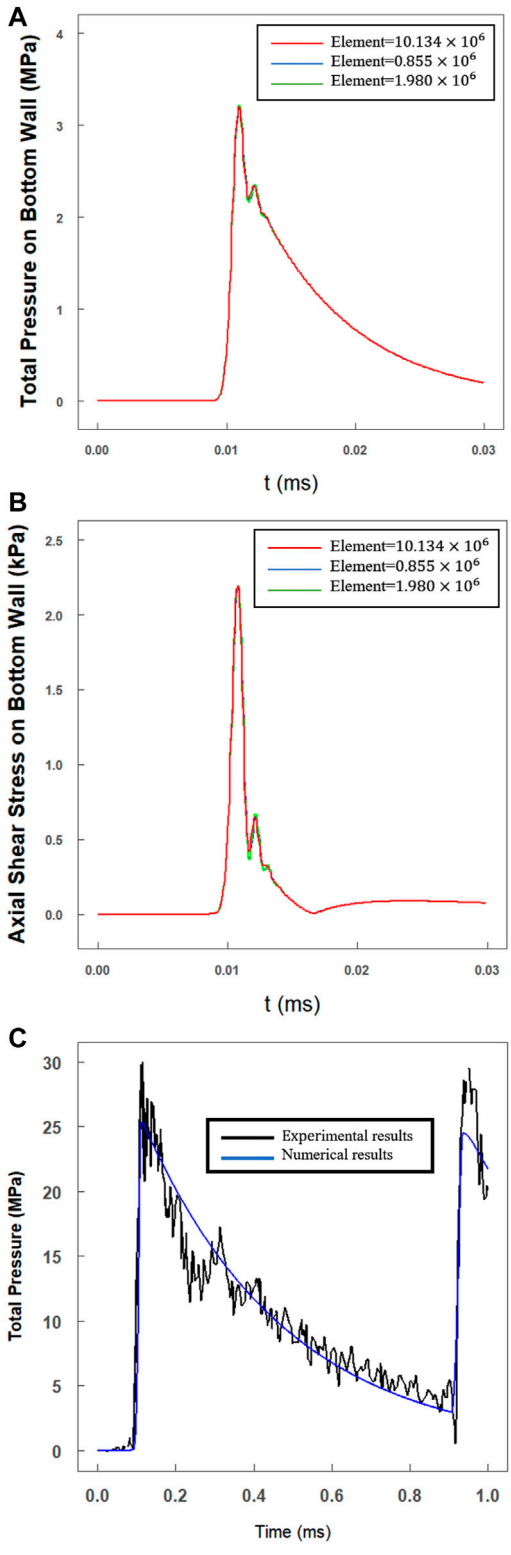

FIGURE 3
Mesh independence analysis and sample comparison results. The total mesh count for testing the independence were about 0.855×10^6 (blue line), 1.98×10^6 (green line), 10.134×10^6 (red line) elements respectively. **(A)** The variations of total pressure (*Continued*)

FIGURE 3 (Continued)
on bottom wall at the monitoring point ($x = 0.25\,X$); **(B)** The variations of axial shear stress on bottom wall at the monitoring point ($x = 0.25\,X$); **(C)** A pressure waveform comparison of experimental results of example and numerical results (black line: experimental results; blue line: numerical results).

In the CFD solver setup, boundary settings comprise the physical description of the fluid flow as shown in Figure 2C. The pressure applied on the inlet boundary has been described as a function of time, (t) in Eq. 40, which simulated the impact process. The outlet was operated under normal pressure (p_0 = 10135 Pa), which could be achieved easily by collecting an extra tank filled with fluid, and the wall was set at a no-slip condition. In addition, there were two settings (heights) for the roughness of the bottom wall: 1×10^{-5} (average height of cells) and 0 m, which helped estimate the effect of cells on the fluid flow.

ANSYS Fluent® (2019R3) was utilized to obtain all the simulation results presented in this paper. In FLUENT, the numerical tech is a finite volume method (FVM). The whole process is transient. As the fluid is considered to be viscous, compressible, isothermal (no heat transfer), isotropic, and single-phase (no cavitation), the semi-implicit method for pressure-linked equations (SIMPLE) can be used as a flow solver. Convergence was defined to be 1×10^{-6} due to the flow characteristics (Martins et al., 2016).

Results

Sample numerical results

A mesh independence analyses were performed using different element size (the original element size was proposed in Section 2.6) by the simulation of pressure and shear stress on bottom wall. The total mesh count for testing the independence were about 0.855×10^6 (blue line), 1.98×10^6 (green line), 10.134×10^6 (red line) elements respectively. The test results were shown in Figures 3A,B which assure a mesh independence of the simulation results in this paper.

We choose a classical water hammer experiment (Inaba and Shepherd, 2010) to assess the modeling method in our work. In this example (shot 62), researchers accelerated a steel projectile (= 0.67 kg, v_{impact} = 18.5 m/s) to impact a specimen tube ($D_{innerdiameter}$ = 38.1 mm, $h_{thick\ wall}$ = 12.74 mm), and the experimental pressure was recorded by strain gauges and a pressure transducer.

In Figure 3C, we compared the experimental results (black line; shot 62, gauge g1) with the numerical results (blue line) calculated with the modeling method in Section 2. The maximum pressure of 25.03 MPa was computed which showed a good match with the

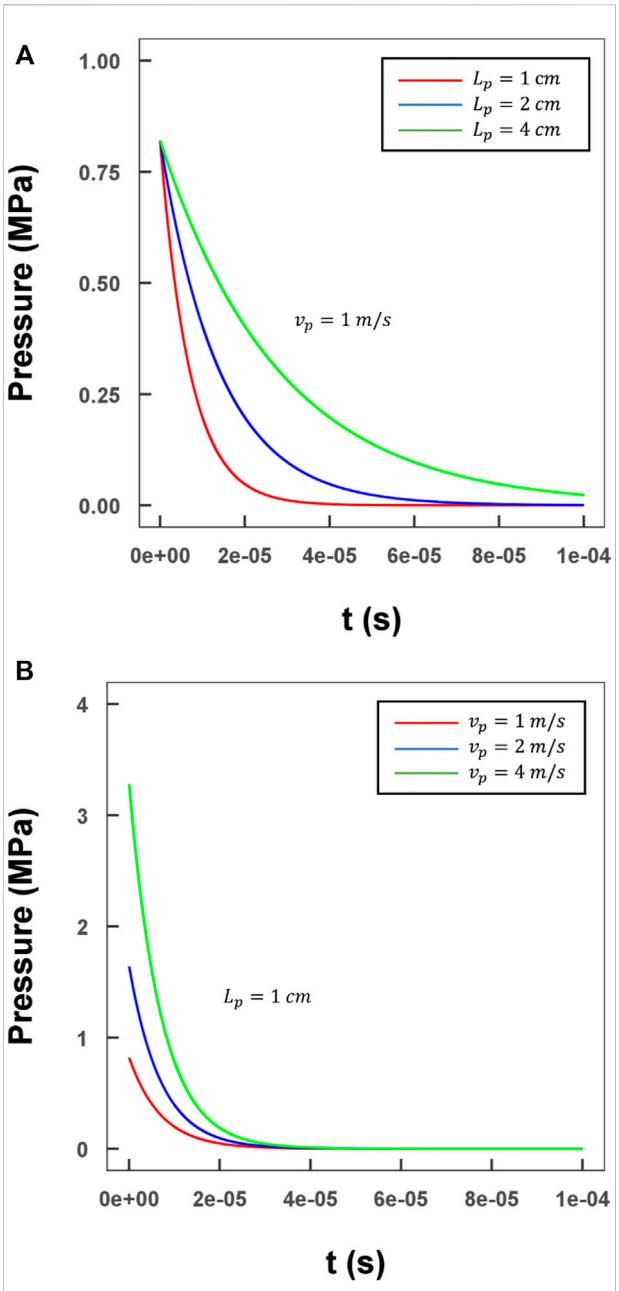

FIGURE 4
Evaluation of the relationship between various lengths/velocities of the projectile and the input pressure profile. **(A)** Three different lengths of projectile with a 1 m/s velocity (green line: 4 cm; blue line: 2 cm; red line: 1 cm); **(B)** Three different lengths of projectile with a 1 cm length (green line: 4 m/s; blue line: 2 m/s; red line: 1 m/s).

peak pressure of 27.20 MPa. Furthermore, the whole trend of the pressure waveform showed a good agreement with the experimental results. For instance, due to the outlet of the specimen tube being closed, a reflected wave could be observed.

Visualization of pressure wave propagation

To visualize and analyze the wave propagation process in detail, as well as the profile of the coupled compression and shear stresses in our method, a representative case with a water-filled channel and a projectile made of polymethyl methacrylate (PMMA) was designed; a practical size was determined as described in Section 2.5. The correlation between the projectile parameters (velocity and length) and the input pressure was assessed, and the results are shown in Figure 4. The maximum value and the duration of the pressure input were adjustable by changing the length and initial velocity of the projectile. This detailed relationship was derived in Section 2.3 (Joukowsky, 1900; Versteeg and Malalasekera, 2007).

As the inlet boundary condition, maximum pressure of 3 MPa was generated by a 0.01 m projectile, which was then used to initiate the wave propagation process. Along the direction of the wave propagation (z -direction), a series of axial middle cross-sections were selected to visualize the wave traveling process in terms of pressure and axial flow velocity distribution at different time steps (Figure 6). Here, we set = $\updownarrow_{tube}/c_f$, and the displayed time steps were $t_1 = 0.25\,T$, $t_2 = 0.50\,T$, *and* $t_3 = 0.75\,T$. After the impact of the projectile, the pressure jumped to ~ 3.2 MPa rapidly, accompanied by a relatively low level of flow velocity (less than 2.3 m/s). As shown in Figure 5, peak pressures at the different time steps did not show an apparent dissipation, while the maximum axial flow velocity slow down slightly. Details on the dissipation values are discussed in Section 3.3. The phase differences calculated by Eq. 7 showed that the wave traveled at an acoustic speed.

Stress distribution analysis of wall/cell cultured area

The bottom wall was defined as a smooth wall area for cell culture. The results at $t = 0.75\,T$ were selected to display the stress distribution in space. Figure 6A shows the compression pressure applied on the bottom wall, which appears to be similar to the compression pressure distributed in the axial plane in Figure 5A. The pressure distributed was almost identical to that in the transverse direction (-direction) (Figure 6B). The axial shear stress (τ_z) is shown in Figure 6C, which exhibited no obvious difference in the transverse direction. The maximum axial shear stress at $t = 0.75\,T$ was nearly 1.9 kPa, which was much higher than the maximum transverse shear stress ($|\tau_{x,max}| < 1$ Pa). From these observations, it was inferred that the transverse shear stress (τ_x) could be neglected, even though it showed an apparent concentration of stress at the edges (Figure 6B).

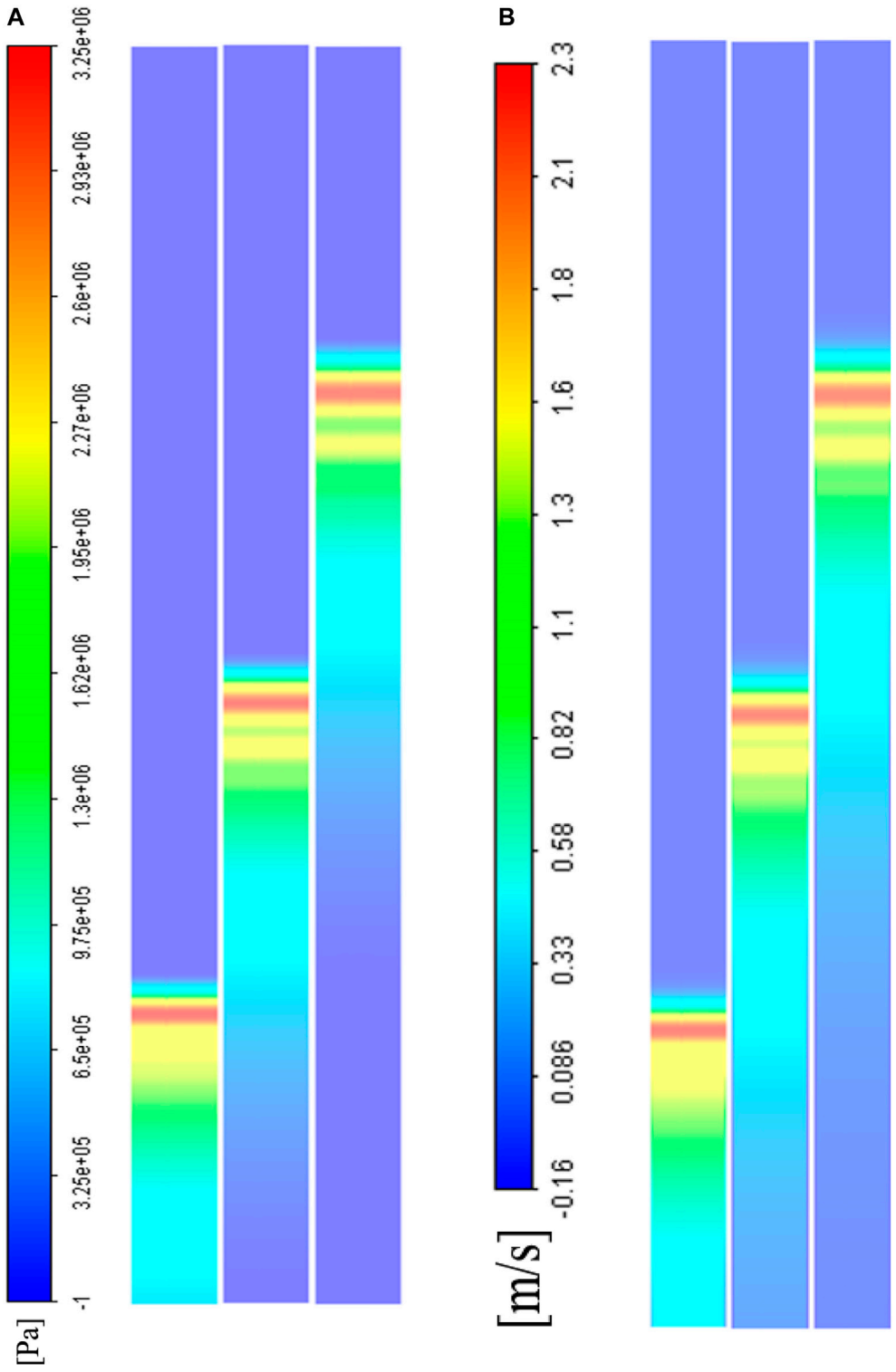

FIGURE 5
A CFD visualization of weak shock wave propagation in the middle axial cross-section at different time steps ($t_1 = 0.25\,T$, $t_2 = 0.50\,T$, $t_3 = 0.75\,T$). **(A)** The total pressure field; **(B)** The axial velocity field.

10.3389/fbioe.2022.1002661

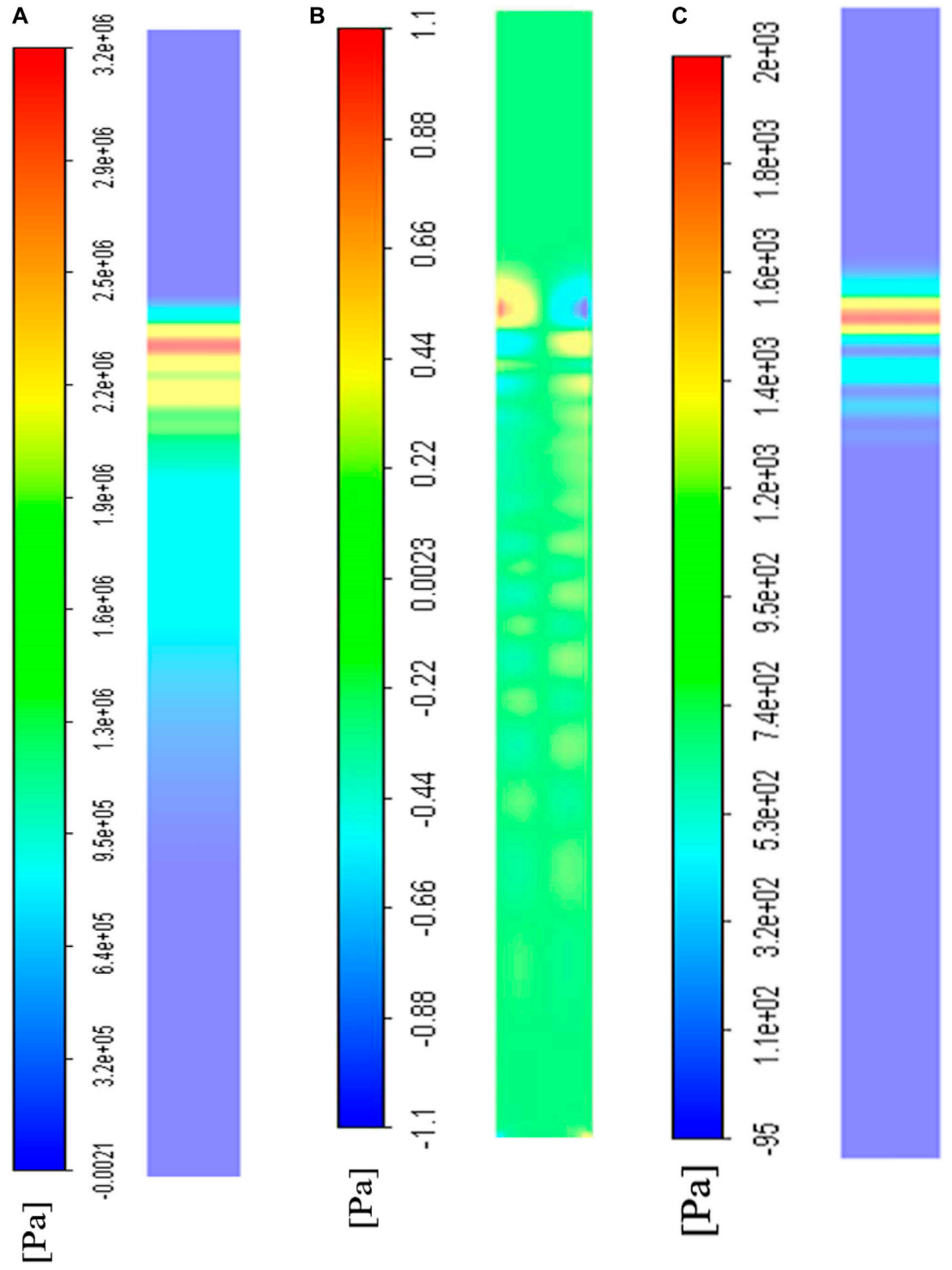

FIGURE 6
The CFD visualization of stress distribution on the bottom wall where cells were cultured at $t = 0.75\ T$ time step. **(A)** The total compression stress distribution; **(B)** The transverse shear stress distribution; **(C)** The axial shear stress distribution.

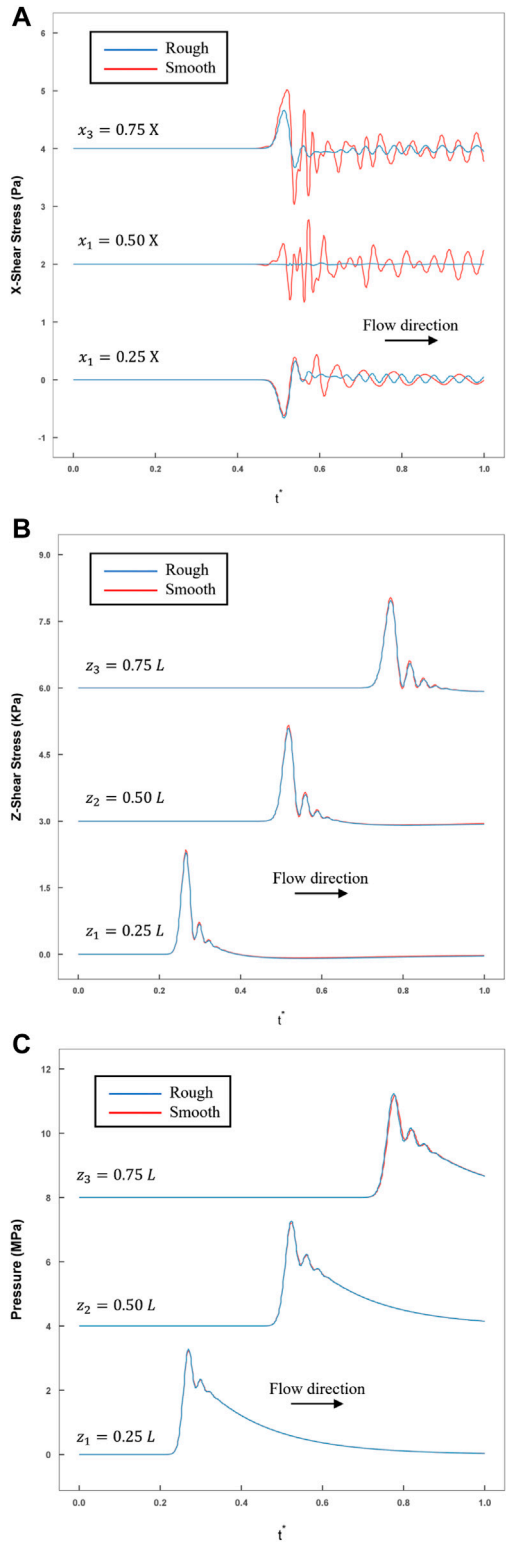

FIGURE 7
The comparison of rough and smooth model historical variations in stress were recorded by monitoring the points calculated by FLUENT (blue line: rough model; red line: smooth model). **(A)** The transverse shear stress recorded at three monitoring points ($x_1 = 0.25\,X$, $x_2 = 0.5\,X$, $x_3 = 0.75\,X$) at the line $z = 0.5\,L$; **(B)** The axial shear stress recorded at three monitoring points ($z_1 = 0.25\,\updownarrow$, $z_2 = 0.5\,\updownarrow$, $z_3 = 0.75\,\updownarrow$) at the line $x = 0.5\,X$: **(C)** Compression stress recorded at three monitoring points ($z_1 = 0.25\,\updownarrow$, $z_2 = 0.5\,\updownarrow$, $z_3 = 0.75\,\updownarrow$) at the line $x = 0.5\,X$.

Effect of cells on stress spatial distribution

To evaluate the influence of cultured cells on the spatial distribution of stress on the bottom wall, the relationship between the two distributions and the density and height of the cells could be written as:

$$\sigma = f\left(\delta_{cell}, \rho_{cell}\right) \tag{44}$$

Where σ is the compression and shear stress on the bottom wall; δ_{cell} is the average height of the cells, and ρ_{cell} is the density of the cells. Normally, the height of the cells, δ_{cell}, was consistent at $\sim 1 \times 10^{-5}$ m and the interval of variation, ρ_{cell}, was $[0, \infty)$. The two boundary conditions were defined as follows: the lower limit situation, i.e., $\rho_{cell} = 0$ (no cell cultured), represented a smooth wall; the upper limit situation, i.e., $\rho_{cell} = \infty$, denoted that countless cell had been cultured on the bottom wall and imparted a roughness of 1×10^{-5} m. By comparing the stress in these two situations, the effect of cells on stress distribution could be assessed (Figure 7). Along the axial and transverse directions, several monitoring points were set to calculate the compression and shear stress: σ (3 points along the axial direction at $x = 0.5\,X$: $z_1 = 0.25\,\updownarrow$, $z_2 = 0.5\,\updownarrow$, $z_3 = 0.75\,\updownarrow$; 3 points along the x direction at $z = 0.5\,L$: $x_1 = 0.25\,X$, $x_2 = 0.5\,X$, $x_3 = 0.75\,X$).

In addition, the temporal variations in τ_x in the transverse direction were also recorded. As the maximum of τ_x was quite small (did not exceed 10^1 Pa) within the interval of $(0.25\,X, 0.75\,X)$, τ_x could be neglected (Figure 7A). As shown in Figures 7B,C, the compression and axial shear stress variations along the axial direction were recorded at the monitoring points, and the same changing trend was observed. Exact statistics on the maximum values are shown in Table 1. Regardless of the maximum value of pressure or axial shear, there was almost no difference between these two conditions in an interval of $(0.25\,\updownarrow, 0.75\,\updownarrow)$. The ρ_{exp} was in the interval of $0 < \rho_{min} \le \rho_{exp} \le \rho_{max} \ll \infty$. Therefore, the smooth boundary condition would be much closer to the actual experimental observations.

Table 1 shows the attenuation of pressure and axial shear stress along the axial direction. In this model, the average reduction was within 1% in every $0.25\,\updownarrow$ (15 mm) for pressure and $\sim$ 6% in every $0.25\,\updownarrow$ for shear stress.

In addition, the temporal variations in the transverse direction are shown in Figure 8, where the monitoring points were set in the middle cross-section ($z = 0.5\,\updownarrow$). The attenuation of either the

TABLE 1 Maximum values of the monitoring points were calculated by FUENT.

	Compression			Axial shear		
	z_1	z_2	z_3	z_1	z_2	z_3
Rough	3.28 MPa	3.26 MPa	3.23 MPa	2.29 kPa	2.09 kPa	1.97 kPa
Smooth	3.24 MPa	3.21 MPa	3.14 MPa	2.35 kPa	2.16 kPa	2.01 kPa
Average ratio (Smooth/Rough)	1.019 ± 0.0782			0.975 ± 0.0029		

pressure or the axial shear stress in the transverse direction was less than 1% . These results imply the great repeatability of this model.

Discussion

In the past, many studies have focused on revealing the mechanical properties of cells with the assistance of interdisciplinary techniques, such as solid mechanics, image processing, and fluid mechanics. Such works have implied that as compared to static or quasi-static loadings, the mechanical properties of cells are likely to show a distinct behavior difference under dynamic loading ($\dot{\epsilon} > 10^0\ s^{-1}$). Considering the length scale of cells, it is difficult to clamp a single cell using traditional dynamic loading methods, such as Split Hopkinson's Pressure Bar (SHPB). Hence, the challenge is how to apply controllable dynamic loading on cells properly and the real-time measurement of cell response during this process.

In this paper, we have proposed a new method for the application of dynamic loading that couple's compression and shear stress synchronously on isolated cells under normal culture conditions. This method describes a case, where an impact loading from a projectile was employed to generate a pressure wave, together with corresponding shear stress due to the fluid viscosity. At the same time, the strain variations in the cell could be captured by a high-speed camera. Eventually, data on the essential stress and strain on the cells were collected to explore the mechanical properties of cells. We established a representative model (rectangular channel filled with water) as shown in Figures 1A,B. With this model, we explained two main questions as elaborated on in Section 2 and Section 3 on the working of this method and its known limitations:

1) How can the weak shock wave generated by projectile impact be calculated? Does the solid structure (channel) affect the flow and how can it reduce the fluid-structure interaction (FSI)?
2) Does the shear stress keep the same phase as the compression stress? Does the existence of cells have a strong influence on stress distribution? How is this related to the positions along the axial and transverse directions?

The basic purpose was to explore the biomechanical mechanism of single cell response to dynamic mechanical loading, where the length scale was focused on 10^{-6} m and the cells were treated as a homogenous element. This length scale had to be taken into consideration due to its influence on the fluid domain meshing and CFD (actually, more factors had been considered during the meshing process). The characteristic length of the channel we designed was 3×10^{-3} m, which was much larger than the size of the cells. Generally, the pressure and wall shear stress were directly assumed when the stresses were applied to the cells, while the approximate treatment relied on the hypothesis that the flow was hydraulically smooth. The estimated average height of the cells was ~ 1×10^{-5} m, therefore, one of the extremely idealized hypotheses was that the bottom wall was occupied by countless cells that were equivalent to a 1×10^{-5} m roughness on the bottom wall. The total pressure and axial shear stress showed that there was only a slight difference between the smooth and rough conditions (within 2%) (Figure 7). In the actual experimental process, the cell density only sparsely facilitated the capture of the strain field by a high-speed camera. Therefore, the effect of cells on the fluid flow could be neglected.

The Doppler effect is commonly used to detect the flow velocity of a flowing fluid, but experimental techniques may render it less reliable on small velocities and the changing profile near the walls (Riasi et al., 2009). Several sophisticated numerical models have been established to more accurately explain the details of the transient flow (Ghidaoui and Kolyshkin, 2001; Martins et al., 2018). It has been proven that CFD performs very well in modeling the pressure wave traveling processes (Mandair, 2020). Therefore, we established the CFD model to help us evaluate the proposed method, and we will consider these evaluation results as a very important reference for future experimental work.

The boundary conditions should be comprehensively considered in CFD modeling as we have described in detail in Section 2 of this article. The criteria of channel size design were not too strict, which allowed us to adjust the details freely according to the actual lab environment, provided that the size details obeyed the above-mentioned limitations of the Knudson number to continuously maintain the fluid. As for the projectile, its material should be kept the same as that of the buffer. Figure 4 shows the means of controlling the amplitude and decay time constant of the initial pressure by the projectile.

The water hammer is a well-known problem. The weak shock wave generated in this problem would induce a sudden pressure

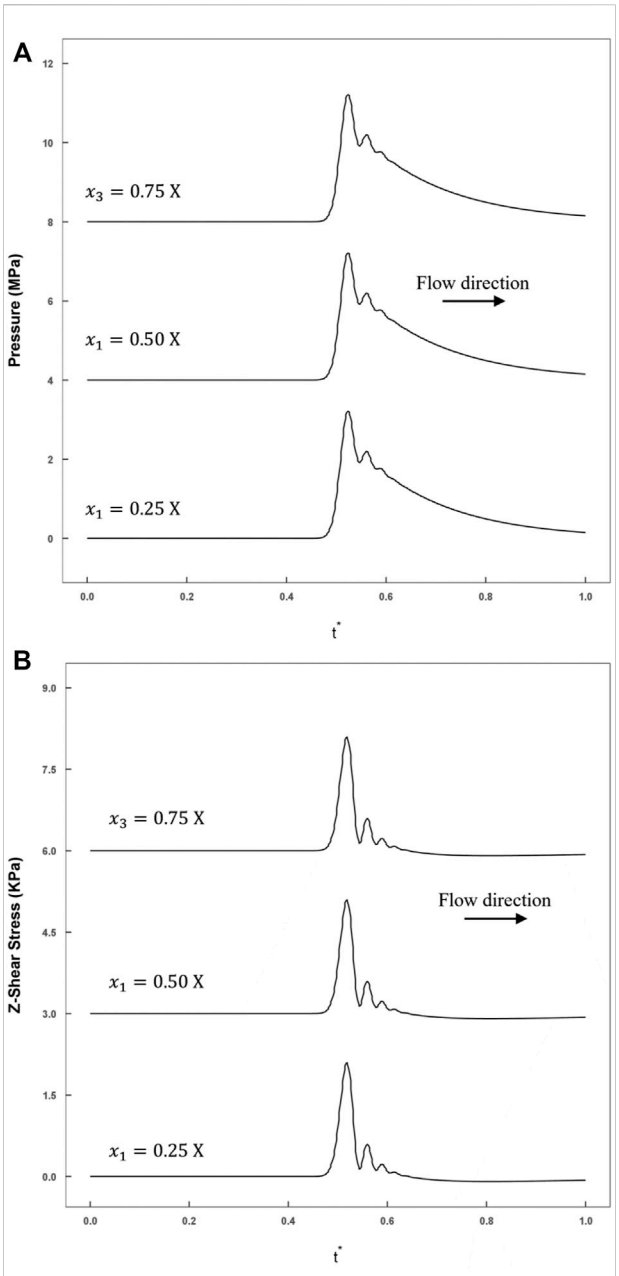

FIGURE 8
The smooth model historical variations in stress recorded by monitoring points calculated by FLUENT (blue line: rough model; red line: smooth model). **(A)** The axial shear stress recorded at three monitoring points ($x_1 = 0.25\,X$, $x_2 = 0.5\,X$, $x_3 = 0.75\,X$) at the line $z = 0.5\,L$; **(B)** The compression stress recordings at three monitoring points ($x_1 = 0.25\,X$, $x_2 = 0.5\,X$, $x_3 = 0.75\,X$) at the line $z = 0.5\,L$.

jump corresponding to the low flow velocity. Accordingly, we described the stress wave propagation in total pressure and the flow velocity forms; we also visualized this process in the middle axial section (Figure 5). In this process, the dissipation effect was mainly due to the fluid viscosity and could not be neglected. We selected several points in the z and x directions on the bottom wall to figure out the proper areas for cell measuring (Figures 6–8). Only the z shear stress changed slightly (6% drop at every 15 *mm* in this example), and the x shear stress was so small that it could be neglected (in the interval of $0.25 - 0.75\,X$). These CFD results give us a high fault tolerance rate in repeating experiments.

Conclusions

In this paper, we focused on the application of dynamic loadings on single cells and revealed their mechanical response. Based on the Water-Hammer theories, we have developed a novel experimental method with a corresponding CFD model to help investigate cell mechanics under dynamic loadings. In this method, cells were normally cultured inside a microchannel. After impact, the stress wave generated applied a coupled compression-shear stress on an isolated living cell inside the microchannel. The results from an example model showed that the stress conditions could be easily controlled by controlling the velocity or length of the projectile. In addition, this method will allow researchers to adjust various design elements of their channels, such as the size, materials, etc., according to their lab's environmental and actual needs, if the new design meets the relevant criteria presented in this study. This model offers repeatability, as a wide area is available for cell strain capturing, where cells suffer from nearly the same stress loadings.

Data availability statement

The original contributions presented in the study are included in the article/supplementary material, further inquiries can be directed to the corresponding authors.

Author contributions

YL, HY, NZ, and DX conceived and designed the research. DX, SW, and NZ derived the theoretical process and the CFD modeling process. DX, NZ, and PZ wrote the paper. All authors reviewed and edited the manuscript.

Funding

This work was supported by the National Natural Science Foundation of China (12002285, 11722220, 61927810), Natural Science Basic Research Program of Shaanxi (2020JZ-11, 2020JQ-126), Fundamental Research Funds for the Central Universities (3102020smxy003), and the Program

of Introducing Talents of Discipline to Universities (the 111 project) (No. BP0719007).

Conflict of interest

The authors declare that the research was conducted in the absence of any commercial or financial relationships that could be construed as a potential conflict of interest.

Publisher's note

All claims expressed in this article are solely those of the authors and do not necessarily represent those of their affiliated organizations, or those of the publisher, the editors and the reviewers. Any product that may be evaluated in this article, or claim that may be made by its manufacturer, is not guaranteed or endorsed by the publisher.

References

Ackroyd, J. (1967). On the laminar compressible boundary layer with stationary origin on a moving flat wall. *Math. Proc. Camb. Phil. Soc.* 63, 871–888. doi:10.1017/s0305004100041840

Afzal, N. (1973). A higher order theory for compressible turbulent boundary layers at moderately large Reynolds number. *J. Fluid Mech.* 57, 1–25. doi:10.1017/s0022112073000996

Alberts, B., Johnson, A., Lewis, J., Raff, M., Roberts, K., and Walters, P. (2002). *Molecular biology of the cell.* 4th edn. New York: Garland Science.

Bao, G., and Suresh, S. (2003). Cell and molecular mechanics of biological materials. *Nat. Mater* 2, 715–725. doi:10.1038/nmat1001

Ben-Dor, G., Igra, O., and Elperin, T. (2000). *Handbook of shock waves, three volume set*. San Diego, CA: Elsevier.

Bush, W. B., and Fendell, F. E. (1972). Asymptotic analysis of turbulent channel and boundary-layer flow. *J. Fluid Mech.* 56, 657–681. doi:10.1017/s0022112072002599

Bush, W. B., and Fendell, F. E. (1973). Asymptotic analysis of turbulent channel flow for mean turbulent energy closures. *Phys. Fluids* 16, 1189–1197. doi:10.1063/1.1694497

Davies, W., and Bernstein, L. (1969). Heat transfer and transition to turbulence in the shock-induced boundary layer on a semi-infinite flat plate. *J. Fluid Mech.* 36, 87–112. doi:10.1017/s0022112069001534

Deshpande, V. S., Heaver, A., and Fleck, N. A. (2006). An underwater shock simulator. *Proc. R. Soc. A* 462, 1021–1041. doi:10.1098/rspa.2005.1604

Desprat, N., Richert, A., Simeon, J., and Asnacios, A. (2005). Creep function of a single living cell. *Biophysical J.* 88, 2224–2233. doi:10.1529/biophysj.104.050278

Dudani, J. S., Gossett, D. R., Tse, T., and Di Carlo, D. (2013). Pinched-flow hydrodynamic stretching of single-cells. *Lab. Chip* 13, 3728–3734. doi:10.1039/c3lc50649e

Dymond, J., and Malhotra, R. (1988). The Tait equation: 100 years on. *Int. J. Thermophys.* 9, 941–951. doi:10.1007/bf01133262

Evans, E., and Yeung, A. (1989). Apparent viscosity and cortical tension of blood granulocytes determined by micropipet aspiration. *Biophysical J.* 56, 151–160. doi:10.1016/s0006-3495(89)82660-8

Ganadhiepan, G., Miramini, S., Patel, M., Mendis, P., and Zhang, L. (2019). Bone fracture healing under Ilizarov fixator: Influence of fixator configuration, fracture geometry, and loading. *Int. J. Numer. Meth Biomed. Engng* 35, (6), e3199. doi:10.1002/cnm.3199

Ghidaoui, M. S., and Kolyshkin, A. A. (2001). Stability analysis of velocity profiles in water-hammer flows. *J. Hydraul. Eng.* 127, 499–512. doi:10.1061/(asce)0733-9429(2001)127:6(499)

Guo, Z., Xu, K., and Wang, R. (2013). Discrete unified gas kinetic scheme for all Knudsen number flows: Low-speed isothermal case. *Phys. Rev. E Stat. Nonlin Soft Matter Phys.* 88, 033305. doi:10.1103/PhysRevE.88.033305

Hamed, D. (2020). *Mechanical analysis of* in vitro *TBI models*.

Hao, Y., Cheng, S., Tanaka, Y., Hosokawa, Y., Yalikun, Y., and Li, M. (2020). Mechanical properties of single cells: Measurement methods and applications. *Biotechnol. Adv.* 45, 107648. doi:10.1016/j.biotechadv.2020.107648

Hoang, H., Galliero, G., Montel, F., and Bickert, J. (2015). Tait equation in the extended corresponding states framework: Application to liquids and liquid mixtures. *Fluid Phase Equilibria* 387, 5–11. doi:10.1016/j.fluid.2014.12.008

Hutarew, G. (1973). *Einführung in die Technische Hydraulik*. Berlin, Heidelberg: Springer.

Inaba, K., and Shepherd, J. E. (2010). Flexural waves in fluid-filled tubes subject to axial impact. *J. Press. Vessel Technol.* 132, 021302. doi:10.1115/1.4000510

Joukowsky, N. (1900). *Über den hydraulischen Stoss in Wasserleitungsröhren, Impériale des Sciences de St.Pétersbourg, Mémoires de l'Académie.*

Kandlikar, S., Garimella, S., Li, D., Colin, S., and King, M. R. (2005). *Heat transfer and fluid flow in minichannels and microchannels*. New York, NY: Elsevier.

Katti, D. R., Katti, K. S., Molla, S., and Kar, S. (2019). Biomechanics of cells as potential biomarkers for diseases: A new tool in mechanobiology. *Encycl. Biomed. Eng.* 13, 1–21. doi:10.1016/b978-0-12-801238-3.99938-0

Korteweg, V. D. (1878). Ueber die Fortpflanzungsgeschwindigkeit des Schalles in elastischen Röhren. *Ann. Phys. Chem.* 241, 525–542. doi:10.1002/andp.18782411206

Lennon, F. (1994). *Shock wave propagation in water*. Manchester, UK: Manchester Metropolitan University.

Mandair, S. (2020). *1D and 3D Water-Hammer Models: The energetics of high friction pipe flow and hydropower load rejection*. Canada: University of Toronto.

Martins, N. M., Carriço, N. J., Ramos, D., and Covas, H. (2014). Velocity-distribution in pressurized pipe flow using CFD: Accuracy and mesh analysis. *Comput. Fluids* 105, 218–230. doi:10.1016/j.compfluid.2014.09.031

Martins, N. M. C., Brunone, B., Meniconi, S., Ramos, H. M., and Covas, D. I. C. (2018). Efficient computational fluid dynamics model for transient laminar flow modeling: Pressure wave propagation and velocity profile changes. *J. Fluids Eng.* 140, 011102. doi:10.1115/1.4037504

Martins, N. M., Soares, A. K., Ramos, H. M., and Covas, D. I. (2016). CFD modeling of transient flow in pressurized pipes. *Comput. Fluids* 126, 129–140. doi:10.1016/j.compfluid.2015.12.002

Mellor, G. L. (1972). The large Reynolds number, asymptotic theory of turbulent boundary layers. *Int. J. Eng. Sci.* 10, 851–873. doi:10.1016/0020-7225(72)90055-9

Melnik, R., and Grossman, B. (1974). Analysis of the interaction of a weak normal shock wave with a turbulent boundary layer. in 7th Fluid and PlasmaDynamics Conference, Palo Alto,CA,U.S.A., 598.doi:10.2514/6.1974-598

Meyers, M. A. (1994). *Dynamic behavior of materials*. John Wiley & Sons.

Mirels, H. (1955). *Laminar boundary layer behind shock advancing into stationary fluid.*

Moeendarbary, E., and Harris, A. R. (2014). Cell mechanics: Principles, practices, and prospects. *WIREs Mech. Dis.* 6, 371–388. doi:10.1002/wsbm.1275

Nagayama, K., Mori, Y., Shimada, K., and Nakahara, M. (2002). Shock Hugoniot compression curve for water up to 1 GPa by using a compressed gas gun. *J. Appl. Phys.* 91, 476–482. doi:10.1063/1.1421630

Nikpour, M., Nazemi, A., Dalir, A. H., Shoja, F., and Varjavand, P. (2014). Experimental and numerical simulation of water hammer. *Arab. J. Sci. Eng.* 39, 2669–2675. doi:10.1007/s13369-013-0942-1

Patterson, L. H. (2020). *The MicroHammer: Investigating cellular response to impact with a microfluidic mems device*. Santa Barbara: University of California.

Patterson, L. H., Walker, J. L., Rodriguez-Mesa, E., Shields, K., Foster, J. S., Valentine, M. T., et al. (2019). Investigating cellular response to impact with a microfluidic MEMS device. *J. Microelectromechanical Syst.* 29, 14–24.

Pelham, R. J., and Wang, Y.-L. (1997). Cell locomotion and focal adhesions are regulated by substrate flexibility. *Proc. Natl. Acad. Sci. U.S.A.* 94, 13661–13665. doi:10.1073/pnas.94.25.13661

Pinnington, R. (1997). The axisymmetric wave transmission properties of pressurized flexible tubes. *J. sound Vib.* 204, 271–289. doi:10.1006/jsvi.1997.0938

Rapp, B. E. (2016). *Microfluidics: Modeling, mechanics and mathematics*. Cambridge, US: William Andrew.

Riasi, A., Nourbakhsh, A., and Raisee, M. (2009). Unsteady velocity profiles in laminar and turbulent water hammer flows. *J. fluids Eng.* 131, 121202. doi:10.1115/1.4000557

Shepherd, J. E., and Inaba, K. (2009). Shock loading and failure of fluid-filled tubular structures. *Dyn. Fail. Mater. Struct.* 5, 153–190. doi:10.1007/978-1-4419-0446-1_6

Smith, R. T. (1973). *Weak shock wave propagation in liquid media*.

Thorley, A., and Guymer, C. (1976). *Pressure surge propagation in thick-walled conduits of rectangular cross section*.

Trepat, X., Grabulosa, M., Puig, F., Maksym, G. N., Navajas, D., and Farré, R. (2004). Viscoelasticity of human alveolar epithelial cells subjected to stretch. *Am. J. Physiology-Lung Cell. Mol. Physiology* 287, L1025–L1034. doi:10.1152/ajplung.00077.2004

Urbanska, M., Muñoz, H. E., Shaw Bagnall, J. S., Otto, O., Manalis, S. R., Di Carlo, D., et al. (2020). A comparison of microfluidic methods for high-throughput cell deformability measurements. *Nat. Methods* 17, 587–593. doi:10.1038/s41592-020-0818-8

Versteeg, H. K., and Malalasekera, W. (2007). *An introduction to computational fluid dynamics: The finite method*. London, UK: Pearson education.

Walters, T. W., and Leishear, R. A. (2018). When the Joukowsky equation does not predict maximum water hammer pressures, in Pressure Vessels and Piping Conference, Prague, Czech Republic: American Society of Mechanical Engineers ASME. doi:10.1115/pvp2018-84050

Yajnik, K. S. (1970). Asymptotic theory of turbulent shear flows. *J. Fluid Mech.* 42, 411–427. doi:10.1017/s0022112070001350

Zhang, L., Gardiner, B. S., Smith, D. W., Pivonka, P., and Grodzinsky, A. (2008). A fully coupled poroelastic reactive-transport model of cartilage. *Mol. Cell Biomech.* 5 (2), 133–153. doi:10.3970/mcb.2008.005.133

Zhang, L., Richardson, M., and Mendis, P. (2012). Role of chemical and mechanical stimuli in mediating bone fracture healing. *Clin. Exp. Pharmacol. Physiol.* 39 (8), 706–710. doi:10.1111/j.1440-1681.2011.05652.x

frontiers | Frontiers in Bioengineering and Biotechnology

TYPE Review
PUBLISHED 31 October 2022
DOI 10.3389/fbioe.2022.1042030

OPEN ACCESS

EDITED BY
Yuhui Li,
Commissariat à l'Energie Atomique et aux Energies Alternatives (CEA), France

REVIEWED BY
Farid Alisafaei,
New Jersey Institute of Technology, United States
Liming Bian,
South China University of Technology, China

*CORRESPONDENCE
Guoyou Huang,
gyhuang@whu.edu.cn
Xiaogang Guo,
gxg22222@zju.edu.cn
Feng Xu,
fengxu@xjtu.edu.cn

†These authors have contributed equally to this work

SPECIALTY SECTION
This article was submitted to Biomechanics, a section of the journal Frontiers in Bioengineering and Biotechnology

RECEIVED 12 September 2022
ACCEPTED 20 October 2022
PUBLISHED 31 October 2022

CITATION
Liu H, Fan P, Jin F, Huang G, Guo X and Xu F (2022), Dynamic and static biomechanical traits of cardiac fibrosis. *Front. Bioeng. Biotechnol.* 10:1042030. doi: 10.3389/fbioe.2022.1042030

Dynamic and static biomechanical traits of cardiac fibrosis

Han Liu[1,2†], Pengbei Fan[1,2†], Fanli Jin[1,2], Guoyou Huang[3*], Xiaogang Guo[4*] and Feng Xu[5,6*]

[1]Henan Key Laboratory of Chinese Medicine for Respiratory Disease, Academy of Chinese Medical Sciences, Henan University of Chinese Medicine, Zhengzhou, China, [2]Collaborative Innovation Center for Chinese Medicine and Respiratory Diseases Co-Constructed by Henan Province and Education Ministry of China, Zhengzhou, China, [3]Department of Engineering Mechanics, School of Civil Engineering, Wuhan University, Wuhan, China, [4]The First Affiliated Hospital, College of Medicine, Zhejiang University, Hangzhou, China, [5]The Key Laboratory of Biomedical Information Engineering of Ministry of Education, School of Life Science and Technology, Xi'an Jiaotong University, Xi'an, China, [6]Bioinspired Engineering and Biomechanics Center (BEBC), Xi'an Jiaotong University, Xi'an, China

Cardiac fibrosis is a common pathology in cardiovascular diseases which are reported as the leading cause of death globally. In recent decades, accumulating evidence has shown that the biomechanical traits of fibrosis play important roles in cardiac fibrosis initiation, progression and treatment. In this review, we summarize the four main distinct biomechanical traits (i.e., stretch, fluid shear stress, ECM microarchitecture, and ECM stiffness) and categorize them into two different types (i.e., static and dynamic), mainly consulting the unique characteristic of the heart. Moreover, we also provide a comprehensive overview of the effect of different biomechanical traits on cardiac fibrosis, their transduction mechanisms, and *in-vitro* engineered models targeting biomechanical traits that will aid the identification and prediction of mechano-based therapeutic targets to ameliorate cardiac fibrosis.

KEYWORDS

cardiac fibrosis, biomechanical traits, myofibroblast, mechanotransduction, mechanical model *in vitro*

1 Introduction

Cardiac fibrosis, also known as myocardial fibrosis, is a common pathology in cardiovascular disease, whose mortality has been regarded as the leading cause of death globally and attracted considerable attention (Schafer et al., 2017; Mensah et al., 2019; Diseases and Injuries, 2020; Alexanian et al., 2021). Cardiac fibrosis is a relatively complex pathological process, caused by persistent or repeated exacerbations of myocardial ischemia and hypoxia (Zhao et al., 2022a), characterized by the excessive accumulation of the extracellular matrix (ECM) components (e.g., collagen and fibronectin) (Henderson et al., 2020; Frangogiannis, 2021). Although cardiac fibrosis is generally considered as a disease of the phenotypic transformation of cardiac fibroblasts and has been studied mainly from a biological perspective (Ma et al., 2018), accumulating

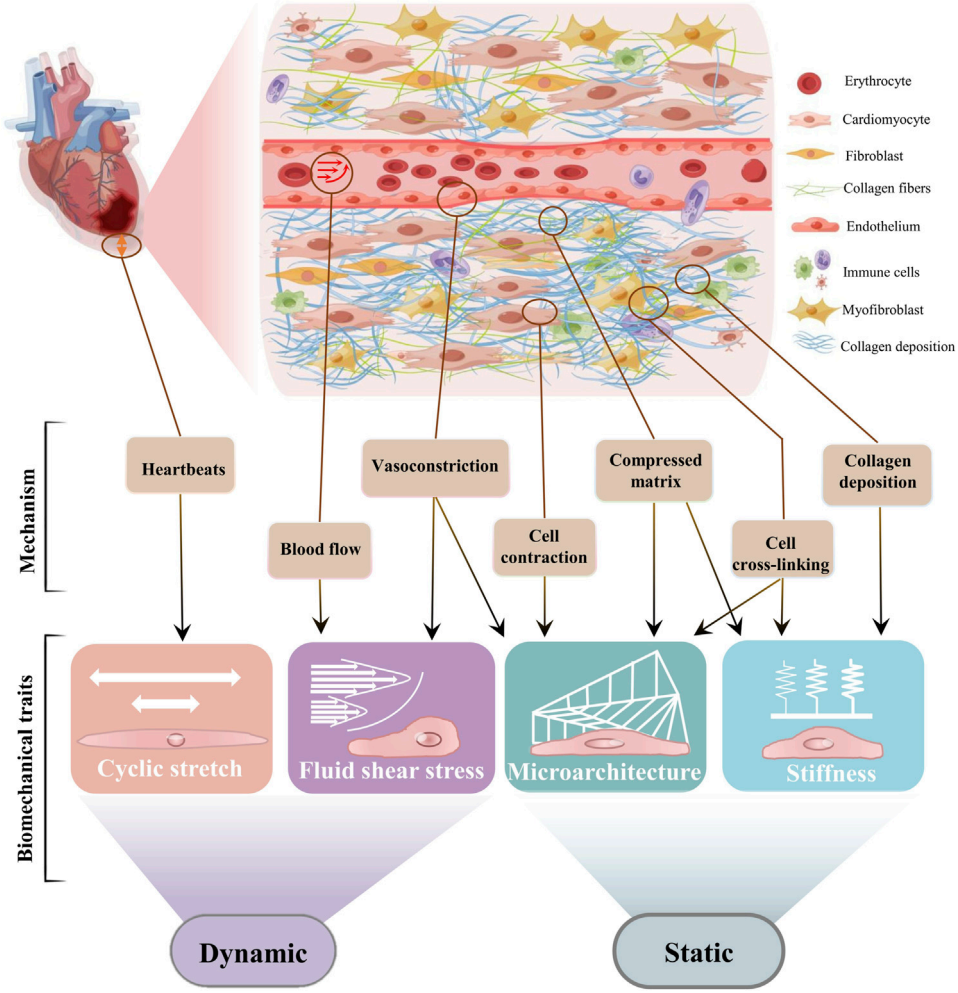

FIGURE 1
The biomechanical traits of cardiac fibrosis. Schematic diagram of cardiac fibrosis ECM was drew online using Figdraw. According to recent progresses of biomechanics, we recommend respectively from two biomechanical types to understand cardiac fibrosis. The fibrotic area must be subjected to a stretch force because of the beating of the heart. The microarchitecture and the fluid shear stress are the mechanical stress contained and transmitted by the solid phase and the liquid phase, respectively. Stiffness is defined as the ability of a material to resist deformation under external forces. The physical interaction between cardiac cells and ECM produces the physical features of cardiac fibrosis through different and interrelated mechanisms. The abnormal contraction and relaxation of the heart cause vascular stretch to increase blood fluid pressure within the site of fibrosis. Cell differentiation, increased fluid shear stress, and matrix deposition result in compressive microarchitecture. Cardiac stretch, matrix deposition, and cross-linking can respectively lead to increased stiffness at the fibrotic site. The microarchitecture leads to the stretching and alignment of the matrix, and tissue stiffening increases the differentiation of cardiac fibroblasts. Fluid flow and excessive strain activate fibroblasts, which then contribute to increased cardiac wall stress and stiffness values and changes in ECM structure.

evidence indicates that the mechanical properties of cardiac tissues, from the macroscale to the microscale, underlie cellular behavior and tissue functions (Orre et al., 2019; Guimaraes et al., 2020). In addition, biomechanical properties of tissue play a critical role in maintaining organ structure and function as well (Peyronnet et al., 2016; Wagh et al., 2021). For example, related to the diastolic function impairment and heart failure, diffuse thickening (a crucial fibrotic manifestation in the process of hypertrophic cardiomyopathy) of tissue caused by cardiac fibrosis might limit cardiac myocytes contractility and impaired ventricular function (de Jong et al., 2011; Cowling et al., 2019). Furthermore, biomechanical cues have been reported as a coconspirator of biological traits in tissue fibrosis initiation, progression and treatment response (Hadjicharalambous et al., 2021; He et al., 2021). However, due to the physical differences in each organ, different organs [e.g., heart (Lemaitre et al., 2021), liver (Kong et al., 2021), and lung (Freeberg et al., 2021)] have their specific mechanical traits as well.

In the heart, the abnormal static biomechanical traits like stiffness or microarchitecture facilitate the progress of cardiac fibrosis *in vivo* (Islam et al., 2021). The change of collagen microarchitecture can regulate myofibroblast differentiation and fibrosis independent of collagen quantity and bulk stiffness by locally modulating cellular mechanosignaling (Seo et al., 2020a). For example, changes in matrix structure and components can alter the cell-matrix and cell-cell interactions and related signal transduction (Ashworth et al., 2020; Yamada et al., 2022). The ECM microarchitecture could be altered by the contractile activity of myofibroblast containing stress fibers as well (Seo et al., 2020b; Davidson et al., 2020). Moreover, increased stiffness can activate signaling pathways that promote fibroblast proliferation and differentiation, which in turn accelerates the progression of cardiac fibrosis (Gourdie et al., 2016; Villar et al., 2022). Besides the static biomechanical traits, cardiac cells are constantly regulated by dynamic biomechanical traits, such as fluid shear and cyclic stretch as generated by blood flow and heartbeats (Fukui et al., 2021; Kotini et al., 2022). For example, abnormal mechanical stretching leads to excess proliferation and differentiation of fibroblasts, resulting in irreversible cardiac fibrosis (Yong et al., 2015; Morley et al., 2018). Dynamic overstretching can also cause microstructural remodeling of the myocardium, which is closely associated with systolic and/or diastolic dysfunction (Caporizzo and Prosser, 2022). Thus, a rigorous description of the biomechanical traits of cardiac fibrosis will contribute to a better understanding of the complex mechanism of fibrosis and the exploration of effective anti-fibrosis therapies.

Although there exist a few reviews on cardiac fibrosis from the aspect of cell biological mechanisms, molecular pathways and therapeutic opportunities (Frangogiannis, 2019a; Park et al., 2019; Frangogiannis, 2021), there is still a lack of one focusing on the biomechanical properties of cardiac fibrosis. Here, we summarize four distinct biomechanical traits (i.e., stretch, fluid shear stress, ECM microarchitecture, and ECM stiffness) and categorize them into two different types (i.e., dynamic and static) (Figure 1). Next, we provide a comprehensive overview of the effect of different biomechanical traits on cardiac fibrosis, their transduction mechanisms, and the *in vitro* engineering models targeting biomechanical traits. We finally conclude with a perspective on important open challenges of the role of other biophysical cues, and future directions like identification of the mechano-based therapeutic targets to ameliorate cardiac fibrosis progression.

2 Static biomechanical traits

2.1 Common static biomechanical traits during cardiac fibrosis

2.1.1 Increased stiffness

Biomechanical microenvironments are associated with heart attacks and may be the source of abnormal signals that drive cardiac cells to adapt to adverse changes. As a static biomechanical characteristic, stiffness refers to the ability of tissue structure to resist elastic deformation when subjected to a force (Levine et al., 2021). Increased stiffness of myocardial tissue (~55 kPa) is an important feature of cardiac fibrosis, due to the excessive transformation of cardiac fibroblasts and accumulation of various components of the ECM, which can be three or four times stiffer than healthy myocardium (~10 kPa) (Berry et al., 2006). In addition, cells can also generate traction to recruit the matrix to make the fibrotic ECM denser, resulting in a significant increase in the local stiffness.

Although the stiffness of fibrotic myocardium (~55 kPa) (Huyer et al., 2015) exceeds the diastolic stiffness of healthy myocardium (~8–10 kPa) (Wang et al., 2019), it is lower than that of systolic myocardium (>100 kPa) (Huyer et al., 2015). When the myocardium is partially stiffened during cardiac fibrosis, immune cells will be recruited and activated to abnormal locations, and then profibrotic factors (e.g., cytokines, growth factors, and chemokines) will be released (Halade and Lee, 2022). Subsequently, the release of these factors [e.g., transforming growth factor-beta (TGF-β), plateau-derived growth factor (PDGF)] leads to the conversion of cardiac fibroblasts into activated myofibroblasts, promoting collagen deposition (Zhang et al., 2015). It is found that mechanical stiffness and TGF-β can synergistically upregulate the deposition of collagen as well (Figure 2). Transformed myofibroblasts exhibit increased secretion ability of ECM proteins, which further stiffen cardiac tissue and activate fibroblasts, ultimately leading to long-term cardiac fibrosis (Boyle et al., 2021).

2.1.2 Abnormal microarchitecture

ECM is a common meshwork structure that is an important organizer of cell microenvironment. Structural features of the ECM can have profound effects on cell behaviors, which are closely related to the performances and functions of tissues. Cardiac ECM mainly consists of fibrillar collagen, fibronectin, glycosaminoglycans, and proteoglycans, which together provide a stabilized structure and viscoelasticity for cells. Pore size and density of cardiac ECM structure determine the available space and provide a physically confined microenvironment for cell growth (Huang et al., 2017; Frangogiannis, 2019b). Following heart injury, changes in the porosity and density of cardiac ECM will accelerate and regulate inflammation, repair, fibrosis and regeneration. Mainly, caused by the abnormal changes of collagen, the structural remodeling of cardiac fibrosis can affect the forces generated by cells and induce electromechanical transduction processes (Garoffolo and Pesce, 2019; Urbanczyk et al., 2020). The biomechanical properties of fibrotic myocardium are influenced by changes in the quality of collagen fibers, such as the shift in collagen types proportion, increased fibronectin

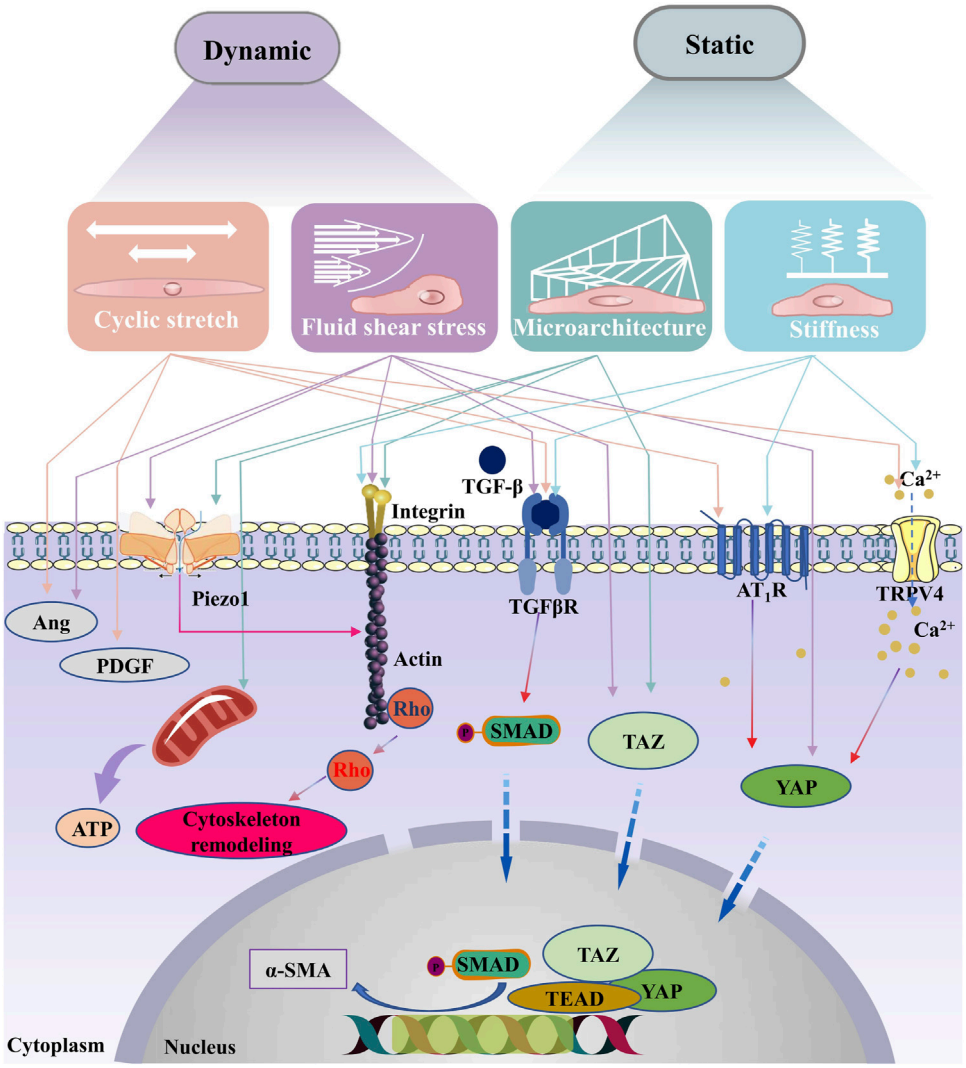

FIGURE 2
Signaling pathways associated with the biomechanical traits of cardiac fibrosis. With the changes of ECM mechanical properties during the process of cardiac fibrosis, myofibroblasts are activated . In classical signaling pathway, the TGF-β receptor's activation induces phosphorylation of the C-terminus of SMAD. The phosphorylated SMADs then form a complex with the co-mediator SMAD, SMAD4, the complex is translocated into the nucleus, where it binds to the gene promoter. Upon myofibroblasts are activated, TGF-β is released from binding proteins in the ECM, leading to sustained activation and contraction of myofibroblasts, finally causing a vicious cycle of fibrotic progression. In addition, integrins which sense changes in external forces can also contribute to the remodeling of the cytoskeleton. Studies have shown that the activation of cell membrane surface mechanosensitive receptors (such as Piezo1, AT_1R and TRPV4) are also key pathways in the vicious cycle of fibrosis. Correlational studies have shown that Piezo1 can be activated by shear stress, stretching and matrix microarchitecture. Ang, Angiopoietin; TGF-β, transforming growth factor-beta; PDGF, plateau-derived growth factor; α-SMA, Piezo1, piezo type mechanosensitive ion channel component 1; alpha-smooth muscle actin; TGFβR, transforming growth factor-beta receptor; TRPV4, transient receptor potential vanilloid type 4; YAP, YES-related proteins; TAZ, transcriptional coactivator with PDZ-binding motif; AT1R, angiotensin type 1 receptor; TEAD, TEA domain transcription factors; SMAD, drosophila mothers against decapentaplegic.

polymerization and increased degree of collagen cross-linking (González et al., 2019). In addition, increased infarct stiffness can prevent left ventricle over-stretch by reducing collagen degradation and facilitating collagen assembly and cross-linking through preservation of the fibronectin network and activation of lysyl oxidase (Voorhees et al., 2015).

The ECM architecture can be rapidly and profoundly regulated by cross-linking reactions enzymatically or non-enzymatically, which can further alter cellular responses and drive disease progression. Collagen cross-linking is a main factor that influences collagen deposition and insolubility of ECM architecture (Neff and Bradshaw, 2021). Firstly, an

enzymatically collagen crosslinking that catalyzed by Lysyl oxidase-like 2 (Loxl2) is essential for cardiac fibrosis and mechanical dysfunction of pathological site (Yang et al., 2016). In addition, excess synthesis and activation of the enzyme Lox significantly increases collagen resistance to the degradation by matrix metalloproteinases (MMPs) (El Hajj et al., 2018). Secondly, the imbalance between MMPs and their tissue inhibitors (TIMP) have important effect on the progress of cardiac fibrosis (Polyakova et al., 2011). Thirdly, growing evidence have indicated that transglutaminases (TGs) is involved in molecular responses underlying the pathogenesis of cardiac fibrosis including collagen cross-linking (Al-U'datt et al., 2022). For non-enzymatical collagen cross-linker, proteoglycan fibromodulin has anti-fibrotic effects through regulating collagen fibrillogenesis in cardiac fibroblasts (Andenæs et al., 2018). For example, Kalamajski et al. have documented a fibromodulin-modulated collagen cross-linking mechanism where fibromodulin binds to a specific part of the collagen domain and also forms a complexus with Lox (Kalamajski et al., 2016). Specifically, increasing collagen I:III ratio would provide additional rigidity to tissue structure, whereas decreasing this ratio would provide elasticity and flexibility to the tissue (Kisling et al., 2019). Furthermore, excessive collagen deposition will lead to ECM stiffening, while such stiffening is considered as a pathological change in cardiac fibrosis, which also impairs the compliance of ECM structure, finally altering cardiac tissue microarchitecture (Davis and Molkentin, 2014; Frangogiannis, 2017). Abnormal microarchitecture can affect signal transduction of cardiac cells, promoting cardiac fibrosis through altering the expression of alpha-smooth muscle actin (α-SMA) in cardiac cells (Kuehlmann et al., 2020; Dooling et al., 2022a). Similarly, the abnormal cross-linking of collagen fibers can inhibit the normal renewal of collagen and further promotes the progress of fibrosis.

2.2 Transduction mechanism of static biomechanical traits

Cell microenvironment regulates cellular mechanical responses by providing reaction forces to balance intracellular traction. The change of cell microenvironment will lead to the change of association mode and binding strength between cell-cell and cell-ECM, and thus change the cell function and phenotype (Figure 2) (D'Urso and Kurniawan, 2020). The increase in mechanical stiffness and the changes in ECM microarchitecture may affect cell behavior through receptor and signal transduction systems. With the changes in those two static properties, the conformation of structural proteins on the cell membrane becomes unstable, which will activate the signal transduction of biochemical factors and create conditions for changing the gene expression in cells. Increased stiffness and abnormal microarchitecture promote latent TGF-β captured by integrin on myofibroblast membranes and then activate TGF-β (Wipff et al., 2007). In addition, increased stiffness and changed microarchitecture also promote the activity of TGF-β receptor, which is a vital component of the TGF-β/SMADs signaling pathway. TGF-β can promote myofibroblasts to produce ECM proteins and collagen (Leask and Abraham, 2004; Vivar et al., 2013), especially in the process of pathological fibrosis after myocardial injury, which increase the stiffness of damaged myocardium.

Moreover, transient receptor potential (TRP) channels enable cells to convert mechanical signals into chemical signals to accommodate the microarchitecture of the fibrous collagen matrix through myosin contractility during myocardial remodeling (Ji and McCulloch, 2021; Jia et al., 2021). Components of the cardiac ECM can actively communicate with cells as well as the nucleus by binding to cell surface receptors (Kalukula et al., 2022; Miroshnikova and Wickström, 2022). For instance, when ECM is stiffened, active TRPV4 will promote the accumulation of Ca^{2+} in cardiac cells (Van den Bergh et al., 2019). The accumulation of Ca^{2+} can further affect Hippo-YAP signaling to promote cardiac fibrosis (Fukui et al., 2021), for example, promoting cytoskeletal tension and nuclear translocation of Yes-related proteins (YAP) in fibroblast cytoplasm exacerbates adverse cardiac remodeling and impairs cardiac function (Alsamman et al., 2020; Mia et al., 2021). Another factor involved in microarchitectural signal transduction is the myocardia related transcription factor, which relates mechanical stress to the transcription activity of α-SMA genes in various myofibroblast progenitor cells through the polymerization state of actin. Myocardia related transcription factor translocases to the nucleus in a RhoA/ROCK-dependent manner on the rigid substrate, accelerating the fibrosis process (Johnson et al., 2014). Integrin and mature focal adhesions are considered as the main molecular bonds between cells and the ECM microarchitecture, which transmit stiffness and para-tensile signals between cells and their microenvironment (Kechagia et al., 2019).

Huang et al. have found that matrix stiffness-induced cardiac myofibroblast differentiation can be mediated by angiotensin II type 1 receptor (AT_1R) and Smad7 (Yong et al., 2016). Niu et al. (2020) have revealed that the YAP pathway is a vital signaling branch downstream of AT_1R receptor in the mechanotransduction of cardiac fibroblast, which may benefit for the development of new treatment of fibrotic diseases. Moreover, Niu et al. (2022) have also discovered a mechanical positive feedback loop between integrin β1 and Piezo1 activation which is initiated by perturbations in matrix stiffness, finally caused the further stiffened environment by fibroblasts. A downstream mediator of mineralocorticoid receptors and insulin receptor activation, the endothelial cell Na^+ channel (EnNaC), has recently been

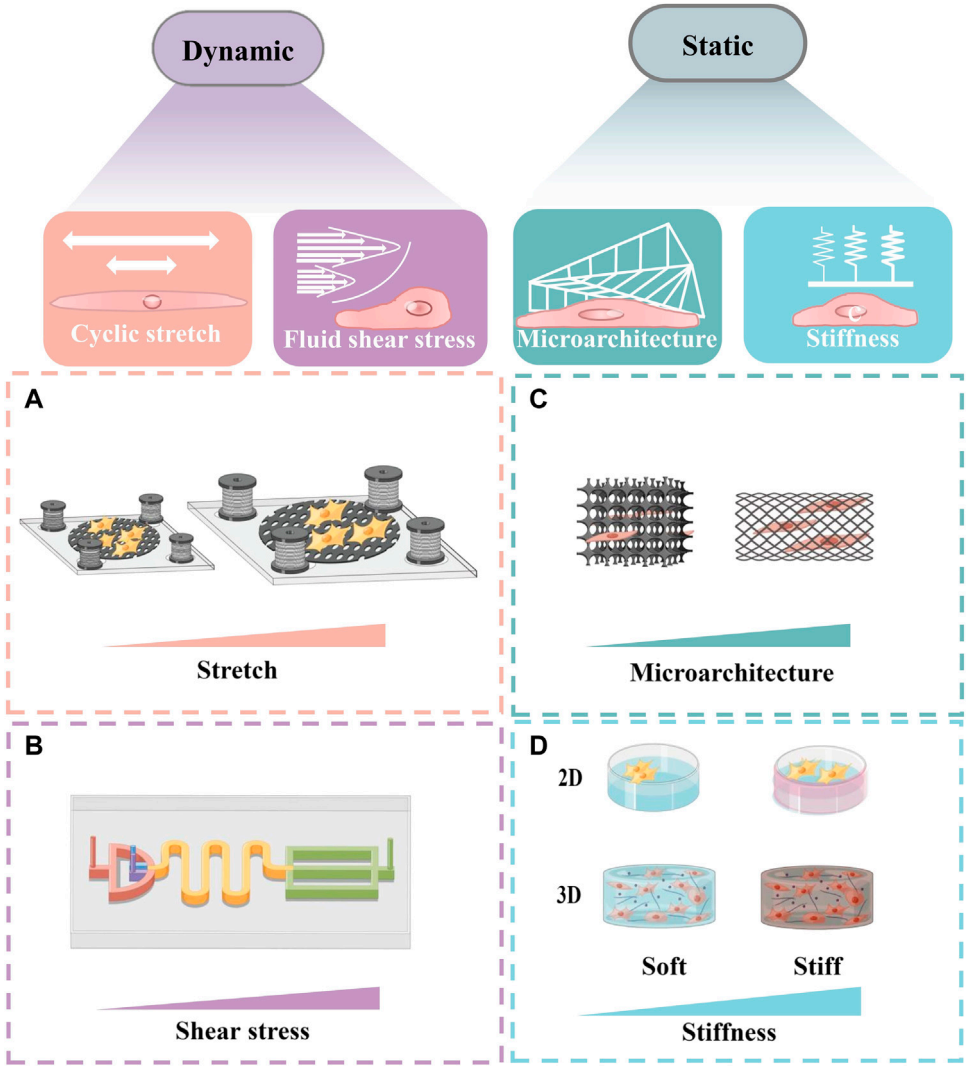

FIGURE 3
Schematic of several in vitro models simulating the change of biomechanical traits. Schematic diagrams were drew online using Figdraw. **(A)** A schematic diagram of a stretch system to apply long-term cyclic stretch to cells. **(B)** A schematic diagram of the equipment, which can generate shear force and rotational shear force respectively to simulate the fluid shear stress *in vitro*. **(C)** A scalable microarchitecture-cultivation platform for engineering cardiac tissues. **(D)** A schematic diagram of cells cultured in different matrix stiffness in 2D and 3D.

identified as a key molecular during cardiovascular fibrosis and tissue stiffening (Kleyman et al., 2018). Increased activity of EnNaC results in a number of negative consequences, including stiffening of the cortical actin cytoskeleton in endothelial cells, impaired endothelial NO release, increased oxidative stress-meditated NO destruction, increased vascular permeability, and stimulation of the inflammatory environment (Hill et al., 2022). Furthermore, Liu et al. (2017) have revealed that NIP3-like protein X (BNIP3L) is a novel mediator of ECM structure pressure through the $[Ca^{2+}]_i$-TGF-β-Smad2/3 pathway in cardiac fibroblasts.

2.3 *In vitro* engineering models to simulate static biomechanical traits

Matrix stiffness is considered to be a key static trait that affects not only the physiological development of the heart, but also the pathological state of cardiac fibrosis. Microarchitecture cue is a vital static trait in cardiac fibrosis as well. At present, many researchers have rebuilt various models mimicking those static traits like stiffness or microarchitecture in two-dimension (2D) or three-dimension (3D) to study the specific mechanism during the progression

of cardiac fibrosis. These models can provide strong support for the studies of prevention and treatment of cardiac fibrosis (Kong et al., 2019; Jia et al., 2021).

2.3.1 2D models

The 2D cardiac fibrosis *in vitro* models are widely used to study the mechanism of cardiac fibrosis, as well as drug screening. Recently, the role of matrix stiffness in inducing myofibroblast activation can be studied by culturing cardiac fibroblasts with mechanically adjustable gelatin hydrogels (Zhou et al., 2019). For example, Lang et al. (2021) have constructed an *in vitro* cardiac fibrosis model by culturing cardiac fibroblasts on polyacrylamide gels with tunable stiffness to investigate the effect of substrate stiffness on the redox state of cardiac fibroblasts. To determine whether YAP is a modulator of perceived microenvironmental stiffness, Niu et al. (2020) made gelatin hydrogels with different stiffnesses (4–41 kPa) to mimic the stiffness of normal and infarcted cardiac tissue. Under the stimulation of different matrix stiffness, they characterized the ratio of nuclear YAP to cytoplasmic YAP and the expression of total YAP in cardiac fibroblasts (Niu et al., 2020).

Compared to *in vivo* kPa level, the stiffer GPa planar culture dish could not replicate the cardiac tissue stiffness well. The modified planar patterning and modifications create a 2D planar culture environment within controllable, single or multiple factors, morphology, and biomechanical stimulation for cell (Duval et al., 2017; Yang et al., 2021a). To make cell shape controllable and sense static microarchitecture, researchers have created micropatterned matrices in 2D planes to alter the shape of cells (Ma et al., 2017). For example, Yeh et al. (2021) have used decellularized ECM to mimic the native microenvironment and obtained more reliable results that better recapitulate *in vivo* fibrosis. With these models, researchers can focus on the effects of microarchitecture and stiffness perceived by cardiac cells on cardiac fibrosis.

2.3.2 3D models

3D microfluidic technologies have been widely used in all walks of life science, which can provide some new methods to simulate static characteristics of cardiac fibrosis *in vitro* (Marsano et al., 2016; Portillo-Lara et al., 2019). Through precisely positioning biomaterials and living cells in 3D biomimetic models, cardiac fibrosis processes can be simulated using tunable biomechanical models to mimic the diversification of stiffness and structures in cardiac fibrosis. In the 3D scale, researchers developed gels with adjustable stiffness to study the significance of stiffness change in fibrosis. For instance, researchers used tunable and biodegradable hydrogels with different concentrations of the modified HA and methacrylated gelatin to control mechanical stiffness to provide fibroblasts with gradient stiffness stimulations, mimicking the state of cardiac fibrosis *in vitro* (Duan et al., 2013). Mooney et al. have developed a modulated nanoscale architecture to tune the rate of stress relaxation of hydrogels for 3D cell culture to study how the architecture of hydrogels regulates stem cell fate and activity (Chaudhuri et al., 2016). Bhattacharjee and Datta (2019) have prepared a 3D porous architecture media and found that individual cells are intermittently and transiently trapped as they move through the pore spaces. This porous architecture media can provide the picture of bacterial motility in complex media, which can be used to predict cell migration. Bian et al. have reported a supramolecular hydrogel that can provide a controlled platform for investigations on cellular responses to dynamic biophysical cues in 3D environment, and they also found that such hydrogel network has impact on cell behaviors including mechanosensing and differentiation in 3D matrix (Yang et al., 2021b). Sadeghi et al. (2017) developed 3D co-culture *in vitro* model with mixed cardiac fibroblasts and cardiomyocytes in gelatin methacryloyl hydrogel. They proved that the fibroblasts can be kept at rest by imitating the physiology stiffness and cell-cell of natural cardiac tissue. And they have validated the practicability of this model by adding TGF-β1 to activate static cardiac fibroblasts in the model and by analyzing the expression of collagen markers.

Researchers have developed numerous decellularized ECM-based bioinks to construct biomimetic tissue microarchitecture, which provides optimal cell adhesion (Schwan et al., 2016; Jang et al., 2017; Yeh et al., 2021). Wang et al. (2018) developed a functional heart tissue that mimics the microarchitecture, physiological, and functional characteristics of natural heart muscle. This model can be used to regulate the phenotypic transformation of fibroblasts and to study fibrosis structure remodeling. Worke et al. have developed an *in vitro* bionic 3D platform to study cell-ECM interaction, which can help us to understand better how microarchitecture affects chemical signals thus affecting the development and deterioration of cardiac fibrosis (Maji and Lee, 2022). Liu et al. (2020) have studied the shape of fibroblasts by controlling the microarchitecture formed by the 3D hybrid hydrogels. This work showed how cell shape affects the cellular response to 3D mechanical and biochemical cues, and has implications for the development of cell shape modulation-specific approaches to treat fibrosis. Worke et al. (2017) have also explored the potential of compressed collagen matrix as a structure mechano-chemical and physiochemical related cardiac fibrosis model system by combining collagen with embryonic cardiomyocytes. In brief, these models provide us with strong support to study static biomechanics of cardiac fibrosis *in vitro* and test anti-fibrotic drugs in promoting real-time assessment of cardiomyocyte function.

3 Dynamic biomechanical traits

3.1 Common dynamic biomechanical traits during cardiac fibrosis

3.1.1 Stretch

The heart is a dynamic organ with the ability to contract and relax in a coordinated manner in space and time. On the organ scale, the dynamic stretch caused by the heartbeat is the predominant biomechanical feature of the myocardium. The progression from injury to fibrosis is a rigid process filled with aggressive immune cells and reconstructed sites, and delayed onset of ventricular stretch can be expected. On the cellular scale, the dynamic stretch originates from the beating of cardiomyocytes and partly from the contraction of myofibroblasts. Recent studies have shown that excessive dynamic stretch may be a powerful stimulator for continuous activation of myofibroblasts and remodeling of cardiac ECM, enabling fibrosis to progress (Kong et al., 2019; Walker et al., 2020). The loss of functional tissue and the reduction of myocardial elasticity and contractility lead to a vicious circle of low mechanical efficiency, which finally causes negative fibrotic remodeling, impaired stretch, and ultimately heart failure (Richardson et al., 2015; Long et al., 2022).

The dynamic contraction properties of cardiac tissue have a vitally biomechanical effect on cardiac fibrosis. Perception of external abnormal stretch signals by cardiac cells and the subsequent biomechanics of cell-ECM interactions can regulate downstream mechanotransduction events (Maurer and Lammerding, 2019), e.g., the differentiation of fibroblasts in healthy myocardium into pathological myofibroblasts in response to mechanical stretch overload of cardiomyocytes. Myofibroblasts are distinctive with the presence of a large number of contractile apparatuses containing actin filaments and related proteins (Mia et al., 2021). These contraction devices have a mechanical conversion function which allows myofibroblasts to convert the excessive stretch they perceived into chemical signals. In addition, actin filaments in myofibroblasts can alter cell shape, promote cell movement and transmit forces to the surrounding matrix environment resulting in ECM reorganization and contraction (Sandbo et al., 2016). Specifically, at the development of fibrosis, fibroblasts undergo phenotypic conversion into myofibroblasts by developing muscle-like features, including formation of contractile actin-myosin bundles (Hinz et al., 2019). Actin and myosin filaments work together to generate force to alter cell shape. It has been reported that the actin filaments may make cell shape more polarized. Due to the fibroblasts had long protrusions, the cells in 3D were stellate in shape, with numerous projections, and thus similar in shape to fibroblasts on 2D tissue culture plastic (Kalson et al., 2015; Yeung et al., 2015). Caused by the abnormal stretch, abnormal constriction of cardiac blood vessels increases and accelerates the progression of heart failure during cardiac fibrosis (Wu et al., 2021).

3.1.2 Fluid shear stress

The human cardiac is a marvelous fluidic system, which is very sensitive to biomechanical and biochemical. As a dynamic biomechanical trait, fluid shear stress is mainly derived from blood flow in the heart (Wang et al., 2022). Multiphasic fluid is contained about many parts. Such as, intracellular stress fibers filled with intracellular fluid at the molecule level, a fibrous network filled with tissue gel in the extracellular matrix at the cellular level, blood flow in capillaries at the tissue level (Feng et al., 2014). Among these types of matter, multiphasic fluids in cardiac show an orderly multiscale spatial flow that determines biological activities (Liu et al., 2022; Stine, 2022). Mechanical shear from blood flow has a major impact on endothelial cell physiology and a key role in initiating vascular regulatory signaling. Appropriate shear stress maintains endothelium homeostasis, while abnormal shear stress in the fibrotic microvascular system may elicit endothelial dysfunction. Endothelial cells do not normally experience the fluid shear of blood flow, but are activated by cytokines at sites of the fibrosis (Kreuger and Phillipson, 2016). In addition, shear stress can modulate the mechanical sensitivity of human blood mononuclear cells (Baratchi et al., 2020). Fluid shear changes at abnormal sites during cardiac fibrosis often cause a range of changes, such as affecting cardiac tissue and cellular morphology.

Caused by the abnormal contraction of the myocardium, the abnormal contraction of blood vessels can lead to higher fluid pressure, and causes abnormal fluid shear stress in the vascular endothelium. The shear stress on endothelial cells can be transmitted to other cells *via* cell-cell and cell-ECM interaction. Continuous blood flow shear loading is also thought to contribute to fibroblast proliferation, migration and differentiation. This process leads to fibrosis, which promotes the progression of many cardiac diseases by blocking myocardial excitation-contraction coupling and interfering with pulse propagation and ECM-dependent signaling pathways. Therefore, over-stretch and fluid shear loads regulate the function of many mechanosensitive ion channels and transmembrane proteins, which interact closely with the ECM to activate a range of signaling pathways to alter cellular function to affect the progression of cardiac fibrosis (Priya et al., 2020).

3.2 Transduction mechanism of dynamic biomechanical traits

From the biomechanical point of view, myocardial tissue can be regarded as an elastic material. Thus, we can explore the specific biomechanical transduction mechanisms caused by abnormal heart contraction in the process of fibrosis from the aspects of dynamic tension and fluid shear stress (Figure 2) (Dooling et al., 2022b; Villalobos Lizardi et al., 2022). Interestingly, the behavior of cells subjected to over-cyclic

stretch on flexible substrate is similar to that on a rigid substrate, which indicates that over-cyclic stretch can replace rigid substrate in stimulating fibroblasts spreading, stress fiber formation and growth (Qian et al., 2013; Cui et al., 2015). The expression of α-SMA can make cells produce mechanical stress, which not only plays an important role in tissue reconstruction and contraction, but also can be used as a mechanical transducer to connect mechanical sensing factors and increase their expression in stretch induction (Balachandran et al., 2011; Zhao et al., 2022b). Myofibroblast contraction activates latent TGF-β from the ECM, which can promote fibroblasts to differentiate into myofibroblasts through inducing smooth muscle myosin and α-SMA expression (Walker et al., 2020). The dynamic contraction of matrix architecture can promote the activation of TGF-β as well, which adds new content to the complex "indirect mechanical induction" mechanism (Hanna et al., 2021). For example, besides promoting cell attachment to microstructure through adhesive spots, TGF-β can also facilitate the specific binding of integrin to the hidden domain (exposed under cyclic stretching) of fibronectin ligands (Zarubova et al., 2022).

Moreover, mechanical sensitive channels on the cell membrane also play an important role during cardiac fibrosis (Saucerman et al., 2019; Stewart and Turner, 2021a). Stretch-activated channels are non-selective cation channels that increase in activity in response to mechanical stress (Lorin et al., 2015). Some stretch-activated channels are thought to contain ion channel proteins from a large family of TRP channels, such as TRPV2 or TRPV4. In the vascular endothelium, local Ca^{2+} influx through TRPV4 plays a vital role in endothelial cell adaptation to hemodynamics (Baratchi et al., 2017). Mechanosensitive Ca^{2+} permeable ion channels are an important class of proteins expressed on circulatory blood cells, responding to mechanical stimuli and participating in the sensing of shear stress (Baratchi et al., 2020). The increase in stretch and fluid shear force caused by cyclic strain can promote the deformation of piezo-type mechanosensitive ion channel component 1 (Piezo1), which in turn promotes cytoskeletal remodeling (Chowdhury et al., 2021; Lai et al., 2021; Liao et al., 2021). In addition, fluid shear stress can also induce TGF-β and angiotensin II type 1 receptor (AT_1R) signals, thus promoting cardiac fibrosis (Stewart and Turner, 2021b; Yang et al., 2021c).

Calcium signaling is also fundamental to cardiac ECM microarchitectural contractility (Terrar, 2020). Due to the regular contraction and relaxation of the myocardium, both fibroblasts and myofibroblasts are affected by cyclic strain in both flexible and rigid microarchitecture. Researchers have found that RhoA is involved in regulating calcium release in response to cardiac stress (Lauriol et al., 2014; Mathiyalagan et al., 2019; Dridi et al., 2020). Studies have shown that dynamic mechanical stimulation can facilitate the release of the PDGF and Angiotensin II (Ang II) (Lisy et al., 2000; Lopez-Bellido et al., 2019). Over expression of PDGF and its receptors, including PDGFR-α and PDGFR-β, can lead to cardiac fibrosis and cardiac ECM protein deposition (Kong et al., 2014). Ang II, a key mediator of the renin-angiotensin-aldosterone system involved in cardiac remodeling (Schorb et al., 1993; Jong et al., 2016), is usually elevated after myocardial injury and causes cardiac fibroblast proliferation and collagen overexpression (Cai et al., 2019; Jana et al., 2021). However, the effect of cardiac ECM microarchitecture on Ang II-induced cardiac remodeling and heart failure remains unknown (Chen et al., 2021). Developing the methods of dynamic biomechanical traits and cardiac cells may find a new therapeutic target for fibrotic diseases.

Cadherin-11 has been described as a senescence-responsive molecular, its expression is suppressed in senescent endothelial cells and such suppression is greater when senescent cells are under shear stress (Mun and Boo, 2010). In addition, cilium of endothelial cells is abundant in regions subjected to low shear stress or disturbed blood flow, while absent in regions with high shear stress (Garoffolo and Pesce, 2019). Furthermore, mechanical deformation of focal adhesion proteins would elicit the activation of stretch-dependent signaling pathways (Riley and Merryman, 2021). For example, focal adhesion kinase is activated by cyclic stretch, which then activates the protein kinase B (AKT) and mitogen-activated protein kinases (MAPK) pathways to promote myofibroblast differentiation (Zebda et al., 2012).

3.3 *In vitro* engineering models to simulate dynamic biomechanical traits

Establishment of *in vitro* models in 2D or 3D allows for the integration of other relevant biomechanical stimuli important to the human myocardium, such as cyclic stretch and ECM structures (Rogers et al., 2019; Veldhuizen et al., 2020). Cardiac fibrosis biomechanical models have attracted extensive attention due to their inclusion of vital dynamic traits. By simulating dynamic stimulus on classic 2D models or stereoscopic 3D models (Bein et al., 2018; Yu and Choudhury, 2019; Vivas et al., 2022), we can mimic dynamic biomechanical traits of cardiac fibrosis *in vitro* well at the multiscale (Table 1).

3.3.1 2D models

Researchers have performed cell culture experiments on various stretchable 2D planes to simulate abnormal stretching that appears in cardiac fibrosis. For example, stretching the cellular structure can recapitulate part of the complex mechanical environment that cardiovascular cells experience *in vivo* (Figure 3A) (Cirka et al., 2016). Studies in which dynamic mechanical stress was applied to cardiac fibroblasts by stretching silicon films revealed a significant increase in fibrotic responses, including cardiac fibrosis, fibroblast proliferation, collagen expression and matrix

TABLE 1 Examples of modeling biomechanical traits in 2D or 3D cell culture.

Models	Biomechanical traits	Uses	Refs
2D			
Oscillating shear model	Fluid shear stress	The activation method of TGF-β1 ubiquitously in a latent form	Kouzbari et al. (2019)
Mechanochemical modeling framework	Cyclic stretch and sub-cellular structures	Predicting the preferred alignment of cells under stretch	Qian et al. (2013)
Hydrogel-based system	Simulation of matrix stiffness after myocardial tissue infarction	Modulating myofibroblast mechanotransduction	Zhao et al. (2014)
Photodegradable PEG based hydrogel system	Stiffness and structure	Spatially varying matrix elasticity and studying the effect of matrix elasticity organization on valvular interstitial cells phenotype	Ma et al. (2017)
Gelatin hydrogels platform	Stiffnesses (4 and 36 kPa)	The proliferative ability of the cardiac fibroblasts cultured on substrates with different stiffnesses	Niu et al. (2020)
Decellularized ECM experimental platform	Microarchitecture and stiffness	Mimicking the native microenvironment more accurately	Yeh et al. (2021)
Engineered biohybrid constructs	Myocardium laminar structure	Measuring myocardial contractility	Grosberg et al. (2011)
3D			
The micro-physiological system	Cyclic stretch	Up to six different biologically independent samples are incorporated in a single device	Mainardi et al. (2021)
3D microscale cell-laden hydrogel platform	Cyclic stretch (10% strain at 1 Hz)	The recapitulation of key stages of cardiac fibrosis (i) proliferation, (ii) fibroblast to myofibroblast phenotypic switch, (iii) matrix deposition and (iv) stiffening	Occhetta et al. (2018)
3D model of human cardiac fibrosis	Stretch triggered by human induced pluripotent stem cell derived cardiomyocytes	The classic hallmarks of fibrosis-induced heart failure including high collagen deposition, increased tissue stiffness, BNP secretion, and passive tension	Mastikhina et al. (2020)
Laser-cut sheets of decellularized myocardium scaffolds	Cyclic stretch, shear stress and microstructure	Assessing the nature of the organization	Jang et al. (2017)
The MVAS-force model	Stretch and microstructure	Linking cell-level phenotypic changes to functional changes	Walker et al. (2020)
The beating heart-on-chip device	Cyclic stretch and microstructure	The beneficial effect of mechanical stimulation on the functional maturation of cardiac microtissues	Ugolini et al. (2018)
3D GelMA-based hydrogel platform	Stretch and stiffness	The activation of cardiac fibroblasts into myofibroblast	Sadeghi et al. (2017)
3D microfluidic cardiac tissue model	Tissue architecture	Recapitulating the native myocardium	Veldhuizen et al. (2020)

metalloproteinase *in vitro* (Yuan et al., 2018). Grosberg et al. (2011) implanted cardiomyocytes on the surface of elastic films to form a layer of cell sheet, such films would deform regularly with the beating of cardiomyocytes. The chip can not only monitor the contractility and electrophysiological properties of cardiomyocytes in real time, but also can be used in pharmacological studies.

Microfabrication can generate shear and rotational shear forces to simulate fluid shear forces (Figure 3B) (Kouzbari et al., 2019). Such technology can provide us with a method to simulate the abnormal fluid shear forces generated in cardiac fibrosis. Chester et al. (2018) used microgel films with viscoelastic properties to explore the significant effect of material stretch on cell adhesion, migration, or myofibroblast differentiation. They found that stretch stimulation had a facilitative effect on early fibrotic response.

3.3.2 3D models

The construction of the 3D cardiac fibrosis pathological model *in vitro* is of great significance for the study of dynamic traits in cardiac fibrosis. For instance, through controlling the concentration of collagen quantitatively and the density of fibroblasts in the cardiac tissue models, van Spreeuwel et al. (2017) found that the increase in the number of fibroblasts significantly reduced myocardial contractility and altered the heart rate. Kong et al. (2019) studied the relationship between mechanical movement and cardiac fibroblast proliferation by applying cyclic compression of gradient amplitude and adjustable frequency on GelMA hydrogel containing cardiac fibroblast. They found an important correlation between stretch stimulation and phenotypic transformation of cardiac fibroblast, which provides new ideas for the prevention and treatment of cardiac fibrosis in the future.

At present, a variety of "cardiac tissue chips" have been developed to simulate and manipulate dynamic mechanical microenvironment of cardiac tissue at the micro-scale by combining with microfabrication or microfluidic technology, providing real-time insights into fibrosis events. Moreover, cardiac tissue chips can offer an extraordinary way to precisely manage different microenvironment signals (e.g., abnormal stretch or fluid shear stress) to construct biomimetic 3D *in vitro* cardiac fibrosis models (Duval et al., 2017; Soon et al., 2021). For example, Zhao et al. (2019) described a scalable tissue-cultivation platform that is cell source agnostic and enables drug testing under electrical pacing (Figure 3C). This controlled 3D platform with multiple cells enabled real-time recordings of cardiomyocytes' active tension, passive shear force and dynamic stretch. Mainardi et al. (2021) developed an *in vitro* fibrosis model which could help to uncover new pathological aspects and to study the crosstalk between cyclic stretch and the most abundant cell types involved in fibrosis.

Additionally, 3D *in vitro* cardiac fibrosis models can better simulate natural myocardial tissue *in vivo*, and also can better mimic complex interactions of cell-cell and cell-ECM, complex mechanical traits and chemical signals (Figure 3D) (Marsano et al., 2016). Occhetta et al. (2018) constructed a 3D *in vitro* cardiac fibrosis model by cyclically stretching cardiac fibroblasts embedded in a 3D hydrogel to simulate an *in vitro* fibrosis-like microenvironment. They have reproduced some of the major fibrosis features within 7 days, and cyclic strain did increase fibroblast proliferation and ECM deposition, resulting in a higher quality scar-like tissue. 3D dynamic devices *in vitro* have provided futuristic platforms for elucidating cardiac ECM remodeling, fibrosis pathophysiology and dynamic contractile function (Savoji et al., 2019), which may provide direction for exploring the therapeutic targets for cardiac fibrosis.

4 Conclusion and outlook

Besides those talked about above, other biomechanical properties in cardiac fibrosis also deserve our attention, like the viscoelastic and anisotropic of the cardiac tissues. Here we have only focused on the elastic enhancement of cardiac fibrosis (increased stiffness) and ignored the changes in viscosity, which adversely affect the understanding of the mechanism of cardiac fibrosis. Noteworthy, for the whole heart, the myocardial tissue is arranged in a spiral shape relative to the ventricular axis, and the forces on cells in different parts of the ventricular wall are anisotropic. The biomechanical behaviors of cardiac tissues at the macroscale are tightly coupled with cellular activities at the microscale, such as cardiac cell perception of external physical signals and subsequent dynamic regulation of cell-ECM interactions downstream of mechanotransduction events (Guo et al., 2022; Zuela-Sopilniak and Lammerding, 2022). Moreover, the connection between the whole cardiac mechanics and the mechanical traits of the fibrotic sites was not mentioned. A comprehensive understanding of the biomechanical features of cardiac fibrosis requires a rigorous and broad perspective on biomechanics and fibrosis. Future research should detail the biomechanical traits of cardiac fibrosis (Park et al., 2022), and more in-depth studies and explorations are needed.

Despite the remarkable progress so far, the comprehensive mechano-regulatory mechanisms of cardiac fibrosis remain elusive, which creates a great need to study cardiac fibrosis further. And finding effective anti-fibrosis therapy will make a significant contribution to the treatment of cardiac fibrosis as well as countless other fibrotic diseases. Because the cardiovascular system is constantly subjected to mechanical forces, increasing researchers have been taking the impact of changes in cardiac biomechanics on cardiac fibrosis seriously (Lyon et al., 2015). Cardiac fibrosis models *in vitro* simulating the process of fibrosis have been a crucial support for the study of effective anti-fibrosis therapy (Deddens et al., 2017), simulating these biomechanical traits *in vitro* may help to explore specific drugs for treating fibrosis. For example, Zhao et al. (2014) fabricated patterned hydrogels using photolithography to simulate the different stiffness of the ECM and the characteristics of matrix architecture, which can be used to test the anti-fibrotic efficacy of candidate drugs and has potential in the study of fibrosis pathology. Rogers et al. (2019) incorporated cardiomyocytes and fibroblasts into a fibrin gel to construct a 3D tissue in a cardiac tissue chip (which undergoes cycles of stretch, pressure, ejection, and relaxation similar to those observed during the cardiac cycle), to explore new drugs to treat cardiac fibrosis. Some investigators simultaneously controlled a variety of complex factors such as chemical cues, mechanical force stimulation, and biological fluids, thereby simulating the structure and functional characteristics of cardiac tissues. Many current models have been able to revolutionize biomedical applications by better mimicking natural tissues (Duval et al., 2017; Rodríguez-Cabello et al., 2022). With these efficient and simulated biomechanical models, these *in vitro* models have broad prospects in studying the physiological and pathological mechanisms of cardiac fibrosis, as well as screening pro-fibrotic and anti-fibrotic drugs. Maybe we can have deeper research on the physiology and pathology of cardiac fibrosis and other diseases in the human body in the future.

Understanding the origin and consequences of the biomechanical characteristics of cardiac fibrosis is a key principle that is critical to improving treatment. Many of the concepts involved are non-intuitive and require a deep and broad understanding of the characteristics and biomechanics of fibrosis. In conclusion, the complexity of biomechanics in the cardiac fibrosis microenvironments requires further exploration

using groundbreaking technologies for the exquisite recapitulation of mechanical crosstalk during fibrosis progression and prediction. We believe understanding these dynamic and static biomechanical traits should pave the way for effective anti-fibrosis strategies for clinical therapy.

Author contributions

All authors listed have made a substantial, direct, and intellectual contribution to the work and approved it for publication.

Funding

This work was financially supported by the National Natural Science Foundation of China (No.11902245 and 11872298), China Postdoctoral Science Foundation (No. 2021M690938), China Postdoctoral Science Foundation Special Funded Project (No. 2022T150197), Henan Province Key R&D and Promotion Special (Scientific and Technical) Project (No. 222102310183), Joint Fund for Regional Innovation and Development of the National Natural Science Foundation of China (key project) (No. U21A20337).

Conflict of interest

The authors declare that the research was conducted in the absence of any commercial or financial relationships that could be construed as a potential conflict of interest.

Publisher's note

References

Al-U'datt, DaG. F., Tranchant, C. C., Al-Dwairi, A., Alqudah, M., Al-Shboul, O., Hiram, R., et al. (2022). Implications of enigmatic transglutaminase 2 (TG2) in cardiac diseases and therapeutic developments. *Biochem. Pharmacol.* 201, 115104. doi:10.1016/j.bcp.2022.115104

Alexanian, M., Przytycki, P. F., Micheletti, R., Padmanabhan, A., Ye, L., Travers, J. G., et al. (2021). A transcriptional switch governs fibroblast activation in heart disease. *NATURE* 595 (7867), 438–443. doi:10.1038/s41586-021-03674-1

Alsamman, S., Christenson, S. A., Yu, A., Ayad, N. M. E., Mooring, M. S., Segal, J. M., et al. (2020). Targeting acid ceramidase inhibits YAP/TAZ signaling to reduce fibrosis in mice. *Sci. Transl. Med.* 12 (557), eaay8798. doi:10.1126/scitranslmed.aay8798

Andenæs, K., Lunde, I. G., Mohammadzadeh, N., Dahl, C. P., Aronsen, J. M., Strand, M. E., et al. (2018). The extracellular matrix proteoglycan fibromodulin is upregulated in clinical and experimental heart failure and affects cardiac remodeling. *PLoS One* 13 (7), e0201422. doi:10.1371/journal.pone.0201422

Ashworth, J. C., Thompson, J. L., James, J. R., Slater, C. E., Pijuan-Galito, S., Lis-Slimak, K., et al. (2020). Peptide gels of fully-defined composition and mechanics for probing cell-cell and cell-matrix interactions *in vitro*. *Matrix Biol.* 85-86, 15–33. doi:10.1016/j.matbio.2019.06.009

Balachandran, K., Alford, P. W., Wylie-Sears, J., Goss, J. A., Grosberg, A., Bischoff, J., et al. (2011). Cyclic strain induces dual-mode endothelial-mesenchymal transformation of the cardiac valve. *Proc. Natl. Acad. Sci. U. S. A.* 108 (50), 19943–19948. doi:10.1073/pnas.1106954108

Baratchi, S., Knoerzer, M., Khoshmanesh, K., Mitchell, A., and McIntyre, P. (2017). Shear stress regulates TRPV4 channel clustering and translocation from adherens junctions to the basal membrane. *Sci. Rep.* 7 (1), 15942. doi:10.1038/s41598-017-16276-7

Baratchi, S., Zaldivia, M. T. K., Wallert, M., Loseff-Silver, J., Al-Aryahi, S., Zamani, J., et al. (2020). Transcatheter aortic valve implantation represents an anti-inflammatory therapy via reduction of shear stress-induced, piezo-1-mediated monocyte activation. *CIRCULATION* 142 (11), 1092–1105. doi:10.1161/circulationaha.120.045536

Bein, A., Shin, W., Jalili-Firoozinezhad, S., Park, M. H., Sontheimer-Phelps, A., Tovaglieri, A., et al. (2018). Microfluidic organ-on-a-chip models of human intestine. *Cell. Mol. Gastroenterol. Hepatol.* 5 (4), 659–668. doi:10.1016/j.jcmgh.2017.12.010

Berry, M. F., Engler, A. J., Woo, Y. J., Pirolli, T. J., Bish, L. T., Jayasankar, V., et al. (2006). Mesenchymal stem cell injection after myocardial infarction improves myocardial compliance. *Am. J. Physiology-Heart Circulatory Physiology* 290 (6), H2196–H2203. doi:10.1152/ajpheart.01017.2005

Bhattacharjee, T., and Datta, S. S. (2019). Bacterial hopping and trapping in porous media. *Nat. Commun.* 10 (1), 2075–2079. doi:10.1038/s41467-019-10115-1

Boyle, P. M., Del Alamo, J. C., and Akoum, N. (2021). Fibrosis, atrial fibrillation and stroke: Clinical updates and emerging mechanistic models. *HEART* 107 (2), 99–105. doi:10.1136/heartjnl-2020-317455

Cai, W., Zhong, S., Zheng, F., Zhang, Y., Gao, F., Xu, H., et al. (2019). Angiotensin II confers resistance to apoptosis in cardiac myofibroblasts through the AT1/ERK1/2/RSK1 pathway. *IUBMB LIFE* 71 (2), 261–276. doi:10.1002/iub.1967

Caporizzo, M. A., and Prosser, B. L. (2022). The microtubule cytoskeleton in cardiac mechanics and heart failure. *Nat. Rev. Cardiol.* 19 (6), 364–378. doi:10.1038/s41569-022-00692-y

Chaudhuri, O., Gu, L., Klumpers, D., Darnell, M., Bencherif, S. A., Weaver, J. C., et al. (2016). Hydrogels with tunable stress relaxation regulate stem cell fate and activity. *Nat. Mat.* 15 (3), 326–334. doi:10.1038/nmat4489

Chen, Y., Wang, L., Huang, S., Ke, J., Wang, Q., Zhou, Z., et al. (2021). Lutein attenuates angiotensin II- induced cardiac remodeling by inhibiting AP-1/IL-11 signaling. *Redox Biol.* 44, 102020. doi:10.1016/j.redox.2021.102020

Chester, D., Kathard, R., Nortey, J., Nellenbach, K., and Brown, A. C. (2018). Viscoelastic properties of microgel thin films control fibroblast modes of migration and pro-fibrotic responses. *BIOMATERIALS* 185, 371–382. doi:10.1016/j.biomaterials.2018.09.012

Chowdhury, F., Huang, B., and Wang, N. (2021). Cytoskeletal prestress: The cellular hallmark in mechanobiology and mechanomedicine. *Cytoskeleton* 78 (6), 249–276. doi:10.1002/cm.21658

Cirka, H., Monterosso, M., Diamantides, N., Favreau, J., Wen, Q., and Billiar, K. (2016). Active traction force response to long-term cyclic stretch is dependent on cell pre-stress. *Biophys. J.* 110 (8), 1845–1857. doi:10.1016/j.bpj.2016.02.036

Cowling, R. T., Kupsky, D., Kahn, A. M., Daniels, L. B., and Greenberg, B. H. (2019). Mechanisms of cardiac collagen deposition in experimental models and human disease. *Transl. Res.* 209, 138–155. doi:10.1016/j.trsl.2019.03.004

Cui, Y., Hameed, F. M., Yang, B., Lee, K., Pan, C. Q., Park, S., et al. (2015). Cyclic stretching of soft substrates induces spreading and growth. *Nat. Commun.* 6, 6333. doi:10.1038/ncomms7333

D'Urso, M., and Kurniawan, N. A. (2020). Mechanical and physical regulation of fibroblast-myofibroblast transition: From cellular mechanoresponse to tissue pathology. *Front. Bioeng. Biotechnol.* 8, 609653. doi:10.3389/fbioe.2020.609653

Davidson, C. D., Jayco, D. K. P., Matera, D. L., DePalma, S. J., Hiraki, H. L., Wang, W. Y., et al. (2020). Myofibroblast activation in synthetic fibrous matrices composed of dextran vinyl sulfone. *Acta Biomater.* 105, 78–86. doi:10.1016/j.actbio.2020.01.009

Davis, J., and Molkentin, J. D. (2014). Myofibroblasts: Trust your heart and let fate decide. *J. Mol. Cell. Cardiol.* 70, 9–18. doi:10.1016/j.yjmcc.2013.10.019

de Jong, S., van Veen, T. A. B., de Bakker, J. M. T., Vos, M. A., and van Rijen, H. V. M. (2011). Biomarkers of myocardial fibrosis. *J. Cardiovasc. Pharmacol.* 57 (5), 522–535. doi:10.1097/fjc.0b013e31821823d9

Deddens, J. C., Sadeghi, A. H., Hjortnaes, J., van Laake, L. W., Buijsrogge, M., Doevendans, P. A., et al. (2017). Modeling the human scarred heart *in vitro*: Toward new tissue engineered models. *Adv. Healthc. Mat.* 6 (3), 1600571. doi:10.1002/adhm.201600571

Diseases, G. B. D., and Injuries, C. (2020). Global burden of 369 diseases and injuries in 204 countries and territories, 1990-2019: A systematic analysis for the global burden of disease study 2019. *LANCET* 396 (10258), 1204–1222. doi:10.1016/S0140-6736(20)30925-9

Dooling, L. J., Saini, K., Anlas, A. A., and Discher, D. E. (2022). Tissue mechanics coevolves with fibrillar matrisomes in healthy and fibrotic tissues. *Matrix Biol.* 111, 153–188. doi:10.1016/j.matbio.2022.06.006

Dooling, L. J., Saini, K., Anlaş, A. A., and Discher, D. E. (2022). Tissue mechanics coevolves with fibrillar matrisomes in healthy and fibrotic tissues. *MATRIX Biol.* 111, 153–188. doi:10.1016/j.matbio.2022.06.006

Dridi, H., Kushnir, A., Zalk, R., Yuan, Q., Melville, Z., and Marks, A. R. (2020). Intracellular calcium leak in heart failure and atrial fibrillation: A unifying mechanism and therapeutic target. *Nat. Rev. Cardiol.* 17 (11), 732–747. doi:10.1038/s41569-020-0394-8

Duan, B., Hockaday, L. A., Kapetanovic, E., Kang, K. H., and Butcher, J. T. (2013). Stiffness and adhesivity control aortic valve interstitial cell behavior within hyaluronic acid based hydrogels. *Acta Biomater.* 9 (8), 7640–7650. doi:10.1016/j.actbio.2013.04.050

Duval, K., Grover, H., Han, L. H., Mou, Y., Pegoraro, A. F., Fredberg, J., et al. (2017). Modeling physiological events in 2D vs. 3D cell culture. *Physiol. (Bethesda)* 32 (4), 266–277. doi:10.1152/physiol.00036.2016

El Hajj, E. C., El Hajj, M. C., Ninh, V. K., and Gardner, J. D. (2018). Inhibitor of lysyl oxidase improves cardiac function and the collagen/MMP profile in response to volume overload. *Am. J. Physiology-Heart Circulatory Physiology* 315 (3), H463–H473. doi:10.1152/ajpheart.00086.2018

Feng, J., Wang, F., Han, X., Ao, Z., Sun, Q., Hua, W., et al. (2014). A "green pathway" different from simple diffusion in soft matter: Fast molecular transport within micro/nanoscale multiphase porous systems. *Nano Res.* 7 (3), 434–442. doi:10.1007/s12274-014-0409-z

Frangogiannis, N. G. (2021). Cardiac fibrosis. *Cardiovasc. Res.* 117 (6), 1450–1488. doi:10.1093/cvr/cvaa324

Frangogiannis, N. G. (2019). Cardiac fibrosis: Cell biological mechanisms, molecular pathways and therapeutic opportunities. *Mol. Asp. Med.* 65, 70–99. doi:10.1016/j.mam.2018.07.001

Frangogiannis, N. G. (2019). The extracellular matrix in ischemic and nonischemic heart failure. *Circ. Res.* 125 (1), 117–146. doi:10.1161/circresaha.119.311148

Frangogiannis, N. G. J. C. R. (2017). Fibroblasts and the extracellular matrix in right ventricular disease. *Cardiovasc Res.* 113 (12), 12. doi:10.1093/cvr/cvx146

Freeberg, M. A. T., Perelas, A., Rebman, J. K., Phipps, R. P., Thatcher, T. H., and Sime, P. J. (2021). Mechanical feed-forward loops contribute to idiopathic pulmonary fibrosis. *Am. J. Pathol.* 191 (1), 18–25. doi:10.1016/j.ajpath.2020.09.008

Fukui, H., Chow, R. W., Xie, J., Foo, Y. Y., Yap, C. H., Minc, N., et al. (2021). Bioelectric signaling and the control of cardiac cell identity in response to mechanical forces. *SCIENCE* 374 (6565), 351–354. doi:10.1126/science.abc6229

Garoffolo, G., and Pesce, M. (2019). Mechanotransduction in the cardiovascular system: From developmental origins to homeostasis and pathology. *Cells* 8 (12), 1607. doi:10.3390/cells8121607

González, A., López, B., Ravassa, S., San José, G., and Díez, J. (2019). The complex dynamics of myocardial interstitial fibrosis in heart failure. Focus on collagen cross-linking. *Biochimica Biophysica Acta - Mol. Cell Res.* 1866 (9), 1421–1432. doi:10.1016/j.bbamcr.2019.06.001

Gourdie, R. G., Dimmeler, S., and Kohl, P. (2016). Novel therapeutic strategies targeting fibroblasts and fibrosis in heart disease. *Nat. Rev. Drug Discov.* 15 (9), 620–638. doi:10.1038/nrd.2016.89

Grosberg, A., Alford, P. W., McCain, M. L., and Parker, K. K. (2011). Ensembles of engineered cardiac tissues for physiological and pharmacological study: Heart on a chip. *Lab. Chip* 11 (24), 4165–4173. doi:10.1039/c1lc20557a

Guimaraes, C. F., Gasperini, L., Marques, A. P., and Reis, R. L. (2020). The stiffness of living tissues and its implications for tissue engineering. *Nat. Rev. Mat.* 5 (5), 351–370. doi:10.1038/s41578-019-0169-1

Guo, Y., Calve, S., and Tepole, A. B. (2022). Multiscale mechanobiology: Coupling models of adhesion kinetics and nonlinear tissue mechanics. *BIOPHYSICAL J.* 121 (4), 525–539. doi:10.1016/j.bpj.2022.01.012

Hadjicharalambous, M., Stoeck, C. T., Weisskopf, M., Cesarovic, N., Ioannou, E., Vavourakis, V., et al. (2021). Investigating the reference domain influence in personalised models of cardiac mechanics : Effect of unloaded geometry on cardiac biomechanics. *Biomech. Model. Mechanobiol.* 20 (4), 1579–1597. doi:10.1007/s10237-021-01464-2

Halade, G. V., and Lee, D. H. (2022). Inflammation and resolution signaling in cardiac repair and heart failure. *EBioMedicine* 79, 103992. doi:10.1016/j.ebiom.2022.103992

Hanna, A., Humeres, C., and Frangogiannis, N. G. (2021). The role of Smad signaling cascades in cardiac fibrosis. *Cell. Signal.* 77, 109826. doi:10.1016/j.cellsig.2020.109826

He, C., Wei, X., Liang, T., Liu, M., Jiang, D., Zhuang, L., et al. (2021). Quantifying the compressive force of 3D cardiac tissues via calculating the volumetric deformation of built-in elastic gelatin microspheres. *Adv. Healthc. Mat.* 10 (16), e2001716. doi:10.1002/adhm.202001716

Henderson, N. C., Rieder, F., and Wynn, T. A. (2020). Fibrosis: From mechanisms to medicines. *NATURE* 587 (7835), 555–566. doi:10.1038/s41586-020-2938-9

Hill, M. A., Jaisser, F., and Sowers, J. R. (2022). Role of the vascular endothelial sodium channel activation in the Genesis of pathologically increased cardiovascular stiffness. *Cardiovasc. Res.* 118 (1), 130–140. doi:10.1093/cvr/cvaa326

Hinz, B., McCulloch, C. A., and Coelho, N. M. (2019). Mechanical regulation of myofibroblast phenoconversion and collagen contraction. *Exp. Cell Res.* 379 (1), 119–128. doi:10.1016/j.yexcr.2019.03.027

Huang, G., Li, F., Zhao, X., Ma, Y., Li, Y., Lin, M., et al. (2017). Functional and biomimetic materials for engineering of the three-dimensional cell microenvironment. *Chem. Rev.* 117 (20), 12764–12850. doi:10.1021/acs.chemrev.7b00094

Huyer, L. D., Montgomery, M., Zhao, Y., Xiao, Y., Conant, G., Korolj, A., et al. (2015). Biomaterial based cardiac tissue engineering and its applications. *Biomed. Mat.* 10 (3), 034004. doi:10.1088/1748-6041/10/3/034004

Islam, S., Boström, K. I., Di Carlo, D., Simmons, C. A., Tintut, Y., Yao, Y., et al. (2021). The mechanobiology of endothelial-to-mesenchymal transition in cardiovascular disease. *Front. Physiol.* 12, 734215. doi:10.3389/fphys.2021.734215

Jana, S., Aujla, P., Hu, M., Kilic, T., Zhabyeyev, P., McCulloch, C. A., et al. (2021). Gelsolin is an important mediator of Angiotensin II-induced activation of cardiac fibroblasts and fibrosis. *FASEB J.* 35 (10), e21932. doi:10.1096/fj.202100038rr

Jang, J., Park, H. J., Kim, S. W., Kim, H., Park, J. Y., Na, S. J., et al. (2017). 3D printed complex tissue construct using stem cell-laden decellularized extracellular matrix bioinks for cardiac repair. *BIOMATERIALS* 112, 264–274. doi:10.1016/j.biomaterials.2016.10.026

Ji, C., and McCulloch, C. A. (2021). TRPV4 integrates matrix mechanosensing with Ca(2+) signaling to regulate extracellular matrix remodeling. *FEBS J.* 288 (20), 5867–5887. doi:10.1111/febs.15665

Jia, Y., Wang, Y., Niu, L., Zhang, H., Tian, J., Gao, D., et al. (2021). The plasticity of nanofibrous matrix regulates fibroblast activation in fibrosis. *Adv. Healthc. Mat.* 10 (8), e2001856. doi:10.1002/adhm.202001856

Johnson, L. A., Rodansky, E. S., Haak, A. J., Larsen, S. D., Neubig, R. R., and Higgins, P. D. (2014). Novel Rho/MRTF/SRF inhibitors block matrix-stiffness and TGF-beta-induced fibrogenesis in human colonic myofibroblasts. *Inflamm. Bowel Dis.* 20 (1), 154–165. doi:10.1097/01.mib.0000437615.98881.31

Jong, W. M., Ten Cate, H., Linnenbank, A. C., de Boer, O. J., Reitsma, P. H., de Winter, R. J., et al. (2016). Reduced acute myocardial ischemia-reperfusion injury in IL-6-deficient mice employing a closed-chest model. *Inflamm. Res.* 65 (6), 489–499. doi:10.1007/s00011-016-0931-4

Kalamajski, S., Bihan, D., Bonna, A., Rubin, K., and Farndale, R. W. (2016). Fibromodulin interacts with collagen cross-linking sites and activates lysyl oxidase. *J. Biol. Chem.* 291 (15), 7951–7960. doi:10.1074/jbc.m115.693408

Kalson, N. S., Lu, Y., Taylor, S. H., Starborg, T., Holmes, D. F., and Kadler, K. E. (2015). A structure-based extracellular matrix expansion mechanism of fibrous tissue growth. *eLife* 4. doi:10.7554/elife.05958

Kalukula, Y., Stephens, A. D., Lammerding, J., and Gabriele, S. (2022). Mechanics and functional consequences of nuclear deformations. *Nat. Rev. Mol. Cell Biol.* 23, 583–602. doi:10.1038/s41580-022-00480-z

Kechagia, J. Z., Ivaska, J., and Roca-Cusachs, P. (2019). Integrins as biomechanical sensors of the microenvironment. *Nat. Rev. Mol. Cell Biol.* 20 (8), 457–473. doi:10.1038/s41580-019-0134-2

Kisling, A., Lust, R. M., and Katwa, L. C. (2019). What is the role of peptide fragments of collagen I and IV in health and disease? *LIFE Sci.* 228, 30–34. doi:10.1016/j.lfs.2019.04.042

Kleyman, T. R., Kashlan, O. B., and Hughey, R. P. (2018). Epithelial Na^+ channel regulation by extracellular and intracellular factors. *Annu. Rev. Physiol.* 80, 263–281. doi:10.1146/annurev-physiol-021317-121143

Kong, M., Lee, J., Yazdi, I. K., Miri, A. K., Lin, Y. D., Seo, J., et al. (2019). Cardiac fibrotic remodeling on a chip with dynamic mechanical stimulation. *Adv. Healthc. Mat.* 8 (3), e1801146. doi:10.1002/adhm.201801146

Kong, P., Christia, P., and Frangogiannis, N. G. (2014). The pathogenesis of cardiac fibrosis. *Cell. Mol. Life Sci.* 71 (4), 549–574. doi:10.1007/s00018-013-1349-6

Kong, W., Lyu, C., Liao, H., and Du, Y. (2021). Collagen crosslinking: Effect on structure, mechanics and fibrosis progression. *Biomed. Mat.* 16 (6), 062005. doi:10.1088/1748-605x/ac2b79

Kotini, M. P., van der Stoel, M. M., Yin, J., Han, M. K., Kirchmaier, B., de Rooij, J., et al. (2022). Vinculin controls endothelial cell junction dynamics during vascular lumen formation. *Cell Rep.* 39 (2), 110658. doi:10.1016/j.celrep.2022.110658

Kouzbari, K., Hossan, M. R., Arrizabalaga, J. H., Varshney, R., Simmons, A. D., Gostynska, S., et al. (2019). Oscillatory shear potentiates latent TGF-β1 activation more than steady shear as demonstrated by a novel force generator. *Sci. Rep.* 9 (1), 6065. doi:10.1038/s41598-019-42302-x

Kreuger, J., and Phillipson, M. (2016). Targeting vascular and leukocyte communication in angiogenesis, inflammation and fibrosis. *Nat. Rev. Drug Discov.* 15 (2), 125–142. doi:10.1038/nrd.2015.2

Kuehlmann, B., Bonham, C. A., Zucal, I., Prantl, L., and Gurtner, G. C. (2020). Mechanotransduction in wound healing and fibrosis. *J. Clin. Med.* 9 (5), 1423. doi:10.3390/jcm9051423

Lai, A., Chen, Y. C., Cox, C. D., Jaworowski, A., Peter, K., and Baratchi, S. (2021). Analyzing the shear-induced sensitization of mechanosensitive ion channel Piezo-1 in human aortic endothelial cells. *J. Cell. Physiol.* 236 (4), 2976–2987. doi:10.1002/jcp.30056

Lang, J., Li, Y., Ye, Z., Yang, Y., Xu, F., Huang, G., et al. (2021). Investigating the effect of substrate stiffness on the redox state of cardiac fibroblasts using scanning electrochemical microscopy. *Anal. Chem.* 93 (14), 5797–5804. doi:10.1021/acs.analchem.0c05284

Lauriol, J., Keith, K., Jaffré, F., Couvillon, A., Saci, A., Goonasekera, S. A., et al. (2014). RhoA signaling in cardiomyocytes protects against stress-induced heart failure but facilitates cardiac fibrosis. *Sci. Signal.* 7 (348), ra100. doi:10.1126/scisignal.2005262

Leask, A., and Abraham, D. J. (2004). TGF-beta signaling and the fibrotic response. *FASEB J.* 18 (7), 816–827. doi:10.1096/fj.03-1273rev

Lemaitre, A. I., Picard, F., Maurin, V., Faure, M., Dos Santos, P., and Girerd, N. (2021). Clinical profile and midterm prognosis of left ventricular thrombus in heart failure. *Esc. Heart Fail.* 8 (2), 1333–1341. doi:10.1002/ehf2.13211

Levine, D. J., Turner, K. T., and Pikul, J. H. (2021). Materials with electroprogrammable stiffness. *Adv. Mat.* 33 (35), e2007952. doi:10.1002/adma.202007952

Liao, J., Lu, W., Chen, Y., Duan, X., Zhang, C., Luo, X., et al. (2021). Upregulation of Piezo1 (piezo type mechanosensitive ion channel component 1) enhances the intracellular free calcium in pulmonary arterial smooth muscle cells from idiopathic pulmonary arterial hypertension patients. *HYPERTENSION* 77 (6), 1974–1989. doi:10.1161/hypertensionaha.120.16629

Lisy, O., Redfield, M. M., Jovanovic, S., Jougasaki, M., Jovanovic, A., Leskinen, H., et al. (2000). Mechanical unloading versus neurohumoral stimulation on myocardial structure and endocrine function *in vivo*. *CIRCULATION* 102 (3), 338–343. doi:10.1161/01.cir.102.3.338

Liu, H., Wu, M., Jia, Y. B., Niu, L. L., Huang, G. Y., and Xu, F. (2020). Control of fibroblast shape in sequentially formed 3D hybrid hydrogels regulates cellular responses to microenvironmental cues. *NPG Asia Mat.* 12 (1), 45. doi:10.1038/s41427-020-0226-7

Liu, W., Wang, X., Mei, Z., Gong, J., Huang, L., Gao, X., et al. (2017). BNIP3L promotes cardiac fibrosis in cardiac fibroblasts through [Ca2+]i-TGF-β-Smad2/3 pathway. *Sci. Rep.* 7 (1), 1906. doi:10.1038/s41598-017-01936-5

Liu, W. T., Cao, Y. P., Zhou, X. H., and Han, D. (2022). Interstitial fluid behavior and diseases. *Adv. Sci.* 9 (6), 2100617. doi:10.1002/advs.202100617

Long, Y., Niu, Y., Liang, K., and Du, Y. (2022). Mechanical communication in fibrosis progression. *Trends Cell Biol.* 32 (1), 70–90. doi:10.1016/j.tcb.2021.10.002

Lopez-Bellido, R., Puig, S., Huang, P. J., Tsai, C. R., Turner, H. N., Galko, M. J., et al. (2019). Growth factor signaling regulates mechanical nociception in flies and vertebrates. *J. Neurosci.* 39 (30), 6012–6030. doi:10.1523/jneurosci.2950-18.2019

Lorin, C., Vogeli, I., and Niggli, E. (2015). Dystrophic cardiomyopathy: Role of TRPV2 channels in stretch-induced cell damage. *Cardiovasc. Res.* 106 (1), 153–162. doi:10.1093/cvr/cvv021

Lyon, R. C., Zanella, F., Omens, J. H., and Sheikh, F. (2015). Mechanotransduction in cardiac hypertrophy and failure. *Circ. Res.* 116 (8), 1462–1476. doi:10.1161/circresaha.116.304937

Ma, H., Killaars, A. R., DelRio, F. W., Yang, C., and Anseth, K. S. (2017). Myofibroblastic activation of valvular interstitial cells is modulated by spatial variations in matrix elasticity and its organization. *BIOMATERIALS* 131, 131–144. doi:10.1016/j.biomaterials.2017.03.040

Ma, Z. G., Yuan, Y. P., Wu, H. M., Zhang, X., and Tang, Q. Z. (2018). Cardiac fibrosis: New insights into the pathogenesis. *Int. J. Biol. Sci.* 14 (12), 1645–1657. doi:10.7150/ijbs.28103

Mainardi, A., Carminati, F., Ugolini, G. S., Occhetta, P., Isu, G., Robles Diaz, D., et al. (2021). A dynamic microscale mid-throughput fibrosis model to investigate the effects of different ratios of cardiomyocytes and fibroblasts. *Lab. Chip* 21 (21), 4177–4195. doi:10.1039/d1lc00092f

Maji, S., and Lee, H. (2022). Engineering hydrogels for the development of three-dimensional *in vitro* models. *Int. J. Mol. Sci.* 23 (5), 2662. doi:10.3390/ijms23052662

Marsano, A., Conficconi, C., Lemme, M., Occhetta, P., Gaudiello, E., Votta, E., et al. (2016). Beating heart on a chip: A novel microfluidic platform to generate functional 3D cardiac microtissues. *Lab. Chip* 16 (3), 599–610. doi:10.1039/c5lc01356a

Mastikhina, O., Moon, B. U., Williams, K., Hatkar, R., Gustafson, D., Mourad, O., et al. (2020). Human cardiac fibrosis-on-a-chip model recapitulates disease hallmarks and can serve as a platform for drug testing. *BIOMATERIALS* 233, 119741. doi:10.1016/j.biomaterials.2019.119741

Mathiyalagan, P., Adamiak, M., Mayourian, J., Sassi, Y., Liang, Y., Agarwal, N., et al. (2019). FTO-dependent N(6)-methyladenosine regulates cardiac function during remodeling and repair. *CIRCULATION* 139 (4), 518–532. doi:10.1161/circulationaha.118.033794

Maurer, M., and Lammerding, J. (2019). The driving force: Nuclear mechanotransduction in cellular function, fate, and disease. *Annu. Rev. Biomed. Eng.* 21, 443–468. doi:10.1146/annurev-bioeng-060418-052139

Mensah, G. A., Roth, G. A., and Fuster, V. (2019). The global burden of cardiovascular diseases and risk factors: 2020 and beyond. *J. Am. Coll. Cardiol.* 74 (20), 2529–2532. doi:10.1016/j.jacc.2019.10.009

Mia, M. M., Cibi, D. M., Binte Abdul Ghani, S. A., Singh, A., Tee, N., Sivakumar, V., et al. (2021). Loss of Yap/taz in cardiac fibroblasts attenuates adverse remodeling and improves cardiac function. *Cardiovasc Res.*.

Miroshnikova, Y. A., and Wickström, S. A. (2022). Mechanical forces in nuclear organization. *Cold Spring Harb. Perspect. Biol.* 14 (1), a039685. doi:10.1101/cshperspect.a039685

Morley, L. C., Shi, J., Gaunt, H. J., Hyman, A. J., Webster, P. J., Williams, C., et al. (2018). Piezo1 channels are mechanosensors in human fetoplacental endothelial cells. *MHR Basic Sci. reproductive Med.* 24 (10), 510–520. doi:10.1093/molehr/gay033

Mun, G. I., and Boo, Y. C. (2010). Identification of CD44 as a senescence-induced cell adhesion gene responsible for the enhanced monocyte recruitment to senescent endothelial cells. *Am. J. Physiology-Heart Circulatory Physiology* 298 (6), H2102–H2111. doi:10.1152/ajpheart.00835.2009

Neff, L. S., and Bradshaw, A. D. (2021). Cross your heart? Collagen cross-links in cardiac health and disease. *Cell. Signal.* 79, 109889. doi:10.1016/j.cellsig.2020.109889

Niu, L., Cheng, B., Huang, G., Nan, K., Han, S., Ren, H., et al. (2022). A positive mechanobiological feedback loop controls bistable switching of cardiac fibroblast phenotype. *Cell Discov.* 8 (1), 84. doi:10.1038/s41421-022-00427-w

Niu, L., Jia, Y., Wu, M., Liu, H., Feng, Y., Hu, Y., et al. (2020). Matrix stiffness controls cardiac fibroblast activation through regulating YAP via AT1 R. *J. Cell. Physiol.* 235 (11), 8345–8357. doi:10.1002/jcp.29678

Occhetta, P., Isu, G., Lemme, M., Conficconi, C., Oertle, P., Raz, C., et al. (2018). A three-dimensional *in vitro* dynamic micro-tissue model of cardiac scar formation. *Integr. Biol.* 10 (3), 174–183. doi:10.1039/c7ib00199a

Orre, T., Rossier, O., and Giannone, G. (2019). The inner life of integrin adhesion sites: From single molecules to functional macromolecular complexes. *Exp. Cell Res.* 379 (2), 235–244. doi:10.1016/j.yexcr.2019.03.036

Park, H-J., Hong, H., Thangam, R., Song, M-G., Kim, J-E., Jo, E-H., et al. (2022). Static and dynamic biomaterial engineering for cell modulation. *Nanomaterials* 12 (8), 1377. doi:10.3390/nano12081377

Park, S., Nguyen, N. B., Pezhouman, A., and Ardehali, R. (2019). Cardiac fibrosis: Potential therapeutic targets. *Transl. Res.* 209, 121–137. doi:10.1016/j.trsl.2019.03.001

Peyronnet, R., Nerbonne, J. M., and Kohl, P. (2016). Cardiac mechano-gated ion channels and arrhythmias. *Circ. Res.* 118 (2), 311–329. doi:10.1161/circresaha.115.305043

Polyakova, V., Loeffler, I., Hein, S., Miyagawa, S., Piotrowska, I., Dammer, S., et al. (2011). Fibrosis in endstage human heart failure: Severe changes in collagen metabolism and MMP/TIMP profiles. *Int. J. Cardiol.* 151 (1), 18–33. doi:10.1016/j.ijcard.2010.04.053

Portillo-Lara, R., Spencer, A. R., Walker, B. W., Sani, E. S., and Annabi, N. (2019). Biomimetic cardiovascular platforms for *in vitro* disease modeling and therapeutic validation. *BIOMATERIALS* 198, 78–94. doi:10.1016/j.biomaterials.2018.08.010

Priya, R., Allanki, S., Gentile, A., Mansingh, S., Uribe, V., Maischein, H. M., et al. (2020). Tension heterogeneity directs form and fate to pattern the myocardial wall. *NATURE* 588 (7836), 130–134. doi:10.1038/s41586-020-2946-9

Qian, J., Liu, H., Lin, Y., Chen, W., and Gao, H. (2013). A mechanochemical model of cell reorientation on substrates under cyclic stretch. *PLoS One* 8 (6), e65864. doi:10.1371/journal.pone.0065864

Richardson, W. J., Clarke, S. A., Quinn, T. A., and Holmes, J. W. (2015). Physiological implications of myocardial scar structure. *Compr. Physiol.* 5 (4), 1877–1909. doi:10.1002/cphy.c140067

Riley, L. A., and Merryman, W. D. (2021). Cadherin-11 and cardiac fibrosis: A common target for a common pathology. *Cell. Signal.* 78, 109876. doi:10.1016/j.cellsig.2020.109876

Rodríguez-Cabello, J. C., Escalera☆, S., Juanes-Gusano☆, D., Santos, M., and Girotti, A. (2022). Designing elastin-like recombinamers for therapeutic and regenerative purposes. *Multifunct. Hydrogels Biomed. Appl.*, 37–62. doi:10.1002/9783527825820.ch3

Rogers, A. J., Miller, J. M., Kannappan, R., and Sethu, P. (2019). Cardiac tissue chips (CTCs) for modeling cardiovascular disease. *IEEE Trans. Biomed. Eng.* 66 (12), 3436–3443. doi:10.1109/tbme.2019.2905763

Sadeghi, A. H., Shin, S. R., Deddens, J. C., Fratta, G., Mandla, S., Yazdi, I. K., et al. (2017). Engineered 3D cardiac fibrotic tissue to study fibrotic remodeling. *Adv. Healthc. Mat.* 6 (11), 1601434. doi:10.1002/adhm.201601434

Sandbo, N., Smolyaninova, L. V., Orlov, S. N., and Dulin, N. O. (2016). Control of myofibroblast differentiation and function by cytoskeletal signaling. *Biochem. Mosc.* 81 (13), 1698–1708. doi:10.1134/s0006297916130071

Saucerman, J. J., Tan, P. M., Buchholz, K. S., McCulloch, A. D., and Omens, J. H. (2019). Mechanical regulation of gene expression in cardiac myocytes and fibroblasts. *Nat. Rev. Cardiol.* 16 (6), 361–378. doi:10.1038/s41569-019-0155-8

Savoji, H., Mohammadi, M. H., Rafatian, N., Toroghi, M. K., Wang, E. Y., Zhao, Y., et al. (2019). Cardiovascular disease models: A game changing paradigm in drug discovery and screening. *BIOMATERIALS* 198, 3–26. doi:10.1016/j.biomaterials.2018.09.036

Schafer, S., Viswanathan, S., Widjaja, A. A., Lim, W. W., Moreno-Moral, A., DeLaughter, D. M., et al. (2017). IL-11 is a crucial determinant of cardiovascular fibrosis. *NATURE* 552 (7683), 110–115. doi:10.1038/nature24676

Schorb, W., Booz, G. W., Dostal, D. E., Conrad, K. M., Chang, K. C., and Baker, K. M. (1993). Angiotensin II is mitogenic in neonatal rat cardiac fibroblasts. *Circ. Res.* 72 (6), 1245–1254. doi:10.1161/01.res.72.6.1245

Schwan, J., Kwaczala, A. T., Ryan, T. J., Bartulos, O., Ren, Y., Sewanan, L. R., et al. (2016). Anisotropic engineered heart tissue made from laser-cut decellularized myocardium. *Sci. Rep.* 6, 32068. doi:10.1038/srep32068

Seo, B. R., Chen, X., Ling, L., Song, Y. H., Shimpi, A. A., Choi, S., et al. (2020). Collagen microarchitecture mechanically controls myofibroblast differentiation. *Proc. Natl. Acad. Sci. U. S. A.* 117 (21), 11387–11398. doi:10.1073/pnas.1919394117

Seo, B. R., Chen, X. Y., Ling, L., Song, Y. H., Shimpi, A. A., Choi, S. Y., et al. (2020). Collagen microarchitecture mechanically controls myofibroblast differentiation. *Proc. Natl. Acad. Sci. U. S. A.* 117 (21), 11387–11398. doi:10.1073/pnas.1919394117

Soon, K., Mourad, O., and Nunes, S. S. (2021). Engineered human cardiac microtissues: The state-of-the-(he)art. *STEM CELLS* 39 (8), 1008–1016. doi:10.1002/stem.3376

Stewart, L., and Turner, N. A. (2021). Channelling the force to reprogram the matrix: Mechanosensitive ion channels in cardiac fibroblasts. *Cells* 10 (5), 990. doi:10.3390/cells10050990

Stewart, L., and Turner, N. A. (2021). Channelling the force to reprogram the matrix: Mechanosensitive ion channels in cardiac fibroblasts. *Cells* 10 (5), 990. doi:10.3390/cells10050990

Stine, C. (2022). *Interstitial fluid flow magnitude and its effects on glioblastoma invasion*. Blacksburg, Commonwealth of Virginia: Virginia Tech.

Terrar, D. A. (2020). Calcium signaling in the heart. *Adv. Exp. Med. Biol.* 1131, 395–443. doi:10.1007/978-3-030-12457-1_16

Ugolini, G. S., Visone, R., Cruz-Moreira, D., Mainardi, A., and Rasponi, M. (2018). Generation of functional cardiac microtissues in a beating heart-on-a-chip. *Methods Cell Biol.* 146, 69–84. doi:10.1016/bs.mcb.2018.05.005

Urbanczyk, M., Layland, S. L., and Schenke-Layland, K. (2020). The role of extracellular matrix in biomechanics and its impact on bioengineering of cells and 3D tissues. *MATRIX Biol.* 85, 1–14. doi:10.1016/j.matbio.2019.11.005

Van den Bergh, G., Opdebeeck, B., D'Haese, P. C., and Verhulst, A. (2019). The vicious cycle of arterial stiffness and arterial media calcification. *Trends Mol. Med.* 25 (12), 1133–1146. doi:10.1016/j.molmed.2019.08.006

van Spreeuwel, A. C. C., Bax, N. A. M., van Nierop, B. J., Aartsma-Rus, A., Goumans, M. T. H., and Bouten, C. V. C. (2017). Mimicking cardiac fibrosis in a dish: Fibroblast density rather than collagen density weakens cardiomyocyte function. *J. Cardiovasc. Transl. Res.* 10 (2), 116–127. doi:10.1007/s12265-017-9737-1

Veldhuizen, J., Cutts, J., Brafman, D. A., Migrino, R. Q., and Nikkhah, M. (2020). Engineering anisotropic human stem cell-derived three-dimensional cardiac tissue on-a-chip. *BIOMATERIALS* 256, 120195. doi:10.1016/j.biomaterials.2020.120195

Villalobos Lizardi, J. C., Baranger, J., Nguyen, M. B., Asnacios, A., Malik, A., Lumens, J., et al. (2022). A guide for assessment of myocardial stiffness in health and disease. *Nat. Cardiovasc. Res.* 1 (1), 8–22. doi:10.1038/s44161-021-00007-3

Villar, K. N. B., Liu, X., and Small, E. M. (2022). Transcriptional regulation of cardiac fibroblast phenotypic plasticity. *Curr. Opin. Physiology* 28, 100556. doi:10.1016/j.cophys.2022.100556

Vivar, R., Humeres, C., Ayala, P., Olmedo, I., Catalan, M., Garcia, L., et al. (2013). TGF-β1 prevents simulated ischemia/reperfusion-induced cardiac fibroblast apoptosis by activation of both canonical and non-canonical signaling pathways. *Biochimica Biophysica Acta - Mol. Basis Dis.* 1832 (6), 754–762. doi:10.1016/j.bbadis.2013.02.004

Vivas, A., van den Berg, A., Passier, R., Odijk, M., and van der Meer, A. D. (2022). Fluidic circuit board with modular sensor and valves enables stand-alone, tubeless microfluidic flow control in organs-on-chips. *Lab. Chip* 22 (6), 1231–1243. doi:10.1039/d1lc00999k

Voorhees, A. P., DeLeon-Pennell, K. Y., Ma, Y., Halade, G. V., Yabluchanskiy, A., Iyer, R. P., et al. (2015). Building a better infarct: Modulation of collagen cross-linking to increase infarct stiffness and reduce left ventricular dilation post-myocardial infarction. *J. Mol. Cell. Cardiol.* 85, 229–239. doi:10.1016/j.yjmcc.2015.06.006

Wagh, K., Ishikawa, M., Garcia, D. A., Stavreva, D. A., Upadhyaya, A., and Hager, G. L. (2021). Mechanical regulation of transcription: Recent advances. *Trends Cell Biol.* 31 (6), 457–472. doi:10.1016/j.tcb.2021.02.008

Walker, M., Godin, M., and Pelling, A. E. (2020). Mechanical stretch sustains myofibroblast phenotype and function in microtissues through latent TGF-β1 activation. *Integr. Biol.* 12 (8), 199–210. doi:10.1093/intbio/zyaa015

Wang, C., Qu, K., Wang, J., Qin, R., Li, B., Qiu, J., et al. (2022). Biomechanical regulation of planar cell polarity in endothelial cells. *Biochimica Biophysica Acta - Mol. Basis Dis.* 1868, 166495. doi:10.1016/j.bbadis.2022.166495

Wang, E. Y., Rafatian, N., Zhao, Y., Lee, A., Lai, B. F. L., Lu, R. X., et al. (2019). Biowire model of interstitial and focal cardiac fibrosis. *ACS Cent. Sci.* 5 (7), 1146–1158. doi:10.1021/acscentsci.9b00052

Wang, Z., Lee, S. J., Cheng, H. J., Yoo, J. J., and Atala, A. (2018). 3D bioprinted functional and contractile cardiac tissue constructs. *Acta Biomater.* 70, 48–56. doi:10.1016/j.actbio.2018.02.007

Wipff, P-J., Rifkin, D. B., Meister, J-J., and Hinz, B. (2007). Myofibroblast contraction activates latent TGF-β1 from the extracellular matrix. *J. Cell Biol.* 179 (6), 1311–1323. doi:10.1083/jcb.200704042

Worke, L. J., Barthold, J. E., Seelbinder, B., Novak, T., Main, R. P., Harbin, S. L., et al. (2017). Densification of type I collagen matrices as a model for cardiac fibrosis. *Adv. Healthc. Mat.* 6 (22), 1700114. doi:10.1002/adhm.201700114

Wu, N., Xu, J., Du, W. W., Li, X., Awan, F. M., Li, F., et al. (2021). YAP circular RNA, circYap, attenuates cardiac fibrosis via binding with tropomyosin-4 and gamma-actin decreasing actin polymerization. *Mol. Ther.* 29 (3), 1138–1150. doi:10.1016/j.ymthe.2020.12.004

Yamada, K. M., Doyle, A. D., and Lu, J. (2022). Cell-3D matrix interactions: Recent advances and opportunities. *Trends Cell Biol.* 32, 883–895. doi:10.1016/j.tcb.2022.03.002

Yang, B., Wei, K., Loebel, C., Zhang, K., Feng, Q., Li, R., et al. (2021). Enhanced mechanosensing of cells in synthetic 3D matrix with controlled biophysical dynamics. *Nat. Commun.* 12 (1), 3514. doi:10.1038/s41467-021-23120-0

Yang, J., Savvatis, K., Kang, J. S., Fan, P., Zhong, H., Schwartz, K., et al. (2016). Targeting LOXL2 for cardiac interstitial fibrosis and heart failure treatment. *Nat. Commun.* 7, 13710. doi:10.1038/ncomms13710

Yang, J., Zhang, Y., Qin, M., Cheng, W., Wang, W., and Cao, Y. (2021). Understanding and regulating cell-matrix interactions using hydrogels of designable mechanical properties. *J. Biomed. Nanotechnol.* 17 (2), 149–168. doi:10.1166/jbn.2021.3026

Yang, R., Tan, C., and Najafi, M. (2021). Cardiac inflammation and fibrosis following chemo/radiation therapy: Mechanisms and therapeutic agents. *INFLAMMOPHARMACOLOGY* 30, 73–89. doi:10.1007/s10787-021-00894-9

Yeh, C. R., Bingham, G. C., Shetty, J., Hu, P., and Barker, T. H. (2021). Decellularized extracellular matrix (ECM) as a model to study fibrotic ECM mechanobiology. *Methods Mol. Biol.* 2299, 237–261. doi:10.1007/978-1-0716-1382-5_18

Yeung, C-Y. C., Zeef, L. A. H., Lallyett, C., Lu, Y., Canty-Laird, E. G., and Kadler, K. E. (2015). Chick tendon fibroblast transcriptome and shape depend on whether the cell has made its own collagen matrix. *Sci. Rep.* 5, 13555. doi:10.1038/srep13555

Yong, K. W., Li, Y., Huang, G., Lu, T. J., Safwani, W. K., Pingguan-Murphy, B., et al. (2015). Mechanoregulation of cardiac myofibroblast differentiation: Implications for cardiac fibrosis and therapy. *Am. J. Physiology-Heart Circulatory Physiology* 309 (4), H532–H542. doi:10.1152/ajpheart.00299.2015

Yong, K. W., Li, Y., Liu, F., Gao, B., Lu, T. J., Abas, W., et al. (2016). Paracrine effects of adipose-derived stem cells on matrix stiffness-induced cardiac myofibroblast differentiation via angiotensin II type 1 receptor and Smad7. *Sci. Rep.* 6 (1), 33067–33113. doi:10.1038/srep33067

Yu, F., and Choudhury, D. (2019). Microfluidic bioprinting for organ-on-a-chip models. *Drug Discov. Today* 24 (6), 1248–1257. doi:10.1016/j.drudis.2019.03.025

Yuan, J., Liu, H., Gao, W., Zhang, L., Ye, Y., Yuan, L., et al. (2018). MicroRNA-378 suppresses myocardial fibrosis through a paracrine mechanism at the early stage of cardiac hypertrophy following mechanical stress. *Theranostics* 8 (9), 2565–2582. doi:10.7150/thno.22878

Zarubova, J., Hasani-Sadrabadi, M. M., Ardehali, R., and Li, S. (2022). Immunoengineering strategies to enhance vascularization and tissue regeneration. *Adv. DRUG Deliv. Rev.* 184, 114233. doi:10.1016/j.addr.2022.114233

Zebda, N., Dubrovskyi, O., and Birukov, K. G. (2012). Focal adhesion kinase regulation of mechanotransduction and its impact on endothelial cell functions. *Microvasc. Res.* 83 (1), 71–81. doi:10.1016/j.mvr.2011.06.007

Zhang, W., Lavine, K. J., Epelman, S., Evans, S. A., Weinheimer, C. J., Barger, P. M., et al. (2015). Necrotic myocardial cells release damage-associated molecular patterns that provoke fibroblast activation *in vitro* and trigger myocardial inflammation and fibrosis *in vivo*. *J. Am. Heart Assoc.* 4 (6), e001993. doi:10.1161/jaha.115.001993

Zhao, H., Li, X., Zhao, S., Zeng, Y., Zhao, L., Ding, H., et al. (2014). Microengineered *in vitro* model of cardiac fibrosis through modulating myofibroblast mechanotransduction. *Biofabrication* 6 (4), 045009. doi:10.1088/1758-5082/6/4/045009

Zhao, M., Wang, L., Wang, M., Zhou, S., Lu, Y., Cui, H., et al. (2022). Targeting fibrosis: Mechanisms and clinical trials. *Signal Transduct. Target. Ther.* 7 (1), 206. doi:10.1038/s41392-022-01070-3

Zhao, X., Kong, Y., Liang, B., Xu, J., Lin, Y., Zhou, N., et al. (2022). Mechanosensitive Piezo1 channels mediate renal fibrosis. *JCI Insight* 7 (7), e152330. doi:10.1172/jci.insight.152330

Zhao, Y., Rafatian, N., Feric, N. T., Cox, B. J., Aschar-Sobbi, R., Wang, E. Y., et al. (2019). A platform for generation of chamber-specific cardiac tissues and disease modeling. *Cell* 176 (4), 913–927.e18. doi:10.1016/j.cell.2018.11.042

Zhou, M., Lee, B. H., Tan, Y. J., and Tan, L. P. (2019). Microbial transglutaminase induced controlled crosslinking of gelatin methacryloyl to tailor rheological properties for 3D printing. *Biofabrication* 11 (2), 025011. doi:10.1088/1758-5090/ab063f

Zuela-Sopilniak, N., and Lammerding, J. (2022). Can't handle the stress? Mechanobiology and disease. *Trends Mol. Med.* 28, 710–725. doi:10.1016/j.molmed.2022.05.010

frontiers | Frontiers in Bioengineering and Biotechnology

TYPE Original Research
PUBLISHED 14 November 2022
DOI 10.3389/fbioe.2022.1062529

OPEN ACCESS

EDITED BY
Yuhui Li,
Commissariat à l'Energie Atomique et aux Energies Alternatives (CEA), France

REVIEWED BY
Dalin Tang,
Worcester Polytechnic Institute, United States
Liang Wang,
Southeast University, China

*CORRESPONDENCE
Aike Qiao,
qak@bjut.edu.cn

SPECIALTY SECTION
This article was submitted to Biomechanics, a section of the journal Frontiers in Bioengineering and Biotechnology

RECEIVED 06 October 2022
ACCEPTED 31 October 2022
PUBLISHED 14 November 2022

CITATION
Qu Z, Wei H, Du T and Qiao A (2022), Computational simulation of stent thrombosis induced by various degrees of stent malapposition.
Front. Bioeng. Biotechnol. 10:1062529.
doi: 10.3389/fbioe.2022.1062529

Computational simulation of stent thrombosis induced by various degrees of stent malapposition

Zhuoran Qu, Hongge Wei, Tianming Du and Aike Qiao*

Faculty of Environment and Life, Beijing University of Technology, Beijing, China

Percutaneous coronary intervention with stent implantation is one of the most commonly used approaches to treat coronary artery stenosis. Stent malapposition (SM) can increase the incidence of stent thrombosis, but the quantitative association between SM distance and stent thrombosis is poorly clarified. The objective of this study is to determine the biomechanical reaction mechanisms underlying stent thrombosis induced by SM and to quantify the effect of different SM severity grades on thrombosis. The thrombus simulation was performed in a continuous model based on the diffusion-convection response of blood substance transport. Simulated models included well-apposed stents and malapposed stents with various severities where the detachment distances ranged from 0 to 400 μm. The abnormal shear stress induced by SM was considered a critical contributor affecting stent thrombosis, which was dependent on changing SM distances in the simulation. The results illustrate that the proportion of thrombus volume was 1.88% at a SM distance of 75 μm (mild), 3.46% at 150 μm, and 3.93% at 400 μm (severe), but that a slight drop (3.18%) appeared at the detachment distance of 225 μm (intermediate). The results indicate that when the SM distance was less than 150 μm, the thrombus rose notably as the gap distance increased, whereas the progression of thrombogenicity weakened when it exceeded 150 μm. Therefore, more attention should be paid when SM is present at a gap distance of 150 μm. Moreover, when the SM length of stents are the same, thrombus tends to accumulate downstream towards the distal end of the stent as the SM distance increases.

KEYWORDS

stent thrombosis, stent malapposition, dynamic thrombus formation, shear-induced thrombus aggregation, computational fluid dynamics, 3D continuum model

1 Introduction

Every year, approximately 5 million percutaneous coronary interventions (PCIs) with stent implantation are performed worldwide to treat coronary artery disease (Torrado et al., 2018; Gori et al., 2019). The complications that arise from PCI are a major concern for a small but significant number of patients even if the complications occur at a relatively

low incidence. Among the complications, the greatest concern is stent thrombosis (ST), which has a 5–45% mortality rate and a 15–20% recurrence rate at 5 years post-intervention. Stent malapposition (SM) has been most frequently found both in early and late ST cases (Koskinas et al., 2012; Mori et al., 2016; Adriaenssens et al., 2017; Im et al., 2019).

SM is one of the inadequate stent deployments and is defined as at least one stent strut being detached from the innermost layer of the vessel wall (Souteyrand et al., 2016; Hudrea et al., 2018). The detachment distance is calculated as the distance between the abluminal face of the strut and the vessel wall and usually ranges from 100 to 500 μm (Foin et al., 2014). Many factors contribute to SM, encompassing procedure-related factors (stent under-expansion, undersizing), plaque-related factors (thrombus dissolution, positive vessel remodeling), and stent-related factors (delayed endothelization, chronic stent recoil) (Taniwaki et al., 2016; Wei et al., 2021). Well-apposed struts can be classified as embedded struts or protruding struts (Giglioli et al., 2020). Embedded struts are buried into the vessel wall and are regarded as "stable." Although protruding struts are covered by neointima, they represent a foreign body interrupting blood flow near the vessel wall. Therefore, protruding struts and malapposed struts are both considered "vulnerable."

To investigate the effect of protruding stents on thrombus formation, an *in vitro* experiment using a step model found that thrombus deposit increased when the protruding part of the struts became larger (Corbett et al., 2010). In other *in vitro* experiments with stents employments, the protruding strut produced less thrombus than in a malapposed situation (Ng et al., 2022) and for the malapposed stents thrombogenicity of the stent rose in tandem with larger SM distances (Foin et al., 2017; Perry-Nguyen et al., 2020).

The hemodynamic mechanism underlying this phenomenon has been studied using computational fluid dynamics (CFD). Some 2D and 3D CFD models have been used to understand how SM distance affects blood flow and thrombogenicity. The protruding and malapposed stent struts disturbed the blood flow and created micro-recirculation, which reduced the flow rate and shear stress, leading to higher blood viscosity and promoting the stagnation of platelets and coagulation factors (Poon et al., 2018). This led to the assumption that SM might be a trigger for the thromboembolic events (De Santis et al., 2013; Rikhtegar et al., 2013). In addition, it has been found that the size and position of the micro-recirculation are related to the SM distance (Chen et al., 2017) and that disturbances in the flow tend to worsen with increasing detachment distance, resulting in enhanced thrombogenicity (Foin et al., 2014; Hudrea et al., 2018). Interestingly, some studies have argued that SM distances might not necessarily produce a greater hemodynamic disturbance when compared to smaller SM distances (Chesnutt and Han, 2016; Gori et al., 2019). According to a patient-specific coronary artery model, the area of adverse wall shear stress in cases of SM is smaller than well-apposed cases (Wei et al., 2021). Other researchers have utilized SM models with different detachment distances to simulate the aggregation of platelets and found that the relationship between detachment distances and thrombogenicity is not always positively correlated (Chesnutt and Han, 2016).

In the aforementioned studies, the correlation between SM distance and ST was generally inferred by comparing the results of CFD simulations and clinical observations or *in vitro* experiments. Most studies were based on qualitative analysis without the process of thrombus formation, which makes it difficult to investigate differences in the severity of thrombus induced by various degrees of SM. Most studies have focused on the effect of SM on flow stagnation as opposed to the biomechanical association between blood flow and thrombus growth. As ST is correlated with platelet activation and coagulation, it is necessary to include blood substances in fluid simulations (Zhang et al., 2022).

Therefore, it is necessary to simulate the dynamic thrombus formation in a SM model in order to precisely clarify variations in ST attributed to different SM distances. The objective of this study is to delineate the biomechanical reaction mechanisms underlying ST induced by malapposition and to quantify the effect of various malapposition severities on thrombosis. We simulated deposition of thrombus in 3D stent-vessel models with different levels of SM and compared the data with previous *in vitro* experiments on ST to validate our simulation results.

2 Methodology

Idealized well-opposed and malapposed models were developed. Blood flow was simulated using CFD and was integrated with the continuous thrombus calculation model. Regions with high probability of thrombus formation were determined by calculating local wall shear stress, residence time, and shear rate. In this section, the details of the thrombus model and the dynamic calculation procedures are described.

2.1 3D SM models

According to the European Association of Percutaneous Cardiovascular Interventions (EAPCI), when more than half of the stent strut thickness is buried into the vessel wall, this is defined as an embedded strut, while a protruding strut refers to a strut where less than 50% of the strut thickness is buried into the vessel wall. A stent with a SM distance of more than 400 μm is considered a severe SM (Foin et al., 2014; Naganuma, 2020). Based on the struts scenarios of several types of stents, vessels in this study were assumed as a rigid circular pipe with a diameter of

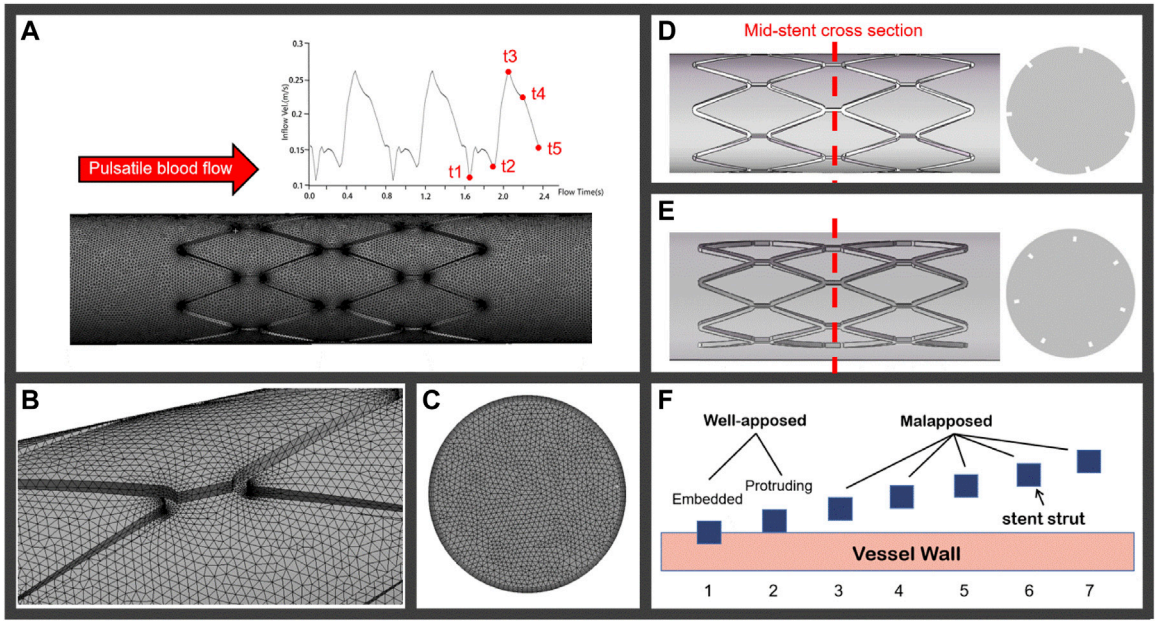

FIGURE 1
(A) Pulsatile coronary blood flow is applied at the inlet of the computational domain for CFD analyses and a meshed computational domain inside an idealized straight vessel; **(B)** tetrahedron elements on the lumen surface; **(C)** increase in mesh density near the inflation layers; **(D)** and **(E)** represent the well-apposed and malapposed idealized stent-vessel model and their cross-sections, respectively; **(F)** stent struts in seven cases categorized as well-apposed and malapposed, the struts in case 1 are simulated as embedded stents and the detachment distances increase from case 2 to case 7.

3.5 mm. The stent model employed was generated as a circular equal-diameter stent with a strut thickness of 0.15 mm. Cases 1 and 2 were modeled as embedded struts and protruding struts, respectively, under the well-apposed category, as shown in Figure 1F. The detachment distances in malapposed models, ranging from 75 μm (Case 3) and 225 μm (Case 5) to 400 μm (Case 7), were classified as mild, intermediate, and severe SM, respectively. Figures 1D,E illustrated the stent-vessel model of case 2 and case 5, respectively. Some researchers have simplified the stent into circular rings to mimic SM (Poon et al., 2018) and only investigated blood flow patterns located in a single strut. The length of the stent extended to 8 mm in our models, enabling us to investigate longitudinal hemodynamic changes and thrombus growth. All stent and vessel models were constructed using the 3D computer aided design software SOLIDWORKS 2016.

2.2 Numerical simulation approaches

2.2.1 Thrombus formation

The thrombus model used in this simulation was developed by Menichini and Xu (2016). Low shear rate tends to induce the deposition of platelets and coagulation factors. Hence, shear rate, relative residence time (RRT), and time-averaged wall shear stress (TAWSS) were adapted as hemodynamic parameters to

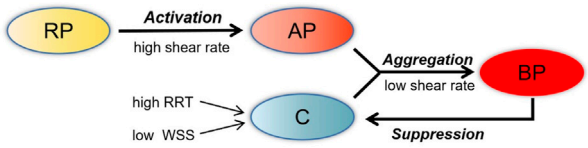

FIGURE 2
Schematic depiction of the thrombosis model. RP, resting platelets; AP, activated platelets; C, coagulation; BP, bounding platelets; RRT, relative residence time; WSS, wall shear stress.

characterize the distribution of stagnancy and shear rate level in the flow. Thrombus formation was simulated by solving the advection–diffusion equation, which describes the transport process of coagulation (C), resting platelets (RP) and activated platelets (AP), shear rate, and RRT with their switching functions determining accumulation of bound platelets (BP). Thrombus is represented by BP concentration. In the model, C represents a series of coagulation factors that participate in the thrombosis reaction, although its concentration does not directly represent a specific coagulation factor. With this thrombus simulation framework, the formation of C was promoted by low TAWSS (<0.2 Pa) and high RRT (>0.9). In the local hemodynamic

environment, AP and high concentration of C promoted thrombus formation, while local high concentrations of BP on the vessel wall depressed the formation of C, as in Figure 2. The governing equations of user-defined scalars were provided in the study of Menichini and Xu (2016). In this study, a number of important changes were made to this thrombus model, which are illustrated in the following paragraphs.

The present thrombus model only considered low shear stress as a reaction term to control the flux input of coagulation and as a factor to increase stagnancy. It is commonly known that high shear stress induced by malapposed struts can activate platelets, which contributes to thrombus aggregation (Chesnutt and Han, 2016). Hence, the reaction source term Si of AP and RP was altered to a sum of two terms as follows (Eq. 1):

$$S_i = K_1[AP][RP] + K_2[RP]\dot{\gamma}\mu \quad (1)$$

,

where the first term on the right represents the activation effect of RP by AP, the second term on the right represents the activation by high shear stress, μ is blood viscosity, $\dot{\gamma}$ is the time average shear rate, and K_1 and K_2 equal 0.5 s^{-1}.

For the initial CFD simulation, blood was treated as shear-thinning fluid as described by the viscosity model developed by Quemada (Marcinkowska-Gapińska et al., 2007), which was adapted to incorporate the reported hematocrit of 35%. In order to simulate the resistance to blood flow after thrombus development, local elements that corresponded to "thrombus formation" were defined as viscoelastic, which was determined using the viscosity function related to flow shear rate and BP (Eq. 2):

$$\mu = \left\{\mu_0 + \mu_\infty\left[1 + (\alpha\dot{\gamma})^2\right]^n\right\}\left(1 + 100\frac{BP^2}{BP^2 + BP_t^2}\right), \quad (2)$$

where μ_0 = 3.45cp and μ_∞ = 56cp, representing blood viscosity at the infinite shear rate and zero shear rate, respectively, α = 3.313 s represents the relaxation time, and n = −0.3216 (Qian et al., 2020). BP_t was set at 20 nmol and the higher the BP concentration, the greater the viscosity of local elements in order to imitate the resistance to blood flow.

2.2.2 Calculation procedures

Numerical simulations of blood flow in the stented vessel were carried out by solving the Naiver–Stokes equations and transport equations using the volume-based algorithm Fluent (v19.0, ANSYS) with user-defined functions (UDF) and user-defined scalar (UDS). Blood was assumed to be an incompressible non-Newtonian fluid with a constant density of 1050 kg/m^3. In each simulation, blood flow CFD was first run over three cardiac cycles, with a cardiac cycle of 0.8 s and time-step increment of 0.01 s. The third cycle was used to calculate RRT, TAWSS, and shear rate over one cycle. The thrombus model was subsequently introduced to simulate formation of thrombus for 1 s. The aforementioned calculation procedure was repeated over five rounds in all the models and the thrombus was accumulated for 5 s in total. After each formation of thrombus, the renewed viscosity coefficient was adapted in the next round of simulation to imitate the resistance present during thrombus growth. The higher the concentration of BP in a local area, the greater the obstruction of blood flow.

The fluid domain was discretized into tetrahedral elements, as in Figure 1B. Figure 1C shows the meshes on the cross section where the mesh density increases near the inflation layers. The computational domain had approximately 4,446,653 elements, and the tetrahedral mesh had a maximum face size of 0.08 mm. Finer meshes with 5,462,027 elements were created to assess mesh sensitivity. Differences in TAWSS peak values between meshes were less than 3%, indicating that mesh independence had been achieved.

2.2.3 Boundary conditions

A transient velocity waveform that imitated the coronary blood flow was applied at the model inlet, as shown in Figure 1A, while the outlet pressure was set as constant zero. A rigid wall was imposed on the fluid domain with a no-slip condition. The coagulation factors and platelets boundary conditions used were similar to those previously described by Menichini and Xu (2016).

3 Results

3.1 Blood flow characteristics

Velocity streamlines were assessed in the longitudinal section of cases 1 to 7 at two time points, t1 and t3, representing inlet velocities at nadir diastole and peak systole, respectively (Figures 3A,B). In case 1, streamlines are smooth over the embedded struts at both time points. However, in case 2, disturbed flow was found near protruding struts with the appearance of a small micro-recirculation on the backward step of the struts, as shown in Figure 3A. In case 3, the recirculation region is larger and surrounds the malapposed struts. With an increasing detachment distance, the malapposed struts separate the blood flow but without micro-recirculation, as seen in cases 4 and 6. In case 5, a slight micro-recirculation is present adjacent to the vessel wall rather than the stent struts. In case 7, two recirculation regions located both proximal and distal to the struts joined to form a large region of disturbed flow enveloping the stent. The distribution of flow velocity in mid-stent cross-sections of the stented area at time point t3 is shown in Figure 3C. Figure 1D shows the location of the cross-sections. A low-velocity region is seen around the stent struts in malapposed cases and moves inwards with increasing SM distances, which is the result of the viscous effect of blood between the stent struts and vessel wall. Overall, fluid perturbations in all stents are greater under the

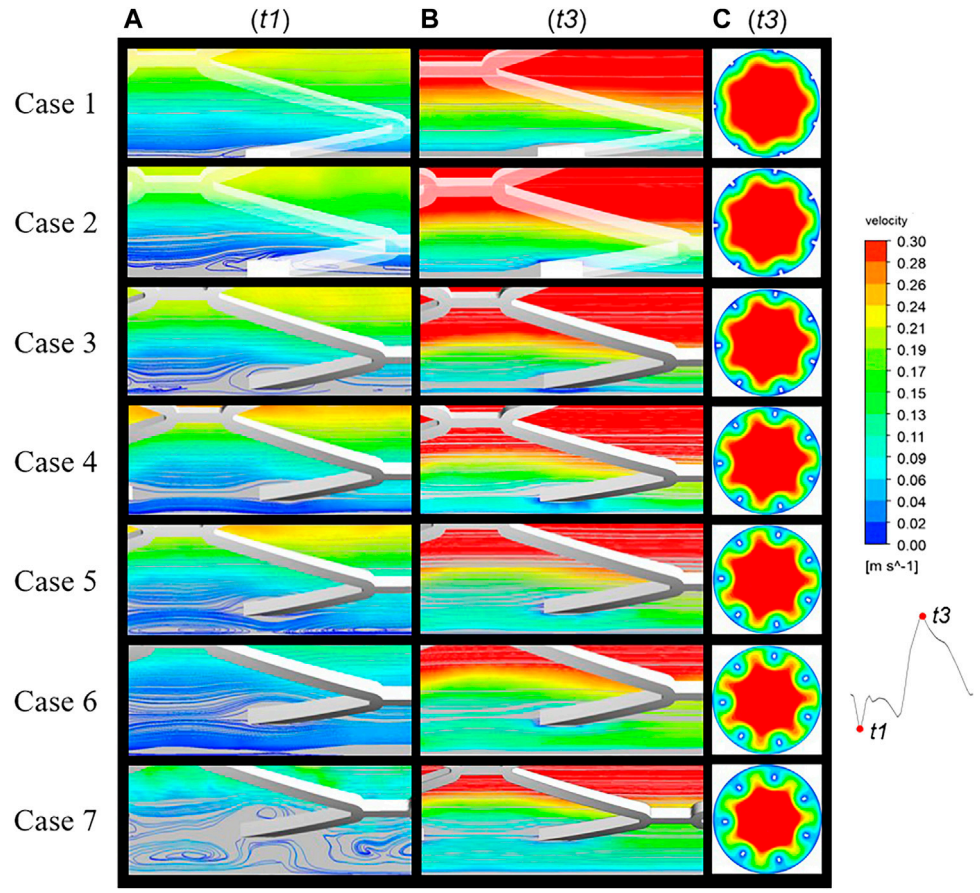

FIGURE 3
Blood flow streamlines at two time points of the cardiac cycle: t1, nadir diastole; t3, peak systole. The flow near the stents was evidently more disturbed at **(A)** (t1) than **(B)** (t3). **(C)** Mid-stent cross-sections of all cases with the regions of low velocity near the struts having migrated from the vessel wall to the interior.

minimum velocity compared to the maximum velocity (Figure 3B). The most pronounced disturbances are observed in the maximum detachment distance, as in case 7. Flow field patterns were significantly affected by various malapposition degrees.

3.2 Wall flux properties and RRT distributions

The histogram in Figure 4 presents the areas of low and high TAWSS on the vessel wall for all cases, which are arranged in order of increasing SM distance. In the thrombosis model, coagulation factors were produced within the area of low TAWSS (≤0.2 Pa) and platelets were activated upon high shear stress (≥6 Pa). In TAWSS contours (Figure 4), regions subjected to low and high TAWSS were isolated and colored blue and red, respectively, and the full range of contour colors is displayed on the stent surfaces. For apposed stents, in case 1 and case 2, low TAWSS surrounded the stent struts and the area within a protruding stent was twice that of an embedded stent. For cases 3 and 4, low TAWSS was localized downstream of the stent connectors. As the detachment distances increased, low TAWSS was gradually concentrated at the distal ends of the vessel wall. The area of low TAWSS exhibited continuous reduction from cases 2 to 7, while high TAWSS emerged at the proximal region in case 4 and increased with the enhancing severity of malapposition. The area of high TAWSS is about nine times larger than that of low TAWSS in severe SM, as reflected in case 7. In this study, low TAWSS tended to occur in the well-apposed and intermediate SM cases where the detachment distance is relatively small; the values of TAWSS on the entire stent surface increased from case 1 to case 7.

The distribution of RRT in longitudinal sections, stent surfaces, and mid-stent cross-sections is shown in Figure 5. In Figure 5A, regions with high RRT gradually moved downstream

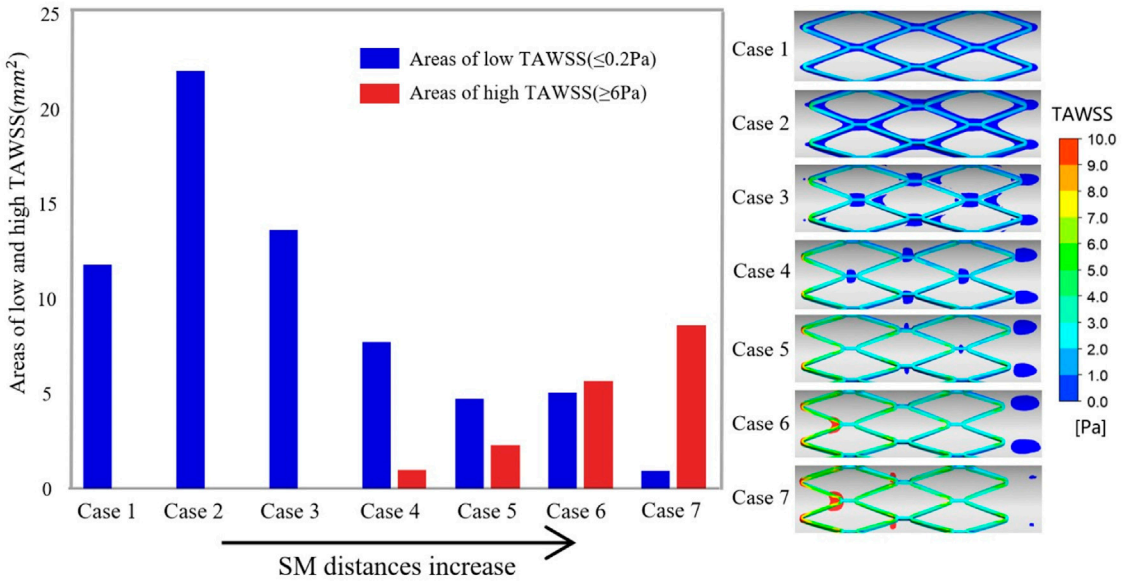

FIGURE 4
Right panel illustrates the complete TAWSS contours on the stent surface and the region of low TAWSS (≤0.2 Pa) and high TAWSS (≥6 Pa) on the vessel wall are colored blue and red, respectively. The histogram shows the area of adverse TAWSS from case 1 to case 7 with the increasing SM distance. The areas correspond to the highlighted region of TAWSS on the vessel wall. TAWSS, time-averaged wall shear stress.

along the boundaries with the increasing SM distances and a similar pattern was observed in the movement of low TAWSS on the vessel wall. Figure 5B shows the stent struts at the middle position of the stent segment. The smallest SM distance of case 3 in malapposed cases had the highest RRT on stent surfaces, with the RRT on the stent surfaces gradually decreasing from case 3 to case 7. High RRT implies an increase in concentration of coagulation factors that is linked to thrombus formation. For the cross-sections in Figure 5C, the region with high RRT was consistent with the region of low flow velocity for case 1 to case 4 and was mainly distributed around the stent struts and vessel wall. For cases 5 to 7, regions with high RRT moved from stent struts to the vessel wall and were eventually distributed between the adjacent struts, while low RRT was distributed around the struts. The combination of high RRT and low TAWSS might increase the likelihood of platelet deposition surrounding the malapposed struts.

3.3 Thrombus formation

BP is regarded as a sign of thrombosis and, in this study, the threshold of BP was fixed at 8 nmol/L. Figure 6 shows the distribution of thrombus for all cases as calculated from the hemodynamic data. Thrombus on the stent surface and vessel wall is shown in Figure 6A and thrombus on the longitudinal sections, mid-stent cross-sections, and distal cross-sections are depicted in Figures 6B–D, respectively. For well-apposed cases 1 and 2 in Figure 6A, only a small degree of thrombus was observed around the stent connectors and thrombus covered a small area on the longitudinal sections and cross-sections (Figures 6B,C). In case 3, thrombus was observed on every strut of the stent, and the cross-section showed that the thrombus grew inward and filled the space between the vessel wall and stent struts and a small amount of thrombus shows on the distal end of the stent. With increasing SM distance, thrombus tends to accumulate on the downstream side of stent segment for case 4 to case 7. Decreasing RRT could be responsible for the reduction in thrombus at the middle position of the stents and the pattern of thrombus movement was in agreement with the distribution of low TAWSS (Figure 4). In case 4, thrombus tended to deposit downstream of the stent strut and covered the whole cross-section of the struts. For case 5 in Figure 6A, the region on the vessel wall covered by thrombus is smaller, while the extent of thrombosis as viewed from both longitudinal sections and cross-sections remained mostly unchanged compared to case 4. As in Figure 6D, for cases 6 and 7, thrombus was only generated at the distal half rather than the middle of the stent. SM distances not only affect the thrombus area on cross-sections bus also the location of thrombus in the longitudinal direction.

Figure 7A shows the area percentage of thrombus on the five cross-sections (a–e) for all cases. For case 1 to case 4, there was little difference in the distribution of thrombus from upstream to downstream of the stent, where the larger the SM distance, the higher the thrombus amount. For cases 5 to

10.3389/fbioe.2022.1062529

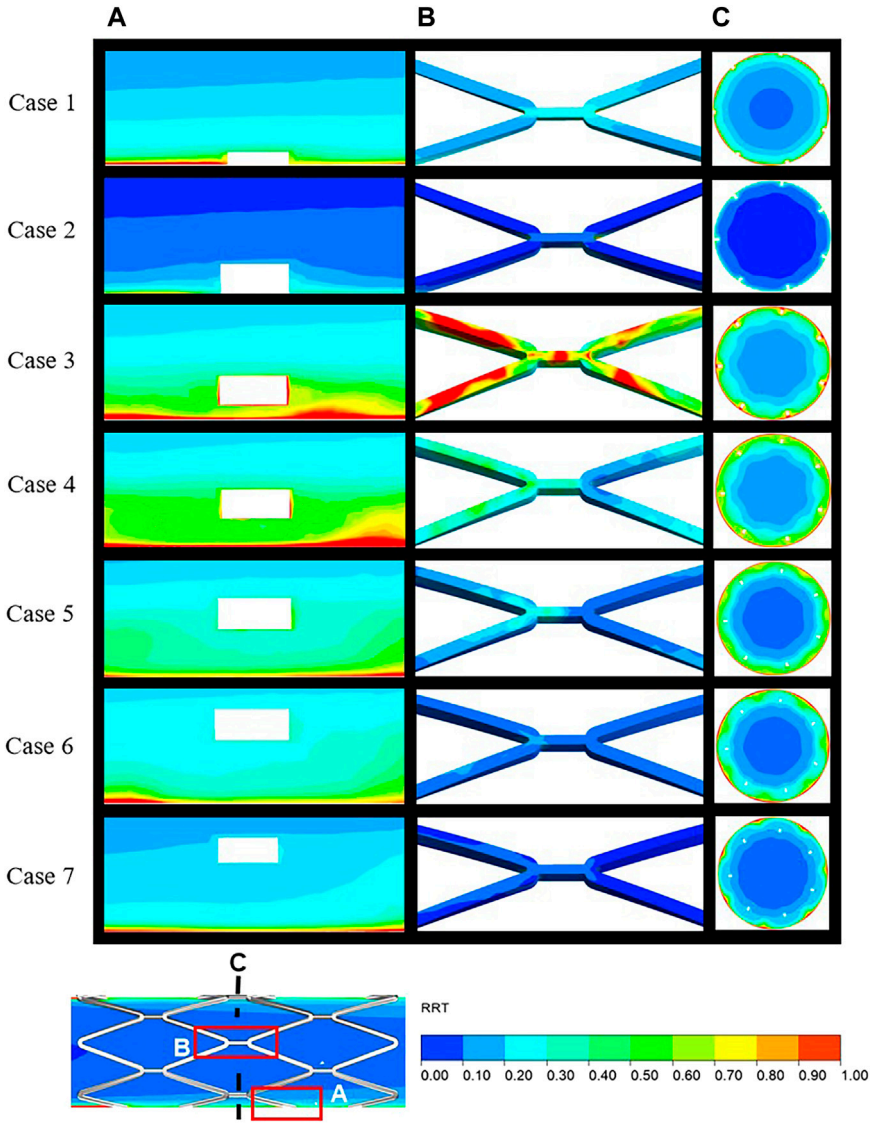

FIGURE 5
Distribution of RRT over the local area in the longitudinal sections **(A)**, stent surface **(B)**, and mid-stent cross-sections **(C)** (locations are illustrated in Figure 6). RRT, relative residence time.

7, a higher amount of thrombus tended to accumulate on the distal end of the stent rather than being uniformly distributed, as can be seen from the slope of the graph (the longer the distance, the more significant the trend). Figure 7B shows the thrombus area proportions in mid-stent cross-section (b) and the thrombus volume proportions with increasing degree of SM. The thrombus volume increased greatly from case 2 to case 4; case 4 had severe thrombosis with the proportion of thrombus volume at 3.46%, which is 35 times that measured for case 2. The proportion of thrombus volume showed a slight downward drop in case 5, with a 3.18% thrombus volume. From case 4 to 7, the severity of the thrombus continued to grow but was less significant; it increased by 14% from case 4 to case 7. The thrombus area proportions in cross-section (b) keep rising from case 1 to case 5, then dropping to zero for cases 6 and 7, most likely because the thrombus deposit moves downstream to the distal end. Overall, there was a rising trend of thrombus presentation in the entire stented segment; in severe malapposed cases, thrombus proportions still increased but were mostly concentrated on a location downstream of the stented segment, which is technically a non-stented area.

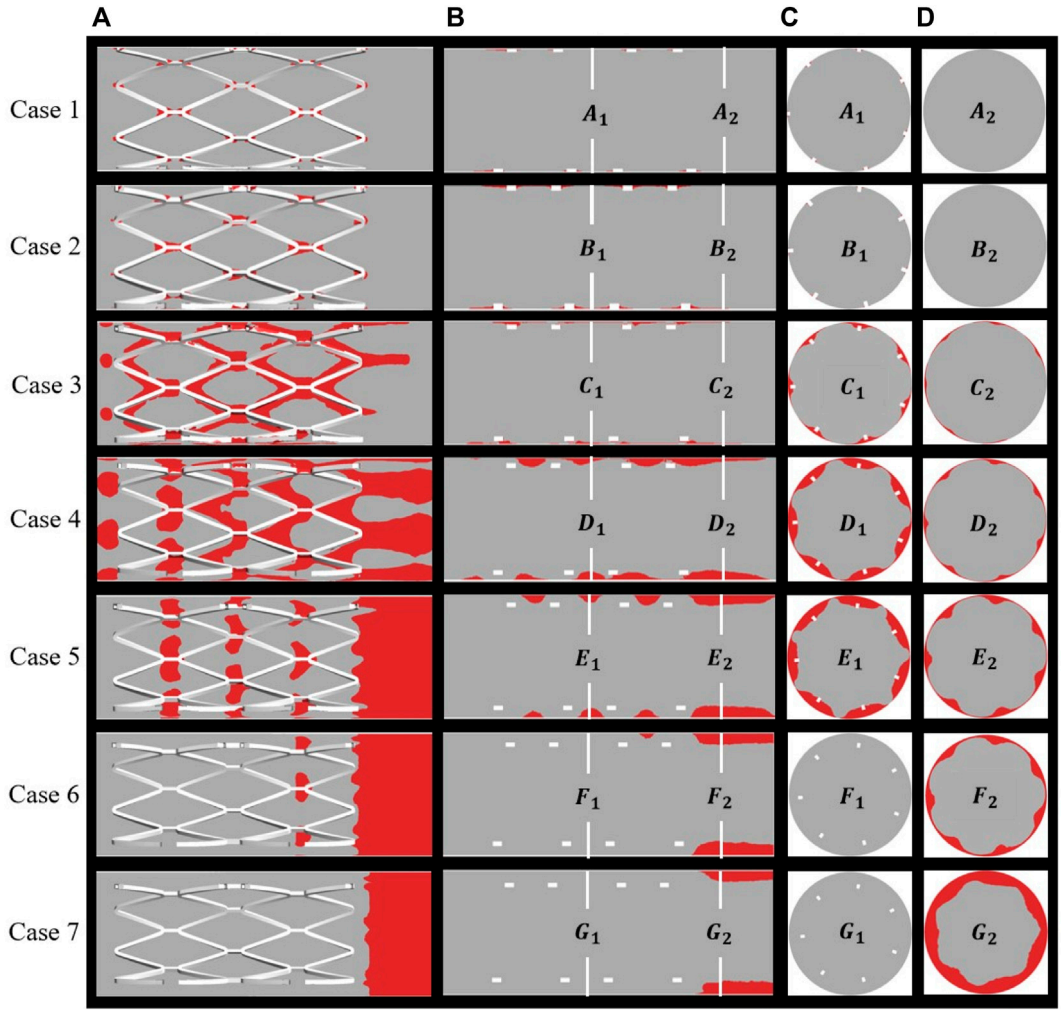

FIGURE 6
Distribution of thrombus at the end of simulation: **(A)** thrombus on the overall perspective; **(B)** thrombus on the longitudinal sections and locations of two cross-sections; **(C)** middle location of the stents; **(D)** distal end of the stents.

3.4 Relationship between viscosity and thrombus

The method for simulating resistance in blood flow of the thrombus has been explained previously. According to Eq. 2, the viscosity of blood flow was associated with shear rate and the concentration of BP, where the local elements presented more viscoelasticity with higher BP values. Figure 8 illustrates the variation in viscosity and growth of thrombus for case 2 and case 4 over the accumulated simulation time. Prior to calculating the time of initial thrombus formation, blood was treated as shear-thinning fluid. As shown in Figure 8A, initially, higher viscosity appeared on the corners of both sides of the protruding struts. Meanwhile, for case 4, lower viscosity was noted at the location around the struts and near the vessel wall and a thin layer of higher viscosity was found closer to the malapposed struts. The viscosity contours at 3 s showed that viscosity increased dramatically with high BP values (Figures 8A,C). In the next simulation, viscosity distribution and hemodynamic characteristics affected thrombus accumulation, as seen in Figures 8B,D, where regions of high viscosity were consistent with the formation of thrombus at 3 s and 5 s. For case 2, thrombus was localized to both sides of the protruding struts. On the other hand, in case 4, thrombus presented on the vessel wall first and then grew inward between the adjacent struts, eventually attaching the malapposed struts.

4 Discussion

In this study, we simulated the formation of thrombosis based on the diffusion-convection response of blood substance

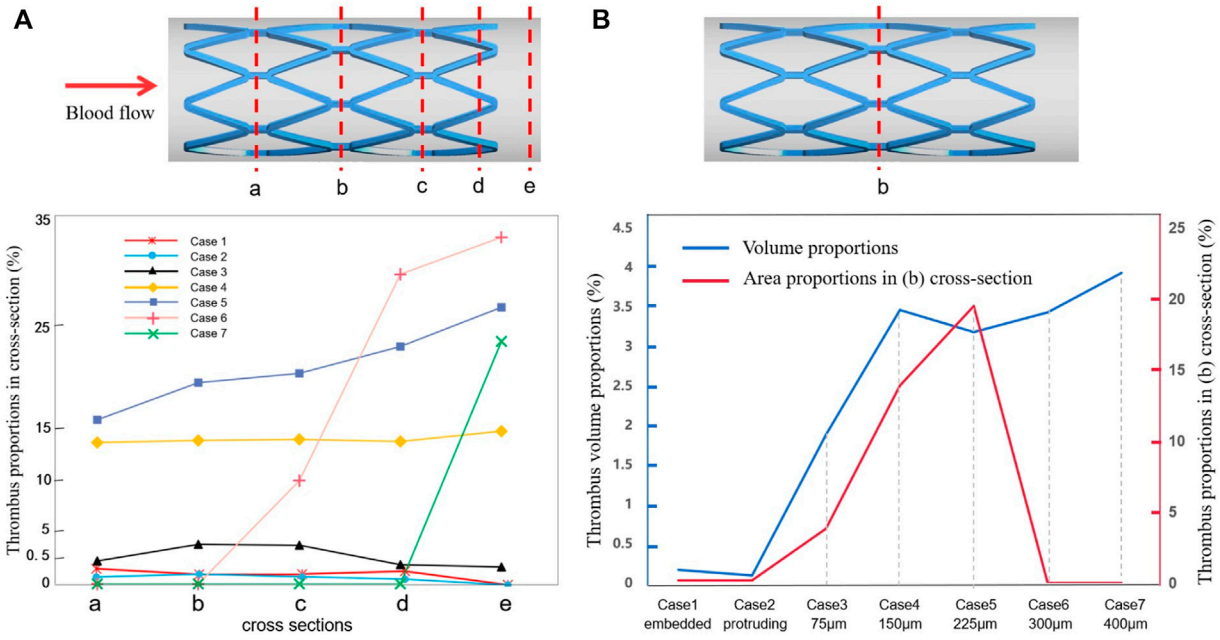

FIGURE 7
Thrombus accumulation amount at the end of simulation: **(A)** thrombus proportions in five cross-sections (a–e) of all cases; **(B)** thrombus area proportions in the mid-stent cross-section (b) and thrombus volume proportions in the fluid domain.

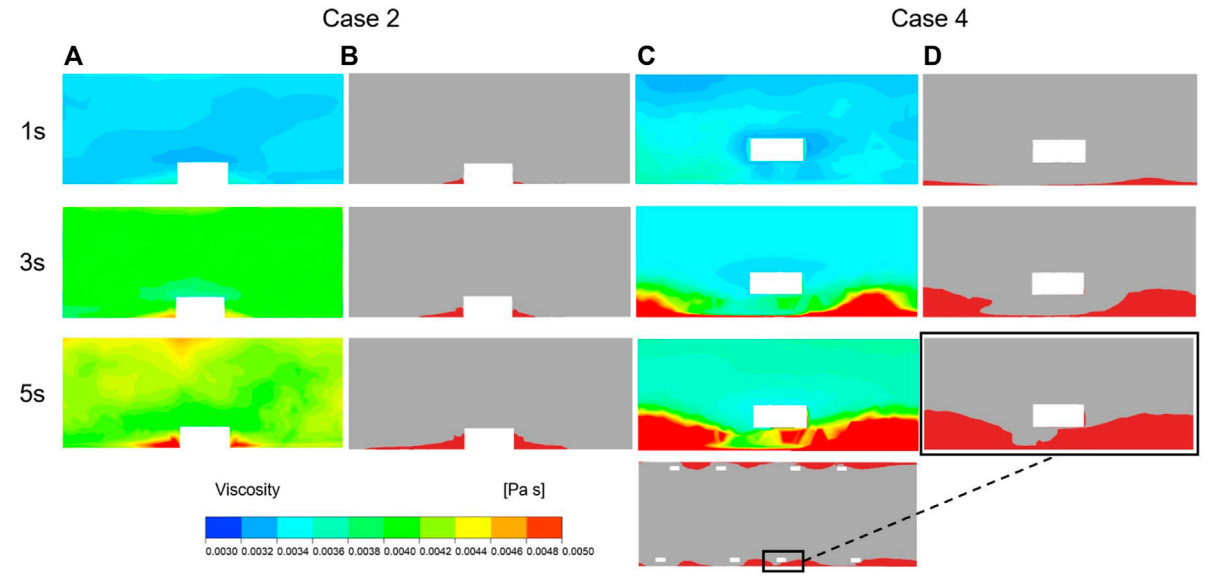

FIGURE 8
Viscosity and thrombus distribution on the longitudinal sections of case 2 and case 4 at three time points of simulation. **(A)** Viscosity distribution of Case 2 after 1 s, 3 s and 5 s of thrombus calculation. **(B)** Thrombus distribution of Case 2 after 1 s, 3 s and 5 s of thrombus calculation. **(C)** Viscosity distribution of Case 4 after 1 s, 3 s and 5 s of thrombus calculation. **(D)** Thrombus distribution of Case 4 after 1 s, 3 s and 5 s of thrombus calculation.

transport. We investigated variation in the amount of thrombus formed under the different degrees of SM and discussed the association between ST and hemodynamic patterns. The formation of BP is directly influenced by the transport of C and AP, whose values depend on the distribution of shear stress and residence time. Higher residence time and low shear stress both directly contributed to a higher thrombosis value. According to a reported hemodynamic analysis based on patient-specific CT scans, areas with TAWSS less than 0.2 Pa corresponded to the location of thrombosis (Menichini et al., 2016), where coagulator input occurred in our simulation. A lower or higher threshold would cause slower thrombus growth or overestimate the amount of thrombus formed. To a certain extent, high shear stress could indirectly lead to thrombus formation by activating platelets. For example, shear stress of more than 6 Pa has been found to be more likely to induce platelet activation compared to normal shear stress (Chesnutt and Han, 2016). We illustrated the distribution of high and low shear stress in Figure 4 to indicate the potential regions of thrombus formation under different SM distances.

It has been suggested that an increase in local blood viscosity may be a significant contributor to ST near malapposed struts (Poon et al., 2018). Thus, it is necessary to consider blood as a shear-thinning fluid with a dynamic viscosity when performing CFD. According to Anand et al. (2003), clot viscosity is much greater than blood viscosity; therefore, in our study, thrombus was included as one of the factors affecting viscosity. Viscosity acted as a marker of the changing hemodynamic characteristics influenced by growing thrombus. The greater the concentration of BP in a specific position, the greater the obstruction in fluid flow. Together, these parameters enabled the imitation of blood resistance caused by thrombus.

Some studies have proposed that a malapposed stent usually has a smaller area of adverse wall shear stress (WSS) than a well-apposed stent (Wei et al., 2021). Although our study observed that the region with low WSS decreased as the degree of SM increased, the area with high WSS increased with the increasing SM distance, as noted in cases 4 to 7. In the preliminary simulation, when we did not take into account high shear-induced platelet activation, due to the decreasing region of low WSS, we observe that the amount of thrombus continued to decline as the SM distance increased, which is contradictory to most clinical observations and *in vitro* experimental results. Taking into consideration the shear-induced platelet activation process, some modifications were included when simulating thrombus formation. In our study, low shear stress promotedthe accumulation of platelets and stagnation of blood flow, while high shear stress activated RP in the local area. We found that the area of thrombus generally increased with the increasing degree of SM but the thrombus volume of a protruding stent was not larger than that of an embedded stent and a slight decrease was noted for case 5 (225 μm). The trend in thrombus development was much more remarkable within a gap

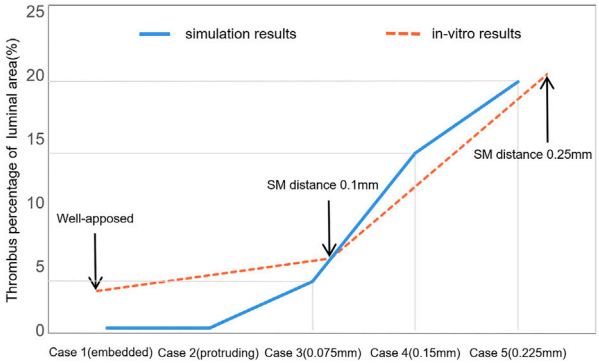

FIGURE 9
Comparison of thrombus amounts between numerical simulation and previous *in vitro* experiments. This illustrates the thrombus proportions of the luminal area with the increasing detachment distance. The two sets of results share the same axial coordinate.

distance of 150 μm compared to distances that exceeded 150 μm. Thus, more attention should be paid to situations where the SM gap distance is of 150 μm, which is equal to the thickness of the stents in our models.

Previously, it has been shown that strut size could affect the local hemodynamic environment whereby thinner struts tend to cause smaller turbulence to the flow and lead to less thrombus (Beier et al., 2016). Chesnutt and Han (2016) simulated SM with a stent thickness twice as small as ours but the trend in thrombus variation was similar. A drop in the degree of thrombus formed appeared at the intermediate SM distance. The largest detachment distance (200 μm) produced more thrombi than the smallest detachment distance (10 μm) but less thrombus than an intermediate detachment distance (25 μm). This similarity in thrombus was attributed to the range of SM distances and the strut size in their simulation being proportionally smaller. Therefore, we assume that both detachment distance and stent thickness could influence ST. The amount of thrombus decreased at intermediate SM because the platelets did not experience more adverse shear stress (both high and low shear stress) around struts with the intermediate detachment distances (225 μm). This suggests that a large detachment distance does not necessarily reflect enhanced thrombogenicity. Even though larger SM distances may not produce a higher degree of thrombus, intermediate or severe SM should be avoided at the clinical level as it would otherwise induce stenosis and delayed neointimal healing (Wei et al., 2021).

A previous *in vitro* experiment simulated thrombus deposition using an artificial step model (Corbett et al., 2010). The investigators found that more thrombus was formed in parallel with the higher steps and this aligns with the data for the embedded case and protruding case in our study where thrombus formation within the cross-sections in case 2 was

slightly more than case 1 because of the larger recirculation created by larger steps. The *in vitro* experiment also identified more thrombi on the backward step rather than the forward. In our study, more thrombi were deposited on the downstream side of the stent struts in cases 3 and 4 where the thrombi tended to accumulate downstream to the distal end of the entire stented segment as SM distances increased. Though the steps and malapposed stents are not identical, a foreign stent in the flow creates a larger recirculation vortex on the backward side, thus leading to more flow stagnation. As the detachment distance increases, the region of flow disturbance becomes larger and causes more thrombi deposit downstream. Figure 4 illustrates the same trend for low TAWSS.

Another previous *in vitro* experiment investigated ST with an incomplete stent apposition (Perry-Nguyen et al., 2020). The thrombus amount was indicated by the stent occlusion of the luminal area and the results of our study and the previous *in vitro* experiment were compared and are displayed in Figure 9. The experimental results were acquired by optical coherence tomography after 15 min perfusion through stents with varying degrees of malapposition relative to the lumen wall. Thrombus burden increased tremendously from well-apposed (0.00 mm) to malapposed (0.25 mm) from the lumen wall; a similar trend can be found in case 1 to case 5. The largest SM distance in our simulation was 0.4 mm in case 7 with a thrombus volume proportion of 3.93% and deposited on the distal non-stented location. With the *in vitro* experiment, stent thrombus almost completely occluded the tube at a SM distance of 0.5 mm; thus, a distance of >500 μm was defined as the severest degree of SM (Foin et al., 2014). This may be due to differences between stents of various diameters and straight stents. The stents used in the experiments only had a larger detachment distance at the proximal end, while the stent in our simulation had a longer area with large detachment distances; thus, the struts near the wall did not restrict the downstream blood flow. This indicates that the detachment distance and also the length of malapposed stents together influence the amount of thrombus on a certain cross-section. When the stents feature a similar length of SM segment, the larger the detachment distance, the greater the accumulation of thrombi downstream to the distal end of the stent.

Differences in the *in vitro* environment are partly responsible for the observed error between the simulation results and *in vitro* results. The perfusion was carried out without the formation of coagulators on the tube and heparin was administered in the device to avoid coagulation; moreover, the running velocity was lower than the average blood velocity in a cardiac cycle. The focus of this study was to investigate the effect of the local hemodynamic environment surrounding malapposed stents on ST. To some extent, the experimental conditions still provide a relatively realistic environment to support our simulation results. Our study provides an idealized model that could eliminate some irrelevant factors such as stenosis vessel or curved stents, which, in addition to SM distances, would influence the blood flow.

The present study has some limitations; for example, we considered the effect both of high shear and low shear on thrombus formation, but the proportion of these two parameters within a clinical environment is unclear. In future work, we will investigate and validate the proportion of the adverse shear impact on thrombus formation to accurately simulate ST. A further limitation is that, based on the idealized model with a single variable, the model does not adequately reflect the realistic and various physiological *in vivo* environments, while the factors affecting thrombosis include differences in individual blood components and vascular morphology as well as postoperative stent conditions.

5 Conclusion

To understand the biomechanical association between SM and the development of thrombus, our study integrated the thrombosis calculation method into SM models. Under the shear-induced thrombus aggregation mechanism, we simulated the transport and activation of blood substances and dynamic thrombus formation through a 3D continuous model with different SM distances to investigate the quantitative association between the severity of SM and the degree of thrombus formation. The framework of thrombus growth took into account the updated fluid domain after thrombus formation and this made it possible to involve not only the effect of disturbed flow on thrombus induced by SM but also their interaction. The results revealed that the thrombogenicity of malapposed stents increased with the growing degree of SM overall but a slight drop in thrombus volume appeared at the intermediate SM (0.225 mm). Because the thrombus tended to accumulate to the distal end as the detachment distance increased, the thrombus located on the stented area did not grow larger despite the increasing thrombogenicity. Our study provides further knowledge by comparing our findings with previous *in vitro* studies to show that SM affects ST differently depending on the severity of SM and also on multiple factors related to flow velocity, stent thickness, and the length of the malapposed segment.

Data availability statement

The original contributions presented in the study are included in the article/supplementary material; further inquiries can be directed to the corresponding author.

Author contributions

ZQ was responsible for modeling, simulation, data analysis, and paper preparation. HW assisted in design of the stent models. TD assisted in data analysis. AQ was responsible for supervision.

Funding

This research was supported by the National Natural Science Foundation of China [grant numbers 12172018 and 12202023] and the Joint Program of Beijing Municipal—Beijing Natural Science Foundation [grant number KZ202110005004].

Conflict of interest

The authors declare that the research was conducted in the absence of any commercial or financial relationships that could be construed as a potential conflict of interest.

Publisher's note

All claims expressed in this article are solely those of the authors and do not necessarily represent those of their affiliated organizations, or those of the publisher, the editors, and the reviewers. Any product that may be evaluated in this article, or claim that may be made by its manufacturer, is not guaranteed or endorsed by the publisher.

References

Adriaenssens, T., Joner, M., Godschalk, T. C., Malik, N., Alfonso, F., Xhepa, E., et al. (2017). Optical coherence tomography findings in patients with coronary stent thrombosis: A report of the prestige consortium (prevention of late stent thrombosis by an interdisciplinary global European effort). *Circulation* 136, 1007–1021. doi:10.1161/CIRCULATIONAHA.117.026788

Anand, M., Rajagopal, K., and Rajagopal, K. R. (2003). A model incorporating some of the mechanical and biochemical factors underlying clot formation and dissolution in flowing blood. *J. Theor. Med.* 5, 183–218. doi:10.1080/1027366041233131741 5

Beier, S., Ormiston, J., Webster, M., Cater, J., Norris, S., Medrano-Gracia, P., et al. (2016). Hemodynamics in idealized stented coronary arteries: Important stent design considerations. *Ann. Biomed. Eng.* 44, 315–329. doi:10.1007/s10439-015-1387-3

Chen, W. X., Poon, E., Thondapu, V., Hutchins, N., Barlis, P., and Ooi, A. (2017). Haemodynamic effects of incomplete stent apposition in curved coronary arteries. *J. Biomech.* 63, 164–173. doi:10.1016/j.jbiomech.2017.09.016

Chesnutt, J. K., and Han, H. C. (2016). Computational simulation of platelet interactions in the initiation of stent thrombosis due to stent malapposition. *Phys. Biol.* 13, 016001. doi:10.1088/1478-3975/13/1/016001

Corbett, S. C., Ajdari, A., Coskun, A. U., and N-Hashemi, H. (2010). *In vitro* and computational thrombosis on artificial surfaces with shear stress. *Artif. Organs* 34, 561–569. doi:10.1111/j.1525-1594.2009.00930.x

De Santis, G., Conti, M., Trachet, B., De Schryver, T., De Beule, M., Degroote, J., et al. (2013). Haemodynamic impact of stent-vessel (mal)apposition following carotid artery stenting: Mind the gaps. *Comput. Methods Biomech. Biomed. Engin.* 16, 648–659. doi:10.1080/10255842.2011.629997

Foin, N., Gutierrez-Chico, J. L., Nakatani, S., Torii, R., Bourantas, C. V., Sen, S., et al. (2014). Incomplete stent apposition causes high shear flow disturbances and delay in neointimal coverage as a function of strut to wall detachment distance: Implications for the management of incomplete stent apposition. *Circ. Cardiovasc. Interv.* 7, 180–189. doi:10.1161/CIRCINTERVENTIONS.113.000931

Foin, N., Lu, S., Ng, J., Bulluck, H., Hausenloy, D. J., Wong, P., et al. (2017). Stent malapposition and the risk of stent thrombosis: Mechanistic insights from an *in vitro* model. *EuroIntervention* 13, e1096–e1098. doi:10.4244/EIJ-D-17-00381

Giglioli, C., Formentini, C., Romano, S. M., Cecchi, E., Baldereschi, G. J., Landi, D., et al. (2020). Vulnerable struts with CRE8, Biomatrix and Xience stents assessed with OCT and their correlation with clinical variables at 6-month follow-up: The CREBX-OCT study. *Int. J. Cardiovasc. Imaging* 36, 217–230. doi:10.1007/s10554-019-01719-1

Gori, T., Polimeni, A., Indolfi, C., Raber, L., Adriaenssens, T., and Munzel, T. (2019). Predictors of stent thrombosis and their implications for clinical practice. *Nat. Rev. Cardiol.* 16, 243–256. doi:10.1038/s41569-018-0118-5

Hudrea, I., Totorean, A., and Gaita, D. (2018). in *Computational fluid dynamics analysis of coronary stent malapposition* (Singapore: Springer Nature Singapore), 761–765.

Im, E., Hong, S. J., Ahn, C. M., Kim, J. S., Kim, B. K., Ko, Y., et al. (2019). Long-term clinical outcomes of late stent malapposition detected by optical coherence tomography after drug-eluting stent implantation. *J. Am. Heart Assoc.* 8, e011817. doi:10.1161/JAHA.118.011817

Koskinas, K. C., Chatzizisis, Y. S., Antoniadis, A. P., and Giannoglou, G. D. (2012). Role of endothelial shear stress in stent restenosis and thrombosis: Pathophysiologic mechanisms and implications for clinical translation. *J. Am. Coll. Cardiol.* 59, 1337–1349. doi:10.1016/j.jacc.2011.10.903

Marcinkowska-Gapińska, A., Gapinski, J., Elikowski, W., Jaroszyk, F., and Kubisz, L. (2007). Comparison of three rheological models of shear flow behavior studied on blood samples from post-infarction patients. *Med. Biol. Eng. Comput.* 45, 837–844. doi:10.1007/s11517-007-0236-4

Menichini, C., Cheng, Z., Gibbs, R. G., and Xu, X. Y. (2016). Predicting false lumen thrombosis in patient-specific models of aortic dissection. *J. R. Soc. Interface* 13, 20160759. doi:10.1098/rsif.2016.0759

Menichini, C., and Xu, X. Y. (2016). Mathematical modeling of thrombus formation in idealized models of aortic dissection: Initial findings and potential applications. *J. Math. Biol.* 73, 1205–1226. doi:10.1007/s00285-016-0986-4

Mori, H., Joner, M., Finn, A. V., and Virmani, R. (2016). Malapposition: Is it a major cause of stent thrombosis? *Eur. Heart J.* 37, 1217–1219. doi:10.1093/eurheartj/ehw006

Naganuma, T. (2020). Acute stent malapposition: Harmful or harmless? *Int. J. Cardiol.* 299, 106–107. doi:10.1016/j.ijcard.2019.08.057

Ng, J., Lian, S. S., Zhong, L., Collet, C., Foin, N., and Ang, H. Y. (2022). Stent malapposition generates stent thrombosis: Insights from a thrombosis model. *Int. J. Cardiol.* 353, 43–45. doi:10.1016/j.ijcard.2022.02.003

Perry-Nguyen, D., Jung, R. G., Labinaz, A., Duchez, A., Dewidar, O., Simard, T., et al. (2020). Evaluation of an *in vitro* coronary stent thrombosis model for preclinical assessment. *Platelets Edinb.* 31, 167–173. doi:10.1080/09537104.2019.1595564

Poon, E., Thondapu, V., Hayat, U., Barlis, P., Yap, C. Y., Kuo, P. H., et al. (2018). Elevated blood viscosity and microrecirculation resulting from coronary stent malapposition. *J. Biomech. Eng.* 140. doi:10.1115/1.4039306

Qian, S., Ma, T., Zhang, N., Liu, X., Zhao, P., Li, X., et al. (2020). Spatiotemporal transfer of nitric oxide in patient-specific atherosclerotic carotid artery bifurcations with MRI and computational fluid dynamics modeling. *Comput. Biol. Med.* 125, 104015. doi:10.1016/j.compbiomed.2020.104015

Rikhtegar, F., Pacheco, F., Wyss, C., Stok, K. S., Ge, H., Choo, R. J., et al. (2013). Compound *ex vivo* and *in silico* method for hemodynamic analysis of stented arteries. *PLoS One* 8, e58147. doi:10.1371/journal.pone.0058147

Souteyrand, G., Amabile, N., Mangin, L., Chabin, X., Meneveau, N., Cayla, G., et al. (2016). Mechanisms of stent thrombosis analysed by optical coherence tomography: Insights from the national PESTO French registry. *Eur. Heart J.* 37, 1208–1216. doi:10.1093/eurheartj/ehv711

Taniwaki, M., Radu, M. D., Zaugg, S., Amabile, N., Garcia-Garcia, H. M., Yamaji, K., et al. (2016). Mechanisms of very late Drug-Eluting stent thrombosis assessed by optical coherence tomography. *Circulation* 133, 650–660. doi:10.1161/CIRCULATIONAHA.115.019071

Torrado, J., Buckley, L., Duran, A., Trujillo, P., Toldo, S., Valle Raleigh, J., et al. (2018). Restenosis, stent thrombosis, and bleeding complications: Navigating between scylla and charybdis. *J. Am. Coll. Cardiol.* 71, 1676–1695. doi:10.1016/j.jacc.2018.02.023

Wei, L., Wang, J., Chen, Q., and Li, Z. (2021). Impact of stent malapposition on intracoronary flow dynamics: An optical coherence tomography-based patient-specific study. *Med. Eng. Phys.* 94, 26–32. doi:10.1016/j.medengphy.2021.06.002

Zhang, J., Li, G., Qu, Y., Guo, Z., Zhang, S., and Li, D. (2022). Fabrication and hemocompatibility evaluation of a robust honeycomb nanostructure on medical pure titanium surface. *ACS Appl. Mat. Interfaces* 14, 9807–9823. doi:10.1021/acsami.1c22818

frontiers | Frontiers in Bioengineering and Biotechnology

TYPE Brief Research Report
PUBLISHED 12 December 2022
DOI 10.3389/fbioe.2022.1028857

OPEN ACCESS

EDITED BY
Guang-Kui Xu,
Xi'an Jiaotong University, China

REVIEWED BY
Domna Kotsifaki,
Duke Kunshan University, China
Mohamed Omar Abdelgawad,
American University of Sharjah, United Arab Emirates

*CORRESPONDENCE
Zhiguo Zhang,
zzg_100@163.com
Jinhua Zhou,
zhoujinhua@ahmu.edu.cn

SPECIALTY SECTION
This article was submitted to Biomechanics, a section of the journal Frontiers in Bioengineering and Biotechnology

RECEIVED 30 August 2022
ACCEPTED 28 November 2022
PUBLISHED 12 December 2022

CITATION
Zhong Z, Zhang C, Liu R, He J, Yang H, Cheng Z, Wang T, Shao M, Fang S, Zhang S, Shi H, Xue R, Zou H, Ke Z, Zhang Z and Zhou J (2022), Chirality and frequency measurement of longitudinal rolling of human sperm using optical trap.
Front. Bioeng. Biotechnol. 10:1028857.
doi: 10.3389/fbioe.2022.1028857

Chirality and frequency measurement of longitudinal rolling of human sperm using optical trap

Zhensheng Zhong[1], Can Zhang[1], Rui Liu[1], Jun He[1], Han Yang[1,2], Zijie Cheng[3], Tao Wang[1], Meng Shao[1], Shu Fang[1], Shengzhao Zhang[1], Hui Shi[1], Rufeng Xue[2], Huijuan Zou[2], Zeyu Ke[1], Zhiguo Zhang[1,2]* and Jinhua Zhou[1]*

[1]School of Biomedical Engineering, Anhui Provincial Institute of Translational Medicine, Anhui Medical University, Hefei, China, [2]Reproductive Medicine Center, Department of Obstetrics and Gynecology, The First Affiliated Hospital of Anhui Medical University, Hefei, China, [3]School of Science & Technology City, University of London, London, United Kingdom

Motility is one of the most critical features to evaluate sperm quality. As longitudinal rolling of human sperm has long been ignored until recently, its detailed dynamics and cellular biological mechanisms are still largely unknown. Here we report an optical-tweezers-based method to evaluate the chirality and frequency of sperm rotation. According to the intensity distribution patterns of off-focus micron-size particles, we established a method to judge the orientation of the sperm head along the optical axis in the optical trap. Together with the rotation direction of the projection of the sperm head, the chirality of longitudinal rolling of sperm can be measured without the application of three-dimensional tracking techniques or complex optical design. By video tracking optically trapped sperm cells from different patients, both rolling chirality and rolling frequency were analyzed. In this study, all the vertically trapped human sperm cells adopt a right-hand longitudinal rolling. The orientation and rolling frequency but not the rolling chirality of sperm in the optical trap are affected by the trap height. The rotation analysis method developed in this study may have clinical potential for sperm quality evaluation.

KEYWORDS

optical tweezers, sperm, longitudinal rolling, rolling chirality, rolling frequency

1 Introduction

Infertility is a global health issue, which affects about 1/6 of couples worldwide (Sharlip et al., 2002). About 2.5%–12% of male population are infertile (Agarwal et al., 2015). As a result, evaluation of sperm quality plays important roles in both diagnosis of infertility and assisted reproductive technology. When sperm pass through the female reproductive tract, both the cervical mucus and the uterotubal junction served as barriers to filter out sperm with poor motility. Therefore, motility is considered as one of the most

critical parameters to quantify the sperm quality, and poor motility is a common symptom of male infertility.

As sperm swims in three dimensions with relatively large velocity, it is a challenge to image the details of sperm moving trajectory. Currently in most sperm motility studies, conventional microscopy techniques, including bright-field, dark-field, and epifluorescence microscopy, have been applied to provide 2D or semi-quantitative 3D information (Bukatin et al., 2015; Hansen et al., 2019). Holographic microscopy and lens-free imaging technique allow quantitative three-dimensional tracking of sperm swimming (Su et al., 2012; Su et al., 2013; Gong et al., 2021). However, these techniques require precise interferometric optical path and the quality of the reconstructed 3D trajectories of swimming sperm depends on the imaging processing algorithm applied. Moreover, clinical sperm sorting technique require viscous solvent such as polyvinylpyrrolidone to reduce the swimming velocity of sperm. Nevertheless, in solutions with high viscosity or viscoelasticity, the rolling probability of bull sperm head is suppressed and the probability of asymmetry flagellar beating is increased, suggesting that the head rolling is potentially involved in sensation to different rheological properties in the female reproductive tract (Zaferani et al., 2021). These two problems can be solved by optical tweezers technique, which has been wildly applied in manipulation of microorganisms and particles (Kotsifaki et al., 2007; Kotsifaki et al., 2013; Serafetinides et al., 2017; Armstrong et al., 2020). By using optical tweezers, the swimming trajectory of a sperm is localized in a small region in the focal plane, which enables long-time recoding of sperm rotations with high temporal resolution without using viscous or viscoelastic solvents (Chow et al., 2017; Schiffer et al., 2020).

Early optical-tweezers based studies of sperm motility mainly focus on the power and force loaded onto the trapped sperm when it escapes the optical trap (Tadir et al., 1989; Tadir et al., 1990; Araujo et al., 1994; Dantas et al., 1995; Konig et al., 1996). By combining optical tweezers and fluorescent microscopy techniques, Nishimura *et al* revealed that the active digestion of sperm mitochondrial DNA is a two-step process: the mitochondrial nucleoid numbers are decreased gradually during spermatogenesis, and they are eliminated rapidly immediately after fertilization. (Nishimura et al., 2006). Previous studies demonstrated that the pre-trapping and post-trapping swimming speeds of a sperm does not change apparently, so that optical trapping enables quantitatively evaluation of sperm motility (Tadir et al., 1989; Nascimento et al., 2006). Since 2006, several optical trapping techniques were applied to achieve automatic and high-throughput sperm motility analysis (Nascimento et al., 2006; Shao et al., 2007a; Shao et al., 2007b; Nascimento et al., 2008; Shi et al., 2008; Dasgupta et al., 2010). Using optical tweezers, Hyun *et al* analyzed the effects of viscosity on sperm motility, discovered that with the increasing of solution viscosity, the curvilinear velocity of sperm decreases but the minimum laser power for trapping the sperm increases (Hyun et al., 2012).

Despite the great achievement of sperm motility studies using optical tweezers, investigation on rotation of optically trapped sperm was not reported until recently. Chow et al unraveled that the traces of sperm head in the optical trap is a 'rose curve' like trajectory in the focal plane (Chow et al., 2017), and Schiffer et al discovered that the head of optically trapped human sperm displayed longitudinal rolling with full 360° rotations at a frequency of about 4–8 Hz, no matter it is CatSper-deficient or not (Schiffer et al., 2020). Nevertheless, without characterizing the orientation of the sperm in the optical trap, these studies did not focus on the longitudinal rolling chirality of sperm.

In this study, we established a method to analyze the longitudinal rolling dynamics of single sperm based on optical trapping technique (Figure 1). The chirality of longitudinal rolling was determined by recognizing both the rolling direction of the projection of the optically trapped sperm head and the orientation of the head along the optical axis. We also analyzed the rolling frequency of sperm cells of different rolling direction. This method may simplify the sperm rolling research, and may have potential clinical values on single-sperm quality examination, which is crucial in intracytoplasmic sperm injection (ICSI) treatment.

2 Materials and methods

2.1 Sample preparation

The human semen samples were collected from five individual patients seeking *in vitro* fertilization treatment at the Reproductive Medicine Center, the First Affiliated Hospital of Anhui Medical University. All patients gave their informed consents prior to their inclusion in this study. The semen sample was diluted in fertilization medium (Cook Medical, United States) and stored in 4°C before the optical trapping experiment in the same day. The sperm samples were further diluted in 10 to 50 folds using fertilization medium before loading on the observation chamber of the home-built optical tweezers instrument (Figure 1A).

2.2 Single-sperm manipulation using optical tweezers

The single-sperm manipulation experiments were performed in a temperature (25 ± 1 °C) controlled room. The optical trap was generated using a fiber laser with a power of ~400 mW (Amonics Ltd. AFL-1064–37-R-CL, Hong Kong, China) (Figure 1A). The laser beam was expanded by a telescope setup of two lenses (L_1 and L_2 in Figure 1A), and focused by a water immersion objective (×60, NA 1.20, Olympus, Japan). The sperm samples of Patient A, B and C were loaded on a coverslip-made chamber with internal height of ~280 μm. To explore the effect when the optical trap is close to upper surface of

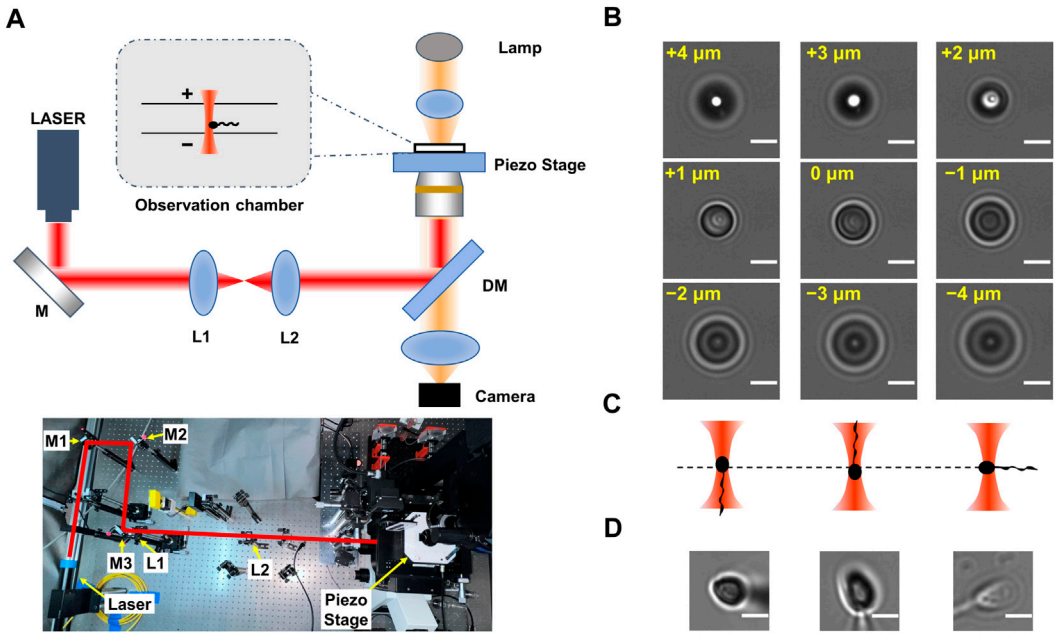

FIGURE 1
Principle of determination of the flagellar orientation of optically trapped sperms. **(A)** Experimental setup. The upper panel is the scheme of experimental setup. Here '+' indicates the orientation that is away from the objective lens and '-' indicates the orientation that is towards the objective lens. The lower panel is the photograph of the optical tweezers device. The optical path is indicated by the red lines. **(B)** Series of images of a 3 μm polystyrene bead stuck at the glass surface. The displacement of the microscope stage was labeled in yellow. **(C)** Scheme of optically trapped sperm with downward, upward, and horizontal flagellum, respectively. **(D)** The typical images of optically trapped sperms. The left, central and right panels showed optically trapped sperms with downward, upward, and horizontal flagellum, respectively. The scale bar of each graph is 3 μm in length.

the chamber, a coverslip-made chamber with internal height of ~140 μm was also used. The optical trap was 10–80 μm above the lower surface of the chamber. Each sperm was trapped for no longer than 20 s. The chamber position was adjusted by a servo-controlled, three-dimensional piezoelectric stage (P-563.3CD, Physik Instrumente, Karlsruhe, Germany). The videos of sperm rotation were recorded by a CMOS camera (MV-SUA231GM-T, MindVision, China) at a frequency of 90 frame per second (for samples from Patient B and C) or 200 frame per second (for samples from Patient A). For each video, a region of interesting (ROI) with a typical size of 90 × 90 pixel was selected using ImageJ, and the rolling direction and rolling frequency of the projection of each sperm head was determined *via* manually frame-by-frame analysis.

3 Results

3.1 Determination of longitudinal rolling charity of sperm head in the optical trap

As the camera records only 2-dimension trajectory of the 3-dimension movement of sperm, to determine the longitudinal rolling charity of sperm, both the relative location between head and tail, as well as the rotation direction of the projection of the sperm head on the camera, should be recognized. The lengths of the head, midpiece and tail of a typical sperm cell are 4–6 μm, 5–7 μm and 50–60 μm, respectively (Cummins and Woodall, 1985), while the focal plane is about 1 μm in depth. If a motile sperm is vertically trapped, most part of its tail should be off-focus. As the fraction of sperm tail adjacent to the midpiece is slightly off-focus, the orientation of sperm tail along the optical axis can be determined by observation of the diffraction pattern of its projection.

By imaging a 3 μm polystyrene bead (ThermoFisher) stuck in the glass surface at difference focal depths (Figure 1B), we determined the relation between the diffraction pattern and the off-focus distance of a micron-size transparent particle. When the particle is 1–4 μm above the focal plane (i.e., it is 1–4 μm more far away from the objective lens than when it is within the focal plane), its central area is brighter than that when the bead center is in the focal plane. Inversely, when the trapped object is 1–4 μm below the focal plane (i.e., it is 1–4 μm closer to the objective lens), its central area is darker.

As the centroid of head of a trapped sperm cell is in the focal plane, whether the sperm tail is above or below the focal

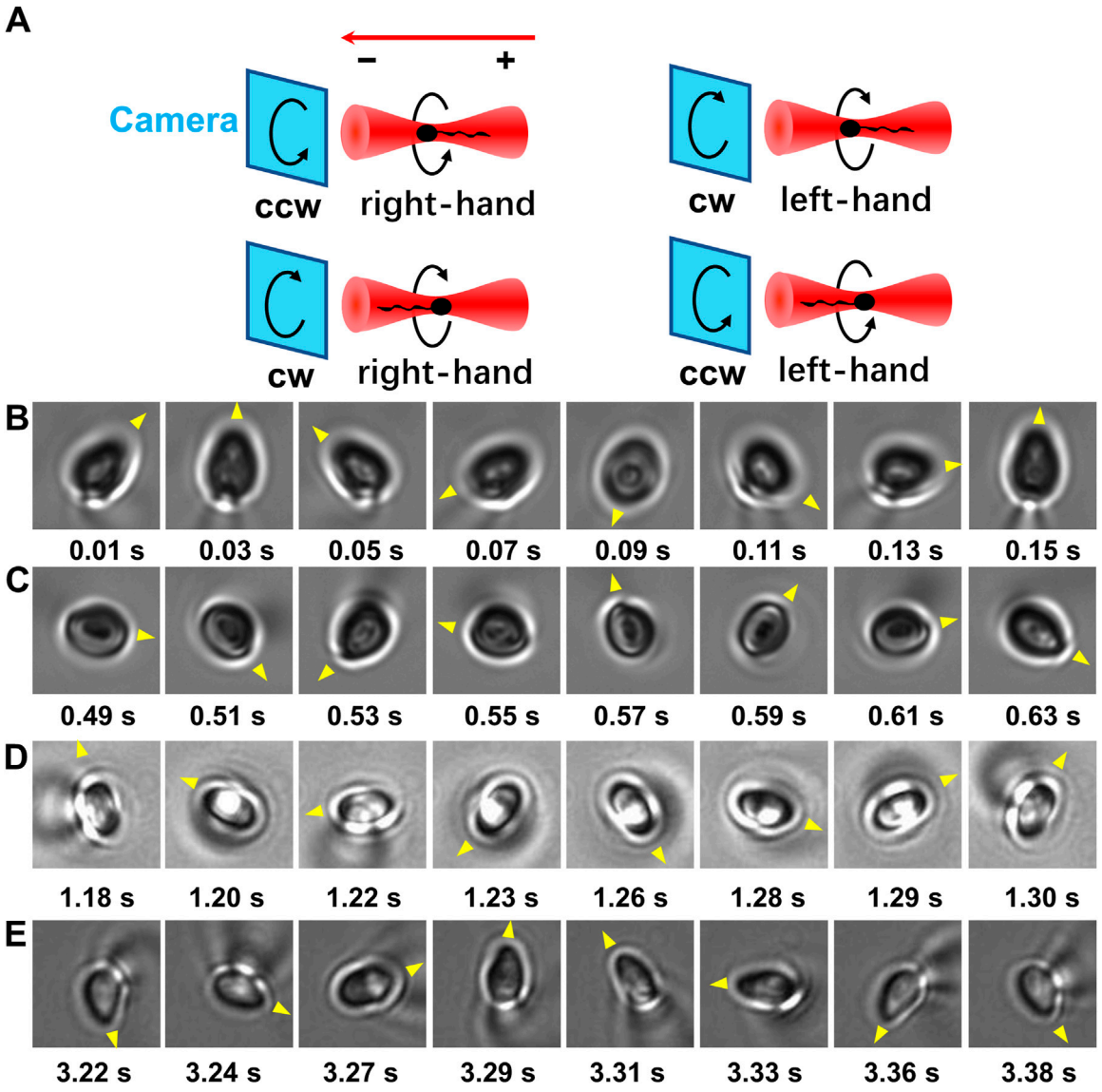

FIGURE 2
The longitudinal rolling chirality of vertically trapped sperm. **(A)** Scheme of vertically trapped sperm with left-hand and right-hand longitudinal rolling chirality. The relations are showed among the orientation of vertically trapped sperm, the rotation direction of the sperm head projection, and the longitudinal rolling chirality of the sperm. Here the red arrow indicates the propagation direction of illimitation light, '+' indicates the orientation of the sperm tail that is away from the objective lens, and '–' indicates the orientation that is towards the objective lens. Noticed that the images of the rolling sperm are recorded by the camera in bottom view. **(B)** A right-handed rolling sperm from Patient A with an upward tail and a counter-clockwise rolling head projection. **(C)** A right-handed rolling sperm from Patient A with a downward tail and a clockwise rolling head projection. **(D)** A right-handed rolling sperm from Patient B with an upward tail and a counter-clockwise rolling head projection. **(E)** A right-handed rolling sperm from Patient C with an upward tail and a counter-clockwise rolling head projection. The yellow triangles indicate the rotation direction of the projection of each sperm head.

plane can be determined according to the relation between the diffraction pattern and the off-focus distance of micron-size object. Once the relative position between the head and tail of the trapped sperm is determined, the orientation of the sperm cell in the optical trap can be determined. Specifically, if the tail of a vertically trapped sperm is downward, it should be beneath the focal plane (i.e., closer to the objective lens) (Figure 1C, left panel). In this situation, the axial part of the tail projection is darker than its edge part as well as the center of projection of the sperm head (Figure 1D, left panel). Inversely, when the sperm tail is downward, it should be above the focal plane (Figure 1C, middle panel). In this case, the axial part of the tail projection is brighter than its edge part as well as the center of projection of the sperm head (Figure 1D,

TABLE 1 Summary of rotation and orientation of optically trapped sperm cells with different trap heights.

	Trap height (μm)	Tail orientation			Number of sperm cells with pausing or stuck behavior[a]	Head rolling frequency (Hz) (mean ± s.e.m.)	Head rolling frequency[a] (Hz) (mean ± s.e.m.)
		Horizontal	Upward	Downward			
A	10	9	2	0	0	7.7 ± 1.1	7.7 ± 1.1
	30	7	4	0	6	4.0 ± 1.2	8.0 ± 0.4
	50	1	4	6	4	5.0 ± 0.9	6.5 ± 0.8
	80	0	2	9	9	2.0 ± 0.7	NS[b]
B	10	82	18	0	11	8.0 ± 0.4	8.7 ± 0.4
C	10	80	10	0	2	7.4 ± 0.3	7.5 ± 0.3
D	120[c]	1	1	28	1	8.6 ± 0.6	8.6 ± 0.6
E	120[c]	1	1	28	1	5.0 ± 0.4	5.1 ± 0.4

[a]Sperm cells with pausing or stuck behavior are excluded.
[b]Sample size is too small to be statistically significant.
[c]The optical trap is 20 μm below the upper surface of the chamber.

middle panel). By contrast, if the sperm is horizontally trapped (Figure 1C, right panel), the intensity distribution pattern of the tail projection is close to that of the sperm head (Figure 1D, right panel). As a result, by comparing the diffraction pattern of the sperm head with that of the tail, the orientation of the sperm head along z axis can be determined. Combining with the rotation direction of the projection of the sperm head from the video, the chirality of the longitudinal rolling of vertically trapped sperm can be further recognized (Figure 2 and Supplementary Videos S1, S2). In detail, a vertically trapped sperm rolls right-handedly along the longitudinal axis, if its tail is upward and the projection of the head rotates counterclockwise, or its tail is downward and the projection of the head rotates clockwise (Figure 2A, upper left and lower left panels). In contrast, a vertically trapped sperm rolls left-handedly if its tail is upward and the projection of the head rotates clockwise, or its tail is downward and the projection of the head rotates counterclockwise (Figure 2A, upper right and lower right panels). Interestingly, we also recorded motion of a morphologically abnormal sperm in previous study, whose trapping position was the midpiece (Supplementary Video S3), and its projection is obviously different from those of morphologically normal spern cells in the trap.

3.2 Effect of optical trap height on the longitudinal rolling of human sperm

As the full length of normal human sperm is 60–70 μm, the height of the optical trap, i.e., the distance between the optical trap center and the lower surface of the chamber, may affect the orientation and rolling behavior of the trapped sperm. To evaluate this effect, 11 sperm cells donated by Patient A were arrested by optical trap when the trap height is 10 μm, and the rolling movement of each sperm was recorded by the camera. Then, the optical trap height was adjusted by controlling the piezo stage, and the rolling movement of the same sperm was also recorded when the trap height was increased to 30, 50, and 80 μm, respectively (Table 1). When the trap height is 10 μm, 9 sperm cells are horizontally oriented and two sperm cells are with upward tail, and no obvious pausing observed during the rolling movement of the sperms. With the trap height increasing, the ratio of horizontally oriented sperm decreased and ratio of sperm with downward tail increased. Moreover, the ratio of sperm with pausing and stuck events also increased. Here, 'pausing' is defined as the longitudinal rolling stops but it restarts later, and 'stuck' is defined as the longitudinal rolling stops and did not restart during the observation. Worth mentioning, those stuck sperm cells without obvious longitudinal rolling exhibit swinging-like movement (Supplementary Video S4). With the trap height increasing, the averaged rolling frequency of the vertically trapped sperm cells decreased. However, when the sperm cells with pausing and stuck events are excluded, the averaged rolling frequency of the vertically trapped sperm cells did not change significantly with different trap heights (Table 1).

3.3 Human sperm from each patient rolls right-handedly

Interestingly, sperm cells with upward tail exhibited counterclockwise rotated projection of the head (Figure 2B), and sperm cells with downward tail exhibited clockwise rotated projection of the head (Figure 2C), i.e., all the vertical trapped sperm cells from Patient A adopted right-handed longitudinal rolling.

TABLE 2 Head rolling frequencies of optically trapped sperm cells with different orientation.

Tail orientation	Number of sperm cells[a]	Head rolling frequency[a] (Hz) (mean ± s.e.m.)
horizontal	163	8.3 ± 0.3
upward	37	6.7 ± 0.6
downward	60	6.9 ± 0.4

[a]Sperm cells with pausing or stuck behavior are excluded.

To further confirm the longitudinal rolling charity of human sperm, 190 motile sperm cells from two more patients were trapped and analyzed using optical tweezers with the trap height of 10 μm (Table 1). Briefly, 162 and 28 sperm cells were trapped with horizontal and upward tail, respectively. No sperm cells with downward tail were observed. For all sperm cells from both patient B and C, all those sperm cells with upward tail exhibited counterclockwise rotated projection of the head (Figures 2D,E), i.e., all the vertical trapped sperm cells adopted right-handed longitudinal rolling, which are the same as those from Patient A.

To explore the effect when the optical trap is close to upper surface of the chamber, we performed the optical trapping experiment of sperm cells from two more patients (D and E) in a thinner chamber (internal height ~140 μm), and the trap height was set to 120 μm, i.e. ~20 μm away from the upper surface (Table 1). Interestingly, in this experimental condition, for each patient, 1, 1 and 28 sperm cells are with horizontal, upward and downward tail, respectively. All the vertical trapped sperm cells from Patient D and E adopted right-handed longitudinal rolling, further indicating the right-handed chirality of longitudinal rolling of human sperm. The asymmetry of the optical force along the z axis may be the major factor leading to the less horizontally oriented sperm cells when the trap is close to the upper surface than to the lower surface, as the maximum restoring force along the negative half of z axis is larger than along the positive half of z-axis (Zhou et al., 2012).

The head rolling frequencies of optically trapped sperm cells with different orientation were also summarized in Table 2. The head rolling frequencies of trapped sperm cells with horizontal, upward and downward tail are 8.3 ± 0.3, 6.7 ± 0.6 and 6.9 ± 0.4 Hz, respectively. The frequencies we observed are in consistent with previous reported values of 4–8 Hz (Schiffer et al., 2020).

4 Discussion

When the sperm head is deviated from the trap center, a torque on the sperm head around the trap center is exerted by the optical field. The sperm head in an optical trap can be considered as a triaxial ellipsoid, and the torque exerted by the optical field automatically regulates the orientation of the ellipsoid to its longest axis parallel to the optic axis, according to our previous theoretical calculations (Zhou et al., 2012; Shao et al., 2019). Because the longest axis of sperm head is parallel to the longitudinal axis of the sperm, sperm cells tend to be vertically trapped. Another torque generated by the beating of sperm tail leads to the longitudinal rolling of the sperm head. These two torques are not in balance, resulting in the rolling of sperm head in the optical trap.

In this study, we unraveled the effect of optical trap height on the rolling behavior of the trapped sperm. Our study indicates that, when the optical trap is close to the lower surface of the chamber, the tail of the trapped sperm is compelled to adopt horizontal or upward orientation, resulting in less interaction with the surface of the chamber. With trap height increasing, the probability of the sperm tail interacts with the surface increases and the pausing and stuck events increase. Noticed that although the normal sperm cell is 70 μm in length, the sperm cells we investigated in the experiment are donated from patients asking for IVF treatment. It is possible that the tail of the trapped sperm is abnormally long, so it may interact with the lower surface of the chamber, even when the trap height is 80 μm above the lower surface. The uncertainty of the trap height may also contribute to the possibility of the interaction. We measured the axial shifting of the optical trap (~1.6 μm/min) by recording the image of a bead stuck in the lower surface of the chamber. These results indicate that the interaction between the sperm tail and the surface of the glass chamber may bring tortional constraint to the sperm and pause the longitudinal rolling of sperm.

In this study, the frequencies of longitudinal rolling of optically trapped sperm were measured manually. The averaged rolling frequencies of sperm cells for five patients are close, and are consistent with previous reports (Smith et al., 2009; Subramani et al., 2014; Schiffer et al., 2020). Besides the longitudinal rolling, the optically trapped sperm may display other rotation motions, such as the precession of the rolling axis around the optical trap center, which increases the complexity of intensity pattern of the rolling sperm by algorithm. Interestingly, it is likely that the right-handed rolling human sperm prefers a left-handed presession (Supplementary Video S5), whose projection of the head on the camera is in accordance with the 'rose curve' like trajectory reported previously (Chow et al., 2017). To achieve automatic measurement of longitudinal rolling frequency in bright-field, physical parameters, such as the coordination of the sperm centroid may be considered in the future.

Previous studies have been reported that counterion and viscosity of medium may significantly affect the rolling behavior of human sperm. Chiffer et al. reported that the rotation frequency of human sperm increases with increasing of bicarbonate concentration, but not with increasing of calcium concentration (Schiffer et al., 2020). Viscosity as well as viscoelasticity of the medium also play complicated roles in the motion of sperm (Schiffer et al., 2020; Zaferani et al., 2021). In this study, to avoid uncertain effects on sperm motion as well as on the optical trap causing by the medium, a standard sperm dilution medium for *in vitro* fertilization (Cook Medical, United States) was used. In the future, using the method developed in this study, we will explore how chemical and physical properties of medium affect the motion and optical trapping of human sperm.

In current clinical practice of ICSI, the single sperm cell for injection is picked manually by trained technicians, which is laborious and the fertilization rate relies on the experience of the technician (Oseguera-Lopez et al., 2019). On the other hand, optical tweezers have been demonstrated as an efficient tool for spermatozoa isolation (Shao et al., 2007b; Auka et al., 2019). Combining the optical-tweezers based single-cell manipulation technique with the sperm rotation characterization method established in this study, automatic evaluation and isolation of single sperm may be achieved in the future, which may reduce the manual subjective error and increase the efficiency of sperm preparation during the ICSI procedures.

5 Conclusion

In summary, we established an optical-tweezers based method to determine the chirality of sperm rotation using optical tweezers, in which three-dimensional tracking technique is not required. Without using complex optical design or data analysis algorithm, the method we established in this study may simplify the research on sperm rotation. Our study indicates that human sperm prefers right-hand longitudinal rolling. The effect of optical trap height on the sperm longitudinal behavior was also investigated in this study.

Data availability statement

The original contributions presented in the study are included in the article/Supplementary Material, further inquiries can be directed to the corresponding authors.

Ethics statement

The studies involving human participants were reviewed and approved by Biomedical Ethics Committee of Anhui Medical University. The patients/participants provided their written informed consent to participate in this study.

Author contributions

ZZ (15th author) and JZ conceived the idea. HY, RX, and HZ prepared the human sperm sample. ZZ (1st author), CZ, RL, and ZK performed the optical trapping experiment. ZZ (1st author), CZ, and JH analyzed the data. ZZ (1st author) and JZ wrote and edited the manuscript. ZC, TW, SF, SZ, and HS contributed to analyzing the data and reviewing the manuscript. MS contributed to constructing the experimental setup. All the authors reviewed and revised the manuscript.

Funding

This research was financially supported by the Key Research and Development Program of Anhui Province in China (2022a05020028), Research Fund of Anhui Institute of Translational Medicine (2021zhyx-B16), Natural Science Foundation of Anhui Province in China (1908085MA14 and 2208085MC54), Doctoral Start-up Research Fund of Anhui Medical University (1403019201), and National Natural Science Foundation of China (12004008).

Conflict of interest

The authors declare that the research was conducted in the absence of any commercial or financial relationships that could be construed as a potential conflict of interest.

Publisher's note

Supplementary material

The Supplementary Material for this article can be found online at: https://www.frontiersin.org/articles/10.3389/fbioe.2022.1028857/full#supplementary-material

References

Agarwal, A., Mulgund, A., Hamada, A., and Chyatte, M. R. (2015). A unique view on male infertility around the globe. *Reprod. Biol. Endocrinol.* 13, 37. doi:10.1186/s12958-015-0032-1

Araujo, E., Jr., Tadir, Y., Patrizio, P., Ord, T., Silber, S., Berns, M. W., et al. (1994). Relative force of human epididymal sperm. *Fertil. Steril.* 62 (3), 585–590. doi:10.1016/S0015-0282(16)56950-7

Armstrong, D. J., Nieminen, T. A., Stilgoe, A. B., Kashchuk, A. V., Lenton, I. C. D., and Rubinsztein-Dunlop, H. (2020). Swimming force and behavior of optically trapped micro-organisms. *Optica* 7 (8), 989–994. doi:10.1364/Optica.394232

Auka, N., Valle, M., Cox, B. D., Wilkerson, P. D., Dawson Cruz, T., Reiner, J. E., et al. (2019). Optical tweezers as an effective tool for spermatozoa isolation from mixed forensic samples. *PLoS One* 14 (2), e0211810. doi:10.1371/journal.pone.0211810

Bukatin, A., Kukhtevich, I., Stoop, N., Dunkel, J., and Kantsler, V. (2015). Bimodal rheotactic behavior reflects flagellar beat asymmetry in human sperm cells. *Proc. Natl. Acad. Sci. U. S. A.* 112 (52), 15904–15909. doi:10.1073/pnas.1515159112

Chow, K. W., Preece, D., and Berns, M. W. (2017). Effect of red light on optically trapped spermatozoa. *Biomed. Opt. Express* 8 (9), 4200–4205. doi:10.1364/BOE.8.004200

Cummins, J. M., and Woodall, P. F. (1985). On mammalian sperm dimensions. *Reproduction* 75 (1), 153–175. doi:10.1530/jrf.0.0750153

Dantas, Z. N., Araujo, E., Jr., Tadir, Y., Berns, M. W., Schell, M. J., and Stone, S. C. (1995). Effect of freezing on the relative escape force of sperm as measured by a laser optical trap. *Fertil. Steril.* 63 (1), 185–188. doi:10.1016/s0015-0282(16)57316-6

Dasgupta, R., Ahlawat, S., Verma, R. S., Shukla, S., and Gupta, P. K. (2010). Optical trapping of spermatozoa using Laguerre-Gaussian laser modes. *J. Biomed. Opt.* 15 (6), 065010. doi:10.1117/1.3526362

Gong, A., Rode, S., Gompper, G., Kaupp, U. B., Elgeti, J., Friedrich, B. M., et al. (2021). Reconstruction of the three-dimensional beat pattern underlying swimming behaviors of sperm. *Eur. Phys. J. E* 44 (7), 87. doi:10.1140/epje/s10189-021-00076-z

Hansen, J. N., Rassmann, S., Jikeli, J. E., and Wachten, D. (2019). SpermQ-A simple analysis software to comprehensively study flagellar beating and sperm steering. *Cells* 8 (1), 10. doi:10.3390/cells8010010

Hyun, N., Chandsawangbhuwana, C., Zhu, Q., Shi, L. Z., Yang-Wong, C., and Berns, M. W. (2012). Effects of viscosity on sperm motility studied with optical tweezers. *J. Biomed. Opt.* 17 (2), 025005. doi:10.1117/1.JBO.17.2.025005

Konig, K., Svaasand, L., Liu, Y., Sonek, G., Patrizio, P., Tadir, Y., et al. (1996). Determination of motility forces of human spermatozoa using an 800 nm optical trap. *Cell. Mol. Biol. (Noisy-le-grand)* 42 (4), 501–509.

Kotsifaki, D., Makropoulou, M., and Serafetinides, A. (2013). "Near infrared optical tweezers and nanosecond ablation on yeast and algae cells," in *Seventeenth international school on quantum electronics: Laser physics and applications*. Editors T. N. Dreischuh and A. T. Daskalova (Washington, United States: SPIE).

Kotsifaki, D., Makropoulou, M., and Serafetinides, A. (2007). "Ultra-violet laser microbeam and optical trapping for cell micromanipulation," in *Saratov fall meeting 2006*. Editor V. V. Tuchin (Washington, United States: SPIE).

Nascimento, J. M., Botvinick, E. L., Shi, L. Z., Durrant, B., and Berns, M. W. (2006). Analysis of sperm motility using optical tweezers. *J. Biomed. Opt.* 11 (4), 044001. doi:10.1117/1.2337559

Nascimento, J. M., Shi, L. Z., Tam, J., Chandsawangbhuwana, C., Durrant, B., Botvinick, E. L., et al. (2008). Comparison of glycolysis and oxidative phosphorylation as energy sources for mammalian sperm motility, using the combination of fluorescence imaging, laser tweezers, and real-time automated tracking and trapping. *J. Cell. Physiol.* 217 (3), 745–751. doi:10.1002/jcp.21549

Nishimura, Y., Yoshinari, T., Naruse, K., Yamada, T., Sumi, K., Mitani, H., et al. (2006). Active digestion of sperm mitochondrial DNA in single living sperm revealed by optical tweezers. *Proc. Natl. Acad. Sci. U. S. A.* 103 (5), 1382–1387. doi:10.1073/pnas.0506911103

Oseguera-Lopez, I., Ruiz-Diaz, S., Ramos-Ibeas, P., and Perez-Cerezales, S. (2019). Novel techniques of sperm selection for improving IVF and ICSI outcomes. *Front. Cell Dev. Biol.* 7, 298. doi:10.3389/fcell.2019.00298

Schiffer, C., Rieger, S., Brenker, C., Young, S., Hamzeh, H., Wachten, D., et al. (2020). Rotational motion and rheotaxis of human sperm do not require functional CatSper channels and transmembrane Ca2+ signaling. *EMBO J.* 39 (4), e102363. doi:10.15252/embj.2019102363

Serafetinides, A., Makropoulou, M., Kotsifaki, D., and Tsigaridas, G. (2017). "Biophotonics for imaging and cell manipulation: Quo vadis?," in *International conference and school on quantum electronics "laser physics and applications" - icsqe 2016*. Editors T. Dreischuh, S. Gateva, A. Daskalova, and A. Serafetinides (Washington, United States: SPIE).

Shao, B., Nascimento, J. M., Shi, L. Z., and Botvinick, E. L. (2007a). Automated motile cell capture and analysis with optical traps. *Methods Cell Biol.* 82, 601–627. doi:10.1016/S0091-679X(06)82021-2

Shao, B., Shi, L. Z., Nascimento, J. M., Botvinick, E. L., Ozkan, M., Berns, M. W., et al. (2007b). High-throughput sorting and analysis of human sperm with a ring-shaped laser trap. *Biomed. Microdevices* 9 (3), 361–369. doi:10.1007/s10544-006-9041-3

Shao, M., Zhang, S., Zhou, J., and Ren, Y.-X. (2019). Calculation of optical forces for arbitrary light beams using the Fourier ray method. *Opt. Express* 27 (20), 27459–27476. doi:10.1364/OE.27.027459

Sharlip, I. D., Jarow, J. P., Belker, A. M., Lipshultz, L. I., Sigman, M., Thomas, A. J., et al. (2002). Best practice policies for male infertility. *Fertil. Steril.* 77 (5), 873–882. doi:10.1016/s0015-0282(02)03105-9

Shi, L. Z., Nascimento, J. M., Chandsawangbhuwana, C., Botvinick, E. L., and Berns, M. W. (2008). An automatic system to study sperm motility and energetics. *Biomed. Microdevices* 10 (4), 573–583. doi:10.1007/s10544-008-9169-4

Smith, D. J., Gaffney, E. A., Gadelha, H., Kapur, N., and Kirkman-Brown, J. C. (2009). Bend propagation in the flagella of migrating human sperm, and its modulation by viscosity. *Cell Motil. Cytoskelet.* 66 (4), 220–236. doi:10.1002/cm.20345

Su, T.-W., Xue, L., and Ozcan, A. (2012). High-throughput lensfree 3D tracking of human sperms reveals rare statistics of helical trajectories. *Proc. Natl. Acad. Sci. U. S. A.* 109 (40), 16018–16022. doi:10.1073/pnas.1212506109

Su, T. W., Choi, I., Feng, J., Huang, K., McLeod, E., and Ozcan, A. (2013). Sperm trajectories form chiral ribbons. *Sci. Rep.* 3, 1664. doi:10.1038/srep01664

Subramani, E., Basu, H., Thangaraju, S., Dandekar, S., Mathur, D., and Chaudhury, K. (2014). Rotational dynamics of optically trapped human spermatozoa. *Sci. World J.* 2014, 1–7. doi:10.1155/2014/154367

Tadir, Y., Wright, W. H., Vafa, O., Ord, T., Asch, R. H., and Berns, M. W. (1990). Force generated by human sperm correlated to velocity and determined using a laser generated optical trap. *Fertil. Steril.* 53 (5), 944–947. doi:10.1016/S0015-0282(16)53539-0

Tadir, Y., Wright, W. H., Vafa, O., Ord, T., Asch, R. H., and Berns, M. W. (1989). Micromanipulation of sperm by a laser generated optical trap. *Fertil. Steril.* 52 (5), 870–873. doi:10.1016/S0015-0282(16)53057-X

Zaferani, M., Javi, F., Mokhtare, A., Li, P., and Abbaspourrad, A. (2021). Rolling controls sperm navigation in response to the dynamic rheological properties of the environment. *Elife* 10, e68693. doi:10.7554/eLife.68693

Zhou, J. H., Zhong, M. C., Wang, Z. Q., and Li, Y. M. (2012). Calculation of optical forces on an ellipsoid using vectorial ray tracing method. *Opt. Express* 20 (14), 14928–14937. doi:10.1364/OE.20.014928

frontiers | Frontiers in Bioengineering and Biotechnology

TYPE Original Research
PUBLISHED 23 January 2023
DOI 10.3389/fbioe.2023.1080241

OPEN ACCESS

EDITED BY
Guang-Kui Xu,
Xi'an Jiaotong University, China

REVIEWED BY
Dechang Li,
Zhejiang University, China
Michael Samaan,
University of Kentucky, United States

*CORRESPONDENCE
He Gong,
gonghe@jlu.edu.cn

SPECIALTY SECTION
This article was submitted to Biomechanics, a section of the journal Frontiers in Bioengineering and Biotechnology

RECEIVED 26 October 2022
ACCEPTED 09 January 2023
PUBLISHED 23 January 2023

CITATION
Gao J, Ren P and Gong H (2023), Morphological and mechanical alterations in articular cartilage and subchondral bone during spontaneous hip osteoarthritis in guinea pigs.
Front. Bioeng. Biotechnol. 11:1080241.
doi: 10.3389/fbioe.2023.1080241

Morphological and mechanical alterations in articular cartilage and subchondral bone during spontaneous hip osteoarthritis in guinea pigs

Jiazi Gao[1], Pengling Ren[2] and He Gong[1]*

[1]Department of Engineering Mechanics, Nanling Campus, Jilin University, Changchun, China, [2]Department of Radiology, Beijing Friendship Hospital, Capital Medical University, Beijing, China

Objectives: This study aimed to investigate the morphological and mechanical changes in articular cartilage and subchondral bone during spontaneous hip osteoarthritis in guinea pigs.

Materials and methods: Hip joints of guinea pigs were investigated at 1, 3, 6, and 9 months of age (hereafter denoted as 1 M, 3 M, 6 M, and 9 M, respectively; n = 7 in each group). Morphological and mechanical alterations during spontaneous hip osteoarthritis in guinea pigs were investigated. The alterations included the micromechanical properties of articular cartilage (stiffness and creep deformation), microstructure of the subchondral bone (bone mineral density, bone volume fraction, trabecular thickness, trabecular number, and trabecular separation), micromorphology of the articular cartilage, and surface nanostructure (grain size and roughness) of the articular cartilage and subchondral bone.

Results: Micromechanical properties of articular cartilage in 1 M showed the lowest stiffness and highest creep deformation with no significant differences in stiffness or creep deformation amongst 3 M, 6 M, and 9 M. Articular cartilage thickness decreased with age. The earliest degeneration of articular cartilage occurred at 6 months of age, characterised by surface unevenness and evident chondrocytes reduction in micromorphology, as well as increased grain size and decreased roughness in nanostructure. No degeneration at micro- or nanostructure of subchondral bone was observed before 9 months.

Conclusion: Morphological degeneration of cartilage occurred before degeneration of mechanical properties. Meanwhile, degeneration of cartilage occurred before degeneration of subchondral bone during hip osteoarthritis. The current study provided novel insights into the structural and micromechanical interaction of hip osteoarthritis, which can serve as a theoretical basis for understanding the formation and progression of osteoarthritis.

KEYWORDS

hip osteoarthritis, cartilage, subchondral bone, morphology, mechanical properties

Introduction

Osteoarthritis is a disease of whole joints and characterised by cartilage degradation, joint inflammation, and abnormal bone remodeling in subchondral bone. The occurrence and development of osteoarthritis are closely related to trauma, overload, and aging (Castaño-Betancourt et al., 2013; Richmond et al., 2013; Barr et al., 2015; Glyn-Jones et al., 2015). Osteoarthritis is a complex condition affecting whole joints, in which degenerations of cartilage and subchondral bone play a pivotal role (Wang et al., 2011; Glyn-Jones et al., 2015; Cucchiarini et al., 2016).

Changes in cartilage morphology and mechanical properties can be used to evaluate the progression of osteoarthritis (Franz et al., 2001; Kraus et al., 2010; Rutgers et al., 2010; Iijima et al., 2014; Zuo et al., 2016; Gatti et al., 2022). Ongoing cartilage destruction may lead to progressive loss in joint function. The characteristic features of articular cartilage degeneration include phenotypic changes in cells, chondrocyte hypertrophy, apoptosis, and progressive fibrillation (Aizah et al., 2019; Harlaar et al., 2022; Salucci et al., 2022). Cartilage covering the whole joint surface is the tissue that directly bears the load. Mechanical failure of articular cartilage may lead to wear of the articular surfaces, pain, and eventual loss of joint function. The cartilage elastic modulus reportedly declines with osteoarthritis progression (Wilusz et al., 2013; Harlaar et al., 2022). The reduction in cartilage compressive stiffness is considered to be one of the first detectable signs of articular cartilage degeneration, that is, changes in mechanical properties occur prior to alterations in the composition of the cartilage matrix (Franz et al., 2001). Thus, evaluating the mechanical properties of the cartilage is important to investigate the degeneration process of osteoarthritis (Iijima et al., 2014; Zuo et al., 2016). Limited by small sample sizes and sample thicknesses, indentation technique is considered to be adequate to characterise the stiffness variation in the articular cartilage for the quantitative assessment of early articular cartilage degeneration (Franz et al., 2001).

Although osteoarthritis was once considered a primary disorder of articular cartilage, the subchondral bone structure is now generally accepted to play an important role in the pathological changes of osteoarthritis. Subchondral bone is particularly associated with cartilage degeneration and is thus a tissue of great interest in the investigation of osteoarthritis. The microstructure of subchondral bone determines its capacity to absorb, distribute, and transfer mechanical loading (Huebner et al., 2002; Barr et al., 2015; Zuo et al., 2016; Finnilä et al., 2017; Peters et al., 2018). Abnormal bone remodeling could be observed during the degeneration process of osteoarthritis. The subchondral bone shows thicker subchondral plate, increased bone density and trabecular bone volume fraction, and decreased trabecular separation and structural model index (SMI) with aggravation of osteoarthritis (Carlson et al., 1996; Ding et al., 2006; Wang et al., 2013; Finnilä et al., 2017), which are considered to result from abnormal mechanoregulated bone adaptation (Iijima et al., 2014).

Osteoarthritis alters the structures of joints at the macro- and microscales and influences the nanostructures of subchondral bone and cartilage. To determine the surface nanostructure of biological tissue (such as grain size and roughness), the use of atomic force microscopy (AFM) is feasible because of its ultrahigh spatial resolution, fine force sensitivity, and versatility under various conditions (Dufrêne, 2002; Hsieh et al., 2008; Stolz et al., 2009; Darling et al., 2010; Wen et al., 2012; Ghosh et al., 2013; Han et al., 2017; Danalache et al., 2019; Plaut et al., 2019). AFM could be used to investigate changes in the morphological properties of chondrocytes and collagen fibrils, as well as topographical variations that may occur in osteoarthritis (Hsieh et al., 2008; Wen et al., 2012), thereby providing a reliable basis for in-depth studies on the osteoarthritis process.

Numerous studies have investigated the mechanical properties and morphology of cartilage and subchondral bone for knee osteoarthritis in different ways, but few studies have been conducted on hip osteoarthritis (Li et al., 2013; Finnilä et al., 2017; Fang et al., 2018; Aizah et al., 2019; Gatti et al., 2022). The hip is the largest weight-bearing joint of human body. Hip osteoarthritis is a disease of whole joints and considered to be one of the main causes of chronic pain and disability in the elderly (Castaño-Betancourt et al., 2013). Investigations on morphological and biochemical changes in hip during the process of osteoarthritis, as well as the relationships between cartilage degeneration and subchondral bone degeneration, is important to understand the causation of osteoarthritis and to select targets for osteoarthritis prevention and treatment. In the current work, we hypothesize that the morphological and mechanical alterations in cartilage and subchondral bone are the main factors inducing hip osteoarthritis. Accordingly, in the current work, hip joints of guinea pigs at 1, 3, 6, and 9 months were investigated to enable a systematic analysis on the morphological and mechanical alterations of articular cartilage and subchondral bone during naturally occurring osteoarthritis, including the microstructure of subchondral bone, surface nanostructures of cartilage, and subchondral bone, as well as the micromechanical properties of articular cartilage, which may provide a basis for the prevention and treatment of osteoarthritis.

Materials and methods

Sample preparation

A total of 28 male Dunkin–Hartley guinea pigs aged 1, 3, 6, and 9 months old (hereafter denoted as 1 M, 3 M, 6 M, and 9 M; seven rats in each age group) were sacrificed *via* intraperitoneal injection of 100 mg/kg pentobarbital. Bilateral proximal femurs were harvested. The right proximal femurs were fixed with 4% paraformaldehyde (PFA) at room temperature for 24 h and then prepared for micro-computed tomography (micro-CT) scanning and morphological analyses. The left proximal femurs were stored at −20 °C prior to micromechanical test and AFM analyses. All procedures were approved by the Ethics Committee of The First Hospital of Jilin University (No. 2020–010).

Bone mineral density and microstructural analysis of subchondral bone

Radiographic images of the proximal femur were obtained with a high-resolution micro-CT system (Skyscan 1,076, Skyscan, Belgium) and then used to determine the microstructure of

subchondral bone and assess the radiographic images of the proximal femur. The spatial resolution for proximal femur scanning was set to 18 μm, and the specimens were scanned at 70 kV and 142 μA with Al 1.0 mm filter. The region of interest of subchondral trabecular bone was selected as the region between the subchondral plate and growth plate. Bone mineral density (BMD), bone volume fraction (BV/TV), trabecular thickness (Tb.Th), trabecular number (Tb.N) and trabecular separation (Tb.Sp) were calculated based on the micro-CT image data sets by using CTAn software (CTAn, Skyscan, Belgium).

Micromorphological analysis of cartilage

After micro-CT scanning, the right femoral heads were fixed in 4% PFA for 3 days and decalcified in ethylenediaminetetraacetic acid for 2 weeks. The samples were then dehydrated in a series of alcohol baths (80%, 90%, and 100%, each for 12 h) before embedding in paraffin. Serial sagittal sections (6 μm thick) were obtained using a rotary microtome (Leica RM2255, Germany). Safranin O/Fast green staining was performed to assess the articular cartilage micromorphology.

Micromechanical test of articular cartilage

Samples were thawed for 6 h at room temperature and attached with cyanoacrylate cement to a testing chamber filled with phosphate buffered saline. An electronic universal testing machine (AG-X plus, Shimadzu, Kyoto, Japan) with a 0.5 mm diameter flat-ended indenter was used, and the indentation test of articular cartilage was performed as described by Iijima et al. (Iijima et al., 2014; Iijima et al., 2015; Iijima et al., 2017). A preload of 0.01 N was applied and equilibration was conducted for 100 s, followed by loading at a strain rate of 0.005 mm/s up to 0.1 N, which was maintained for 300 s. Dynamic stiffness (0.01 N load divided by displacement in the load–displacement curve; Iijima et al., 2017) and creep deformation (deformation of the cartilage from before to after the application of the test load for 300 s at 0.1 N) were obtained (Iijima et al., 2014; Iijima et al., 2015; Iijima et al., 2017).

Nanostructure analysis of articular cartilage and subchondral bone

Proximal femoral bone specimens with a thickness of 2 mm were cut perpendicular to the femoral neck axis. The samples were then dehydrated in a series of alcohol baths (80%, 90%, and 100%, each for 24 h), ultrasonically cleaned in alcohol for 5 min, and naturally dried at room temperature (Ren et al., 2018).

Each sample was attached horizontally onto the sample disk and imaged with an AFM system (Agilent 5,500, Agilent Technologies, United States). Imaging was performed under ambient conditions in standard AFM tapping mode using a commercial Silicon AFM probe (Tap300AI-G, Budget Sensors Instruments, Bulgaria) with a 125 μm cantilever length, a 40 Nm^{-1} constant force, a 300 kHz resonant frequency, and a tip radius less than 10 nm. Articular cartilage and subchondral bone were scanned and the images were obtained (positions of articular cartilage and subchondral bone for AFM scanning are shown in Figure 1). The size of mineral grains and roughness were measured using NanoScope Analysis version 1.4.0. (Milovanovic et al., 2011).

Statistical analysis

Data analysis was performed with SPSS 19.0 software (SPSS statistics, IBM Inc., United States). For each group the median and interquartile ranges (IOR, 25th-75th percentile) were calculated. The differences of all the age groups were analysed by the Kruskal–Wallis H test of K independent-sample non-parametric test. Subsequently, Dunn's multiple comparisons test was performed to determine the differences between groups. The significance level of P was selected as 0.05.

Results

BMD and microstructural changes in subchondral bone with age

Figure 2 shows the typical radiographic images of the proximal femurs at different months of age. Open growth plates were observed at the femoral heads of 1 M and 3 M. The growth plate was fully closed at 6 M.

BMD and microstructural parameters of the subchondral bone varied obviously with the animal age (Table 1). Increased BMD, BV/TV, and Tb.Th were observed at 3M, 6 M and 9 M with significant difference from 1M ($p < 0.05$). No difference amongst the groups was observed with respect to Tb.N and SMI ($p > 0.05$).

Micromorphological changes in articular cartilage with age

Figure 3 shows the typical histology images of articular cartilage with Safranin O/Fast green staining. The thickness of articular cartilage decreased from 1 M to 9 M with the tidal line formed at 3 M. The earliest degeneration of articular cartilage occurred at 6 months of age, characterised by surface unevenness and evident chondrocyte reduction. The degeneration of collagen staining was obvious at 9 months of age.

Changes in micromechanical properties of articular cartilage with age

The 1 M group showed the lowest stiffness and the highest creep deformation ($p < 0.05$; Table 2). No significant differences in stiffness or creep deformation amongst 3 M, 6 M and 9 M were observed ($p > 0.05$; Table 2). Typical load–displacement curves at 1 M, 3 M, 6 M, and 9 M are shown in Figure 4, and the articular cartilage of 1 M had the largest displacement under the same load.

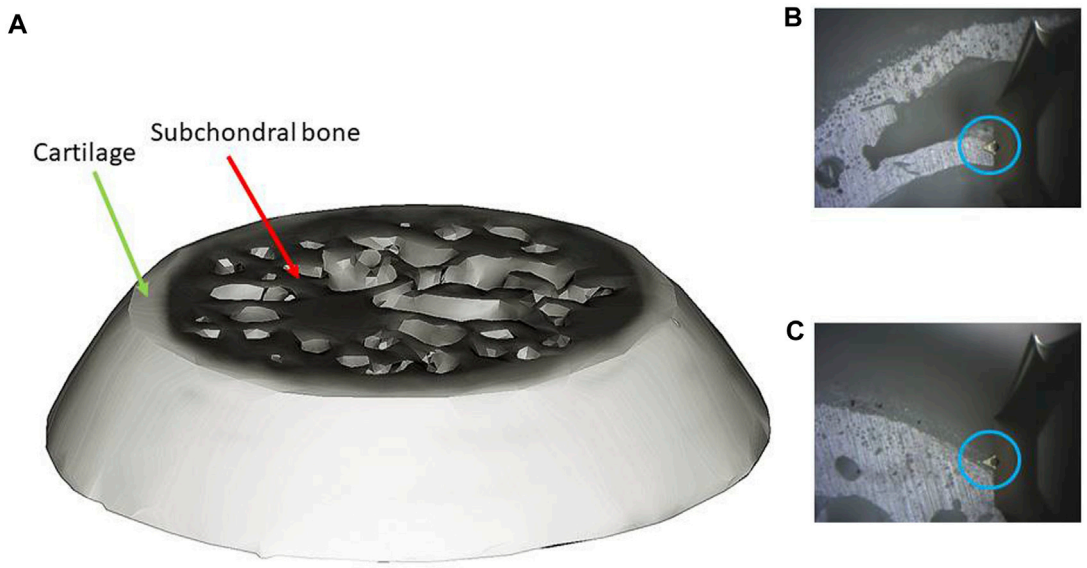

FIGURE 1
AFM scanning ((**A**): bone sample; **(B)** scanning positon of subchondral bone; **(C)** scanning positon of cartilage; blue circle: AFM tip).

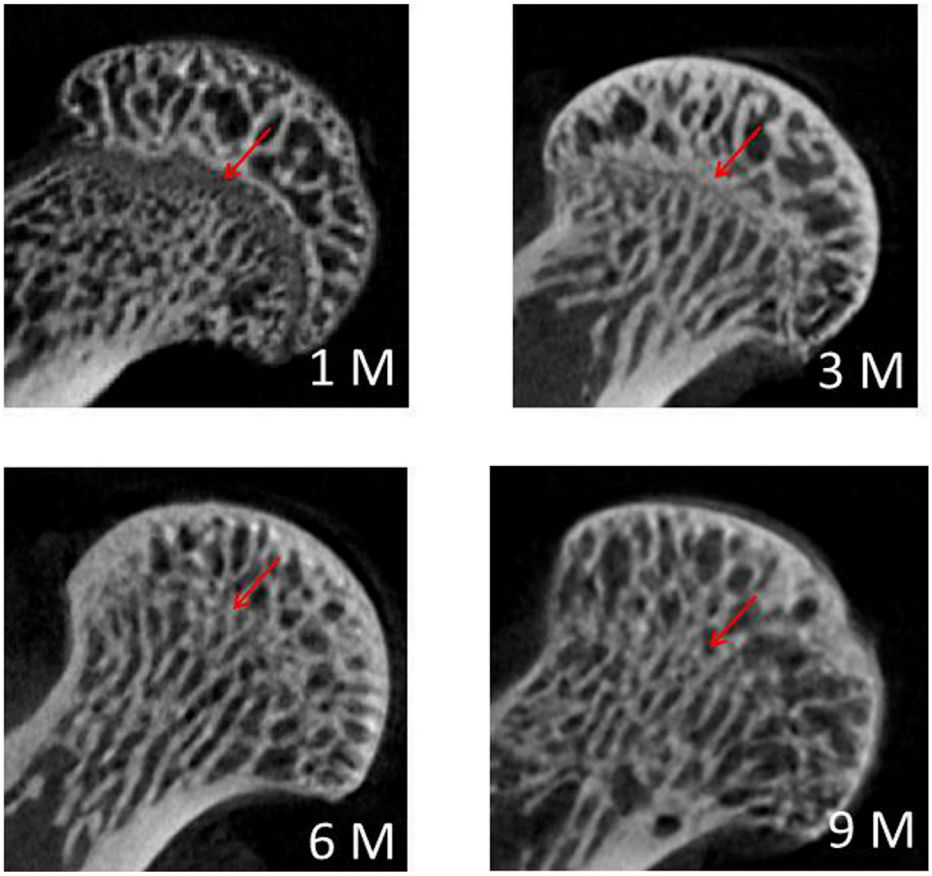

FIGURE 2
Typical radiographic images of the proximal femurs at 1 M, 3 M, 6 M and 9 M (red arrow: growth plate).

TABLE 1 BMD and microstructural parameters of the subchondral bone.

Group (M)	BMD (g/cm^3)	BV/TV (%)	Tb.Th (mm)	Tb.N (1/mm)	Tb.Sp (mm)
1	0.478 (0.455, 0.497)	39.055 (34.126, 41.816)	0.132 (0.117, 0.139)	3.001 (2.786, 3.126)	0.230 (0.209, 0.238)
3	0.560[a](0.537, 0.580)	46.817[a](44.326, 50.818)	0.158[a](0.153, 0.170)	2.905 (2.828, 2.973)	0.249 (0.237, 0.265)
6	0.635[a,b](0.601, 0.653)	57.530[a,b](53.129, 58.883)	0.186[a,b](0.178, 0.200)	3.028 (2.855, 3.130)	0.249 (0.231, 0.261)
9	0.658[a,b](0.586, 0.690)	60.627[a,b](51.033, 64.423)	0.187[a,b](0.180, 0.205)	3.064 (2.858, 3.216)	0.229 (0.205, 0.259)

Values are presented as median (IQR).
[a]Significantly different from 1 M; $p < 0.05$.
[b]Significantly different from 3 M; $p < 0.05$.

TABLE 2 Micro-mechanical properties of the articular cartilage at 1 M, 3 M, 6 M and 9 M.

Group (M)	Dynamic stiffness (N/mm)	Creep deformation (μm)
1	1.064 (0.992, 1.320)	18.051 (11.112, 22.601)
3	2.366[a](2.115, 2.739)	11.323[a](9.051, 16.020)
6	2.103[a](1.815, 2.693)	14.255[a](10.231, 14.661)
9	2.148[a](1.846, 2.870)	12.184[a](8.222, 18.317)

Values are presented as median (IQR).
[a]Significantly different from 1 M; $p < 0.05$.

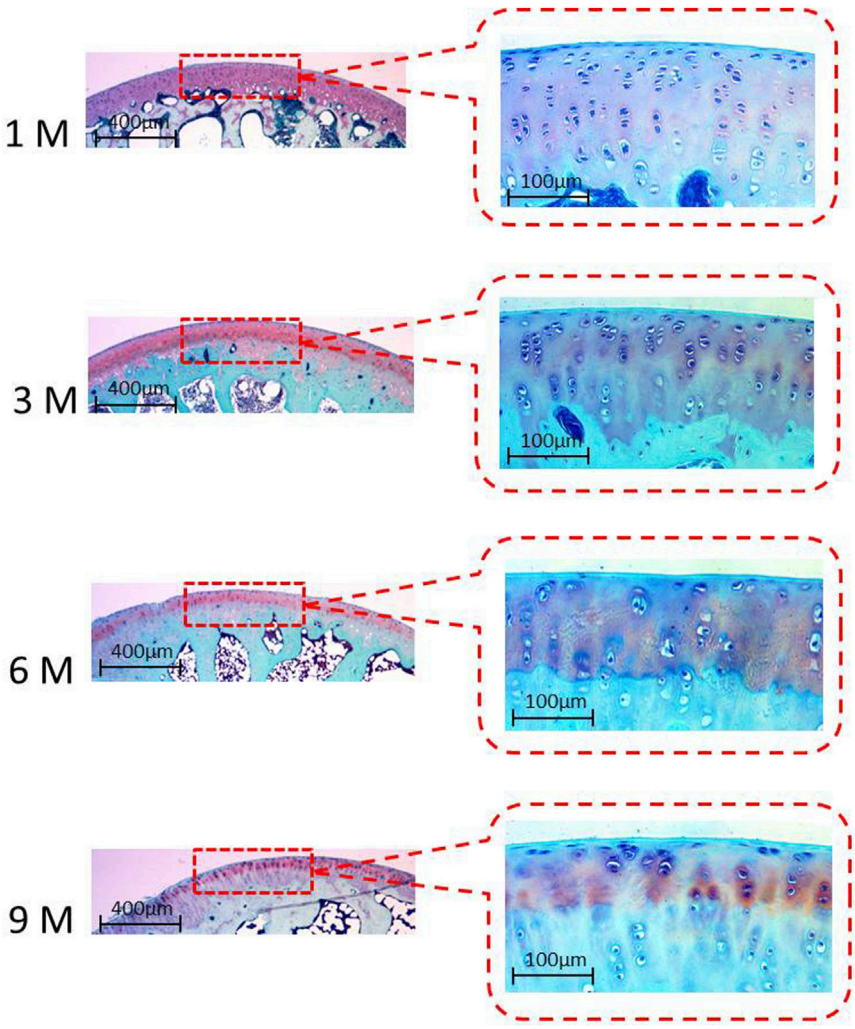

FIGURE 3
Typical histology images of articular cartilage with Safranin O/Fast green staining at 1 M, 3 M, 6 M and 9M.

TABLE 3 Grain size and roughness from AFM image analysis.

Group (M)	Subchondral bone		Cartilage	
	Grain size (nm)	Roughness (nm)	Grain size (nm)	Roughness (nm)
1	41.588 (37.583, 48.050)	9.360 (6.908, 12.455)	79.946 (73.008, 82.798)	3.931 (2.439, 4.451)
3	37.712 (33.822, 39.776)	8.385 (6.548, 10.545)	58.256 (45.029, 61.277)	4.034 (4.019, 4.980)
6	42.151 (39.339, 44.269)	9.815 (7.908, 13.300)	43.197[a](32.255, 52.005)	4.858[a](4.154, 5.394)
9	47.370 (42.293, 58.290)	8.620 (6.485, 9.248)	45.536[a](33.380, 48.348)	5.510[a](5.454, 6.157)

Values are presented as median (IQR).
[a]Significantly different from 1 M; $p < 0.05$.

Nanostructure changes in articular cartilage and subchondral bone with age

Typical AFM images of the subchondral bone are shown in Figure 5. In the images, a continuous phase of bone material was found, and obvious mineral crystallinity was observed. Neither grain size nor roughness showed any age-related differences amongst groups ($p > 0.05$; Table 3).

Figure 6 shows the typical AFM images of the cartilage. Obvious particles were observed on the cartilage surface. More particles could be observed in 6 M and 9 M. The 1 M group showed the highest grain size and the lowest roughness with significant differences from 6 M to 9 M ($p < 0.05$; Table 3). Grain size obviously decreased from 1 M to 3 M ($p < 0.05$; Table 3). The roughness values of 6 M and 9 M were significantly higher than that of 1 M ($p < 0.05$; Table 3).

Discussion

In this study, hip joints of guinea pigs at 1, 3, 6, and 9 months of age were selected to investigate the morphological and mechanical changes in articular cartilage and subchondral bone during spontaneous hip osteoarthritis. The results obtained in the current study showed that, the morphological and mechanical degenerations of cartilage occurred before those of subchondral bone during the progression of spontaneous hip osteoarthritis. In addition, the morphological degeneration of cartilage occurred before degeneration of mechanical properties.

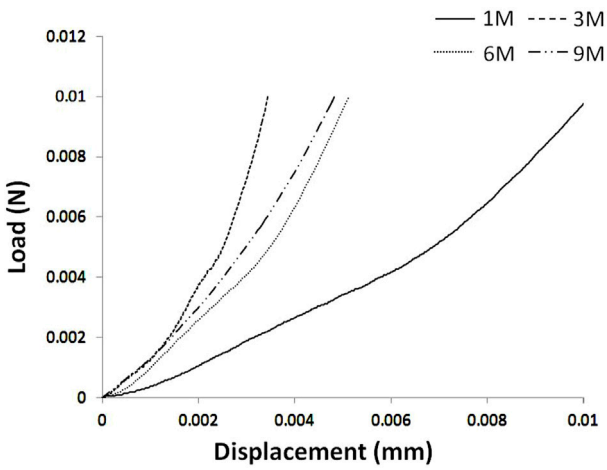

FIGURE 4
Typical load-displacement curves of articular cartilages at 1 M, 3 M, 6 M and 9 M.

Osteoarthritis can occur spontaneously in guinea pigs (Kraus et al., 2010; Cucchiarini et al., 2016; Samvelyan et al., 2021). Owing to the strong histological similarities between spontaneous osteoarthritis and human primary osteoarthritis, guinea pigs are commonly used in osteoarthritis studies (Cucchiarini et al., 2016; Samvelyan et al., 2021). In the current study, no obvious characteristics of osteoarthritis were found in the hip joints of guinea pigs at the macro level. However, obvious chondrocyte degeneration and surface structural degeneration related to the development of osteoarthritis were observed at the micro- and nanoscales at 6 months of age, indicating the onset of cartilage degeneration, which were considered to be the early markers of the spontaneous osteoarthritis.

Osteoarthritis is far from being a static disease. It has very distinct characteristics during the different stages of disease progression. Subchondral bone is generally believed to play a substantial role in the degeneration process of osteoarthritis; nevertheless, whether the initial change in osteoarthritis occurs first in bone or in articular cartilage is still controversial. Numerous studies have suggested that subchondral bone changes occur before any signs of degradation in the overlying cartilage emerge. Such changes are characterised by subchondral bone nanostructure changes and acceleration of bone turnover (Radin and Rose, 1986; Li et al., 2013; Wang et al., 2013; Fang et al., 2018; Aizah et al., 2019). However, many researchers still believe that bone changes occur following the degeneration of articular cartilage, or at least at the same time as the degradation of articular cartilage (Li et al., 2013; Finnilä et al., 2017). In the current study, the growth plates of the femoral heads were found to be fully closed at 6 M, indicating skeletal maturity and cessation of longitudinal bone growth. Age-related increases in BMD, BV/TV, and Tb.Th were observed from 1 M to 6 M, with no significant difference of BMD or any microstructural parameter observed between 6 M and 9 M, that is, no obvious degeneration of femoral subchondral bone in guinea pigs existed before 9 months of age. Different from the earliest degeneration of articular cartilage on the medial tibial plateau in guinea pigs observed at 3 months of age (Bendele and Hulman, 1988), the earliest degeneration of articular cartilage on the proximal femur occurred at 6 months of age (characterised by unevenness of cartilage surface and evident chondrocytes reduction, as well as increased grain size and decreased roughness in nanostructure) in the present study. Thus, based on the results obtained herein, the degeneration of

10.3389/fbioe.2023.1080241

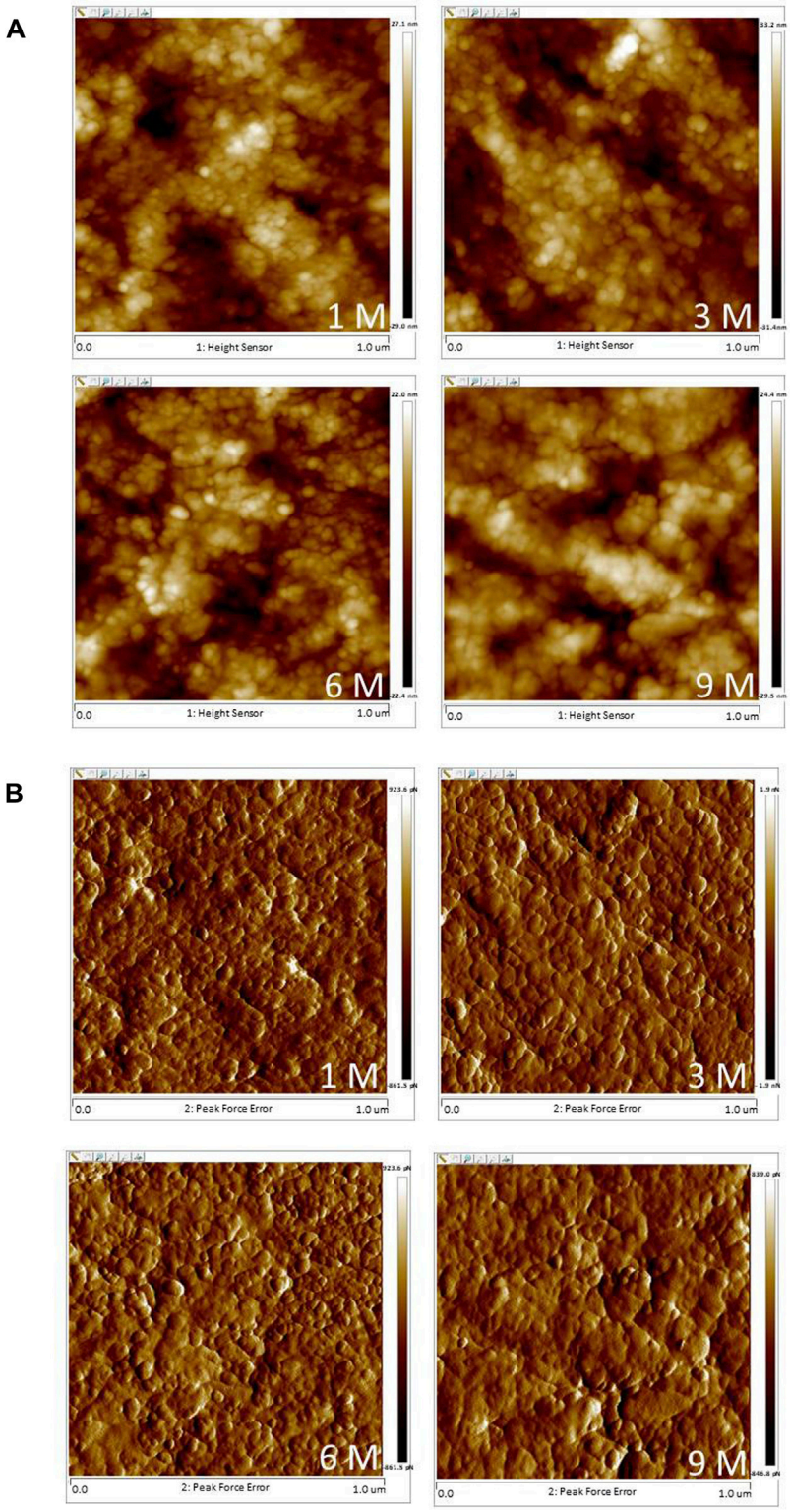

FIGURE 5
Typical AFM images of the subchondral bone at 1 M, 3 M, 6 M and 9 M (**(A)**: height images, **(B)** phase images; 1 μm × 1 μm scan area).

articular cartilage may have preceded the subchondral-bone changes in hip osteoarthritis in guinea pigs. Cartilage repair may be an available treatment modality for early osteoarthritis. Physical therapy, such as muscle-strengthening exercises (Bartholdy et al., 2017; Yuenyongviwat et al., 2020); aerobic exercises (Iijima et al., 2015; Kabiri et al., 2018); pulsed electromagnetic field (Ciombor et al., 2003; Yang et al., 2021); extracorporeal shock wave therapy (Chen et al., 2020); ultrasound therapy (Dantas et al., 2021); as well as drug therapy,

10.3389/fbioe.2023.1080241

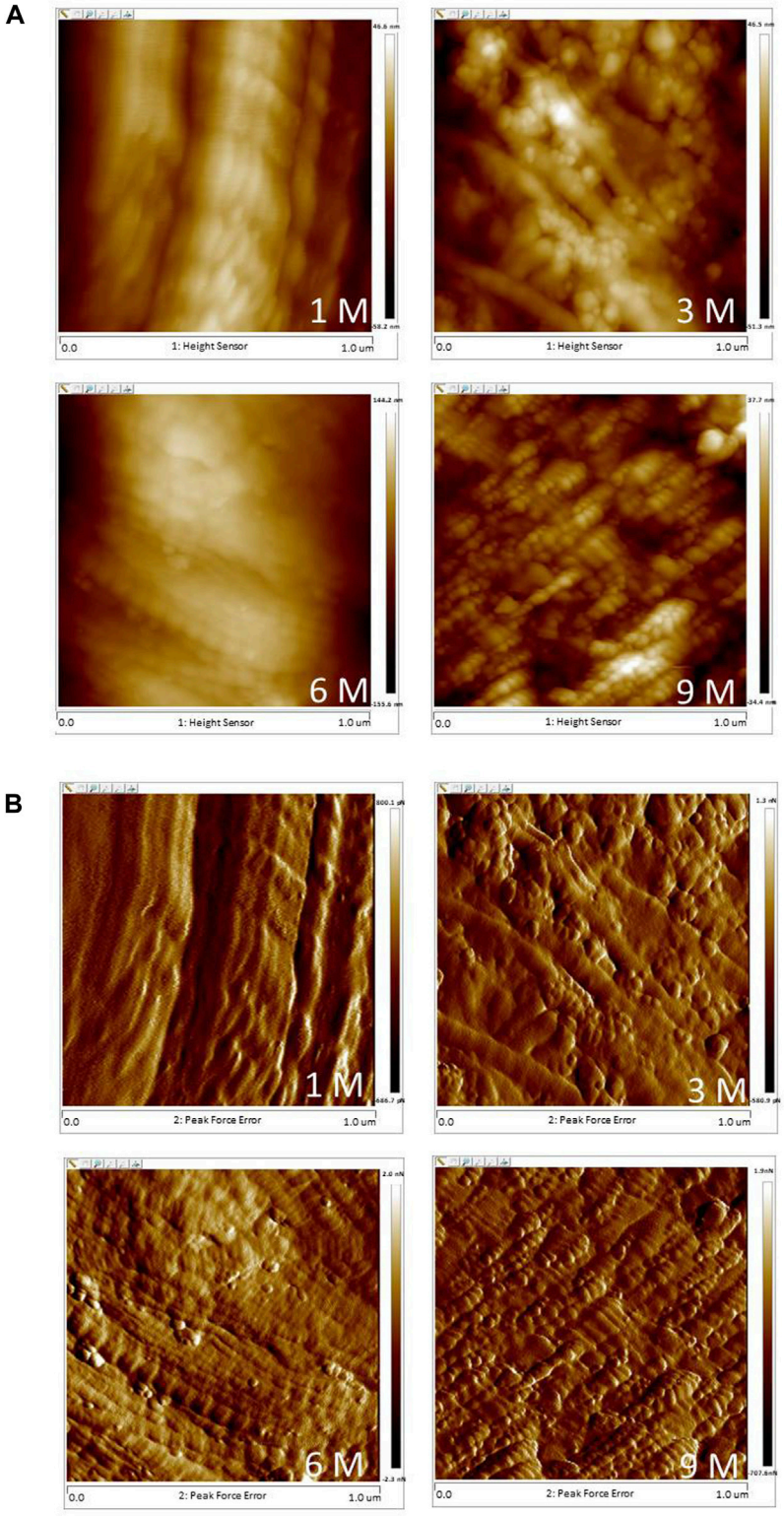

FIGURE 6
Typical AFM images of the articular cartilage at 1 M, 3 M, 6 M and 9 M (**(A)**: height images, **(B)** phase images; 1 μm × 1 μm scan area).

such as Glucosamine and chondroitin (Fransen et al., 2015), may potentially delay or treat cartilage degeneration effectively. Meanwhile, the molecular mechanism of cartilage degeneration should be further investigated (Ni et al., 2021; Sun et al., 2021; Liu et al., 2022) in order to find targeted drugs that can inhibit cartilage degeneration and delay or prevent disease progression.

A previous study has shown that the mechanical properties of tibial articular cartilage are affected by meniscus (cartilage covered by

menisci differs in mechanical properties from that uncovered) (Harlaar et al., 2022). Different from tibial articular cartilage, the proximal femoral articular cartilage has a smooth surface and no tissue coverage that affects its mechanical properties. Decreased mechanical properties are considered to be a remarkable sign of articular-cartilage degeneration (Franz et al., 2001; Fang et al., 2018; Harlaar et al., 2022). In the current work, significantly increased stiffness and decreased creep deformation of the proximal femoral articular cartilage were found from 1 M to 3 M ($p < 0.05$), with no significant changes observed from 3 M to 9 M ($p > 0.05$). This finding indicated that the proximal femoral articular cartilage matured at 3 months. Although no significant differences were found, 6 M and 9 M showed lower stiffness than 3 M which may be related to the degeneration of articular cartilage morphology that occurred at 6 months of age.

Based on its capacity of acquiring 3D surface topographical data at sub-micro- and nanoscales, AFM is extensively used to evaluate the surface characterisations of biological tissues at the nanoscale (Dufrêne, 2002; Stolz et al., 2009; Ghosh et al., 2013; Iijima et al., 2015; Iijima et al., 2017; Ren et al., 2018; Plaut et al., 2019). In the current study, nanostructure changes in articular cartilage and subchondral bone were observed by AFM. Roughness and grain size of trabecular bone were closely related to bone remodeling activity. Large roughness and grain size are considered to be due to delayed bone remodeling and can decrease the mechanical properties of bone at the macroscale (Milovanovic et al., 2011; Milovanovic et al., 2012). However, the present work showed no significant changes in grain size and roughness of subchondral bone amongst different groups, i.e., no degeneration (or at least no abnormal bone remodeling) of subchondral bone occurred.

Observation of nanoscale cartilage-surface characterisations can provide new insights into the initiation and progression of osteoarthritis. Articular cartilage changes due to aging and osteoarthritis could be clearly demonstrated in nanostructure before their morphological changes can be observed, and these architectural changes are then extended to the micro- and macroscales to inflict progressive and irreversible structural and functional damages (Stolz et al., 2009). The present study showed that the roughness of articular cartilage surfaces increased continuously from 1 M to 9 M with the degeneration of articular cartilage, which was consistent with previous ones (Ghosh et al., 2013; Wang et al., 2013). Moreover, the presence of particles on the surface of articular cartilage was obvious from 3 M to 9 M. These changes in the micromechanical properties of articular cartilage may be associated with the changes in nanostructure, thereby further confirming the degeneration of articular cartilage.

The current study should be considered in light of two limitations. First, only hip joints were investigated. In guinea pigs, the mechanical properties and morphological changes in knee articular cartilage and subchondral bone during the development of spontaneous osteoarthritis differ from those of the hip joint. Thus, whilst investigating osteoarthritis, in-depth investigation on knee cartilage and subchondral bone during the development of osteoarthritis and comparison with the hip joint are highly significant in elucidating the mechanism of osteoarthritis occurrence and development. Second limitation of this study is that no degeneration of the hip subchondral bone occurred before 9 months of age. Considering the important role of subchondral bone in the occurrence and development of osteoarthritis, further studies on the mechanical properties and morphological changes in subchondral bone in guinea pigs over the age of 9 months are required. Nevertheless, although restricted by these limitations, changes in articular cartilage and subchondral bone of the hip joint in guinea pigs were carefully investigated. Thus, the results may provide insights into the means of preventing and treating hip osteoarthritis.

Conclusion

Morphological and micromechanical properties changes in hip cartilage and subchondral bone of guinea pigs at 1, 3, 6, and 9 months were investigated. No degeneration of subchondral bone was observed before 9 months. The earliest degeneration of articular cartilage was observed at 6 months of age and characterised by structural changes at the micro- and nanoscales. Micro- and nanostructural degeneration of cartilage in hip joint occurred before the degeneration of mechanical properties. Structural and mechanical degenerations of cartilage occurred before those of subchondral bone during the progression of spontaneous hip osteoarthritis in guinea pigs. Age-related changes in articular cartilage and bone properties can serve as a theoretical basis for further research on osteoarthritis formation and progression.

Data availability statement

The raw data supporting the conclusion of this article will be made available by the authors, without undue reservation.

Ethics statement

The animal study was reviewed and approved by Ethics Committee of The First Hospital of Jilin University.

Author contributions

JG: Conceived and designed the experiments. Acquired, analyzed, and interpreted the data. Wrote and edited the manuscript. PR: Performed the animal experiments. Acquired, analyzed, and interpreted the data. HG: Designed the experiments. Proofreaded the manuscript. Supervised the project.

Funding

This work was supported by the National Natural Science foundation of China (No. 12272029), and the Natural Science foundation of Jilin Province (No. 20200201260JC).

Conflict of interest

The authors declare that the research was conducted in the absence of any commercial or financial relationships that could be construed as a potential conflict of interest.

Publisher's note

References

Aizah, N., Chong, P. P., and Kamarul, T. (2019). Early alterations of subchondral bone in the rat anterior cruciate ligament transection model of osteoarthritis. *Cartilage* 13, 1322S–1333S. doi:10.1177/1947603519878479

Barr, A. J., Campbell, T. M., Hopkinson, D., Kingsbury, S. R., Bowes, M. A., and Conaghan, P. G. (2015). A systematic review of the relationship between subchondral bone features, pain and structural pathology in peripheral joint osteoarthritis. *Arthritis Res. Ther.* 17 (1), 228. doi:10.1186/s13075-015-0735-x

Bartholdy, C., Juhl, C., Christensen, R., Lund, H., Zhang, W., and Henriksen, M. (2017). The role of muscle strengthening in exercise therapy for knee osteoarthritis: A systematic review and meta-regression analysis of randomized trials. *Semin. Arthritis Rheum.* 47 (1), 9–21. doi:10.1016/j.semarthrit.2017.03.007

Bendele, A. M., and Hulman, J. F. (1988). Spontaneous cartilage degeneration in Guinea pigs. *Arthritis Rheum.* 31 (4), 561–565. doi:10.1002/art.1780310416

Carlson, C. S., Loeser, R. F., Purser, C. B., Gardin, J. F., and Jerome, C. P. (1996). Osteoarthritis in cynomolgus macaques. III: Effects of age, gender, and subchondral bone thickness on the severity of disease. *J. Bone Min. Res.* 11 (9), 1209–1217. doi:10.1002/jbmr.5650110904

Castaño-Betancourt, M. C., Rivadeneira, F., Bierma-Zeinstra, S., Kerkhof, H. J., Hofman, A., Uitterlinden, A. G., et al. (2013). Bone parameters across different types of hip osteoarthritis and their relationship to osteoporotic fracture risk. *Arthritis Rheum.* 65 (3), 693–700. doi:10.1002/art.37792

Chen, L., Ye, L., Liu, H., Yang, P., and Yang, B. (2020). Extracorporeal shock wave therapy for the treatment of osteoarthritis: A systematic review and meta-analysis. *Biomed. Res. Int.* 2020, 1907821–1907915. doi:10.1155/2020/1907821

Ciombor, D. M., Aaron, R. K., Wang, S., and Simon, B. (2003). Modification of osteoarthritis by pulsed electromagnetic field-a morphological study. *Osteoarthr. Cartil.* 11 (6), 455–462. doi:10.1016/s1063-4584(03)00083-9

Cucchiarini, M., de Girolamo, L., Filardo, G., Oliveira, J. M., Orth, P., Pape, D., et al. (2016). Basic science of osteoarthritis. *J. Exp. Orthop.* 3 (1), 22. doi:10.1186/s40634-016-0060-6

Danalache, M., Kleinert, R., Schneider, J., Erler, A. L., Schwitalle, M., Riester, R., et al. (2019). Changes in stiffness and biochemical composition of the pericellular matrix as a function of spatial chondrocyte organisation in osteoarthritic cartilage. *Osteoarthr. Cartil.* 27 (5), 823–832. doi:10.1016/j.joca.2019.01.008

Dantas, L. O., Osani, M. C., and Bannuru, R. R. (2021). Therapeutic ultrasound for knee osteoarthritis: A systematic review and meta-analysis with grade quality assessment. *Braz J. Phys. Ther.* 25 (6), 688–697. doi:10.1016/j.bjpt.2021.07.003

Darling, E. M., Wilusz, R. E., Bolognesi, M. P., Zauscher, S., and Guilak, F. (2010). Spatial mapping of the biomechanical properties of the pericellular matrix of articular cartilage measured *in situ* via atomic force microscopy. *Biophys. J.* 98 (12), 2848–2856. doi:10.1016/j.bpj.2010.03.037

Ding, M., Danielsen, C. C., and Hvid, I. (2006). Age-related three-dimensional microarchitectural adaptations of subchondral bone tissues in guinea pig primary osteoarthrosis. *Calcif Tissue Int.* 78 (2), 113–122. doi:10.1007/s00223-005-0028-5

Dufrêne, Y. F. (2002). Atomic force microscopy, a powerful tool in microbiology. *J. Bacteriol.* 184 (19), 5205–5213. doi:10.1128/jb.184.19.5205-5213.2002

Fang, H., Huang, L., Welch, I., Norley, C., Holdsworth, D. W., Beier, F., et al. (2018). Early changes of articular cartilage and subchondral bone in the DMM mouse model of osteoarthritis. *Sci. Rep.* 8 (1), 2855. doi:10.1038/s41598-018-21184-5

Finnilä, M., Thevenot, J., Aho, O. M., Tiitu, V., Rautiainen, J., Kauppinen, S., et al. (2017). Association between subchondral bone structure and osteoarthritis histopathological grade. *J. Orthop. Res.* 35 (4), 785–792. doi:10.1002/jor.23312

Fransen, M., Agaliotis, M., Nairn, L., Votrubec, M., Bridgett, L., Su, S., et al. (2015). Glucosamine and chondroitin for knee osteoarthritis: a double-blind randomised placebo-controlled clinical trial evaluating single and combination regimens. *Ann. Rheum. Dis.* 74 (5), 851–858. doi:10.1136/annrheumdis-2013-203954

Franz, T., Hasler, E. M., Hagg, R., Weiler, C., Jakob, R. P., and Mainil-Varlet, P. (2001). *In situ* compressive stiffness, biochemical composition, and structural integrity of articular cartilage of the human knee joint. *Osteoarthr. Cartil.* 9 (6), 582–592. doi:10.1053/joca.2001.0418

Gatti, A. A., Keir, P. J., Noseworthy, M. D., and Maly, M. R. (2022). Investigating acute changes in osteoarthritic cartilage by integrating biomechanics and statistical shape models of bone: data from the osteoarthritis initiative. *MAGMA* 35 (5), 861–873. doi:10.1007/s10334-022-01004-8

Ghosh, S., Bowen, J., Jiang, K., Espino, D. M., and Shepherd, D. E. (2013). Investigation of techniques for the measurement of articular cartilage surface roughness. *Micron* 44, 179–184. doi:10.1016/j.micron.2012.06.007

Glyn-Jones, S., Palmer, A. J., Agricola, R., Price, A. J., Vincent, T. L., Weinans, H., et al. (2015). Osteoarthritis. *Lancet* 386 (9991), 376–387. doi:10.1016/S0140-6736(14)60802-3

Han, B., Nia, H. T., Wang, C., Chandrasekaran, P., Li, Q., Chery, D. R., et al. (2017). AFM-nanomechanical test: An interdisciplinary tool that links the understanding of cartilage and meniscus biomechanics, osteoarthritis degeneration, and tissue engineering. *ACS Biomater. Sci. Eng.* 3 (9), 2033–2049. doi:10.1021/acsbiomaterials.7b00307

Harlaar, J., Macri, E. M., and Wesseling, M. (2022). Osteoarthritis year in review 2021: mechanics. *Osteoarthr. Cartil.* 30 (5), 663–670. doi:10.1016/j.joca.2021.12.012

Hsieh, C. H., Lin, Y. H., Lin, S., Tsai-Wu, J. J., Herbert Wu, C. H., and Jiang, C. C. (2008). Surface ultrastructure and mechanical property of human chondrocyte revealed by atomic force microscopy. *Osteoarthr. Cartil.* 16 (4), 480–488. doi:10.1016/j.joca.2007.08.004

Huebner, J. L., Hanes, M. A., Beekman, B., TeKoppele, J. M., and Kraus, V. B. (2002). A comparative analysis of bone and cartilage metabolism in two strains of Guinea-pig with varying degrees of naturally occurring osteoarthritis. *Osteoarthr. Cartil.* 10 (10), 758–767. doi:10.1053/joca.2002.0821

Iijima, H., Aoyama, T., Ito, A., Tajino, J., Nagai, M., Zhang, X., et al. (2014). Immature articular cartilage and subchondral bone covered by menisci are potentially susceptive to mechanical load. *Bmc Musculoskel Dis.* 15, 101. doi:10.1186/1471-2474-15-101

Iijima, H., Aoyama, T., Ito, A., Yamaguchi, S., Nagai, M., Tajino, J., et al. (2015). Effects of short-term gentle treadmill walking on subchondral bone in a rat model of instability-induced osteoarthritis. *Osteoarthr. Cartil.* 23 (9), 1563–1574. doi:10.1016/j.joca.2015.04.015

Iijima, H., Ito, A., Nagai, M., Tajino, J., Yamaguchi, S., Kiyan, W., et al. (2017). Physiological exercise loading suppresses post-traumatic osteoarthritis progression via an increase in bone morphogenetic proteins expression in an experimental rat knee model. *Osteoarthr. Cartil.* 25 (6), 964–975. doi:10.1016/j.joca.2016.12.008

Kabiri, S., Halabchi, F., Angoorani, H., and Yekaninejad, S. (2018). Comparison of three modes of aerobic exercise combined with resistance training on the pain and function of patients with knee osteoarthritis: A randomized controlled trial. *Phys. Ther. Sport* 32, 22–28. doi:10.1016/j.ptsp.2018.04.001

Kraus, V. B., Huebner, J. L., DeGroot, J., and Bendele, A. (2010). The OARSI histopathology initiative - recommendations for histological assessments of osteoarthritis in the Guinea pig. *Osteoarthr. Cartil.* 18, S35–S52. doi:10.1016/j.joca.2010.04.015

Li, G., Yin, J., Gao, J., Cheng, T. S., Pavlos, N. J., Zhang, C., et al. (2013). Subchondral bone in osteoarthritis: insight into risk factors and microstructural changes. *Arthritis Res. Ther.* 15 (6), 223. doi:10.1186/ar4405

Liu, D., Cai, Z. J., Yang, Y. T., Lu, W. H., Pan, L. Y., Xiao, W. F., et al. (2022). Mitochondrial quality control in cartilage damage and osteoarthritis: new insights and potential therapeutic targets. *Osteoarthr. Cartil.* 30 (3), 395–405. doi:10.1016/j.joca.2021.10.009

Milovanovic, P., Potocnik, J., Djonic, D., Nikolic, S., Zivkovic, V., Djuric, M., et al. (2012). Age-related deterioration in trabecular bone mechanical properties at material level: nanoindentation study of the femoral neck in women by using AFM. *Exp. Gerontol.* 47 (2), 154–159. doi:10.1016/j.exger.2011.11.011

Milovanovic, P., Potocnik, J., Stoiljkovic, M., Djonic, D., Nikolic, S., Neskovic, O., et al. (2011). Nanostructure and mineral composition of trabecular bone in the lateral femoral neck: implications for bone fragility in elderly women. *Acta Biomater.* 7 (9), 3446–3451. doi:10.1016/j.actbio.2011.05.028

Ni, B., Pei, W., Qu, Y., Zhang, R., Chu, X., Wang, Y., et al. (2021). MCC950, the NLRP3 inhibitor, protects against cartilage degradation in a mouse model of osteoarthritis. *Oxid. Med. Cell Longev.* 2021, 1–14. doi:10.1155/2021/4139048

Peters, A. E., Akhtar, R., Comerford, E. J., and Bates, K. T. (2018). The effect of ageing and osteoarthritis on the mechanical properties of cartilage and bone in the human knee joint. *Sci. Rep.* 8 (1), 5931. doi:10.1038/s41598-018-24258-6

Plaut, J. S., Strzelecka-Kiliszek, A., Bozycki, L., Pikula, S., Buchet, R., Mebarek, S., et al. (2019). Quantitative atomic force microscopy provides new insight into matrix vesicle mineralization. *Arch. Biochem. Biophys.* 667, 14–21. doi:10.1016/j.abb.2019.04.003

Radin, E. L., and Rose, R. M. (1986). Role of subchondral bone in the initiation and progression of cartilage damage. *Clin. Orthop. Relat. Res.* 213 (213), 34–40. doi:10.1097/00003086-198612000-00005

Ren, P., Niu, H., Gong, H., Zhang, R., and Fan, Y. (2018). Morphological, biochemical and mechanical properties of articular cartilage and subchondral bone in rat tibial plateau are age related. *J. Anat.* 232 (3), 457–471. doi:10.1111/joa.12756

Richmond, S. A., Fukuchi, R. K., Ezzat, A., Schneider, K., Schneider, G., and Emery, C. A. (2013). Are joint injury, sport activity, physical activity, obesity, or occupational activities predictors for osteoarthritis? A systematic review. *J. Orthop. Sports Phys. Ther.* 43 (8), 515–B19. doi:10.2519/jospt.2013.4796

Rutgers, M., van Pelt, M. J., Dhert, W. J., Creemers, L. B., and Saris, D. B. (2010). Evaluation of histological scoring systems for tissue-engineered, repaired and osteoarthritic cartilage. *Osteoarthr. Cartil.* 18 (1), 12–23. doi:10.1016/j.joca.2009.08.009

Salucci, S., Falcieri, E., and Battistelli, M. (2022). Chondrocyte death involvement in osteoarthritis. *Cell Tissue Res.* 389 (2), 159–170. doi:10.1007/s00441-022-03639-4

Samvelyan, H. J., Hughes, D., Stevens, C., and Staines, K. A. (2021). Models of osteoarthritis: Relevance and new insights. *Calcif. Tissue Int.*109 (3), 243–256. doi:10.1007/s00223-020-00670-x

Stolz, M., Gottardi, R., Raiteri, R., Miot, S., Martin, I., Imer, R., et al. (2009). Early detection of aging cartilage and osteoarthritis in mice and patient samples using atomic force microscopy. *Nat. Nanotechnol.* 4 (3), 186–192. doi:10.1038/nnano.2008.410

Sun, K., Guo, J., Yao, X., Guo, Z., and Guo, F. (2021). Growth differentiation factor 5 in cartilage and osteoarthritis: A possible therapeutic candidate. *Cell Prolif.* 54 (3), e12998. doi:10.1111/cpr.12998

Wang, M., Shen, J., Jin, H., Im, H. J., Sandy, J., and Chen, D. (2011). Recent progress in understanding molecular mechanisms of cartilage degeneration during osteoarthritis. *Ann. N. Y. Acad. Sci.* 1240, 61–69. doi:10.1111/j.1749-6632.2011.06258.x

Wang, T., Wen, C. Y., Yan, C. H., Lu, W. W., and Chiu, K. Y. (2013). Spatial and temporal changes of subchondral bone proceed to microscopic articular cartilage degeneration in Guinea pigs with spontaneous osteoarthritis. *Osteoarthr. Cartil.* 21 (4), 574–581. doi:10.1016/j.joca.2013.01.002

Wen, C. Y., Wu, C. B., Tang, B., Wang, T., Yan, C. H., Lu, W. W., et al. (2012). Collagen fibril stiffening in osteoarthritic cartilage of human beings revealed by atomic force microscopy. *Osteoarthr. Cartil.* 20 (8), 916–922. doi:10.1016/j.joca.2012.04.018

Wilusz, R. E., Zauscher, S., and Guilak, F. (2013). Micromechanical mapping of early osteoarthritic changes in the pericellular matrix of human articular cartilage. *Osteoarthr. Cartil.* 21 (12), 1895–1903. doi:10.1016/j.joca.2013.08.026

Yang, X., Guo, H., Ye, W., Yang, L., and He, C. (2021). Pulsed electromagnetic field attenuates osteoarthritis progression in a murine destabilization-induced model through inhibition of TNF-α and IL-6 signaling. *Cartilage* 13, 1665S–1675S. doi:10.1177/19476035211049561

Yuenyongviwat, V., Duangmanee, S., Iamthanaporn, K., Tuntarattanapong, P., and Hongnaparak, T. (2020). Effect of hip abductor strengthening exercises in knee osteoarthritis: a randomized controlled trial. *BMC Musculoskelet. Disord.* 21 (1), 284. doi:10.1186/s12891-020-03316-z

Zuo, Q., Lu, S., Du, Z., Friis, T., Yao, J., Crawford, R., et al. (2016). Characterization of nano-structural and nano-mechanical properties of osteoarthritic subchondral bone. *Bmc Musculoskel Dis.* 17, 367. doi:10.1186/s12891-016-1226-1

frontiers | Frontiers in Bioengineering and Biotechnology

TYPE Review
PUBLISHED 22 February 2023
DOI 10.3389/fbioe.2023.1018012

OPEN ACCESS

EDITED BY
Jinlin Song,
Chongqing Medical University, China

REVIEWED BY
Tarek El-Bialy,
University of Alberta, Canada
Fengyuan Zhao,
Peking University Third Hospital, China
Francesco D'Aiuto,
University College London,
United Kingdom
Wu Lin,
China Medical University, China

*CORRESPONDENCE
Lijun Liu,
liulijun@jlu.edu.cn
Yanmin Zhou,
zhouym@jlu.edu.cn

SPECIALTY SECTION
This article was submitted to Biomechanics, a section of the journal Frontiers in Bioengineering and Biotechnology

RECEIVED 12 August 2022
ACCEPTED 10 February 2023
PUBLISHED 22 February 2023

CITATION
Aimaijiang M, Liu Y, Zhang Z, Qin Q, Liu M, Abulikemu P, Liu L and Zhou Y (2023), LIPUS as a potential strategy for periodontitis treatment: A review of the mechanisms.
Front. Bioeng. Biotechnol. 11:1018012.
doi: 10.3389/fbioe.2023.1018012

LIPUS as a potential strategy for periodontitis treatment: A review of the mechanisms

Maierhaba Aimaijiang, Yiping Liu, Zhiying Zhang, Qiuyue Qin, Manxuan Liu, Palizi Abulikemu, Lijun Liu* and Yanmin Zhou*

Jilin Provincial Key Laboratory of Tooth Development and Bone Remodeling, Hospital of Stomatology, Jilin University, Changchun, China

Periodontitis is a chronic inflammatory condition triggered by oral bacteria. A sustained inflammatory state in periodontitis could eventually destroy the alveolar bone. The key objective of periodontal therapy is to terminate the inflammatory process and reconstruct the periodontal tissues. The traditional Guided tissue regeneration (GTR) procedure has unstable results due to multiple factors such as the inflammatory environment, the immune response caused by the implant, and the operator's technique. Low-intensity pulsed ultrasound (LIPUS), as acoustic energy, transmits the mechanical signals to the target tissue to provide non-invasive physical stimulation. LIPUS has positive effects in promoting bone regeneration, soft-tissue regeneration, inflammation inhibition, and neuromodulation. LIPUS can maintain and regenerate alveolar bone during an inflammatory state by suppressing the expression of inflammatory factors. LIPUS also affects the cellular behavior of periodontal ligament cells (PDLCs), thereby protecting the regenerative potential of bone tissue in an inflammatory state. However, the underlying mechanisms of the LIPUS therapy are still yet to be summarized. The goal of this review is to outline the potential cellular and molecular mechanisms of periodontitis-related LIPUS therapy, as well as to explain how LIPUS manages to transmit mechanical stimulation into the signaling pathway to achieve inflammatory control and periodontal bone regeneration.

KEYWORDS

low-intensity pulsed ultrasound, periodontal inflammation, alveolar bone, mechanism, bone regeneration, mechanotransduction

1 Introduction

Periodontitis is one of the most common chronic inflammatory non-communicable diseases among humans. The local inflammatory state caused by periodontitis leads to the progressive destruction of the periodontal supporting structures (gingiva, alveolar bone, and periodontal ligament), which may even lead to the loss of teeth (Kinane et al., 2017). Periodontitis is the inflammatory outcome of dysbiosis of the oral microbiota (dental plaque) and the interaction of such microorganisms with the host's immune defense system (Pihlstrom et al., 2005; Pan et al., 2019a). According to recently developed clinical practice guideline by the European Federation of Periodontology, the treatments of periodontitis aim at controlling the supragingival and subgingival biofilm and calculus, local or systemic anti-inflammatory treatment, or further regeneration of periodontal loss or resection of lesions to minimize the complexity of periodontitis treatment (West et al., 2021;

Herrera et al., 2022). As periodontitis develops, the balance between bone formation and bone resorption in the alveolar bone is disrupted by the state of chronic inflammation (Usui et al., 2021). Cell populations such as PDLCs, which contain stem cells with multiple differentiation capacities, experience prolonged ischemia, and hypoxia, depriving the periodontium of its regenerative microenvironment (Wang et al., 2020; Liu et al., 2021). GTR and bone grafting are currently the more commonly used methods to address periodontal bone loss. However, GTR remains unpredictable and clinical outcomes vary depending on the challenge of the host's intraoral microbial biofilm, multiple risk factors (e.g., diabetes, smoking, dental plaque, and contact between the bone graft and non-vascular tooth surface), and the skill and experience of the practitioner (Vaquette et al., 2018; Liang et al., 2020). If there was a treatment strategy that targeted the pathogenesis of periodontitis, it could more effectively address the tissue loss due to inflammation.

The growth of new tissue and organs requires mechanical signals (Vining and Mooney, 2017; Steppe et al., 2020; Guo et al., 2021). Ultrasound stimulation appeared as a safe and non-invasive mechanical stimulation and has shown promise as a treatment for tissue regeneration (Daeschler et al., 2018; de Lucas et al., 2020; Liao et al., 2021). LIPUS is already widely used both in various clinical applications and fundamental research (Xin et al., 2016; Xie et al., 2019; Elvey et al., 2020). It has been acknowledged as a non-invasive physical stimulation for therapeutic purposes, delivering acoustic energy to the targeted tissue (de Lucas et al., 2021; Ichijo et al., 2021; Watanabe et al., 2021). Unlike high-intensity ultrasound, LIPUS has drawn attention for its minimal thermal effects (Xin et al., 2016). LIPUS is usually generated by a piezoelectric sensor, which converts electrical energy into mechanical force. The periodic acoustic waves that LIPUS generated can cause vibration and collision in the target tissue through the medium. In the process, cavitation, acoustic flow, and mechanical stimulation, as the main non-thermal effects of LIPUS, generate microbubbles and microjets to achieve the results (Lin et al., 2016). This non-thermal mechanism may also be explained by the influence of acoustic streaming during the action of LIPUS on the tissue. This acoustic flow may alter the local microenvironment of the cells, affecting the potassium content and calcium content of the cells after ultrasound exposure (Tanaka et al., 2015). Generally, the output frequencies of LIPUS range from 1 to 3 MHz. The ultrasound intensity of LIPUS therapy is within the range of 0.02–1 W/cm^2 spatial average temporal average (SATA) and the treatment duration is 5–30 min per day (Kaur and El-Bialy, 2020; Al-Dboush et al., 2021).

LIPUS has also been used in clinical trials for fracture healing, and compelling clinical data demonstrate its effectiveness in bone fracture healing, especially in some high-risk non-union cases that are not suitable for surgery (Zura et al., 2015a; Rutten et al., 2016; Leighton et al., 2017; Bhan et al., 2021). Former studies have demonstrated that LIPUS is responsible for accelerating bone reparations through both upregulating osteogenic-specific genes and downregulating osteoclast differentiation (Costa et al., 2018; Meng et al., 2018). LIPUS also effectively provides the mechanical force beneficial to soft tissue regeneration (Lai et al., 2021), regulating inflammation and neuromodulation (Xu et al., 2021; Song et al., 2022). Studies have shown that LIPUS has several positive effects on dentofacial remodeling, especially in root and alveolar bone resorption after orthodontic treatment. Kasahara et al. (2017) found in a controlled experiment that LIPUS stimulation decreased the atrophic alterations of periodontal structures associated with the lack of functional occlusion after orthodontic treatment. Interestingly, LIPUS produces opposite impacts on osteoblasts and osteoclasts during orthodontic movements, thus significantly reducing root resorption without compromising tooth movement (Inubushi et al., 2013; Feres et al., 2016). Diabetes also harms the effectiveness of orthodontic treatment, including a reduction in bone regeneration on the tension side and a decrease in the number of PDLCs. However, LIPUS can ensure the efficacy of orthodontic treatment by increasing the bone remodeling on the tension side and the number of bone resorption traps on the compression side (Alshihah et al., 2020).

Prolonged inflammation and periodontal bone destruction are the most severe consequences of periodontitis. LIPUS provides optimization for the existing advanced tissue regeneration technology in some experimental cases and also provides a new prospect for alveolar bone reconstruction in periodontitis (Figure 1). The mechanical stimulation provided by LIPUS can convert into biochemical signals and trigger downstream cascade reactions (Carina et al., 2018). Many studies have concentrated on the positive results and efficiency of LIPUS activation. However, before LIPUS therapy can be used in clinical periodontitis, the complete mechanism of its action in experimental periodontitis needs to be elucidated. In recent years, with the increasing attention to the treatment of LIPUS, more and more studies have focused on clarifying its therapeutic mechanism through its biological effects. The research of LIPUS in tissue regeneration as well as inflammation regulation has laid the foundation for studying its mechanism in periodontal tissue reconstruction. In light of the latest information available, the biological effects of LIPUS typically comprise the regulation of cell proliferation, migration, and differentiation *via* activating various molecular pathways. The precise mechanism by which mechanical stimuli are perceived and integrated into the periodontal regeneration process is not yet fully elucidated. Filling this vacancy can lead to enhanced treatment strategies for periodontitis and significantly shorten the duration of treatment. Therefore, this review aimed at summarizing and discussing the therapeutic mechanism of LIPUS and placing emphasis on how LIPUS manages to transfer mechanical stimulation into the signaling pathway to achieve inflammatory regulation and alveolar bone regeneration in experimental periodontitis. To push forward the progress of the mechanism study, we also point out the potential signaling pathways for further exploration.

2 Therapeutic mechanisms of LIPUS treatment

LIPUS has the potential for a wide range of applications, including bone healing, soft-tissue regeneration, inflammatory response inhibition, and neuromodulation, among others. The high-frequency pressure waves generated by LIPUS can produce mechanical stimulation in the targeted tissue and trigger biochemical events for tissue healing and regeneration. The involved therapeutic mechanisms for LIPUS-stimulated tissue

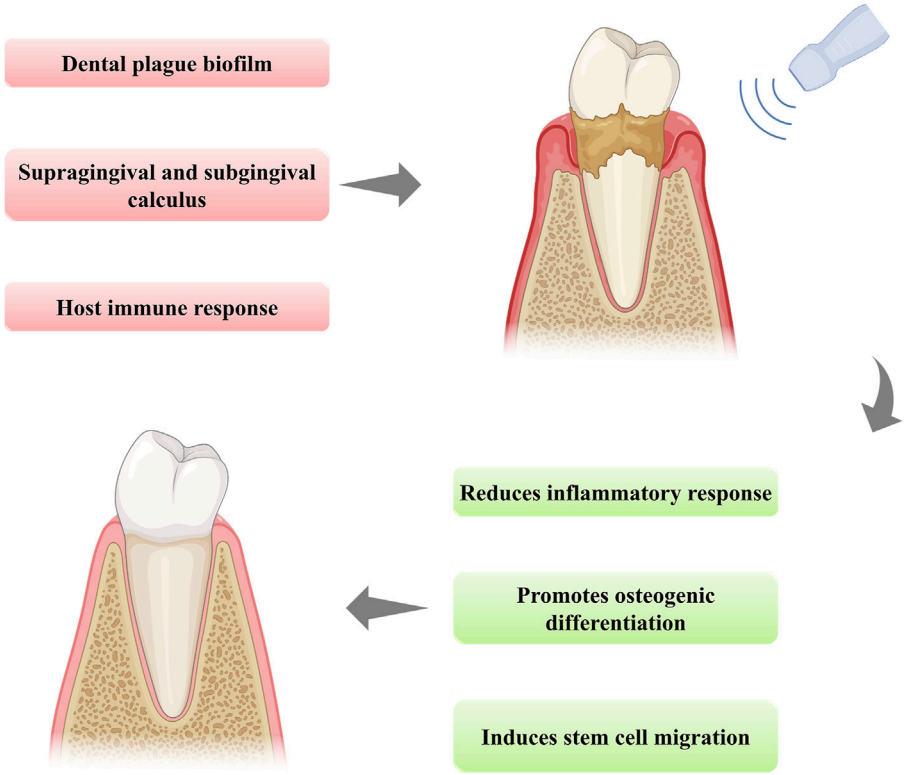

FIGURE 1
The schematic illustration of the function of LIPUS treatment in periodontitis.

healing have not been fully elucidated. Nevertheless, mechanical stress and/or fluid microfluidics are likely to be responsible for the biophysical effects of LIPUS (Tanaka et al., 2015). And when these events impact the cell plasma membrane, they trigger intracellular signal transduction and subsequent gene transcription.

2.1 LIPUS in bone regeneration therapy

As an active and dynamic tissue, bone is undergoing constant remodeling with proper biochemical and mechanical stimulations (Rowe et al., 2022). Appropriate mechanical stimulation of the bone is of crucial importance to preserve both the volume and structural stability of the bone. When the bone is subjected to mechanical loading, it promotes bone remodeling by enhancing the production and metabolism of osteoclasts and osteoblasts (Wang et al., 2022a). Various cellular activities, including those of cell proliferation, differentiation, gene expression, and protein synthesis, are activated and maintained by mechanical stimulation (Qin et al., 2020). Since the U.S. FDA approved the first LIPUS device for bone healing in 1994, extensive research has been carried out regarding fracture healing and presented desirable outcomes (Zura et al., 2015b). In 2018, Yusuf et al. reported a retrospective observational study that was conducted on clinical patients diagnosed with delayed or non-union, and 12 out of 18 patients successfully achieved full radiological union (Mirza et al., 2019). Subsequently, in 2019, Michael and his team performed a retrospective cohort study on non-unions of the distal upper limb treated with LIPUS (alone, or in conjunction with surgery). All patients underwent a low-intensity (30 mW/cm^2) pulsed ultrasound treatment for 20 min/day over the fracture site for at least 3 months resulting in a final union rate of 62% overall (Elvey et al., 2020). These early studies provided the basis for in-depth research on LIPUS in the field of bone regeneration.

The use of LIPUS in bone fracture treatment appears to be successful at all phases of the fracture healing process, including regulating inflammation, accelerating vascularization, ossification, and eventually bone remodeling (Zhang et al., 2017a). The ability of LIPUS to influence different stages of bone healing indicates that LIPUS works through multiple mechanisms. As extensively shown *in vitro* studies, LIPUS increases the expression of genes related to bone formation, such as Runx-2, osteocalcin, TGF-β, collagen type I, and X, alkaline phosphatase (ALP), aggrecan, Insulin-like growth factor-1 (IGF-1) and bone sulfur protein (Pan et al., 2019b; He et al., 2021; Maung et al., 2021). Apart from that, LIPUS has also been described to promote protein synthesis and calcium absorption in different osteoblast cell lines (Tassinary et al., 2018). Mechanotransduction is the mechanism that has been put forward to explain the process where the mechanical signal is converted into a biological signal. This signal conversion is normally accomplished through mechanosensitive cells within the tissue. Notably, the main regulators of bone mechanosensation and mechanotransduction are osteocytes (Uda et al., 2017; Jiang et al., 2019; Shimizu et al., 2021). Osteocytes are the main moderators of

bone homeostasis. They directly regulate local calcium concentration and indirectly control the osteoblasts and osteoclasts' activities *via* the secretion of important regulatory factors. Shimizu et al. (2021) discovered that LIPUS stimulation alters gene expression patterns in osteoblasts. Osteoblasts promote the LIPUS-facilitated fracture healing through transcriptional regulation of the early growth response protein 1 and 2 (Egr1, and Egr2), forkhead box Q1 (FoxQ1), JunB, and nuclear factor of activated T-cells c1 (NFATc1). When mechanical stimulation induces fluid shear stress around osteocytes, integrins and kinase pathways act as mechanosensory to promote a series of cascade reactions (Geoghegan et al., 2019; McCarthy and Camci-Unal, 2021). Integrins activation results in the establishment of focal adhesions or focal contacts. Focal adhesions consist of several proteins including talin, paxillin, focal adhesion kinase (FAK), p130Cas, and vinculin (Stewart et al., 2020). According to research, LIPUS can phosphorylate FAK (Sang et al., 2021). As a consequence of the activated FAK, phosphor-inositol 3 kinase (PI3K) and protein kinase B (AKT) is subsequently phosphorylated, which triggers the integrin/phosphatidylinositol 3-OH kinase/Akt pathway (Zhang et al., 2016). In addition, the researchers revealed that the integrin/phosphatidylinositol 3-OH kinase/AKT pathway causes the formation of cyclooxygenase-2 (COX-2), which consequently raises prostaglandin-E2 (PGE2) level (Wang et al., 2018c), resulting in enhanced mineralization effect of osteoblasts (Harrison et al., 2016). Another major effect of LIPUS during bone healing progress is improved vascularization. Jacqueline et al. have proved that LIPUS upregulates the expression of vascular endothelial growth factor (VEGF) (Crossman et al., 2019).

2.2 LIPUS-induced anti-inflammatory effects

Inflammation plays a significant role in the tissue repair process, including timely activation and diminution. However, the prolonged inflammatory state will eventually cause destructive outcomes. In the last few decades, physical therapy has been used mostly in the field of rehabilitation. The outcomes of several studies in recent years have shown that physical therapy is also a promising anti-inflammatory approach (d'Agostino et al., 2015; Gardner et al., 2019). LIPUS functions in the regulation of inflammation by modulating the behavior of different cell types. Leukocytes play a critical role in the process of tissue healing. The inflammatory response is triggered immediately after injury, and leukocytes aggregate to clean up foreign material for inhibiting bacterial infection, which is beneficial to the subsequent tissue repair (Eming et al., 2017). As reported, this process can be regulated by mechanical stimulation like LIPUS by affecting the inflammatory infiltration stage (Rai et al., 2017). LIPUS has a bi-directional effect on leukocytes. LIPUS promotes the infiltration of white blood cells in the early stage of inflammation in repair, which helps clean the wounded area. While during the final phase of inflammatory repair, LIPUS reduces leukocyte infiltration, which will help prevent further tissue destruction (da Silva Junior et al., 2017). Feltham established the post-traumatic osteoarthritis (OA) model by creating an intra-articular fracture (IAF) in the right knee of rats and performed an experimental study. They reported a major decline in synovial leukocyte infiltration in the LIPUS-treated group in comparison to the control group (Feltham et al., 2021). In addition, LIPUS treatment decreased the infiltration of $CD68^+$ macrophages in the synovium and the level of interleukin (IL)-1β in the joint fluid. Acoustic pressure waves have also been documented to affect the cell behavior of macrophages. For instance, in a rat model of hypothermic injury, da Silva Junior et al. (2017) showed that LIPUS lessened the number of inflammatory macrophages M1 after 1 day of treatment and increased the number of anti-inflammatory or reparative macrophages M2 after 2 days. We can conclude that LIPUS could alleviate persistent inflammatory responses by a decrease of M1 macrophages and enhancing tissue repair by increasing the M2 macrophages. These results well indicated the potential application of LIPUS in inflammatory diseases, while more research is required to explore the full mechanism.

Lipopolysaccharide (LPS) is associated with the pathogenesis of multiple diseases, such as osteoarthritis (Huang and Kraus, 2016), Alzheimer's disease (Kim et al., 2021), coronary artery disease, and periodontitis (Liljestrand et al., 2017; Xu et al., 2020). And macrophages are among the target cells of LPS. In 2017, Zhang et al. (2017b) studied U937 macrophages and observed that LIPUS suppressed the expression of inflammatory factors induced by LPS, such as tumor necrosis factor-α (TNF-α), IL-1β, IL-6, and IL-8. They also discovered that this inhibition effect was activated by suppressing the toll-like receptor 4 (TLR 4)-nuclear factor κB (NF-κB) signaling pathway. Furthermore, LIPUS inhibited LPS-induced expression of nucleus pulposus (NP) inflammatory factors TNF-α and IL-1β also by obstructing the NF-κB signaling pathway. Fei et al. investigated the inflammatory response of an OA model developed in a C57BL/6 mouse with the anterior cruciate ligament transaction method. They discovered that as a consequence of activating focal adhesion kinase (FAK) signaling, LIPUS induced a decline in the expression of inflammatory cytokines TNF-α, IL-6, and IL-8 in the synovial fluid of OA mice (Sang et al., 2021). Zhang et al. (2020) also showed that LIPUS ameliorated synovial inflammation by inhibiting the secretion of mature IL-1β production in macrophages. And this process was achieved through the sequestosome-1 (SQSTM1) dependent autophagic degradation of pyruvate kinase isoenzyme type M2 (PKM). They also reported that LIPUS treatment attenuated the LPS-induced inflammatory response in RAW264.7 macrophages and reduced the LPS-induced increase in pro-inflammatory cytokines (TNF-α and IL-6) (Zheng et al., 2019). Their study was the first to demonstrate that LIPUS diminishes the active inflammatory response in acute viral myocarditis by activating caveolin-1 and suppressing the stimulation of mitogen-activated protein kinase (MAPK) signaling. LIPUS regulates inflammation by inhibiting inflammatory factors, however, LIPUS activates or suppresses different signaling pathways in different cell types.

2.3 Soft-tissue regeneration

It is reported that LIPUS treatment accelerates soft tissue regeneration, including tendon healing, ligament healing, intervertebral disc resorption, and cartilage recovery (Chen et al.,

2019a; Li S. et al., 2021). This is especially because tissues such as tendons, ligaments, and cartilage have to bear a huge mechanical load in the body, and the application of LIPUS in the process of healing or tissue development can provide beneficial mechanical force. LIPUS has been reported to have beneficial effects on bone tendon healing by promoting fibroblast synthesis, collagen formation, and angiogenic, chondrogenic, and osteogenic activities (İnceoğlu et al., 2021). In a controlled study, an animal model of Achilles tendon injury has shown a more significantly increased in mature collagen fibers formation, improved biomechanical properties, and increased tissue regeneration rates under LIPUS treatment as opposed to the non-stimulation group (Lai et al., 2021). Human periodontal ligament cells (HPDLCs) play a fundamental role in periodontal regeneration. Low-intensity ultrasound had a similar effect on the activation of connective tissue cells, such as human osteoblast-like cell lines and HPDLCs (Jiang et al., 2019). There is also evidence from a recent study on a porcine model that the application of LIPUS on the oral mucosa expedites the repair of the masticatory mucosa (Chauvel-Picard et al., 2021). However, soft-tissue healing remains less studied than bone healing area. Like bone-healing research, LIPUS in soft tissue research still requires more randomized human clinical trials with controlled uniform parameters to obtain more systematic data to support alone and in combination with other stimulation methods.

2.4 Neuromodulation

The non-thermal neuro-modulatory effects of LIPUS were first reported by Tyler et al. (2008) demonstrating that LIPUS can remotely modulate neuronal circuits by activating action potentials and synaptic transmission. Many groups have established neuroprotective and reversible neuromodulation of LIPUS *in vitro* and *in vivo* since Tyler et al. (2008) published their results. Low-intensity ultrasound, like traditional pharmaceutical, electrical, magnetic, and optical treatments, can be used for functional neuromodulation. However, as distinguished from them, with a task-specific design ultrasound allows reversible, non-invasive neuromodulation with millimeter-level spatial resolution, without thermal effects (<0.01°) (Fini and Tyler, 2017). Lu et al. have successfully proved the positive role of LIPUS in preventing neuron degeneration in Parkinson's disease (PD) by suppressing 1-Methyl- 4-phenylpyridinium (MPP+) evoked neurotoxicity and mitochondria malfunction (Zhao et al., 2017). They argued that pretreatment of PC12 cells with LIPUS would make contributions to protecting the cells from MPP + exposure (a major neurotoxic metabolite of PD) *via* modulating the antioxidative proteins to alleviate oxidative stress. They also pointed out several pathways as the underlying mechanism, for instance, the K2P channel and stretched-activated ion channel-mediated downstream pathways. The protective and regulatory effects of LIPUS on dopaminergic neurons were discussed in the most recent research (Chen et al., 2021). They developed PD models induced by 1-methyl-4-phenyl-1,2,3,6-tetrahydropyridine (MPTP) and MPP+ and explored the neuroprotective effect of LIPUS. This resulted that LIPUS exerts its neuroprotective effect by attenuating the central neurotoxicity of MPTP in mice, reducing the loss of tyrosine hydroxylase positive neurons in the substantia nigra pars compacta, and decreasing the apoptosis in the substantia nigra section. In addition, LIPUS was able to suppress MPP + -induced inhibition of dopaminergic neuronal activity and increase apoptosis and control the accretion of reactive oxygen species (ROS) and MPP + -induced decreases in membrane potential.

3 The mechanisms of LIPUS in treating experimental periodontitis

Based on the global burden of disease study in 2019, from 1990 to 2019, the global prevalence of periodontitis increased by 99.0% (Wu et al., 2022). The global burden of periodontitis has dramatically increased. Without adequate intervention, the chronically activated inflammatory state can lead to the progressive destruction of periodontal bone. Besides, periodontitis has been associated with diverse systemic diseases, including cardiovascular disease, diabetes, respiratory disease, and rheumatoid arthritis, according to several studies (Nazir, 2017). In recent decades, there are various treatment modalities available for periodontal regenerative therapy. Among them, regenerative surgery such as GTR has become the preferred solution to bone loss caused by periodontitis. However, infections due to foreign body reactions caused by bacteria or the implant material at the wound site continue to limit the clinical effectiveness of GTR technology (Lin et al., 2019). In addition, the success rate of the GTR procedure depends to a large extent on the operator's surgical experience (Vaquette et al., 2018). Therefore, it is imperative to develop a method to accelerate periodontal regeneration. LIPUS has been increasingly studied in the field of tissue regeneration in recent years, and its mechanisms in bone regeneration and inflammation control have been considerably explored. Wang et al. (2022b) observed through an *in vivo* experimental study that LPIUS promotes new bone formation in the setting of periodontitis. In addition, they found that LIPUS is also effective in reducing inflammation and promoting angiogenesis, thus providing a favorable microenvironment for periodontal regeneration. Currently, LIPUS has shown advantages in both periodontal inflammation control and periodontal bone regeneration studies. However, there is still a lack of mechanism summarization and clarification in this area. In order to achieve more effective and precise clinical translation, it is necessary to fill this gap.

Previous studies have indicated that LIPUS can increase the proliferative activity of cells and enhance osteogenic differentiation (Baehni and Tonetti, 2010; Jiang et al., 2019). In terms of the periodontal field, studies have pointed out that LIPUS stimulation inhibits various inflammatory gene expressions and upregulates osteogenic differentiation-related genes (Tan et al., 2021). To elucidate the underlying mechanism of LIPUS in periodontitis, the periodontal cells were subjected to a specific ultrasound stimulation; however, loading parameters and time schedules varied among the studies (Table 1). Periodontal bone tissue originally possesses endogenous regenerative potential. There is evidence that a subpopulation subset of gingival fibroblasts (GFs), gingival mesenchymal stem cells (GMSCs), exhibit surface markers of mesenchymal stem cells (MSCs) and share an osteogenic differentiation potential similar to that of osteoprogenitor cells (Jin et al., 2015; Diar-Bakirly and El-Bialy, 2021). There has also

TABLE 1 Biological effects of LIPUS on periodontal ligament cells.

Cell types	Frequency (MHz)	Ultrasound intensity (SATA)	Treatment duration	Main outcomes	References
PDLFs	1.5	30 mW/cm^2	20 min/day	Suppresses inflammatory effects of LPS-PG, IL-1β, and TNF-α	Augustine et al. (2021)
				Promote BMP9-induced osteogenesis through ROCK1	
PDLCs	1.5	90 mW/cm^2	30 min/day	Inhibits IL-6 and IL-8 gene expression	Leewananthawet et al. (2019)
				Increases expression of osteogenic markers (Runx2, OPN, OSX, and OCN)	
				Inhibits NF-κB signaling pathway	
PDLCs	1.5	90 mW/cm^2	20 min/day	Increases mRNA expression of BSP, COL-3, OPN, and calcium deposition	Liu et al. (2020)
PDLSCs	1.0	250 and 750 mW/cm^2	5, 20 min/day	Increases proliferation	Gao et al. (2017)
				Immediate activation of JNK, MAPK	
				Significant increase in phosphorylated p38 MAPK	
PDLSCs	1.5	30, 60 and 90 mW/cm^2	30 min/day	Increases cell migration	Kechagia et al. (2019)
				Increases the mRNA and protein levels of TWIST1 and SDF-1	
PDLCs	1.5	90 mW/cm^2	20 min/day	Increases osteogenic differentiation (ALP, OCN) and mineralization	Xu et al. (2020)
				Increases expression of Runx2 and integrin β1	
PDLCs	1.5	90 mW/cm^2	30 min/day	Increases expression of osteogenic markers (ALP, Runx2) and matrix mineralization	Chen et al. (2019c)
				Inhibits miR-182 expression and promotes FOXO1 accumulation	
PDLCs	1.5	90 mW/cm^2	2 h	Increases mRNA and protein expression of autophagic genes Beclin-1 and LC3	Ying et al. (2020)
				Decreases IL-6 expression	
PDLSCs	1.5	90 mW/cm^2	30 min/day	Increases proliferation, matrix mineralization and osteogenic differentiation (ALP, Runx2)	Li et al. (2020a)
				Decreases IL-6 and IL-8 expression	
				UPR pathway involved	
PDLSCs	1.5	90 mW/cm^2	30 min/day	Increases cell proliferation, matrix mineralization and expression of Runx2, OPN, OCN, COL-1, ALP, integrinβ-1	Li S. et al. (2021)

SATA, spatial average temporal average; PDLFs, periodontal ligament fibroblasts; PDLCs, periodontal ligament cells; PDLSCs, periodontal ligament, periodontal ligament stem cells; LPS-PG, porphyromonas gingivalis lipopolysaccharide; IL, interleukin; TNF-α, tumour necrosis factor alpha; BMP, bone morphogenetic protein; ROCK1, rho-associated kinase 1; Runx2, runt-related transcription factor 2; OPN, osteopontin; OSX, osterix; OCN, osteocalcin; NF-κB, nuclear factor-κB; BSP, bone sialoprotein; COL, collagen; JNK, c-Jun NH2-terminal kinase; MAPK, mitogen-activated protein kinases; TWIST1, twist family bHLH, transcription factor 1; SDF-1, stromal cell-derived factor 1; ALP, alkaline phosphatase; FOXO, forkhead box O; LC3, light chain 3; UPR, unfolded protein response.

been successful induction of osteogenic differentiation of GFs, which fully demonstrates the tissue regenerative potential of periodontal tissues (Mostafa et al., 2011; Liu et al., 2017). Another major cell type in periodontal connective tissue is periodontal ligament cells (PDLCs). PDLCs are a heterogeneous cell population inclusive of osteogenic progenitor cells and MSCs that can develop cementum, bone, and the periodontal ligament tissue itself (Yamamoto et al., 2018). Like bone marrow stromal cells, PDLCs can give rise to mesodermal and skeletal tissue regeneration. In the meantime, PDLCs also provide a beneficial microenvironment for bone deposition through the synthesis and release of growth factors, cytokines, colony-stimulating, and factors neurotransmitters (Chang et al., 2020). MSCs in the periodontal ligament, periodontal ligament stem cells (PDLSCs), also serve an important purpose in periodontal tissue regeneration (Zhai et al., 2019). Several *in vitro* studies have revealed the effect of varying intensities of LIPUS on the behavior of cementoblasts (Inubushi et al., 2008) and PDLCs, GFs, and osteoblasts (Inubushi et al., 2008). Nesrine et al. concluded that LIPUS can contribute to the osteogenic differentiation of GFs by upregulating the expression of osteogenic genes such as ALP and OCN (Mostafa et al., 2009). Studies have shown that LIPUS can improve the vitality, proliferation, migration, and multilineage differentiation of PDLSCs, and these effects of LIPUS may be regulated *via* various signaling pathways (Tan et al.,

2021). In addition to this, LIPUS also exhibited a positive effect in enhancing the pluripotency of periodontal ligament cells. These characteristics have also motivated the study of LIPUS in periodontitis (El-Bialy et al., 2012). However, the related mechanisms still lack a systematic overview for a more effective clinical translation.

3.1 LIPUS induces stem cells migration

The mechanical stimuli in the process of bone remodeling realize the balance of regeneration and absorption of bone tissue through mechanotransduction (Ascolani et al., 2021). The role of mechanotransduction in periodontal regeneration was reflected in regulating cell migration (Wang et al., 2018b), proliferation (Huelter-Hassler et al., 2017), differentiation (He et al., 2019; Papadopoulou et al., 2020), and suppressing inflammatory factors *via* mechanosensory elements within cells. Restorative cell migration is a critical step in periodontal tissue repair. Endogenous MSCs have been shown to enhance tissue healing by homing to the site of injury (Lin et al., 2017). Previous studies have shown that BMSCs are motivated by a specific chemotactic factor released at the fracture site, thus migrating to the damaged area, and differentiating into osteoblasts to repair the fracture (Zhang et al., 2018). In addition, the mobilization of MSCs is involved in the homeostasis of periodontal tissues. Thus, the homing of stem cells from the surrounding healthy periodontal tissue into remodeling sites would presumably play an important role during *in situ* periodontal bone regeneration.

Research has gathered evidence that homing of PDLSCs is a potential mechanism of LIPUS-mediated periodontal tissue regeneration. PDLSCs are mechanosensitive cells and have an essential effect on tissue homeostasis and repair (Men et al., 2020). Previous studies showed that LIPUS possesses the ability to accelerate fracture healing by activating the migration of osteogenic progenitors to the damaged sites. Also, stromal cell-derived factor 1 (SDF-1), a type of chemokine that is vital for stem cell homing, is upregulated in the fracture site under LIPUS stimulation. To further investigate, WANG et al. conducted experiments on PDLSCs and revealed that LIPUS treatment facilitates the gene and protein expression of SDF-1 in PDLSCs (Wang et al., 2018b). Blocking SDF-1 or its receptor, C-X-C motif chemokine receptor 4 (CXCR4), significantly inhibits the secretion of SDF-1 and LIPUS-induced cell migration. These results indicate that the SDF-1/CXCR4 pathway is an important molecular mechanism underlying the LIPUS-induced stem cell migration. However, how mechanical signals are sensed and thus cause the activation of this signaling pathway? Recently, twist family bHLH transcription factor 1 (TWIST1) is regarded as having a fundamental role in the remodeling of the alveolar bone-periodontal ligament interface. Besides TWIST1 was reported to increase SDF-1 expression in a dose-dependent modality. WANG et al. further verified the role of TWIST1 in PDLSCs. They discovered that the knockdown of TWIST1 not only suppressed the LIPUS-induced SDF-1 expression but also blocked the LIPUS-induced stem cell migration. Therefore, we have concluded that TWIST1 acts as a mechanical stress sensor during mechanotransduction. When periodontal defects are treated with LIPUS stimulation, TWIST1 in PDLSCs will be activated and induce SDF-1 secretion. Eventually, LIPUS promotes PDLSC homing *via* the SDF-1/CXCR4 pathway to achieve periodontal bone regeneration (Figure 2). Naturally, cell migration is dependent on the involvement of adhesion proteins such as integrins and FAK activation. There is also strong evidence that LIPUS can regulate the migration of BMSCs by activating the FAK-ERK signaling pathway (Chen et al., 2019d). However, studies of this pathway in LIPUS-promoted migration of PDLCs are still absent.

However, the migration of PDLCs was not completely abolished by the blockade of TWIST1, suggesting that the existence of compensatory mechanisms may be possible. MSC migration is enhanced by the expression of additional chemokine receptors such as CCR1, CCR4, and CCR7, according to a previous study. As a result, the processes by which MSCs are mobilized to periodontal tissues in response to LIPUS are yet to be fully explored.

3.2 LIPUS promotes stem cells osteogenic differentiation

Human periodontal ligament cells (HPDLCs) possess various differentiation abilities and can facilitate the regeneration of periodontal tissues by differentiating into osteoblasts and cementoblasts (Zhu and Liang, 2015). The osteogenic differentiation capacity of HPDLSCs plays an essential role in the process of periodontal bone tissue reconstruction. The application of LIPUS can enhance the osteogenic differentiation of HPDLSCs by regulating related signaling pathways (Li H. et al., 2021). MAPK signaling pathway is an important mechanism underlying the osteogenic differentiation of HPDLSCs (Wang et al., 2018a). Mammalian MAP kinases are comprised of the extracellular signal-regulated kinase (ERK) family, the p38 kinase family, and the c-Jun N-terminal kinase family (JNK, also known as stress-activated protein kinase or SAPK) (Roskoski, 2012). Ren et al. (2013) confirmed that the p38 MAPK signaling pathway participates in the LIPUS-induced osteogenic differentiation of HPDLCs through the significant increase in LIPUS-induced ALP secretion, osteocalcin production, and calcium deposition (Huang et al., 2018). In a similar study, Gao et al. (2016) used specific MAPK inhibitors that further confirmed the role of specific MAPK pathways in the PDLSC proliferative response to ultrasound. They found that JNK and p38 may be both involved in the stimulation of PDLSC proliferation. Later in 2017, they also confirmed that phosphorylated JNK and p38 MAPK were increased mainly in PDLSCs over 24 h after LIPUS stimulation (Gao et al., 2017).

It is understood that LIPUS generates mechanical stresses, which can affect specific cellular mechanical transduction components, such as integrins, focal adhesion complexes, membrane receptors, ion channels, and cytoskeleton components. Integrins, which connect the cytoskeleton to the extracellular matrix and mediate a variety of signaling cascades, are also involved in the transduction of mechanical stimuli to biochemical signals (Kechagia et al., 2019). When LIPUS signals are delivered to integrins, the binding of varied adhesion junction proteins is triggered. One of the crucial focal adhesion proteins in the conversion of LIPUS signaling from mechanical to biochemical signals is focal adhesion kinase (FAK), which regulates integrin-mediated signaling triggered by LIPUS (Zhang et al., 2017a). Integrin β1 is implicated in the remodeling

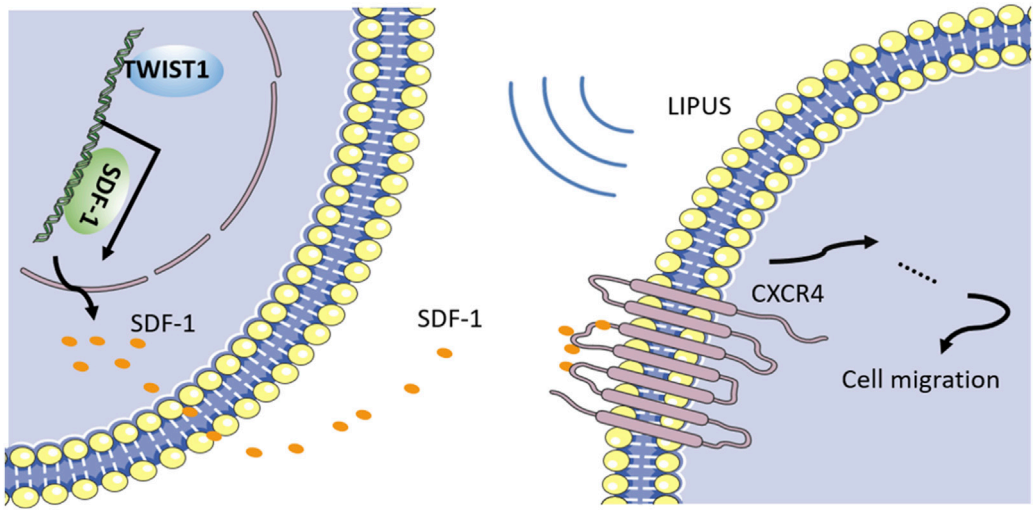

FIGURE 2
LIPUS promotes PDLSCs migration through SDF-1/CXCR4 signaling pathway.

of the periodontium in response to mechanical stimulation as a mechanoreceptor on the cell membrane (Molina et al., 2001). Hu et al. (2014) proved that integrin β1-dependent signaling transduction was included in the LIPUS-induced osteogenic differentiation of HPDLCs. When the mechanical signals from LIPUS reach the HPDLCs, the integrin β1-dependent signaling pathway will be activated and presumably activates the MAPK pathway. Finally, LIPUS facilitates Runx2 expression, ALP secretion, osteocalcin production, and calcium deposition in HPDLCs.

HPDLCs can initiate osteogenic differentiation *via* stimulation of cytokines and growth factors such as platelet-derived growth factor (Yang et al., 2022), epidermal growth factor, transforming growth factor (Li and Zhang, 2015), and bone morphogenetic protein (BMP) (Khanna-Jain et al., 2010). Of those factors, BMP has been identified as a key mediator in osteoblast differentiation regulation. It was shown that LIPUS plays a significant role in the BMP-induced osteogenic differentiation of PDLCs. Yang et al. (2014) discovered in their early study that BMP-2 and BMP-6 expression in HPDLCs increased after daily LIPUS treatment. They also explored that this process is achieved through the BMP-Smad signaling pathway. As an early response to mechanical signals generated by LIPUS, Smad transcription factors in PDLCs are phosphorylated on serine residues by the BMP receptor complex. Smads are categorized into 3 classes: receptor-regulated Smads, common Smads, and inhibitory Smads, and each of them has a particular function (Miyazawa and Miyazono, 2017). Once the receptor-regulated Smads (Smad1/5/8) are phosphorylated, receptor-regulated Smads dissociate from the receptor, connect to common Smad (Smad4), and enter the nucleus. In the nucleus, heteromeric Smad complexes function as effectors of BMP signaling by mediating transcription-related genes to upregulate multiple osteogenic differentiation makers.

In bone tissue, FOXO (Forkhead box O), a large family of forkhead transcription factors plays a crucial role in osteogenesis (Chen et al., 2019b). Some scholars have also investigated the mechanism of FOXO1 involvement in LIPUS-promoted osteogenic differentiation of HPDLCs. By knocking down the FOXO1, Chen et al. (2019c) discovered a major decrease in the level of osteogenic differentiation markers (like ALP, and Runx2) in HPDLCs. A collection of FOXO1-sensitive miRNAs, including miR-182, miR-183, and miR-705, have been revealed to be important regulators of osteogenic differentiation (Pitto et al., 2008; Wang et al., 2016). On this basis, Chen et al. (2019c) also found that LIPUS stimulation could inhibit miR-182 and thus attenuate its inhibitory effect on FOXO-1 accumulation. PI3K/Akt signaling pathway is another basic and traditional level of FOXO1 activity regulation, in addition to miRNA-mediated post-transcriptional regulation (Xing et al., 2018). LIPUS was discovered to induce Akt phosphorylation, which prevented active FOXO1 excessive accumulation by driving nucleus FOXO1 translocation to the cytoplasm and helping to maintain the balance of FOXO1 activity. Phosphorylated-Akt produced two 14-3-3 protein binding sites on FOXO1, and the FOXO1-14-3-3 binding complex was transported from the nucleus to the cytoplasm, where the bound 14-3-3 protein inhibited FOXO1 from returning to the nucleus. In osteoblasts, FOXO1 was revealed to be phosphorylated at Thr-24, Ser-256, and Ser-319 *via* the PI3K/Akt pathway (Fukunaga et al., 2005), while the phosphorylation sites in HPDLCs subject to LIPUS were unknown. In addition, miR-182 was discovered to retain FOXO1 in the nucleus in human hepatic cells by reducing Akt phosphorylation, indicating the intricacy and potential balance capacity of miR-182 on FOXO1 activity. Taken together, Chen et al. have concluded that miR-182 converts LIPUS stimulation into the biochemical signal FOXO1 and contributes to enhanced osteogenic differentiation in HPDLCs. Besides, LIPUS increases cytoplasm translocation of FOXO1 *via* PI3K/Akt pathway. However, the potential role of miR-182 in LIPUS-mediated Akt phosphorylation within HPDLCs is subject to further study. The mechanism by which LIPUS regulates the osteogenic differentiation of PDLCs is elucidated in Figure 3.

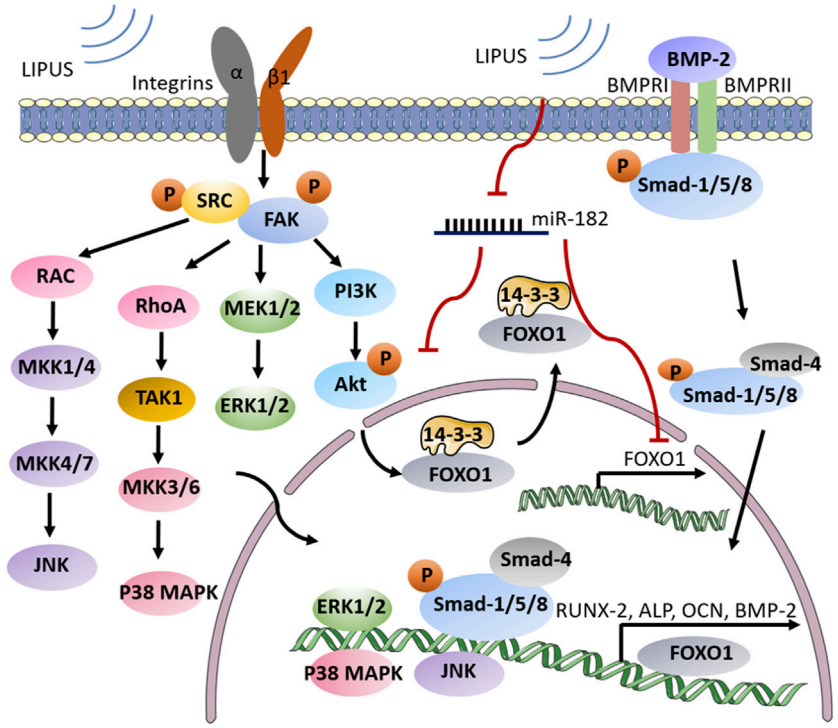

FIGURE 3
Schematic illustration of LIPUS enhancing osteogenic differentiation in periodontal tissue. LIPUS promotes FAK phosphorylation through integrin β1 and subsequently activates MAPK signaling, enabling the transcription of osteogenic-related signaling factors. Meanwhile, LIPUS can reverse the inhibitory effect of miR-182 on FOXO1 by inhibiting it, and prevent the overexpression of FOXO1 through PI3K/Akt pathway. The BMP receptor complex is also activated by LIPUS stimulation and promotes the expression of RUNX-2, ALP, OCN and other osteogenic genes through the BMP-Smad signaling pathway.

3.3 LIPUS modulates inflammatory response in periodontitis

Dental plaque biofilm is the initiating factor of periodontitis, host inflammatory and immune responses to microorganisms inside the biofilm can leave the subgingival environment in a state of ischemia and hypoxia. The anaerobic environment causes *Porphyromonas gingivalis (P. gingivalis)*, the key pathogen underlying progressive periodontitis and severe periodontitis, to become the dominant bacterium in the biofilm. As an important virulence factor in (*P. gingivalis*), *lipopolysaccharide* (LPS) is able to stimulate signaling factors such as Toll-like receptor-4 (TLR4) leading to unwanted host inflammatory responses. An inflammatory state will greatly weaken the self-renewal and multiple differentiation ability of periodontal tissue. NF-κB pathway has an important part in the TLR-mediated secretion of pro-inflammatory signals (cytokines, chemokines, and adhesion molecules) (Xu et al., 2020). As a major pathogenic factor in exacerbating periodontitis, LPS can increase periodontal inflammation by activating the intracellular NF-κB signaling pathway through TLR4. Activation of the NF-κB signaling pathway, on the other hand, impairs the osteogenic differentiation of PDLSCs. The microenvironment of periodontitis has a great impact on the osteogenic differentiation ability of cells. The persistent inflammatory condition arrests the differentiation of osteoblasts and increases the numbers and activity of osteoclasts. Oxidative stress is considered one of the pathophysiological mechanisms driving periodontitis, according to numerous research (Sczepanik et al., 2020). Oxidative stress hinders the osteogenic differentiation of PDLCs and reduces their regenerative potential (Kuang et al., 2020). Furthermore, the inflammatory state imposes endoplasmic reticulum stress (ERS), a pathological state that invokes an intracellular unfolded protein response (UPR), on PDLSCs leading to decreased osteogenic differentiation (Qiao et al., 2021; Tan et al., 2022). ERS is actuated by the accretion of unfolded and misfolded proteins in the endoplasmic reticulum (ER) (Wang et al., 2016). During ERS, cells react to changes in protein folding by activating a response called UPR. Up until now, UPR is initiated through three ER transmembrane transducers, including protein kinase R-like ER kinase (PERK), activating transcription factor 6 (ATF6) and inositol acquisition enzyme 1 (IRE1) (Ghemrawi and Khair, 2020; Read and Schröder, 2021). However, LIPUS provides more targeted inhibition of these pro-inflammatory mechanisms. LIPUS suppresses *lipopolysaccharide (LPS)*-induced inflammatory chemokines, diminishing oxidative stress and UPR, protecting periodontal osteogenic differentiation potential while regulating inflammation-related signaling pathways (Figure 4).

NF-κB signaling pathway is closely involved in periodontal inflammation. TLR4/MyD88/NF-κB signaling played an important role in the LPS-induced inflammatory response of periodontal tissue. Nakao et al. (2014) showed that LIPUS

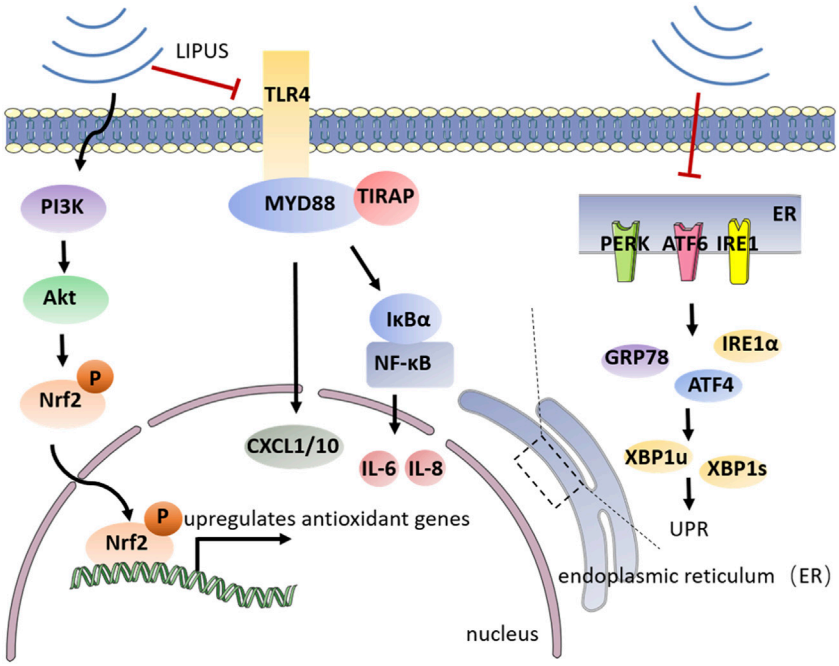

FIGURE 4
Schematic illustration of the mechanism by which LIPUS regulates periodontal inflammation. LIPUS can release UPR and reduce the secretion of chemokines such as IL-6, IL-8, and CXCL1/10 by inhibiting TLR4-mediated NF-κB signaling pathway and specific transmembrane signaling transducers on the endoplasmic reticulum surface. LIPUS can also activate the PIS/Atk signaling pathway to further upregulate antioxidant genes and alleviate oxidative stress.

interferes with the TLR4-MyD88/TIRAP signaling pathway in osteoblasts, thereby inhibiting the gene expression of the LPS-induced chemokines CXCL1 and CXCL10. And Liu et al. suggested that LIPUS reduces the inflammatory factors of U937 and potentiated the viability and osteogenic differentiation of PDLC *in vitro* (Zhang et al., 2017b). A recent study conducted by Liu et al. (2020) demonstrated with persuasive evidence that LIPUS inhibits the NF-κB signaling pathway by preventing the phosphorylation of IκBα and translocation of p65 into the nucleus. Therefore, LIPUS inhibits the secretion of IL-6 and IL-8 and modifies the osteogenic differentiation potential of hPDLCs in an inflammatory environment. However, the results of this experiment do not clarify whether LIPUS has a time-dependent effect on anti-inflammation, which needs further improvement. However, the results of this experiment did not elucidate whether LIPUS has an anti-inflammatory time-dependent property, which needs further improvement. Also, whether the duration of the LIPUS application plays a role in the alteration of signaling pathways needs further experimental validation. In addition, (Kusuyama et al. (2019) have also discovered that LIPUS treatment significantly suppressed LPS-induced mRNA expression of IL family cytokines, RANKL, and chemokines in periodontal ligament fibroblasts (PDLFs). And they explored that ROCK1, a molecule that mainly participated in cytoskeletal rearrangement after Rho activation, is involved in the suppression of inflammatory response by LIPUS.

As an effective treatment, LIPUS can effectively regulate inflammation, thus providing an improved microenvironment for the osteogenic differentiation of cells. It was found that LIPUS stimulation was effective in reducing oxidative stress in periodontitis and alleviating the inhibition of osteogenic differentiation and alveolar bone destruction caused by oxidative stress. (Ying et al. (2020) demonstrated that LIPUS acts to protect alveolar bone from oxidative stress by upregulating and activating nuclear factor erythroid 2-related factor 2 (Nrf2). Nrf2, as a redox-sensitive transcription factor, derives upregulation of a series of antioxidant genes that protect tissue against oxidative stress (Leewananthawet et al., 2019; Li et al., 2019). PI3K/Akt is a widely recognized upstream regulator of Nrf2, and activation of PI3K/AKT directly reduces the degradation of Nrf2 by facilitating its phosphorylation and accelerating its translocation to the nucleus (Li et al., 2018). By utilizing a pharmacological inhibitor of the PI3K/Akt pathway, Ying et al. (2020) also exhibited that the PI3K/AKT pathway promotes LIPUS-mediated upregulation of nuclear Nrf2. Therefore, it can be understood that LIPUS can effectively protect against tissue damage due to oxidative stress in experimental periodontal inflammation.

PDLSCs are a set of MSCs with multidirectional differentiation potential. They can serve an important purpose in the reconstruction of periodontal bone tissue in a healthy periodontal state. However, the intracellular ERS state caused by the inflammatory microenvironment severely affects the osteogenic differentiation potential of stem cells, thus leading to increased bone loss after periodontitis. Li et al. (2020a) demonstrated that through the inhibition of ERS, LIPUS reduces inflammation and facilitates osteogenesis in the LPS-induced inflammatory

environment. And the UPR-related genes IRE1α, GRP78, and ATF4 were also downregulated after LIPUS treatment. LIPUS treatment also suppressed the expression of XBP1u and XBP1s, the target genes of IRE1α in the UPR pathway. Meanwhile, LIPUS increased the expressions of RUNX2 and ALP, indicating that LIPUS improves the osteogenic differentiation potential of PDLSCs *via* inhibiting UPR. While the specific pathway included in the use of LIPUS and the regulation of the UPR still need so further investigation.

Autophagy is a catabolic process in which cells decompose their unneeded proteins, macromolecular complexes, and organelles, passing them into lysosomes so and enabling them to survive (Saha et al., 2018). Clinical studies show that autophagy is a requirement in the inflammatory microenvironment to protect PDLSCs from apoptosis (An et al., 2016). Li et al. (2020b) have demonstrated that LIPUS stimulation can induce mRNA and protein expression of the autophagy pathway related-proteins, such as LC3 and Beclin-1, in LPS-pretreated HPDLCs. LIPUS pretreatment significantly reduces IL-6 release in lipopolysaccharide-stimulated HPDLCs. However, the autophagy inhibitor, 3-Methyladenine, causes an increase in the level of IL-6, which indicates the involvement of autophagy in the LIPUS anti-inflammatory mechanism in HPDLCs.

4 Summary and prospects

Periodontitis is a widespread oral disease that causes alveolar bone destruction. If properly contained, early-state periodontitis has a good prognosis. However, severe bone loss, a complication of more advanced periodontitis, is still a puzzle for clinicians. LIPUS provides a new inspiration for tissue regeneration. In contrast to high-intensity ultrasound applied for tissue heating, LIPUS provides mainly non-thermal effects, including microbubbles and microjets caused by cavitation, acoustic flow, mechanical stimulation, etc. and in this article, we thoroughly discussed the underlying mechanism of LIPUS-mediated periodontal bone regeneration. As a mechanical signal, LIPUS activates different signaling pathways *via* mechanotransduction and subsequently regulates cell behavior. LIPUS can activate the homing of endogenous MSCs as well as osteogenic progenitor cells to the defected area by activating the TWIST/SDF-1 signaling pathway. When LIPUS reaches the damaged tissue, intracellular TWIST1 is activated to promote the expression of SDF-1, which in turn serves to promote the expression of genes related to cell migration through its corresponding receptors. However, studies on how periodontal ligament cells perceive mechanical signals from LIPUS and translate them into the expression of signaling molecules that promote migration remain imperfect. Besides, LIPUS regulates the osteogenic differentiation of PDLCs through the involvement of signaling pathways such as MAPK, BMP-Smad, and cytokines such as FOXO. In periodontal tissue, integrin β1 functions as a sensory transducer of mechanical stimulation from LIPUS, promoting FAK phosphorylation and thereby activating a series of downstream cascade responses. MAPK signaling pathway activated by phosphorylation of FAK increases the expression of ERK1/2, p38 MAPK, and JNK and thus contributes to the transcription of osteogenic differentiation genes. LIPUS increases the expression of Runx2, ALP, and the mineralized bone nodule formation by promoting the transcriptional function of FOXO1. By inhibiting the FOXO1-sensitive miRNA miR-182, LIPUS ensured the normal transcription of FOXO1 in the nucleus. In this process, the translocation of FOXO1 from the nucleus to the cytoplasm can be achieved through the PI3K/Akt signaling pathway thus avoiding the excessive accumulation of FOXO1 in the nucleus. In addition, LIPUS upregulates osteogenic differentiation gene markers in periodontal cells by enabling the nuclear transport of the Smad complexes through the BMP-Smad signaling pathway. In the meantime, LIPUS generates mechanical signals that inhibit the release of inflammatory factors, oxidative stress, and UPR activated by periodontitis, and modulates periodontal inflammation by regulating cellular autophagy. When exposed to LIPUS, the signaling pathway promoting antioxidant gene transcription was activated, while the TLR-mediated NF-κB and UPR-related signaling pathways associated with pro-inflammation were inhibited. LIPUS phosphorylates transcription factor Nrf2 through PI3K/Akt signaling pathway and promotes antioxidant genes to reduce oxidative stress and periodontitis-induced tissue damage. LIPUS also suppressed the TLR-mediated NF-κB signaling pathway, while interfering with the TLR4-MyD88-TIRAP complex to reduce the release of LPS-induced chemokines. In addition, LIPUS could inhibit UPR-induced inflammatory response by suppressing the ER transmembrane transducers and their downstream genes.

Nevertheless, the mechanism of LIPUS-induced periodontal bone tissue regeneration remains incomplete. Although the current study can describe the general mechanism of the effect of LIPUS on periodontal bone regeneration, however, many details need to be refined. The current research had not proposed the optimal LIPUS stimulation parameters corresponding to various cells. Different intensities and stimulation durations may reveal different signaling pathways of mechanotransduction, so we believe that the research on LIPUS needs to be further improved on this aspect to obtain more rigorous results. LIPUS gradually possesses a more significant place in the field of regeneration medicine. And a thorough knowledge of the molecular mechanism behind LIPUS-related treatments will pave the way for better clinical application.

Author contributions

Conceptualization, LL, and YZ; methodology, ZZ; software, ML; writing—original draft preparation, MA and QQ; writing—review and editing, MA, YL, and PA; visualization, MA. All authors have read and agreed to the published version of the manuscript.

Acknowledgments

We thank the authors of the references for providing the data of the final manuscript.

Conflict of interest

The authors declare that the research was conducted in the absence of any commercial or financial relationships that could be construed as a potential conflict of interest.

Publisher's note

References

Al-Dboush, R. e., Esfahani, A. N., and El-Bialy, T. (2021). Impact of photobiomodulation and low-intensity pulsed ultrasound adjunctive interventions on orthodontic treatment duration during clear aligner therapy. *Angle Orthod.* 91 (5), 619–625. doi:10.2319/112420-956.1

Alshihah, N., Alhadlaq, A., El-Bialy, T., Aldahmash, A., and Bello, I. O. (2020). The effect of low intensity pulsed ultrasound on dentoalveolar structures during orthodontic force application in diabetic *ex-vivo* model. *Archives Oral Biol.* 119, 104883. doi:10.1016/j.archoralbio.2020.104883

An, Y., Liu, W., Xue, P., Zhang, Y., Wang, Q., and Jin, Y. (2016). Increased autophagy is required to protect periodontal ligament stem cells from apoptosis in inflammatory microenvironment. *J. Clin. Periodontology* 43 (7), 618–625. doi:10.1111/jcpe.12549

Ascolani, G., Skerry, T. M., Lacroix, D., Dall'Ara, E., and Shuaib, A. (2021). Analysis of mechanotransduction dynamics during combined mechanical stimulation and modulation of the extracellular-regulated kinase cascade uncovers hidden information within the signalling noise. *Interface Focus* 11 (1), 20190136. doi:10.1098/rsfs.2019.0136

Augustine, R., Dan, P., Hasan, A., Khalaf, I. M., Prasad, P., Ghosal, K., et al. (2021). Stem cell-based approaches in cardiac tissue engineering: Controlling the microenvironment for autologous cells. *Biomed. Pharmacother. = Biomedecine Pharmacother.* 138, 111425. doi:10.1016/j.biopha.2021.111425

Baehni, P., and Tonetti, M. S. (2010). Conclusions and consensus statements on periodontal health, policy and education in europe: A call for action - consensus view 1Conclusions and consensus statements on periodontal health, policy and education in europe: A call for action--consensus view 1. Consensus report of the 1st European workshop on periodontal education. *Eur. J. Dent. Educ. Official J. Assoc. Dent. Educ. Eur.* 14 (1), 2–3. doi:10.1111/j.1600-0579.2010.00619.x

Bhan, K., Patel, R., Hasan, K., Pimplé, M., Sharma, S., Nandwana, V., et al. (2021). Fracture nonunions and delayed unions treated with low-intensity pulsed ultrasound therapy: A clinical series. *Cureus* 13 (8), e17067. doi:10.7759/cureus.17067

Carina, V., Costa, V., Pagani, S., De Luca, A., Raimondi, L., Bellavia, D., et al. (2018). Inhibitory effects of low intensity pulsed ultrasound on osteoclastogenesis induced *in vitro* by breast cancer cells. *J. Exp. Clin. cancer Res. CR* 37 (1), 197. doi:10.1186/s13046-018-0868-2

Chang, M., Lin, H., Fu, H., Wang, J., Yang, Y., Wan, Z., et al. (2020). CREB activation affects mesenchymal stem cell migration and differentiation in periodontal tissues due to orthodontic force. *Int. J. Biochem. Cell Biol.* 129, 105862. doi:10.1016/j.biocel.2020.105862

Chauvel-Picard, J., Korn, P., Corbin, S., Brosset, S., Bera, J.-C., and Gleizal, A. (2021). Stimulation of oral mucosal regeneration by low intensity pulsed ultrasound: An *in vivo* study in a porcine model. *J. Prosthodont. Res.* 65 (1), 46–51. doi:10.2186/jpr.jpor_2019_345

Chen, C., Zhang, T., Liu, F., Qu, J., Chen, Y., Fan, S., et al. (2019a). Effect of low-intensity pulsed ultrasound after autologous adipose-derived stromal cell transplantation for bone-tendon healing in a rabbit model. *Am. J. Sports Med.* 47 (4), 942–953. doi:10.1177/0363546518820324

Chen, D., Gong, Y., Xu, L., Zhou, M., Li, J., and Song, J. (2019b). Bidirectional regulation of osteogenic differentiation by the FOXO subfamily of Forkhead transcription factors in mammalian MSCs. *Cell Prolif.* 52 (2), e12540. doi:10.1111/cpr.12540

Chen, D., Xiang, M., Gong, Y., Xu, L., Zhang, T., He, Y., et al. (2019c). LIPUS promotes FOXO1 accumulation by downregulating miR-182 to enhance osteogenic differentiation in hPDLCs. *Biochimie* 165, 219–228. doi:10.1016/j.biochi.2019.08.005

Chen, J., Jiang, J., Wang, W., Qin, J., Chen, J., Chen, W., et al. (2019d). Low intensity pulsed ultrasound promotes the migration of bone marrow-derived mesenchymal stem cells via activating FAK-ERK1/2 signalling pathway. *Artif. Cells, Nanomedicine, Biotechnol.* 47 (1), 3603–3613. doi:10.1080/21691401.2019.1657878

Chen, X., Wang, D., Zhang, L., Yao, H., Zhu, H., Zhao, N., et al. (2021). Neuroprotective effect of low-intensity pulsed ultrasound on the mouse MPTP/MPP+ model of dopaminergic neuron injury. *Ultrasound Med. Biol.* 47 (8), 2321–2330. doi:10.1016/j.ultrasmedbio.2021.03.034

Costa, V., Carina, V., Fontana, S., De Luca, A., Monteleone, F., Pagani, S., et al. (2018). Osteogenic commitment and differentiation of human mesenchymal stem cells by low-intensity pulsed ultrasound stimulation. *J. Cell. Physiology* 233 (2), 1558–1573. doi:10.1002/jcp.26058

Crossman, J., Alzaheri, N., Abdallah, M.-N., Tamimi, F., Flood, P., Alhadainy, H., et al. (2019). Low intensity pulsed ultrasound increases mandibular height and Col-II and VEGF expression in arthritic mice. *Arch. Oral Biol.* 104, 112–118. doi:10.1016/j.archoralbio.2019.05.032

d'Agostino, M. C., Craig, K., Tibalt, E., and Respizzi, S. (2015). Shock wave as biological therapeutic tool: From mechanical stimulation to recovery and healing, through mechanotransduction. *Int. J. Surg.* 24 (Pt B), 147–153. doi:10.1016/j.ijsu.2015.11.030

da Silva Junior, E. M., Mesquita-Ferrari, R. A., França, C. M., Andreo, L., Bussadori, S. K., and Fernandes, K. P. S. (2017). Modulating effect of low intensity pulsed ultrasound on the phenotype of inflammatory cells. *Biomed. Pharmacother. = Biomedecine Pharmacother.* 96, 1147–1153. doi:10.1016/j.biopha.2017.11.108

Daeschler, S. C., Harhaus, L., Schoenle, P., Boecker, A., Kneser, U., and Bergmeister, K. D. (2018). Ultrasound and shock-wave stimulation to promote axonal regeneration following nerve surgery: A systematic review and meta-analysis of preclinical studies. *Sci. Rep.* 8 (1), 3168. doi:10.1038/s41598-018-21540-5

de Lucas, B., Pérez, L. M., Bernal, A., and Gálvez, B. G. (2021). Application of low-intensity pulsed therapeutic ultrasound on mesenchymal precursors does not affect their cell properties. *PloS One* 16 (2), e0246261. doi:10.1371/journal.pone.0246261

de Lucas, B., Pérez, L. M., Bernal, A., and Gálvez, B. G. (2020). Ultrasound therapy: Experiences and perspectives for regenerative medicine. *Genes* 11 (9), 1086. doi:10.3390/genes11091086

Diar-Bakirly, S., and El-Bialy, T. (2021). Human gingival fibroblasts: Isolation, characterization, and evaluation of CD146 expression. *Saudi J. Biol. Sci.* 28 (4), 2518–2526. doi:10.1016/j.sjbs.2021.01.053

El-Bialy, T., Alhadlaq, A., and Lam, B. (2012). Effect of therapeutic ultrasound on human periodontal ligament cells for dental and periodontal tissue engineering. *Open Dent. J.* 6, 235–239. doi:10.2174/1874210601206010235

Elvey, M. H., Miller, R., Khor, K. S., Protopapa, E., Horwitz, M. D., and Hunter, A. R. (2020). The use of low-intensity pulsed ultrasound in hand and wrist nonunions. *J. Plastic Surg. Hand Surg.* 54 (2), 101–106. doi:10.1080/2000656x.2019.1693393

Eming, S. A., Wynn, T. A., and Martin, P. (2017). Inflammation and metabolism in tissue repair and regeneration. *Sci. (New York, N.Y.)* 356 (6342), 1026–1030. doi:10.1126/science.aam7928

Feltham, T., Paudel, S., Lobao, M., Schon, L., and Zhang, Z. (2021). Low-intensity pulsed ultrasound suppresses synovial macrophage infiltration and inflammation in injured knees in rats. *Ultrasound Med. Biol.* 47 (4), 1045–1053. doi:10.1016/j.ultrasmedbio.2020.12.019

Feres, M. F. N., Kucharski, C., Diar-Bakirly, S., and El-Bialy, T. (2016). Effect of low-intensity pulsed ultrasound on the activity of osteoclasts: An *in vitro* study. *Archives Oral Biol.* 70, 73–78. doi:10.1016/j.archoralbio.2016.06.007

Fini, M., and Tyler, W. J. (2017). Transcranial focused ultrasound: A new tool for non-invasive neuromodulation. *Int. Rev. Psychiatry (Abingdon, Engl.* 29 (2), 168–177. doi:10.1080/09540261.2017.1302924

Fukunaga, K., Ishigami, T., and Kawano, T. (2005). Transcriptional regulation of neuronal genes and its effect on neural functions: Expression and function of forkhead transcription factors in neurons. *J. Pharmacol. Sci.* 98 (3), 205–211. doi:10.1254/jphs.fmj05001x3

Gao, Q., Cooper, P. R., Walmsley, A. D., and Scheven, B. A. (2017). Role of piezo channels in ultrasound-stimulated dental stem cells. *J. Endod.* 43 (7), 1130–1136. doi:10.1016/j.joen.2017.02.022

Gao, Q., Walmsley, A. D., Cooper, P. R., and Scheven, B. A. (2016). Ultrasound stimulation of different dental stem cell populations: Role of mitogen-activated protein kinase signaling. *J. Endod.* 42 (3), 425–431. doi:10.1016/j.joen.2015.12.019

Gardner, A. W., Parker, D. E., and Montgomery, P. S. (2019). Changes in vascular and inflammatory biomarkers after exercise rehabilitation in patients with symptomatic peripheral artery disease. *J. Vasc. Surg.* 70 (4), 1280–1290. doi:10.1016/j.jvs.2018.12.056

Geoghegan, I. P., Hoey, D. A., and McNamara, L. M. (2019). Integrins in osteocyte biology and mechanotransduction. *Curr. Osteoporos. Rep.* 17 (4), 195–206. doi:10.1007/s11914-019-00520-2

Ghemrawi, R., and Khair, M. (2020). Endoplasmic reticulum stress and unfolded protein response in neurodegenerative diseases. *Int. J. Mol. Sci.* 21 (17), E6127. doi:10.3390/ijms21176127

Guo, H., Huang, S., Yang, X., Wu, J., Kirk, T. B., Xu, J., et al. (2021). Injectable and self-healing hydrogels with double-dynamic bond tunable mechanical, gel-sol transition and drug delivery properties for promoting periodontium regeneration in periodontitis. *ACS Appl. Mater. interfaces* 13 (51), 61638–61652. doi:10.1021/acsami.1c18701

Harrison, A., Lin, S., Pounder, N., and Mikuni-Takagaki, Y. (2016). Mode and mechanism of low intensity pulsed ultrasound (LIPUS) in fracture repair. *Ultrasonics* 70, 45–52. doi:10.1016/j.ultras.2016.03.016

He, D., Wang, J., Li, Y., Wu, G., Zhu, G., and Chen, L. (2021). Low-intensity pulsed ultrasound promotes aggrecan expression via ZNT-9 in temporomandibular joint chondrocytes. *Gene* 768, 145318. doi:10.1016/j.gene.2020.145318

He, Y., Xu, H., Xiang, Z., Yu, H., Xu, L., Guo, Y., et al. (2019). YAP regulates periodontal ligament cell differentiation into myofibroblast interacted with RhoA/ROCK pathway. *J. Cell. Physiology* 234 (4), 5086–5096. doi:10.1002/jcp.27312

Herrera, D., Sanz, M., Kebschull, M., Jepsen, S., Sculean, A., Berglundh, T., et al. (2022). Treatment of stage IV periodontitis: The EFP S3 level clinical practice guideline. *J. Clin. Periodontology* 49, 4–71. doi:10.1111/jcpe.13639

Hu, B., Zhang, Y., Zhou, J., Li, J., Deng, F., Wang, Z., et al. (2014). Low-intensity pulsed ultrasound stimulation facilitates osteogenic differentiation of human periodontal ligament cells. *PloS One* 9 (4), e95168. doi:10.1371/journal.pone.0095168

Huang, H., Yang, R., and Zhou, Y.-H. (2018). Mechanobiology of periodontal ligament stem cells in orthodontic tooth movement. *Stem Cells Int.* 2018, 1–7. doi:10.1155/2018/6531216

Huang, Z., and Kraus, V. B. (2016). Does lipopolysaccharide-mediated inflammation have a role in OA? *Nat. Rev. Rheumatol.* 12 (2), 123–129. doi:10.1038/nrrheum.2015.158

Huelter-Hassler, D., Tomakidi, P., Steinberg, T., and Jung, B. A. (2017). Orthodontic strain affects the Hippo-pathway effector YAP concomitant with proliferation in human periodontal ligament fibroblasts. *Eur. J. Orthod.* 39 (3), 251–257. doi:10.1093/ejo/cjx012

Ichijo, S., Shindo, T., Eguchi, K., Monma, Y., Nakata, T., Morisue, Y., et al. (2021). Low-intensity pulsed ultrasound therapy promotes recovery from stroke by enhancing angio-neurogenesis in mice *in vivo*. *Sci. Rep.* 11 (1), 4958. doi:10.1038/s41598-021-84473-6

İnceoğlu, A., Şahin, F., Akkaya, N., Ök, N., Yörükoğlu, Ç., Mete, G., et al. (2021). Effects of low-density pulsed ultrasound treatment on transforming growth factor-beta, collagen level, histology, biomechanics, and function in repaired rat tendons. *Turkish J. Phys. Med. Rehabilitation* 67 (2), 167–174. doi:10.5606/tftrd.2021.5118

Inubushi, T., Tanaka, E., Rego, E. B., Kitagawa, M., Kawazoe, A., Ohta, A., et al. (2008). Effects of ultrasound on the proliferation and differentiation of cementoblast lineage cells. *J. Periodontology* 79 (10), 1984–1990. doi:10.1902/jop.2008.080081

Inubushi, T., Tanaka, E., Rego, E. B., Ohtani, J., Kawazoe, A., Tanne, K., et al. (2013). Ultrasound stimulation attenuates resorption of tooth root induced by experimental force application. *Bone* 53 (2), 497–506. doi:10.1016/j.bone.2013.01.021

Jiang, X., Savchenko, O., Li, Y., Qi, S., Yang, T., Zhang, W., et al. (2019). A review of low-intensity pulsed ultrasound for therapeutic applications. *IEEE Trans. bio-medical Eng.* 66 (10), 2704–2718. doi:10.1109/tbme.2018.2889669

Jin, S. H., Lee, J. E., Yun, J. H., Kim, I., Ko, Y., and Park, J. B. (2015). Isolation and characterization of human mesenchymal stem cells from gingival connective tissue. *J. Periodontal Res.* 50 (4), 461–467. doi:10.1111/jre.12228

Kasahara, Y., Usumi-Fujita, R., Hosomichi, J., Kaneko, S., Ishida, Y., Shibutani, N., et al. (2017). Low-intensity pulsed ultrasound reduces periodontal atrophy in occlusal hypofunctional teeth. *Angle Orthod.* 87 (5), 709–716. doi:10.2319/121216-893.1

Kaur, H., and El-Bialy, T. (2020). Shortening of overall orthodontic treatment duration with low-intensity pulsed ultrasound (LIPUS). *J. Clin. Med.* 9 (5), E1303. doi:10.3390/jcm9051303

Kechagia, J. Z., Ivaska, J., and Roca-Cusachs, P. (2019). Integrins as biomechanical sensors of the microenvironment. *Nat. Rev. Mol. Cell Biol.* 20 (8), 457–473. doi:10.1038/s41580-019-0134-2

Khanna-Jain, R., Agata, H., Vuorinen, A., Sándor, G. K. B., Suuronen, R., and Miettinen, S. (2010). Addition of BMP-2 or BMP-6 to dexamethasone, ascorbic acid, and β-glycerophosphate may not enhance osteogenic differentiation of human periodontal ligament cells. *Growth Factors (Chur, Switz.* 28 (6), 437–446. doi:10.3109/08977194.2010.495719

Kim, H. S., Kim, S., Shin, S. J., Park, Y. H., Nam, Y., Kim, C. W., et al. (2021). Gram-negative bacteria and their lipopolysaccharides in Alzheimer's disease: Pathologic roles and therapeutic implications. *Transl. Neurodegener.* 10 (1), 49. doi:10.1186/s40035-021-00273-y

Kinane, D. F., Stathopoulou, P. G., and Papapanou, P. N. (2017). Periodontal diseases. *Nat. Rev. Dis. Prim.* 3, 17038. doi:10.1038/nrdp.2017.38

Kuang, Y., Hu, B., Feng, G., Xiang, M., Deng, Y., Tan, M., et al. (2020). Metformin prevents against oxidative stress-induced senescence in human periodontal ligament cells. *Biogerontology* 21 (1), 13–27. doi:10.1007/s10522-019-09838-x

Kusuyama, J., Nakamura, T., Ohnishi, T., Albertson, B. G., Ebe, Y., Eiraku, N., et al. (2019). Low-intensity pulsed ultrasound promotes bone morphogenic protein 9-induced osteogenesis and suppresses inhibitory effects of inflammatory cytokines on cellular responses via Rho-associated kinase 1 in human periodontal ligament fibroblasts. *J. Cell. Biochem.* 120 (9), 14657–14669. doi:10.1002/jcb.28727

Lai, W. C., Iglesias, B. C., Mark, B. J., and Wang, D. (2021). Low-intensity pulsed ultrasound augments tendon, ligament, and bone-soft tissue healing in preclinical animal models: A systematic review. *Arthrosc. J. Arthrosc. Relat. Surg. Official Publ. Arthrosc. Assoc. N. Am. Int. Arthrosc. Assoc.* 37 (7), 2318–2333.e3. doi:10.1016/j.arthro.2021.02.019

Leewananthawet, A., Arakawa, S., Okano, T., Daitoku Kinoshita, R., Ashida, H., Izumi, Y., et al. (2019). Ozone ultrafine bubble water induces the cellular signaling involved in oxidative stress responses in human periodontal ligament fibroblasts. *Sci. Technol. Adv. Mater.* 20 (1), 590–599. doi:10.1080/14686996.2019.1614980

Leighton, R., Watson, J. T., Giannoudis, P., Papakostidis, C., Harrison, A., and Steen, R. G. (2017). Healing of fracture nonunions treated with low-intensity pulsed ultrasound (LIPUS): A systematic review and meta-analysis. *Injury* 48 (7), 1339–1347. doi:10.1016/j.injury.2017.05.016

Li, H., Deng, Y., Tan, M., Feng, G., Kuang, Y., Li, J., et al. (2020a). Low-intensity pulsed ultrasound upregulates osteogenesis under inflammatory conditions in periodontal ligament stem cells through unfolded protein response. *Stem Cell Res. Ther.* 11 (1), 215. doi:10.1186/s13287-020-01732-5

Li, H., Zhou, J., Zhu, M., Ying, S., Li, L., Chen, D., et al. (2021). Low-intensity pulsed ultrasound promotes the formation of periodontal ligament stem cell sheets and ectopic periodontal tissue regeneration. *J. Biomed. Mater. Res. Part A* 109 (7), 1101–1112. doi:10.1002/jbm.a.37102

Li, J., Li, Y., Pan, S., Zhang, L., He, L., and Niu, Y. (2019). Paeonol attenuates ligation-induced periodontitis in rats by inhibiting osteoclastogenesis via regulating Nrf2/NF-κB/NFATc1 signaling pathway. *Biochimie* 156, 129–137. doi:10.1016/j.biochi.2018.09.004

Li, J., Zhang, Q., Ren, C., Wu, X., Zhang, Y., Bai, X., et al. (2018). Low-intensity pulsed ultrasound prevents the oxidative stress induced endothelial-mesenchymal transition in human aortic endothelial cells. *Cell. Physiology Biochem. Int. J. Exp. Cell. Physiology, Biochem. Pharmacol.* 45 (4), 1350–1365. doi:10.1159/000487561

Li, R., and Zhang, Q. (2015). HtrA1 may regulate the osteogenic differentiation of human periodontal ligament cells by TGF-β1. *J. Mol. Histology* 46 (2), 137–144. doi:10.1007/s10735-015-9612-9

Li, S., Xu, Z., Wang, Z., Xiang, J., Zhang, T., and Lu, H. (2021). Acceleration of bone-tendon interface healing by low-intensity pulsed ultrasound is mediated by macrophages. *Phys. Ther.* 101, pzab055. doi:10.1093/ptj/pzab055

Li, Y., Sun, C., Feng, G., He, Y., Li, J., and Song, J. (2020b). Low-intensity pulsed ultrasound activates autophagy in periodontal ligament cells in the presence or absence of lipopolysaccharide. *Archives Oral Biol.* 117, 104769. doi:10.1016/j.archoralbio.2020.104769

Liang, Y., Luan, X., and Liu, X. (2020). Recent advances in periodontal regeneration: A biomaterial perspective. *Bioact. Mater.* 5 (2), 297–308. doi:10.1016/j.bioactmat.2020.02.012

Liao, Q., Li, B. J., Li, Y., Xiao, Y., Zeng, H., Liu, J. M., et al. (2021). Low-intensity pulsed ultrasound promotes osteoarthritic cartilage regeneration by BMSC-derived exosomes via modulating the NF-κB signaling pathway. *Int. Immunopharmacol.* 97, 107824. doi:10.1016/j.intimp.2021.107824

Liljestrand, J. M., Paju, S., Buhlin, K., Persson, G. R., Sarna, S., Nieminen, M. S., et al. (2017). Lipopolysaccharide, a possible molecular mediator between periodontitis and coronary artery disease. *J. Clin. Periodontology* 44 (8), 784–792. doi:10.1111/jcpe.12751

Lin, G., Reed-Maldonado, A. B., Lin, M., Xin, Z., and Lue, T. F. (2016). Effects and mechanisms of low-intensity pulsed ultrasound for chronic prostatitis and chronic pelvic pain syndrome. *Int. J. Mol. Sci.* 17 (7), E1057. doi:10.3390/ijms17071057

Lin, W.-C., Yao, C., Huang, T.-Y., Cheng, S.-J., and Tang, C.-M. (2019). Long-term *in vitro* degradation behavior and biocompatibility of polycaprolactone/cobalt-substituted hydroxyapatite composite for bone tissue engineering. *Dent. Mater. Official Publ. Acad. Dent. Mater.* 35 (5), 751–762. doi:10.1016/j.dental.2019.02.023

Lin, W., Xu, L., Zwingenberger, S., Gibon, E., Goodman, S. B., and Li, G. (2017). Mesenchymal stem cells homing to improve bone healing. *J. Orthop. Transl.* 9, 19–27. doi:10.1016/j.jot.2017.03.002

Liu, K., Han, B., Meng, H., and Hou, J. (2017). Influence of rs2228570 on transcriptional activation by the vitamin D receptor in human gingival fibroblasts and periodontal ligament cells. *J. Periodontology* 88 (9), 915–925. doi:10.1902/jop.2017.170030

Liu, S., Zhou, M., Li, J., Hu, B., Jiang, D., Huang, H., et al. (2020). LIPUS inhibited the expression of inflammatory factors and promoted the osteogenic differentiation capacity of hPDLCs by inhibiting the NF-κB signaling pathway. *J. Periodontal Res.* 55 (1), 125–140. doi:10.1111/jre.12696

Liu, Z., He, Y., Xu, C., Li, J., Zeng, S., Yang, X., et al. (2021). The role of PHF8 and TLR4 in osteogenic differentiation of periodontal ligament cells in inflammatory environment. *J. Periodontology* 92 (7), 1049–1059. doi:10.1002/JPER.20-0285

Maung, W. M., Nakata, H., Miura, M., Miyasaka, M., Kim, Y.-K., Kasugai, S., et al. (2021). Low-intensity pulsed ultrasound stimulates osteogenic differentiation of periosteal cells *in vitro*. *Tissue Eng. Part A* 27 (1-2), 63–73. doi:10.1089/ten.tea.2019.0331

McCarthy, C., and Camci-Unal, G. (2021). Low intensity pulsed ultrasound for bone tissue engineering. *Micromachines* 12 (12), 1488. doi:10.3390/mi12121488

Men, Y., Wang, Y., Yi, Y., Jing, D., Luo, W., Shen, B., et al. (2020). Gli1+ periodontium stem cells are regulated by osteocytes and occlusal force. *Dev. Cell* 54 (5), 639–654.e6. doi:10.1016/j.devcel.2020.06.006

Meng, J., Hong, J., Zhao, C., Zhou, C., Hu, B., Yang, Y., et al. (2018). Low-intensity pulsed ultrasound inhibits RANKL-induced osteoclast formation via modulating ERK-c-Fos-NFATc1 signaling cascades. *Am. J. Transl. Res.* 10 (9), 2901–2910.

Mirza, Y. H., Teoh, K. H., Golding, D., Wong, J. F., and Nathdwarawala, Y. (2019). Is there a role for low intensity pulsed ultrasound (LIPUS) in delayed or nonunion following arthrodesis in foot and ankle surgery? *Foot Ankle Surg. Official J. Eur. Soc. Foot Ankle Surg.* 25 (6), 842–848. doi:10.1016/j.fas.2018.11.004

Miyazawa, K., and Miyazono, K. (2017). Regulation of TGF-β family signaling by inhibitory Smads. *Cold Spring Harb. Perspect. Biol.* 9 (3), a022095. doi:10.1101/cshperspect.a022095

Molina, T., Kabsch, K., Alonso, A., Kohl, A., Komposch, G., and Tomakidi, P. (2001). Topographic changes of focal adhesion components and modulation of p125FAK activation in stretched human periodontal ligament fibroblasts. *J. Dent. Res.* 80 (11), 1984–1989. doi:10.1177/00220345010800110701

Mostafa, N. Z., Uludağ, H., Dederich, D. N., Doschak, M. R., and El-Bialy, T. H. (2009). Anabolic effects of low-intensity pulsed ultrasound on human gingival fibroblasts. *Archives Oral Biol.* 54 (8), 743–748. doi:10.1016/j.archoralbio.2009.04.012

Mostafa, N. Z., Uludağ, H., Varkey, M., Dederich, D. N., Doschak, M. R., and El-Bialy, T. H. (2011). *In vitro* osteogenic induction of human gingival fibroblasts for bone regeneration. *Open Dent. J.* 5, 139–145. doi:10.2174/1874210601105010139

Nakao, J., Fujii, Y., Kusuyama, J., Bandow, K., Kakimoto, K., Ohnishi, T., et al. (2014). Low-intensity pulsed ultrasound (LIPUS) inhibits LPS-induced inflammatory responses of osteoblasts through TLR4-MyD88 dissociation. *Bone* 58, 17–25. doi:10.1016/j.bone.2013.09.018

Nazir, M. A. (2017). Prevalence of periodontal disease, its association with systemic diseases and prevention. *Int. J. Health Sci.* 11 (2), 72–80.

Pan, W., Wang, Q., and Chen, Q. (2019a). The cytokine network involved in the host immune response to periodontitis. *Int. J. Oral Sci.* 11 (3), 30. doi:10.1038/s41368-019-0064-z

Pan, Y.-L., Ma, Y., Guo, Y., Tu, J., Guo, G.-P., Ma, S. M., et al. (2019b2001). Effects of Clematis chinensis Osbeck mediated by low-intensity pulsed ultrasound on transforming growth factor-β/Smad signaling in rabbit articular chondrocytes. *J. Med. Ultrasonics* 46 (2), 177–186. doi:10.1007/s10396-018-0920-z

Papadopoulou, A., Cantele, A., Koletsi, D., Eliades, T., and Kletsas, D. (2020). Short- and long-term treatment with TNF-α inhibits the induction of osteoblastic differentiation in cyclic tensile-stretched periodontal ligament fibroblasts. *Eur. J. Orthod.* 42 (4), 396–406. doi:10.1093/ejo/cjaa042

Pihlstrom, B. L., Michalowicz, B. S., and Johnson, N. W. (2005). Periodontal diseases. *Lancet (London, Engl.* 366 (9499), 1809–1820. doi:10.1016/s0140-6736(05)67728-8

Pitto, L., Ripoli, A., Cremisi, F., Simili, M., and Rainaldi, G. (2008). microRNA(interference) networks are embedded in the gene regulatory networks. *Cell cycle* 7 (16), 2458–2461. doi:10.4161/cc.7.16.6455

Qiao, D., Zhang, Z., Zhang, Y., Chen, Q., Chen, Y., Tang, Y., et al. (2021). Regulation of endoplasmic reticulum stress-autophagy: A potential therapeutic target for ulcerative colitis. *Front. Pharmacol.* 12, 697360. doi:10.3389/fphar.2021.697360

Qin, L., Liu, W., Cao, H., and Xiao, G. (2020). Molecular mechanosensors in osteocytes. *Bone Res.* 8, 23. doi:10.1038/s41413-020-0099-y

Rai, M. F., Duan, X., Quirk, J. D., Holguin, N., Schmidt, E. J., Chinzei, N., et al. (2017). Post-traumatic osteoarthritis in mice following mechanical injury to the synovial joint. *Sci. Rep.* 7, 45223. doi:10.1038/srep45223

Read, A., and Schröder, M. (2021). The unfolded protein response: An overview. *Biology* 10 (5), 384. doi:10.3390/biology10050384

Ren, L., Yang, Z., Song, J., Wang, Z., Deng, F., and Li, W. (2013). Involvement of p38 MAPK pathway in low intensity pulsed ultrasound induced osteogenic differentiation of human periodontal ligament cells. *Ultrasonics* 53 (3), 686–690. doi:10.1016/j.ultras.2012.10.008

Roskoski, R. (2012). ERK1/2 MAP kinases: Structure, function, and regulation. *Pharmacol. Res.* 66 (2), 105–143. doi:10.1016/j.phrs.2012.04.005

Rowe, P., Koller, A., and Sharma, S. (2022). "Physiology, bone remodeling,". StatPearls Publishing %* Copyright © 2022 in *StatPearls* (Treasure Island (FL): StatPearls Publishing LLC). Available at: http://www.ncbi.nlm.nih.gov/books/NBK499863/) (%L NBK499863 %U.

Rutten, S., van den Bekerom, M. P. J., Sierevelt, I. N., and Nolte, P. A. (2016). Enhancement of bone-healing by low-intensity pulsed ultrasound: A systematic review. *JBJS Rev.* 4 (3), e6. doi:10.2106/jbjs.rvw.o.00027

Saha, S., Panigrahi, D. P., Patil, S., and Bhutia, S. K. (2018). Autophagy in health and disease: A comprehensive review. *Biomed. Pharmacother. = Biomedecine Pharmacother.* 104, 485–495. doi:10.1016/j.biopha.2018.05.007

Sang, F., Xu, J., Chen, Z., Liu, Q., and Jiang, W. (2021). Low-intensity pulsed ultrasound alleviates osteoarthritis condition through focal adhesion kinase-mediated chondrocyte proliferation and differentiation. *Cartilage* 13 (2), 196S–203S. doi:10.1177/1947603520912322

Sczepanik, F. S. C., Grossi, M. L., Casati, M., Goldberg, M., Glogauer, M., Fine, N., et al. (2020). Periodontitis is an inflammatory disease of oxidative stress: We should treat it that way. *Periodontology* 84 (1), 45–68. doi:10.1111/prd.12342

Shimizu, T., Fujita, N., Tsuji-Tamura, K., Kitagawa, Y., Fujisawa, T., Tamura, M., et al. (2021). Osteocytes as main responders to low-intensity pulsed ultrasound treatment during fracture healing. *Sci. Rep.* 11 (1), 10298. doi:10.1038/s41598-021-89672-9

Song, W.-S., Sung, C.-Y., Ke, C.-H., and Yang, F.-Y. (2022). Anti-inflammatory and neuroprotective effects of transcranial ultrasound stimulation on Parkinson's disease. *Ultrasound Med. Biol.* 48 (2), 265–274. doi:10.1016/j.ultrasmedbio.2021.10.001

Steppe, L., Liedert, A., Ignatius, A., and Haffner-Luntzer, M. (2020). Influence of low-magnitude high-frequency vibration on bone cells and bone regeneration. *Front. Bioeng. Biotechnol.* 8, 595139. doi:10.3389/fbioe.2020.595139

Stewart, S., Darwood, A., Masouros, S., Higgins, C., and Ramasamy, A. (2020). Mechanotransduction in osteogenesis. *Bone and Jt. Res.* 9 (1), 1–14. doi:10.1302/2046-3758.91.bjr-2019-0043.r2

Tan, J., Zhou, Y., Luo, J., Wu, X., Liu, H., Wang, W., et al. (2022). High glucose inhibits the osteogenic differentiation of periodontal ligament stem cells in periodontitis by activating endoplasmic reticulum stress. *Ann. Transl. Med.* 10 (4), 204. doi:10.21037/atm-22-6

Tan, Y., Guo, Y., Reed-Maldonado, A. B., Li, Z., Lin, G., Xia, S.-J., et al. (2021). Low-intensity pulsed ultrasound stimulates proliferation of stem/progenitor cells: What we need to know to translate basic science research into clinical applications. *Asian J. Androl.* 23 (6), 602–610. doi:10.4103/aja.aja_25_21

Tanaka, E., Kuroda, S., Horiuchi, S., Tabata, A., and El-Bialy, T. (2015). Low-intensity pulsed ultrasound in dentofacial tissue engineering. *Ann. Biomed. Eng.* 43 (4), 871–886. doi:10.1007/s10439-015-1274-y

Tassinary, J. A. F., Lunardelli, A., Basso, B. d. S., Dias, H. B., Catarina, A. V., Stülp, S., et al. (2018). Low-intensity pulsed ultrasound (LIPUS) stimulates mineralization of MC3T3-E1 cells through calcium and phosphate uptake. *Ultrasonics* 84, 290–295. doi:10.1016/j.ultras.2017.11.011

Tyler, W. J., Tufail, Y., Finsterwald, M., Tauchmann, M. L., Olson, E. J., and Majestic, C. (2008). Remote excitation of neuronal circuits using low-intensity, low-frequency ultrasound. *PloS One* 3 (10), e3511. doi:10.1371/journal.pone.0003511

Uda, Y., Azab, E., Sun, N., Shi, C., and Pajevic, P. D. (2017). Osteocyte mechanobiology. *Curr. Osteoporos. Rep.* 15 (4), 318–325. doi:10.1007/s11914-017-0373-0

Usui, M., Onizuka, S., Sato, T., Kokabu, S., Ariyoshi, W., and Nakashima, K. (2021). Mechanism of alveolar bone destruction in periodontitis - periodontal bacteria and inflammation. *Jpn. Dent. Sci. Rev.* 57, 201–208. doi:10.1016/j.jdsr.2021.09.005

Vaquette, C., Pilipchuk, S. P., Bartold, P. M., Hutmacher, D. W., Giannobile, W. V., and Ivanovski, S. (2018). Tissue engineered constructs for periodontal regeneration: Current status and future perspectives. *Adv. Healthc. Mater.* 7 (21), e1800457. doi:10.1002/adhm.201800457

Vining, K. H., and Mooney, D. J. (2017). Mechanical forces direct stem cell behaviour in development and regeneration. *Nat. Rev. Mol. Cell Biol.* 18 (12), 728–742. doi:10.1038/nrm.2017.108

Wang, L., Wu, F., Song, Y., Duan, Y., and Jin, Z. (2018a). Erythropoietin induces the osteogenesis of periodontal mesenchymal stem cells from healthy and periodontitis sources via activation of the p38 MAPK pathway. *Int. J. Mol. Med.* 41 (2), 829–835. doi:10.3892/ijmm.2017.3294

Wang, L., Wu, F., Song, Y., Li, X., Wu, Q., Duan, Y., et al. (2016). Long noncoding RNA related to periodontitis interacts with miR-182 to upregulate osteogenic differentiation in periodontal mesenchymal stem cells of periodontitis patients. *Cell Death Dis.* 7 (8), e2327. doi:10.1038/cddis.2016.125

Wang, L., You, X., Zhang, L., Zhang, C., and Zou, W. (2022a). Mechanical regulation of bone remodeling. *Bone Res.* 10 (1), 16. doi:10.1038/s41413-022-00190-4

Wang, W., Yuan, C., Geng, T., Liu, Y., Zhu, S., Zhang, C., et al. (2020). Lipopolysaccharide inhibits osteogenic differentiation of periodontal ligament stem cells partially through toll-like receptor 4-mediated ephrinB2 downregulation. *Clin. Oral Investig.* 24 (10), 3407–3416. doi:10.1007/s00784-020-03211-w

Wang, Y., Li, J., Qiu, Y., Hu, B., Chen, J., Fu, T., et al. (2018b). Low-intensity pulsed ultrasound promotes periodontal ligament stem cell migration through TWIST1-mediated SDF-1 expression. *Int. J. Mol. Med.* 42 (1), 322–330. doi:10.3892/ijmm.2018.3592

Wang, Y., Newman, M. R., and Benoit, D. S. W. (2018c). Development of controlled drug delivery systems for bone fracture-targeted therapeutic delivery: A review. *Eur. J. Pharm. Biopharm. Official J. Arbeitsgemeinschaft Fur Pharmazeutische Verfahrenstechnik e.V* 127, 223–236. doi:10.1016/j.ejpb.2018.02.023

Wang, Y., Xiao, Q., Zhong, W., Zhang, C., Yin, Y., Gao, X., et al. (2022b). Low-intensity pulsed ultrasound promotes periodontal regeneration in a beagle model of furcation involvement. *Front. Bioeng. Biotechnol.* 10, 961898. doi:10.3389/fbioe.2022.961898

Watanabe, T., Matsumoto, Y., Nishimiya, K., Shindo, T., Amamizu, H., Sugisawa, J., et al. (2021). Low-intensity pulsed ultrasound therapy suppresses coronary adventitial inflammatory changes and hyperconstricting responses after coronary stent implantation in pigs *in vivo*. *PloS One* 16 (9), e0257175. doi:10.1371/journal.pone.0257175

West, N., Chapple, I., Claydon, N., D'Aiuto, F., Donos, N., Ide, M., et al. (2021). BSP implementation of European S3 - level evidence-based treatment guidelines for stage

I-III periodontitis in UK clinical practice. *J. Dent.* 106, 103562. doi:10.1016/j.jdent.2020.103562

Wu, L., Zhang, S. Q., Zhao, L., Ren, Z. H., and Hu, C. Y. (2022). Global, regional, and national burden of periodontitis from 1990 to 2019: Results from the Global Burden of Disease study 2019. *J. Periodontology* 93 (10), 1445–1454. doi:10.1002/jper.21-0469

Xie, S., Jiang, X., Wang, R., Xie, S., Hua, Y., Zhou, S., et al. (2019). Low-intensity pulsed ultrasound promotes the proliferation of human bone mesenchymal stem cells by activating PI3K/AKt signaling pathways. *J. Cell. Biochem.* 120 (9), 15823–15833. doi:10.1002/jcb.28853

Xin, Z., Lin, G., Lei, H., Lue, T. F., and Guo, Y. (2016). Clinical applications of low-intensity pulsed ultrasound and its potential role in urology. *Transl. Androl. Urology* 5 (2), 255–266. doi:10.21037/tau.2016.02.04

Xing, Y.-Q., Li, A., Yang, Y., Li, X.-X., Zhang, L.-N., and Guo, H.-C. (2018). The regulation of FOXO1 and its role in disease progression. *Life Sci.* 193, 124–131. doi:10.1016/j.lfs.2017.11.030

Xu, M., Wang, L., Wu, S., Dong, Y., Chen, X., Wang, S., et al. (2021). Review on experimental study and clinical application of low-intensity pulsed ultrasound in inflammation. *Quantitative Imaging Med. Surg.* 11 (1), 443–462. doi:10.21037/qims-20-680

Xu, W., Zhou, W., Wang, H., and Liang, S. (2020). Roles of Porphyromonas gingivalis and its virulence factors in periodontitis. *Adv. Protein Chem. Struct. Biol.* 120, 45–84. doi:10.1016/bs.apcsb.2019.12.001

Yamamoto, T., Ugawa, Y., Kawamura, M., Yamashiro, K., Kochi, S., Ideguchi, H., et al. (2018). Modulation of microenvironment for controlling the fate of periodontal ligament cells: The role of rho/ROCK signaling and cytoskeletal dynamics. *J. Cell Commun. Signal.* 12 (1), 369–378. doi:10.1007/s12079-017-0425-3

Yang, F., Zhang, R., Xu, J., Du, J., Leng, S., Zhang, L., et al. (2022). Comparative effects of concentrated growth factors on the biological characteristics of periodontal ligament cells and stem cells from apical papilla. *J. Endod.* S0099-2399, 00339.

Yang, Z., Ren, L., Deng, F., Wang, Z., and Song, J. (2014). Low-intensity pulsed ultrasound induces osteogenic differentiation of human periodontal ligament cells through activation of bone morphogenetic protein-smad signaling. *J. Ultrasound Med. Official J. Am. Inst. Ultrasound Med.* 33 (5), 865–873. doi:10.7863/ultra.33.5.865

Ying, S., Tan, M., Feng, G., Kuang, Y., Chen, D., Li, J., et al. (2020). Low-intensity Pulsed Ultrasound regulates alveolar bone homeostasis in experimental Periodontitis by diminishing Oxidative Stress. *Theranostics* 10 (21), 9789–9807. doi:10.7150/thno.42508

Zhai, Q., Dong, Z., Wang, W., Li, B., and Jin, Y. (2019). Dental stem cell and dental tissue regeneration. *Front. Med.* 13 (2), 152–159. doi:10.1007/s11684-018-0628-x

Zhang, B., Chen, H., Ouyang, J., Xie, Y., Chen, L., Tan, Q., et al. (2020). SQSTM1-dependent autophagic degradation of PKM2 inhibits the production of mature IL1B/IL-1β and contributes to LIPUS-mediated anti-inflammatory effect. *Autophagy* 16 (7), 1262–1278. doi:10.1080/15548627.2019.1664705

Zhang, J., Wan, Q., Yu, X., Cheng, G., Ni, Y., and Li, Z. (2018). Low-dose nicotine reduces the homing ability of murine BMSCs during fracture healing. *Am. J. Transl. Res.* 10 (9), 2796–2809.

Zhang, N., Chow, S. K.-H., Leung, K.-S., and Cheung, W.-H. (2017a). Ultrasound as a stimulus for musculoskeletal disorders. *J. Orthop. Transl.* 9, 52–59. doi:10.1016/j.jot.2017.03.004

Zhang, X., Hu, B., Sun, J., Li, J., Liu, S., and Song, J. (2017b). Inhibitory effect of low-intensity pulsed ultrasound on the expression of lipopolysaccharide-induced inflammatory factors in U937 cells. *J. Ultrasound Med. Official J. Am. Inst. Ultrasound Med.* 36 (12), 2419–2429. doi:10.1002/jum.14239

Zhang, X., Hu, Z., Hao, J., and Shen, J. (2016). Low intensity pulsed ultrasound promotes the extracellular matrix synthesis of degenerative human nucleus pulposus cells through FAK/PI3K/Akt pathway. *Spine* 41 (5), E248–E254. doi:10.1097/brs.0000000000001220

Zhao, L., Feng, Y., Shi, A., Zhang, L., Guo, S., and Wan, M. (2017). Neuroprotective effect of low-intensity pulsed ultrasound against MPP+-Induced neurotoxicity in PC12 cells: Involvement of K2P channels and stretch-activated ion channels. *Ultrasound Med. Biol.* 43 (9), 1986–1999. doi:10.1016/j.ultrasmedbio.2017.04.020

Zheng, C., Wu, S.-M., Lian, H., Lin, Y.-Z., Zhuang, R., Thapa, S., et al. (2019). Low-intensity pulsed ultrasound attenuates cardiac inflammation of CVB3-induced viral myocarditis via regulation of caveolin-1 and MAPK pathways. *J. Cell. Mol. Med.* 23 (3), 1963–1975. doi:10.1111/jcmm.14098

Zhu, W., and Liang, M. (2015). Periodontal ligament stem cells: Current status, concerns, and future prospects. *Stem Cells Int.* 2015, 1–11. doi:10.1155/2015/972313

Zura, R., Della Rocca, G. J., Mehta, S., Harrison, A., Brodie, C., Jones, J., et al. (2015a). Treatment of chronic (>1 year) fracture nonunion: Heal rate in a cohort of 767 patients treated with low-intensity pulsed ultrasound (LIPUS). *Injury* 46 (10), 2036–2041. doi:10.1016/j.injury.2015.05.042

Zura, R., Mehta, S., Della Rocca, G. J., Jones, J., and Steen, R. G. (2015b). A cohort study of 4,190 patients treated with low-intensity pulsed ultrasound (LIPUS): Findings in the elderly versus all patients. *BMC Musculoskelet. Disord.* 16, 45. doi:10.1186/s12891-015-0498-1

frontiers | Frontiers in Bioengineering and Biotechnology

TYPE Review
PUBLISHED 05 May 2023
DOI 10.3389/fbioe.2023.1165651

OPEN ACCESS

EDITED BY
Guang-Kui Xu,
Xi'an Jiaotong University, China

REVIEWED BY
Guanbin Song,
Chongqing University, China
Mathieu Hautefeuille,
Sorbonne Université, France

*CORRESPONDENCE
Dongyuan Lü,
lvdongy@imech.ac.cn
Mian Long,
mlong@imech.ac.cn

RECEIVED 14 February 2023
ACCEPTED 18 April 2023
PUBLISHED 05 May 2023

CITATION
Wu Y, Li N, Shu X, Li W, Zhang X, Lü D and Long M (2023), Biomechanics in liver regeneration after partial hepatectomy. *Front. Bioeng. Biotechnol.* 11:1165651. doi: 10.3389/fbioe.2023.1165651

Biomechanics in liver regeneration after partial hepatectomy

Yi Wu[1,2], Ning Li[1,2], Xinyu Shu[1,2], Wang Li[1,2], Xiaoyu Zhang[1,2], Dongyuan Lü[1,2]* and Mian Long[1,2]*

[1]Center for Biomechanics and Bioengineering, Beijing Key Laboratory of Engineered Construction and Mechanobiology and Key Laboratory of Microgravity (National Microgravity Laboratory), Institute of Mechanics, Chinese Academy of Sciences, Beijing, China, [2]School of Engineering Sciences, University of Chinese Academy of Sciences, Beijing, China

The liver is a complicated organ within the body that performs wide-ranging and vital functions and also has a unique regenerative capacity after hepatic tissue injury and cell loss. Liver regeneration from acute injury is always beneficial and has been extensively studied. Experimental models including partial hepatectomy (PHx) reveal that extracellular and intracellular signaling pathways can help the liver recover to its equivalent size and weight prior to an injury. In this process, mechanical cues possess immediate and drastic changes in liver regeneration after PHx and also serve as main triggering factors and significant driving forces. This review summarized the biomechanics progress in liver regeneration after PHx, mainly focusing on PHx-based hemodynamics changes in liver regeneration and the decoupling of mechanical forces in hepatic sinusoids including shear stress, mechanical stretch, blood pressure, and tissue stiffness. Also discussed were the potential mechanosensors, mechanotransductive pathways, and mechanocrine responses under varied mechanical loading *in vitro*. Further elucidating these mechanical concepts in liver regeneration helps establish a comprehensive understanding of the biochemical factors and mechanical cues in this process. Proper adjustment of mechanical loading within the liver might preserve and restore liver functions in clinical settings, serving as an effective therapy for liver injury and diseases.

KEYWORDS

liver regeneration, partial hepatectomy, hemodynamics, mechanical loading, mechanotransduction

1 Introduction

The liver is the largest substantive organ in the mammalian body and undertakes many key physiological activities within the body. It is mainly responsible for the absorption, storage, metabolism, and redistribution of substances including sugars, lipids, sterols, proteins, and vitamins. The liver also has functions in immune regulation and defensive response, detoxification, biotransformation, and bile synthesis and secretion (Michalopoulos, 2007; Powell et al., 2021). As a unique organ, the liver has a powerful regenerative capability to guarantee its mass, structure, and stability of broad hepatic functions (Michalopoulos, 2007). Recently, liver-related diseases such as hepatitis, fatty liver, cirrhosis, and liver cancer have become one of the main causes of death worldwide (Sallberg and Pasetto, 2020; Powell et al., 2021). The resection of liver lesions is a vital treatment and effectively exploring the potential of liver regeneration is the key to the

survival of postoperative patients. Living donor liver transplantation utilizes the ability of liver regeneration to alleviate the problem of recipient insufficiency and donor shortage. However, challenges still remain in keeping the liver outside the body and maintaining its metabolic activity (Giwa et al., 2017; de Vries et al., 2019). Therefore, understanding the regeneration mechanisms of the liver yields both biological significance and potential applications for the treatment of liver injury and diseases (Campana et al., 2021).

Liver regeneration refers to the process of proliferation, migration, and differentiation of various hepatic cells by the combined regulation of various factors to restore the normal size and function of the liver. In contrast to the regrowth of limbs in lower vertebrates containing stem cells at the cut surface, the resected parts of the liver do not grow back from the cut surface, but instead, expand the tissue mass from the remaining lobes to compensate for the lost tissues (Fausto et al., 2006; Cordero-Espinoza and Huch, 2018), suggesting that liver regeneration is a compensatory process of liver growth regulated by the requirements of functional recovery rather than morphological regeneration. Depending on the characteristics of liver injury, liver regeneration can be classified into two patterns, acute liver regeneration and chronic liver regeneration. Acute liver regeneration is initiated after PHx or a high concentration of chemical injury in a short time, during which all the existing mature cells proliferate to replenish the liver mass. Chemical injury not only causes a regenerative response but also induces an inflammatory response. The degree of liver injury is related to the time and dose of administration. However, chronic liver regeneration is activated by inflammation, viruses, or toxins in continuous time, which yields adverse effects and hinders optimal liver function, leading to cirrhosis and even liver cancer (Forbes and Newsome, 2016; Michalopoulos, 2017; Michalopoulos and Bhushan, 2021). Hepatocyte self-replication mainly contributes to liver regeneration after PHx, while liver progenitor cells (LPCs), which can differentiate into either liver cells or bile duct cells, serve as an alternative pathway for acute regeneration when the tissue injury is too severe to initiate sufficient proliferation of hepatocytes (Li et al., 2020; Zhu et al., 2020). Furthermore, LPCs also appear in hepatic fibrosis and the amount is correlated with the severity of fibrosis in chronic liver diseases (Williams et al., 2014; So et al., 2020).

At present, the protocols for liver injury induction and regeneration mainly include surgical operation and chemical induction (Forbes and Newsome, 2016; Huang et al., 2021). Chemicals are usually toxic to the liver and will cause an inflammatory response, massive necrosis, and high mortality if the dose, frequency, and method of administration are not well controlled. In contrast, PHx serves as the commonly used model in liver regeneration, mainly due to the exact removal of the hepatic mass, the precise timing of stimuli, the minimized hepatocytes damage, and the pure regenerative response without an inflammatory response (Higgins and Anderson, 1931; Michalopoulos and DeFrances, 1997). PHx was primarily invented by Higgins and Anderson in 1931 (Higgins and Anderson, 1931). Since then, this method has been gradually accepted as the commonly used model in rats and a standard procedure has been formed for rodents (Mitchell and Willenbring, 2008). The PHx model completely retains the structure of the main portal vein, inferior vena cava, common bile duct, and hepatic artery, presenting both mechanical and perfusion damage to the liver. It is close to the clinical liver transplantation procedure with valuable experimental results for reference. The characteristics of the liver regeneration model constructed by PHx are as follows: 1) Since a single liver lobe is removed and the process does not lead to a large amount of necrosis of residual liver tissue, the initiation of residual liver regeneration is relatively independent of the inflammatory response, which helps to better explore the direct initiation factors of liver regeneration. 2) The model has good repeatability and stability, and the operation can be completed in approximately 20 min by a skilled surgeon. 3) The regeneration reaction caused by PHx is immediate and can be used as the starting point of the whole regeneration process when the surgery is completed. After PHx, the peaks of DNA synthesis and mitosis in hepatocytes vary depending on different species (24 h in rats and 36–48 h in mice) (Michalopoulos, 2013). Furthermore, PHx has high accuracy in quantifying the degree of liver resection, low complication rate, high surgical success rate, and good repeatability (Forbes and Newsome, 2016; Christ et al., 2021). Based on the above advantages, liver regeneration after PHx is a suitable model to help understand the complexity of signaling pathways for tissue growth, and is widely used in the treatment of clinical liver diseases (*e.g.*, living donor liver transplantation, liver cancer).

Biochemical cues-based liver regeneration theory related to PHx has been extensively investigated, covering the cell proliferation dynamics (Michalopoulos and DeFrances, 1997), the morphologic changes (Michalopoulos, 2007), the extracellular matrix (ECM) reconstruction (Michalopoulos and Bhushan, 2021), and the complete or auxiliary mitogens-mediated signaling pathways (Fausto et al., 2006; Michalopoulos, 2017). Indeed two main signaling pathways, complete mitogens-dependent and auxiliary mitogens-dependent, are found to interact with each other (Taub, 2004). All the events during liver regeneration are finely tuned in time and space (Michalopoulos, 2007). Briefly, the hepatocytes are the first to proliferate with DNA synthesis peaking at 24 h in rats, while DNA synthesis occurs later in the nonparenchymal cells (NPCs). Major complete mitogens include hepatocyte growth factor (HGF) and its receptor c-Met, together with epidermal growth factor (EGF), transforming growth factor-α (TGF-α), as well as heparin-binding EGF-like growth factor (HB-EGF) and their receptor epidermal growth factor receptor (EGFR) (Kimura et al., 2023). Several auxiliary mitogens, such as tumor necrosis factor-α (TNF-α), interleukin-6 (IL-6), and bile acids can orchestrate and optimize the timing and intensity of intracellular signals essential for controlling hepatocyte proliferation and paracrine cell interactions (Michalopoulos, 2013; Michalopoulos, 2017; Tao et al., 2017). These signaling molecules are mainly derived from the paracrine of NPCs, the deposition in ECM and the portal circulation (Michalopoulos and Bhushan, 2021; Shu et al., 2022). After PHx in rodents, liver histology gradually starts to restore at 3–4 days, most of the liver mass is restored within 7–8 days, and the complete restoration is achieved within 3 weeks (Michalopoulos and DeFrances, 1997; Michalopoulos, 2007; Michalopoulos, 2017; Michalopoulos and Bhushan, 2021).

Elucidating those priming factors is one of the hot topics in the field of liver regeneration. There are three broad categories of recognized triggers: biochemical factors, endothelial cell stretch,

and sinusoidal shear stress. Studies on the triggering mechanism of liver regeneration after PHx and partial liver transplantation cannot ignore the role of mechanical forces. For example, mechanical stretch on portal vein endothelial cells promotes the release of IL-6 from endothelial cells. After right hepatic portal vein embolization, the diameter of intrahepatic portal vein branches in the residual liver is increased by 150% compared with that in the control group, accompanied by a significant increase in IL-6 secretion (Kawai et al., 2002). Meanwhile, applying the same amount of mechanical stretch to cultured vascular endothelial cells significantly increases the release of IL-6 within 6 h (Kobayashi et al., 2003). On the other hand, after partial liver transplantation or PHx, the volume of the residual liver decreases relatively due to the unchanged total portal blood flow, leading to increased portal perfusion in liver tissue per unit volume and increased portal pressure which results in enhanced shear stress in hepatic sinusoid space. A hepatic sinusoid is a double-barrel structure composed of sinusoid space and Disse space, and hepatocytes are exposed to portal pressure directly through fenestrae on liver sinusoid endothelial cells (LSECs). Therefore, hepatocytes, LSECs, and vascular endothelial cells are all affected by shear stress caused by high portal pressure. Various cell surface receptors found in regulating shear stress on the surface of vascular endothelial cells (Yee and Revel, 1978; Koch and Leffert, 1979) may serve as candidates for liver regeneration. The increased shear stress in the sinusoids due to portal hyperperfusion after PHx or partial liver transplantation may result from the release of regeneration-related factors acting on these receptors. In addition, excessive shear stress after major liver resection leads to liver failure, while the decreased portal shear stress after portal shunt surgery may atrophy the liver until it reaches the new portal pressure and shear stress equilibrium point (Sato et al., 1997; Abshagen et al., 2008). Shear stress also increases the diameter of blood vessels, affects the expression of c-jun, c-myc, c-fos, and other regenerative early genes, and induces the increase of nitrogen oxide synthase (eNOS) expression in LSECs, thereby inducing liver regeneration (Sato et al., 1997; Niiya et al., 1999; Lalor et al., 2006). Recently, hepatocyte heterogeneity has been shown to appear after PHx (Chen et al., 2020), segregating hepatocytes into different functional subgroups based on distinct gene expression patterns including both resting hepatocytes and those with high expression of specific function-related and proliferation-related genes (Walesky et al., 2020; Chembazhi et al., 2021). However, the mechanisms of how resting hepatocytes can transform into a proliferative state and how liver regeneration is initiated still need to be further clarified based on those hemodynamic factors. While attention has been focused on the signaling molecules that promote liver regeneration, the triggers and initiation that induce these changes are not fully understood. Evidently, the mechanism of liver regeneration is extremely complex with highly coordinated proliferative responses of various effector cells, involving several pathways and multiple factors, and the loss of function from a single gene rarely leads to the complete abolition of liver regeneration (Michalopoulos and Bhushan, 2021). Specifically, considering the complex mechanical microenvironments within the liver, mechanical factors may serve as additional candidates playing a direct role in this process. In this review, biomechanical regulation in liver regeneration was discussed specifically in PHx, together with underlying mechanical signaling pathways.

2 Mechanical environments in liver regeneration

2.1 Hemodynamics in liver regeneration

The liver is a highly vascularized organ that has a unique blood supply. Blood pumped from the heart supplies oxygen to the liver through the hepatic artery, accounting for 1/3 of the total blood volume, while blood from the intestines and spleen converges through the portal vein to metabolize and detoxify substances, accounting for 2/3 of the total volume (Lautt and Greenway, 1987; Eipel et al., 2010). Under physiological conditions, blood pressure in the hepatic artery is close to that of the aorta at approximately 90 mmHg (Balogh et al., 2004; Eipel et al., 2010) but much lower in the portal vein varying from 3 to 10 mmHg (Kumar et al., 2008; Eipel et al., 2010). The blood flow from the portal vein and hepatic artery intersects at the hepatic sinusoids and slowly flows from the edge of the hepatic lobule into the central vein, inferior lobule vein, collecting vein, hepatic vein, and finally into the inferior vena cava. When blood flows into the hepatic sinusoids, where the pressure declines from the periportal to the pericentral region, and the average pressure within sinusoids is estimated to be 1–5 mmHg for the gradient from the portal vein to the inferior vena cava (Kumar et al., 2008; Feng et al., 2014). The hepatocytes take up oxygen from the hepatic arteries and the nutrients brought in by the hepatic portal vein are absorbed, synthesized, and processed in the hepatocytes and the new substances generated are circulated in the body. The blood flow velocity through the hepatic sinusoids is slow, approximately 200–330 μm/s measured by the distance-time image of red blood cells using a two-photon laser scanning microscope, which is positively correlated with low blood pressure within the sinusoids (Cantre et al., 2008; Fan et al., 2019). Low blood pressure and low flow velocity within the sinusoids facilitate the exchange of oxygen, nutrients, and waste products between the circulating blood and the liver (GroSse-Segerath and Lammert, 2021).

On the other hand, 2/3 PHx causes significant perfusion and hemodynamics alterations within the liver remnants, presented on both the macrovascular (portal vein) and the microvascular (sinusoids) scales. After 2/3 PHx, the entire flow needs to traverse through a capillary bed whose cross-section is mathematically down to one-third of the original, a threefold increase in portal vein flow per liver volume (Michalopoulos, 2007; GroSse-Segerath and Lammert, 2021). Compared with those physiological cases, the number of vessels is decreased in the remaining liver and the vessels dilate to allow the same amount of blood to pass through the reduced liver tissues, leading to an increase in portal vein flow rate per liver mass, from 120 to 300 mL/min·g liver tissue (Cantre et al., 2008; Rabbany and Rafii, 2018). In this case, the average blood flow velocity within the hepatic sinusoids increases to 450–500 μm/s in rats and 600 μm/s in mice (Cantre et al., 2008; Marlini et al., 2016; Ishikawa et al., 2021). Intravital fluorescence microscopy reveals that the diameter of sinusoids increases from 6.4 to 7.1 μm in rats after PHx because of the increased pressure within the sinusoids, while liver sections in

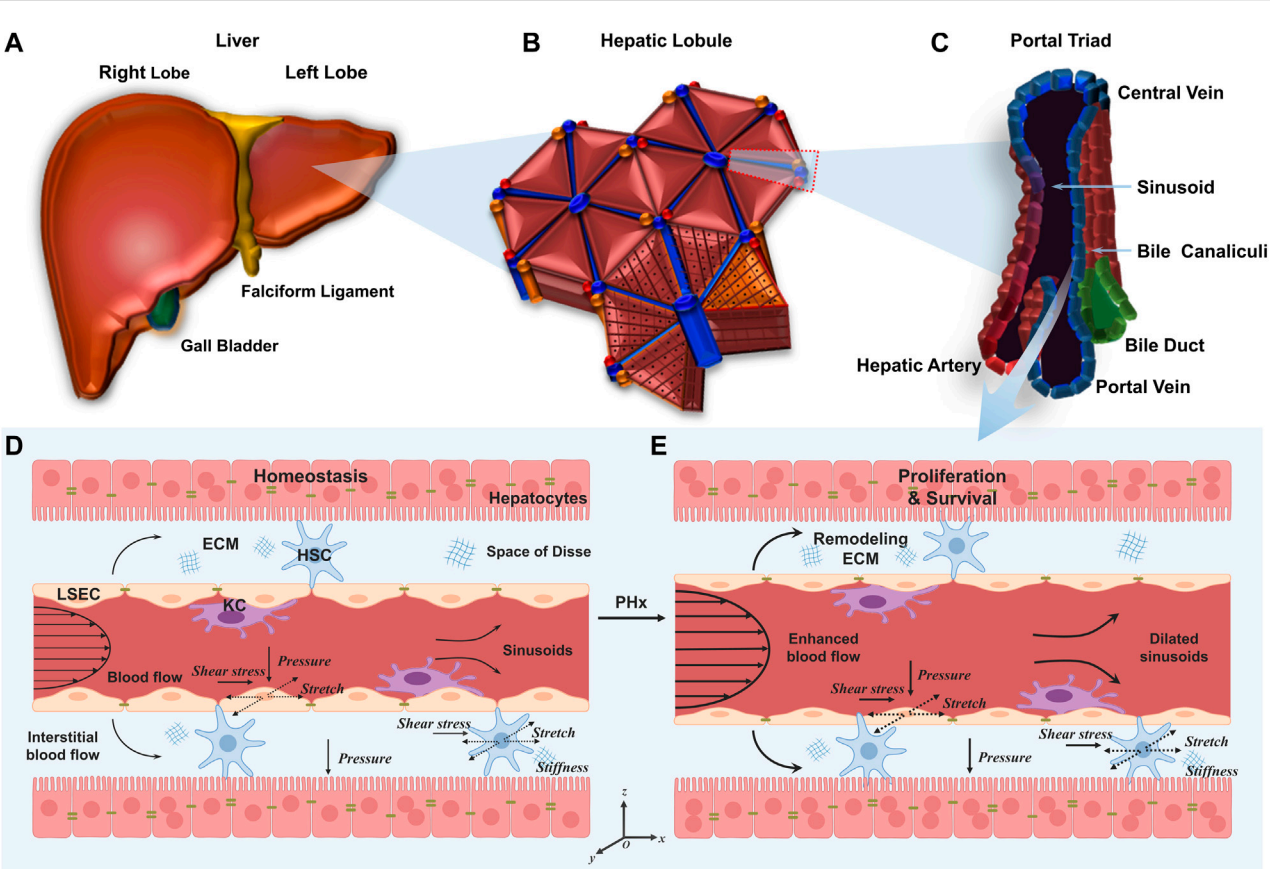

FIGURE 1
Multiscale microstructures of the liver and its mechanical microenvironment in the normal liver and the liver after PHx. **(A–C)** Plotted are the human liver **(A)**, hepatic lobule **(B)**, and portal triad **(C)**. **(D, E)** Schematics of hepatic sinusoids in the normal liver **(D)** and the liver after PHx **(E)**. In the former, hepatocytes are mitotically quiescent. Physiological blood flow applies shear stress and mechanical stretch on LSECs, and physiological interstitial flow applies shear stress and mechanical stretch on HSCs. In the latter, enhanced blood flow induces high shear stress and stretch on LSECs and HSCs. Those remaining hepatocytes enter the cell cycle to promote cell proliferation.

mice before and 1 h after PHx show a more significant increase in sinusoidal diameter (Lorenz et al., 2018).

A body of evidence indicates that the early hemodynamic changes after PHx are critical, and these alterations induce an overall series of events throughout the entire organ that resembles a wound-healing response (Sato et al., 1997; Michalopoulos, 2007; Yagi et al., 2020). To verify the effect of hemodynamics on liver regeneration after PHx, several methods have been subsequently developed to assess its effect on liver regeneration by altering hemodynamics. The portohepatic shunt (PHS) procedure is targeted at diverting the blood flow surrounding the liver to bypass and split the blood flow directly into the inferior vena cava (Marubashi et al., 2004). Portal pressure and liver weight index are relatively stable in the PHS group compared with the PHx model, illustrating the necessity of the portal hyperdynamic state for liver regeneration. Another method, PHx with partial portal ligation (PHPL) is performed by suturing the vessel to reduce the portal diameter and the blood flow (Balogh et al., 2004). Liver tissue blood flow and liver/body weight recovery ratios are significantly lower in the PHPL group than in the PHx group. There are also some methods to alter hemodynamics without removing the lobes. Portal vein embolization (PVE) is performed to embolize the right portal vein with fibrin glue (Eipel et al., 2010). The diameter of the left anterior portal branch is significantly larger and the volume of the non-embolized hepatic lobe is significantly larger after embolization. The selective portal vein branch ligation (PVL) is the same as those described for PHx, except that those liver lobes are ligated instead of resected (Lautt and Greenway, 1987). Portal venous pressure after PVL increases to the same extent following PHx, which is positively correlated with the shear stress in the liver. These models suggest that decreasing portal venous flow on the basis of PHx attenuates liver regeneration while increasing blood flow by embolization, and ligation has the same effect as liver regeneration (Gock et al., 2011).

Early hemodynamics studies considered increased shear stress to be responsible for the increased portal venous pressure after PHx (Schoen et al., 2001). Unfortunately, the effect of blood flow after PHx is quite complex, and the hemodynamic and biochemical factors in blood cannot be decoupled *in vivo*. The increase of portal blood flow per liver mass also causes an increase in the availability per hepatocyte of biochemical factors derived from the intestine and pancreas. These biochemical factors include EGF and insulin, as well as nutrients derived from the food supply. In this regard, *in vivo* studies done by altering blood flow make it hard to

determine whether liver regeneration is induced by hemodynamic effects or the effects of biochemical factors in the blood (Michalopoulos, 2007; Michalopoulos and Bhushan, 2021; Pibiri and Simbula, 2022). To explore whether hemodynamic effects or biochemical factors in the blood are critical for hepatocyte proliferation and liver regeneration, a cell-based mathematical model is developed, which shows that both biochemical factors and hemodynamic effects are important during liver regeneration (Hohmann et al., 2014). Furthermore, complicated hemodynamic changes at the sinusoidal scale can be further translated into mechanical microenvironments acting on the cells within the hepatic sinusoids. Thus, it is important to quantify the mechanical microenvironment within hepatic sinusoids and explore the underlying roles of various mechanical factors in the liver regeneration process by decoupling the complex mechanical environment *in vitro*.

2.2 Mechanical environments within hepatic sinusoids during liver regeneration

The liver is composed of different lobes (Figure 1A) that are further divided into numerous hexagonal lobules (Figure 1B), as the basic architectural unit of the liver demarcated by the "portal triad" consisting of the portal vein, bile duct, and hepatic artery. In each lobule, a central vein runs through the lobule center and liver plates formed by hepatocytes are radially aligned (Figure 1C). Hepatocytes constitute 80% of the liver to implement most of the hepatic functions, and the remaining 20% consists of NPCs mainly including LSECs, hepatic stellate cells (HSCs) and Kupffer cells (KCs) (Taub, 2004). The wall of hepatic sinusoids is lined with LSECs. HSCs are in the space of Disse and KCs are in the hepatic sinusoids (Lautt and Greenway, 1987). The existence of permeable fenestrae in sinusoidal endothelium probably enables blood flow to get through the space of Disse underneath the endothelium (Hu et al., 2017). With this complex and dynamic microenvironment, hepatic cells are continuously exposed to mechanical stimuli (Nishii et al., 2018).

Under physiological conditions, the portal vein continues to carry the entire outflow from the intestine, spleen, and pancreas to each hepatic lobule (Figure 1D). As the main cells lining the sinusoids, LSECs are subjected to blood flow that generates two major forces (Rabbany and Rafii, 2018). First, radial blood pressure is applied to the wall of the hepatic sinusoids which, in turn, leads to cyclic stretch and elongation of LSEC layers both perpendicular and parallel to the blood flow, respectively (Anwar et al., 2012). Second, the friction force arising from viscous blood flow over LSEC layers causes axial shear stress (Marubashi et al., 2004). Adjacent HSCs are also likely subjected to cyclic stretch generated by the change in sinusoidal pressure as well as the interstitial blood flow-induced shear stress in the space of Disse (Yi et al., 2015; Wang et al., 2021; Chen et al., 2022). In addition, HSCs persistently produce ECM and the varied ECM stiffness, in turn, manipulates the behaviors of hepatic cells (Long et al., 2022). Finally, hepatocytes are subjected to hydrostatic pressure and interstitial flow within the liver parenchyma (You et al., 2019).

Specifically, after PHx, there are immediate and drastic mechanical changes in the liver (Figure 1E). This hemodynamic change affects the microstructures of hepatic sinusoids, including the increased sinusoidal diameter, the increased blood flow velocity, the enlarged fenestration, the disappearance of sieve-plate appearance, and the widening of inter-cellular spaces, which takes almost 10 days until the entire structure returns to the normal (Morsiani et al., 1998). This vasodilation generates high shear stress and circumferential or axial stretch on LSECs, subsequently inducing the expression and secretion of proteases that degrade and remodel the ECM, thus altering the ECM stiffness and the mechanics of cell-matrix interactions (Song et al., 2017). The threefold increase in portal vein flow also enhances the shear stress and cyclic stretch applied on HSCs in the space of Disse (Rohn et al., 2020). All of these cues suggest that mechanics may serve as one of the earliest events which provide the initiating signals for liver regeneration. Unfortunately, the mechanisms involved in the increased portal vein flow and other mechanical cues as early signals for liver regeneration are not fully understood (Michalopoulos, 2011). Considering the rapid mechanical alterations during liver regeneration, the pronounced changes within hepatic sinusoids, the direct act on LSECs or HSCs, and the fast and direct transcriptional regulation (Tajik et al., 2016) of mechanotransductive signaling, it seems to be particularly important to clarify the roles in differential mechanical cues in liver regeneration after PHx.

3 Living donor liver transplantation and mechanical regulation

Liver transplantation is the only effective method and plays an important role in the treatment of end-stage liver disease. However, the shortage of donor livers is always the main problem plaguing its clinical application. A variety of strategies have been developed, including living donor liver transplantation, xenotransplantation, hepatocyte transplantation, increasing the sources of cadaver donor livers, using marginal donor livers, and multiple recipients of one liver. Living donor liver transplantation (LDLT) is highly regarded and has gradually become an effective solution to deal with this challenge. Since the first orthotopic liver transplantation was performed by Starzl in 1969 (Starzl et al., 1969), liver transplantation has developed rapidly. In 1984, reduced-size liver transplantation (RLT) was first proposed to expand the sources of donor livers for pediatric liver transplantation (Bismuth and Houssin, 1984). Since then, the idea of dividing organs, i.e., one liver between two recipients, was proposed to adapt to the increasingly acute disparity between supply and demand of organ transplantation, which laid a theoretical foundation for the development of split liver transplantation (SLT) (Pichlmayr et al., 1988). In 1989, Raia et al. reported the first living donor liver transplant (Raia et al., 1989), and then Strong et al. (Strong et al., 1990) first successfully transplanted the liver of a mother to her son. In 1996, the first adult-to-adult living donor liver transplantation (ALDLT) was performed successfully (Lo et al., 1997). Due to the wide range of applications, the number of LDLTs has increased rapidly in recent years. LDLT involves removing a

piece of liver from a healthy donor and giving it to the recipient. Although LDLT has certain deficiencies at present (such as the risk of donor death, the related complications of the donor liver, and the adverse psychological effects on donor and recipient), the advantages of LDLT have been widely recognized by the transplant community. Liver regeneration after LDLT is a precise process involving the proliferative responses of multiple effector cells and the regulation of various cytokines and growth factors. The effects of evident hepatic hemodynamic changes on liver regeneration in the donor and recipient have gradually attracted attention, as discussed below.

3.1 Hemodynamic changes of the donor's liver after PHx and the effect on liver regeneration

Currently, the surgical methods of living donor liver transplantation mainly include left liver transplantation, right liver transplantation, and double liver lobe liver transplantation. In LDLT, the volume of the right donor liver is significantly larger than that of the left donor liver, and the postoperative hemodynamics is altered greatly. Right hemihepatectomy changes the blood circulation of the whole liver, and the pressure and flow velocity inside the portal vein increases correspondingly in the early postoperative period. High perfusion of the portal vein and relatively narrow diameter of the hepatic vein determine the liver function in the early postoperative period. Therefore, various indicators of liver function increase rapidly and reach a peak 1 day after the operation. With the self-regulation of the human body and the gradual stabilization of liver hemodynamics, various liver function indicators gradually return to normal levels within 1 week. Rapid liver regeneration within 2 weeks after surgery is presumably due to the increased liver blood flow and enhanced bile acid absorption (Everson et al., 2013), and appropriately increased portal vein pressure could significantly stimulate the release of factors related to liver blood sinus regeneration, serving as the inducement factor of liver regeneration. Shear stress caused by increased portal blood flow on the vascular wall is conducive to the release of vascular endothelial growth factor, IL-6, and carbon monoxide, thus initiating the regeneration of parenchymal liver cells. Hemodynamic changes in the early postoperative period of the donor are favorable factors for liver regeneration, and the rapid regeneration of the liver further promotes the hemodynamic stability of the entire liver. The early increase in portal vein flow velocity may be attributed to the fact that the liver vascular bed decreases sharply and the blood flow into the liver increases while the total visceral blood flow remains unchanged. The portal vein flow accounts for 75% of the blood flow into the liver, leading to the gradual widening of portal vein diameter to adapt to the changes in liver hemodynamics. With the widening of the portal vein diameter, portal vein flow velocity gradually decreases. After the hepatic artery resistance index decreases sharply in the hepatic vascular bed, the blood flow resistance into the liver increases, and the resistance index increases significantly in the early postoperative period. With the gradual widening of the portal vein and the rapid regeneration of the liver, the blood flow resistance of the liver gradually decreases, and the liver artery resistance index presents a gradual downward trend in the later period. In the process of adapting to the changes in liver hemodynamics, the diameter of the hepatic vein increases accordingly while the velocity of the hepatic vein decreased.

3.2 Hemodynamic changes of the recipient's liver after LDLT and the effect on liver regeneration

After LDLT, the effective vascular bed in the liver is reduced and the blood volume of the entire portal system should be taken over by the remaining partial liver. Therefore, the opening of the portal vein of the transplanted liver faces the problem of excessive perfusion of the portal blood from the graft regardless of the preoperative portal hypertension symptoms. The posterior pulse velocity of patients with cirrhosis is sharply increased after living donor liver transplantation, and the portal blood flow was significantly enhanced after liver transplantation, accompanied by increased peripheral vascular resistance. Compared with non-cirrhotic patients (such as fulminant liver failure and liver tumors), patients with chronic cirrhosis experience a greater increase in backdoor blood flow after transplantation (Piscaglia et al., 1999). Compared with the donor, blood flow in the open back vein of the graft increased significantly (García-Valdecasas et al., 2003). The increased value of portal blood flow and arterial resistance index in the recipient are significantly higher than those in the donor: the portal-arterial blood flow is still placed in a state of dynamic balance. In the early postoperative period, portal blood flow increases significantly, hepatic artery blood flow decreases, and the portal-arterial blood flow balance is broken (Sugimoto et al., 2007). Elevated portal pressure-induced liver regeneration is first identified after hepatectomy or portal embolization. The increased portal pressure after hepatectomy or portal vein embolization leads to increased portal shear stress in the hepatic sinusoids, thus inducing a liver regeneration response. This mechanism has been proven to be an important initiating factor in inducing liver regeneration response in animal experiments (Niiya et al., 1999; Kawai et al., 2002). The rate of early postoperative regeneration in the portal hypertension group was significantly higher than that in the portal hypertension group. Considering the adverse effects of portal hypertension on graft liver function recovery and postoperative survival rate, further studies are needed to define an ideal portal pressure range that is conducive to accelerating liver regeneration without damaging liver function recovery.

4 *In vitro* mechanical loading mimicking liver regeneration

The regeneration mechanism is immediately initiated after liver resection. Hepatocyte proliferation compensates for the lost or injured liver tissue and maintains the physiological function of the liver. This process is regulated by liver regeneration factors secreted by liver NPCs, such as LSECs and HSCs. Prior to the

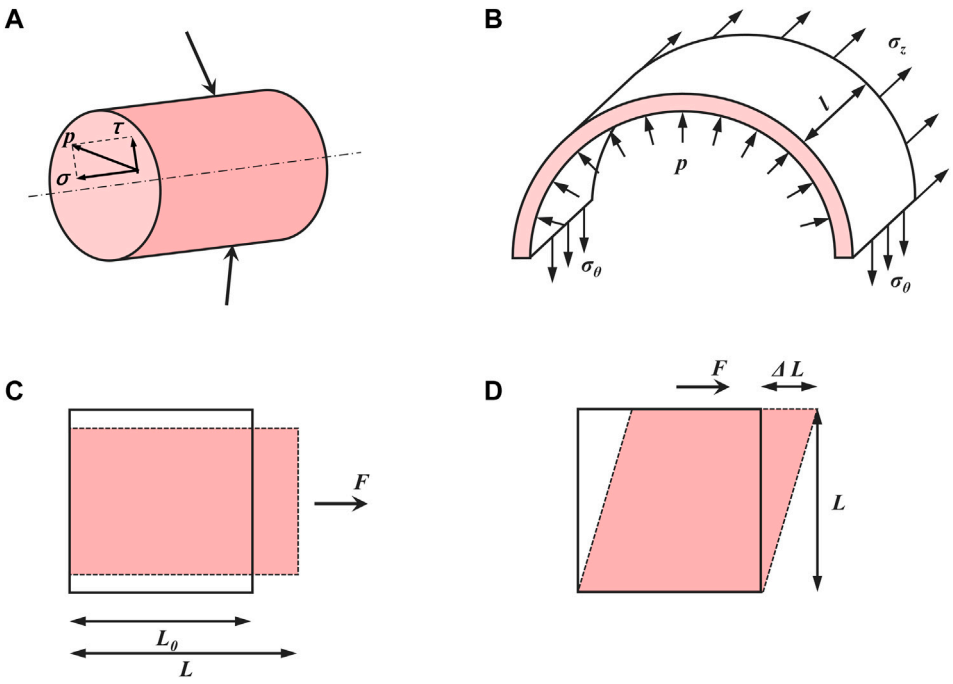

FIGURE 2
Basic concepts in mechanics of materials. **(A)** Stress (p) can be divided into normal stress (σ) and shear stress (τ). **(B)** The relationship between inner pressure and induced stretch in a thin-walled cylinder. **(C)** Normal strain (ε) and **(D)** shear strain (γ).

changes in the orderly expressions of liver regeneration factors, the portal vein hemodynamics changed significantly due to the increased blood flow sustained by the remaining liver tissues (Sallberg and Pasetto, 2020). However, these changes in hepatic sinusoids caused by increased portal blood flow are complicated as the multiple mechanical factors are coupled together. For example, external forces applied on LSECs can be further translated into the shear stress acting on the surface and the circumferential stretch on the cells within the sinusoids (Morsiani et al., 1998; Shu et al., 2021; Li et al., 2022; Long et al., 2022). To further decouple the contributions of those individual mechanical factors in liver regeneration after PHx, *in vitro* mechanical loading studies have been applied to mimic *in vivo* hepatic sinusoids after PHx and elucidate mechanically-related possible molecular mechanisms, especially in the decoupled forces in the liver microenvironment such as shear stress/stretch.

4.1 Shear stress

Shear stress (in Pa or dyne/cm^2), denoted as τ, is the shear component coplanar with a material cross-section (Janmey and Miller, 2011) (Figure 2A). Particularly in biology, shear stress is defined as the frictional force generated by the viscous biofluid flow within the lumen of a blood vessel. Within hepatic sinusoids, shear stress is directly caused by blood flow and exerts shear forces on LSECs and adjacent HSCs (Simonetto et al., 2015). LSECs can in turn secrete vasodilators such as NO that affect HSCs within the space of Disse to regulate blood flow (DeLeve et al., 2008; Fernandez, 2015). To date, the exact shear stress within hepatic sinusoids or the space of Disse *in vivo* has not been measured directly and accurately in human or animal models due to the tiny scale and varied sizes of the hepatic sinusoids as well as the vascular permeability induced by LSEC fenestrae (Poisson et al., 2017; Rohn et al., 2020).

Various *in vitro* loading techniques have been developed to study the cellular responses and mechanisms under shear stress. A parallel-plate flow chamber is an ideal device to apply dynamic shear stress *in vitro*, in which the flow is generated through a media reservoir and a peristaltic pump to mimic the *in vivo* environment (Wang et al., 2019). Shear stress in the parallel-plate flow chamber is calculated using the following formula (Ahsan and Nerem, 2010):

$$\tau = \frac{6\mu Q}{bh^2} \quad (1)$$

where μ is the blood viscosity (dyne·s/cm^2), Q is the volume flow rate (cm^3/s), which refers to the volume of fluid passing through a certain cross-section of the blood vessel per unit time, h is the chamber channel height (cm) and b is the chamber width (cm).

LSECs are the main cell type affected by the changes of shear stress after PHx within sinusoids (De Rudder et al., 2021). For example, a significant increase in the accumulated vasodilators nitric oxide (NO) is presented when primary rat LSECs are exposed to a laminar flow at 14.1 dyne/cm^2 for 30 min (Shah et al., 1997). This is consistent with the rapidly enhanced secretion response using a bioreactor for real-time NO production at 3 dyne/cm^2 for 24 h on primary rat LSECs (Illa et al., 2014). This shear stress-induced NO

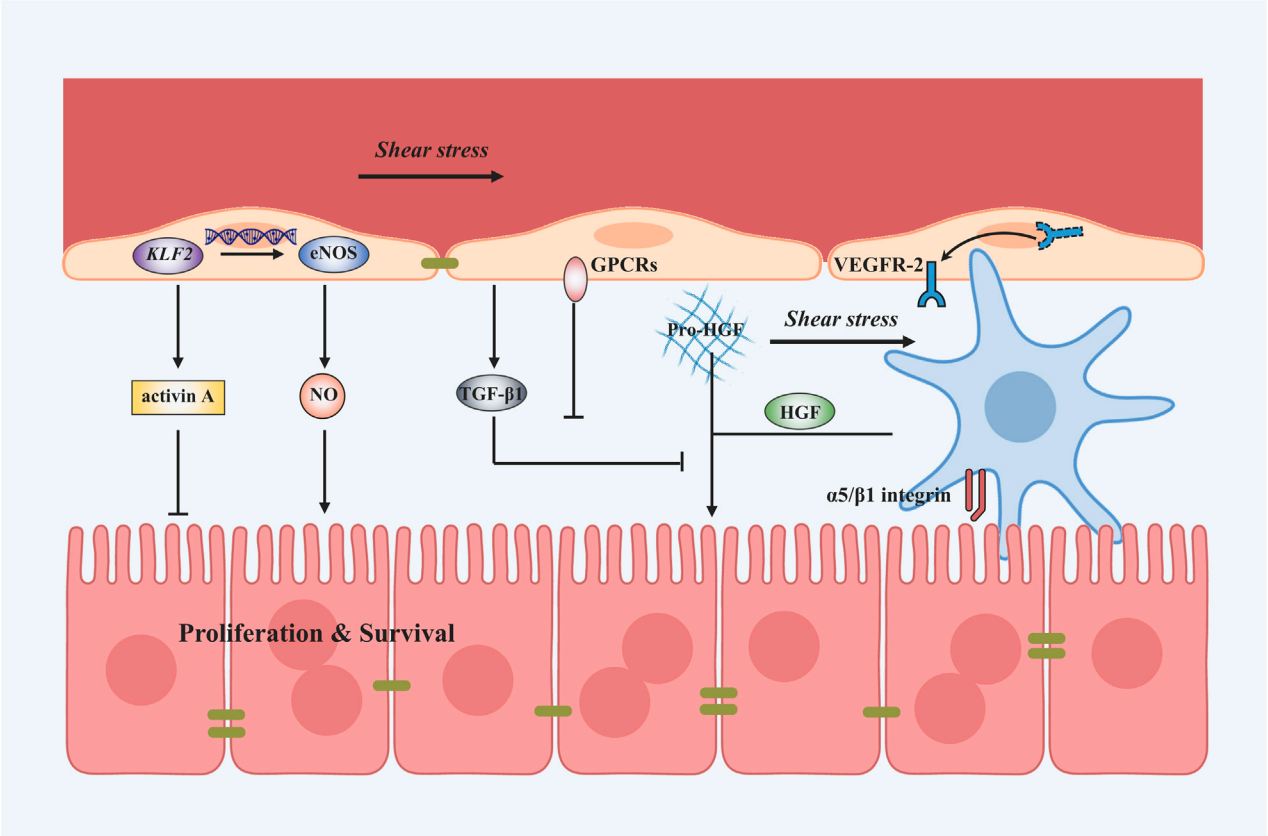

FIGURE 3
Shear stress-induced mechanotransduction signals in liver regeneration after PHx. Applying shear stress upregulates KLF2 and thus the expression of eNOS and NO. Shear stress can also downregulate TGF-β1 secretion to promote the process of liver regeneration mediated by GPCRs. Besides, VEGFR-2 is translocated to the plasma membrane and might induce angiocrine signals. Shear stress application also activates HSCs to secrete HGF by α5/β1 integrin. A vast amount of dissolved matrix-bound pro-HGF proteins tend to enter the blood flow after shear stress.

release reinforces the sensitivity of hepatocytes against HGF and therefore triggers the liver regeneration cascade (Wang and Lautt, 1998; Schoen et al., 2001; Golse et al., 2013). In other endothelial cell models, those mechanosensors such as caveolae and ion channels can activate various signaling cascades to regulate NO production by eNOS, suggesting that the response of LSECs may also promote liver regeneration via eNOS-dependent NO secretion (Abshagen et al., 2008; Mei and Thevananther, 2011; Song et al., 2017). Furthermore, inhibiting inducible nitric oxide synthase (iNOS) severely suppresses liver regeneration after PHx in mice (Rai et al., 1998). Laminar shear stress in primary rat LSECs at 14.1 dyne/cm^2 increases endothelium-specific transcription factor Kruppel-like factor 2 (KLF2) mRNA expressions (Gracia-Sancho et al., 2011; Marrone et al., 2013), which then induces the expression of eNOS, consolidating those KLF2-eNOS-NO signaling mediated by shear stress. However, increased KLF2 expression can also induce an anti-proliferative secretome, which attenuates liver regeneration (Manavski et al., 2017). Moreover, vascular endothelial cell growth factor receptor-2 (VEGFR-2) is responsive to laminar shear stress by translocating from perinuclear distribution to membrane and cytoskeletal localization at 10 dyne/cm^2 for 15 min with co-localized VE-cadherin (Braet et al., 2004). In the early phases of liver regeneration, VEGFR-2-Id1-mediated inductive angiogenesis in LSECs, through the release of angiocrine factors Wnt2 and HGF, provokes hepatic proliferation, and subsequently, VEGFR-2-Id1-dependent proliferative angiogenesis reconstitutes liver mass (Ding et al., 2010). Transforming growth factor-β1 (TGF-β1), which is known as an inhibitor of hepatocyte proliferation, is observed in a markedly decreased concentration in the culture medium when primary rat LSECs are exposed to a laminar flow at 15 dyne/cm^2 for 24 h. At the same loading condition, an increase in the intracellular Ca^{2+} level and the phosphorylation status of Erk1/2 are observed after shear stress, indicating that LSECs have the ability to sense shear stress, which in turn induces TGF-β1 production through the G-protein-coupled receptors (GPCRs)-MAPK axis (Hu et al., 2014; Ishikawa et al., 2021). Shear stress not only has a role in the initiation of liver regeneration and the decrease in the late stage of liver regeneration but also induced cellular senescence to blunt liver regeneration (Duan et al., 2022). Genes associated with senescence, such as P16, P53, P21 Pai1, and Gata4 had an upregulated expression when LSECs are subjected to flow conditions with 7.05 dyne/cm^2 shear stress compared with 14.1 dyne/cm^2 shear stress, which is mediated by Notch activation. In addition to *in vitro* cell loading, *in vitro* microarrays have also been used to study the process of liver regeneration. A three-dimensional platform called structurally

TABLE 1 Summary of typical mechanical stimuli and cellular responses during liver regeneration.

Mechanical cues	Cell types	Modes	Parameters	Testing indexes	References
Shear stress	Primary rat LSECs	Laminar flow	14.1 dyne/cm^2, 30 min	NO	Shah et al. (1997)
	Primary rat LSECs	Laminar flow	3 dyne/cm^2, 24 h	NO	Illa et al. (2014)
	Primary rat LSECs	Laminar flow	14.1 dyne/cm^2, 24 h	eNOS, KLF2	Marrone et al. (2013)
	Primary rat LSECs	Laminar flow	14.1 dyne/cm^2, 12 h	KLF2	Gracia-Sancho et al. (2011)
	Primary rat LSECs	Laminar flow	10 dyne/cm^2, 15 min	VEGFR-2	Braet et al. (2004)
	Primary murine LSECs	Laminar flow	15 dyne/cm^2, 3 d	TGF-β1, GPCRs	Braet et al. (2004)
	Primary murine LSECs	Laminar flow	7.05 dyne/cm^2, 14.1 dyne/cm^2, 24 h	P16, P53, P21 Pai1, and Gata4	Duan et al. (2022)
	Primary rat HSCs	Pulsatile flow	2.9 dyne/cm^2, 15 dyne/cm^2, 29 dyne/cm^2, 2.5 Hz, 1 h	HGF α5/β1 integrin	Rohn et al. (2020)
Stretch	Primary human LSECs	Uniaxial stretch	50%, 1 Hz 6 h 12 h 24 h 48 h	Length, IL-6, HGF, TNF-α	Kawai et al. (2002)
	Primary human LSECs	Uniaxial stretch	20% constant, 30 min and 20%, 0.5 Hz, 1 h	Length, activated β1 integrin, p-VEGFR-3, HGF, IL-6, TNF-α, MMP-9	Lorenz et al. (2018)
	Primary murine LSECs	Cyclic biaxial stretch	20%, 1 Hz, 4 h	IL-6	Hilscher et al. (2019)
	Primary rat HSCs	Uniaxial stretch	30%, 1 h	HGF	Rohn et al. (2020)
	Primary human and murine HSCs	Cyclic biaxial stretch	10%, 0.5 Hz, 24 h	Fibronectin fibril assembly	Simonetto et al. (2015)
	LI90 cell lines	Cyclic biaxial stretch	10%, 0.5 Hz, 24 h	MMP-1 MMP-2, TIMP-l and TIMP-2	Goto et al. (2004)

vascularized hepatic ensembles for analyzing regeneration was established to model multiple aspects of human liver regeneration. Exposure of endothelium-lined channels to fluid flow increases the secretion of liver regeneration-associated factors such as HGF as well as cell-cycle entry of primary human hepatocytes embedded within the device (Chhabra et al., 2022). To some extent, the role of fluid shear depends on its magnitude as the excessive increases in shear stress could be detrimental, contributing to stunted liver growth via the release of hepatocyte growth-inhibiting signals and leading to suboptimal liver regeneration (Lorenz et al., 2018).

Not only LSECs but also HSCs are affected by varied shear stresses since there is a permeable flow in the space of Disse across the porous endothelium from the mainstream. For example, primary rat HSCs that are exposed to laminar pulsatile flow ranging from 2.9 dyne/cm^2, 15 dyne/cm^2 to 29 dyne/cm^2 at 2.5 Hz for 1 h present increased HGF mRNA expression and the enhanced HGF secretion into the medium, consistent with a reduction of those matrix-bound pro-HGF proteins after applying shear stress (Rohn et al., 2020). Meanwhile, the impaired mechanosensing via α5β1 integrin in HSCs that contributes to the reduction of HGF release indicates that α5/β1 integrin is an important mechanosensor in HSCs involved in shear-induced liver regeneration.

Collectively, shear stress can promote liver regeneration by elevating the release of NO and decreasing the secretion of TGF-β1 in LSECs. It can also stimulate liver regeneration by increasing the secretion of HGF in HSCs (Figure 3). This process is referred to as mechanocrine signaling, where changes in mechanical forces are transduced into the secretion of angiocrine signals that affect neighboring cells (Hilscher et al., 2019; Soydemir et al., 2020). NO secreted by LSECs can not only regulate liver regeneration but also relax the vessel through a negative feedback loop. Loading parameters and cellular responses after shear stress are shown in Table 1.

4.2 Mechanical stretch and pressure

Mechanical stretch is another major hemodynamic force originating from blood flow and is applied on the vessel lumen. In hepatic sinusoids, the stretch is mainly caused by the pressure of blood flow and is applied on LSECs as well as adjacent HSCs (Simonetto et al., 2015). After PHx, the increase in blood flow causes circumferential as well as axial vessel wall expansion, resulting in stretching LSECs and other cell types along the vessel wall (Figure 2B). These lined cells sense the cyclic strain (ε)

(Figure 2C) in the direction of stretch, defined as (Charras and Yap, 2018):

$$\varepsilon = (L - L_0)/L_0 \quad (2)$$

Here the endothelium has an original length L_0 and is stretched to a length L by the tension acting perpendicular to its surface. Based on the changes in hepatic sinusoidal diameter after 2/3 PHx, the strain on the LSECs after LSECs is estimated to be 10%–20% (Lorenz et al., 2018). The shear strain (γ) (Figure 2D) is defined as the deformation in the direction of the shear force divided by the original length perpendicular to it (Charras and Yap, 2018):

$$\gamma = \Delta L/L_0 \quad (3)$$

Commercialized Flexcell tension systems and STREX cell-stretching devices are usually used to apply mechanical stretch *in vitro*. Here, cells are seeded on silicone membranes and subjected to cyclic stretch for a period of time with proper strain amplitude and frequency (Zhang et al., 2021).

To examine if cyclic stretch applied to LSECs is involved in the regenerative process after PHx, primary human LSECs cultured on an elastic silicone membrane are subjected to a continuous uni-axial stretch at a strain of 50% and 1 Hz, mimicking the percent increase in the diameter of the portal branch after PVE (Kawai et al., 2002). IL-6 secretion is enhanced while TNF-α and HGF secretions remained unchanged with mechanical stretch within 6–48 h. While this is the first attempt to address whether the alterations in mechanical stretch contribute to liver regeneration-associated cytokine releases, this issue received limited attention in the past decades until mechanical stretch created by the passage of blood through the liver was found to activate the signaling pathways that promote the production of angiocrine factors and the proliferation of hepatocytes (Lorenz et al., 2018). A uni-axial stretch at 20% strain for 30 min and immediately afterward at 20% strain, 0.5 Hz for 1 h was applied to primary human LSECs, mimicking the mechanically-induced sinusoids widening during liver growth or regeneration after PHx. Stretch induces the increased secretion of HGF mediated by activated β1 integrin and phosphorylated VEGFR-3. Enhanced IL-6 and TNF-α secretion, as well as increased matrix metalloproteinase-9 (MMP-9) activity, were also found. Furthermore, those supernatants collected from stretched LSECs also promote the proliferation and inhibited the apoptosis of hepatocytes, suggesting that the mechanotransduction alone is sufficient to turn on the angiocrine signals and cause *in vitro* proliferation and survival of human primary hepatocytes. Evidently, stretch patterns (static vs. cyclic, or uni-axial vs. biaxial) and loading parameters (such as magnitude, frequency, and duration) are critical in the mechanotransductive process (Rabbany and Rafii, 2018). A biaxial, cyclic stretch at 20% strain and 1 Hz was applied to mouse primary LSECs, attempting to recapitulate those pulsatile forces induced by congestion in which mechanical stretch was generated by vascular strain and increased intrahepatic pressure likely resulted in a stretch similar to that after PHx (Hilscher et al., 2019). Even different from the cases of liver regeneration, these stretched-mediated outcomes present the upregulated IL-6 or selectin transcriptions and integrin signaling.

Similar to the findings in shear stress, not only LSECs but also HSCs can sense the cyclic strain based on the expanded sinusoidal diameter. Applying a 30% strain stretch for 1 h to rat primary HSCs that mimics high blood flow enhanced HGF release (Rohn et al., 2020). To simulate the intrahepatic pressure-induced stretch during congestion, applying a cyclic uniform stretch at 10% strain and 0.5 Hz for 24 h to human or murine primary HSCs is able to remarkably increase fibronectin expression and fibril assembly, thus varying the matrix stiffness (Simonetto et al., 2015). Meanwhile, applying a 10% strain at 0.5 Hz for 24 h on LI90 cell lines that mimics mechanical stretch induced by increasing portal blood flow, causes increased MMP-1 and decreased MMP-2 and tissue inhibitor of metalloproteinases-1 (TIMP-1) and TIMP-2 production, suggesting that HSCs are activated by mechanical stretch at the early phase of portal hypertension and that the matrix stiffness has changed (Goto et al., 2004).

Taken together, LSECs and HSCs can respond to mechanical stretch and secrete angiocrine factors that serve as critical regulators of liver regeneration. Existing works usually conflate hemodynamic changes with shear stress, while it is also fundamental that stretching LSECs or HSCs during vasodilation induces angiocrine signals that contribute to liver regeneration (Figure 4). Evidently, angiocrine signals derived from stretching LSECs and HSCs are an important component of intercellular communication and have a key role in organ growth, regeneration, and disease (Marrone et al., 2016). Loading parameters and cellular responses after mechanical stretch are shown in Table 1.

Fluid pressure denotes the hydrostatic pressure exerted outside the blood vessel. Inside the liver, it is applied to LESCs from surrounding hepatic sinusoids and to hepatocytes and HSCs from liver parenchyma. After PHx, the mainstream or interstitial pressure varies transiently with the progress of liver regeneration. From a mechanical viewpoint, this pressure variation is usually coupled with the shear stress and mechanical stretch described above, since the PHx operation can induce simultaneous changes in blood flow, sinusoidal vasodilation, and intrahepatic pressure. Thus, only a few studies have been conducted to isolate the pressure effects on hepatic functions. As an example, placing HepG2 and Huh-7 cell lines under a pressure of 15 mmHg for 24 h significantly increases their proliferation and invasion, with several associated pathways including PI3K-Akt, focal adhesion, integrin, FOXO, and Hippo signaling analyzed from their differentially expressed mRNAs (Shen et al., 2019).

4.3 Stiffness

Stiffness is the extent to which a material resists deformation in response to an applied force. It is usually applied to define the rigidity of the tissue in biology. For example, a stiff matrix provides higher resistance than a soft one, as shown by bone vs. liver or a cirrhotic vs. normal liver (Wells, 2008). Atomic force microscopy (AFM) is often applied to determine the stiffness of liver tissues, matrix fiber, or hepatic cells *in vitro*.

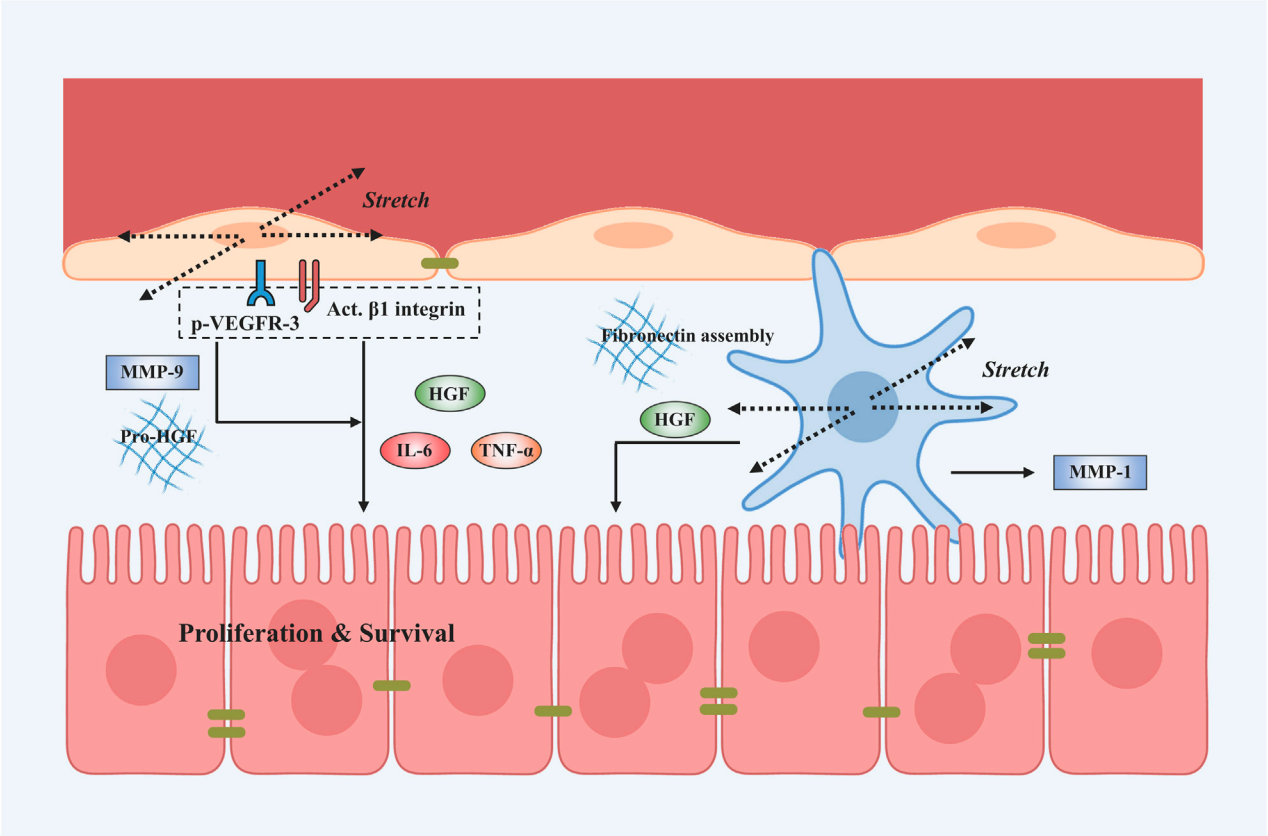

FIGURE 4
Stretch-induced mechanotransduction signals in liver regeneration after PHx. Applying the stretch activates β1 integrin and its interactions with VEGFR-3 on LSECs. Subsequently, LSECs are able to secrete angiocrine signals such as HGF, IL-6, and TNF-α and activate MMP-9 to stimulate the proliferation and survival of hepatocytes. The stretch application also activates HSCs to secrete HGF and MMP-1 and stimulates fibronectin fibril assembly by HSCs.

Most of the studies that deal with liver stiffness are referred to in the context of liver fibrosis and cirrhosis, whereas the matrix composition and stiffness are also varied during regeneration. After PHx, those elevated expressions of those key molecules such as urokinase plasminogen activator (uPA) and MMP-9 can activate matrix remodeling, and, therefore, release inactive, single-chain HGF bound to the hepatic matrix and change the substrate stiffness (Mueller et al., 2002; Michalopoulos, 2007). Substrate stiffness plays an indispensable role in hepatocyte proliferation, as exemplified by the fact that Huh7 and HepG2 cells cultured on polyacrylamide gel with higher stiffness of 12 kPa resulted in at least a two-fold increase in the cell number compared with cells cultured on a softer substrate of 1 kPa, where substrate stiffness was also measured using AFM (Schrader et al., 2011). A proteomics-based approach for determining the changes in liver ECM composition during liver regeneration reveals that an increase in collagen and a decrease in elastic fibers lead to rearrangement and increased ECM stiffness. These changes regulate hepatocyte proliferation in the regenerating liver (Klaas et al., 2016).

It is well known that liver regeneration is slow after fibrosis or cirrhosis (Xue et al., 2013), but the underlying mechanism is not well understood. After 70% PHx, the level of TNF-α mRNA in the residual liver of healthy rats increases rapidly, reaches a peak at 6 h after PHx, and then decreases slowly. However, the level of TNF-α mRNA in the remaining liver remains quite low at 6–12 h after surgery and then increases slowly until reaching a peak at 24 h after surgery. The peak value is dramatically lower than normal ones and then decreases rapidly. The results of intrahepatic IL-6 mRNA levels of a sclerosed liver also remain quite low at 6–12 h after surgery, and then rise slowly until 72 h after surgery. The peak value is much lower than the normal one and its declination is slow, while the long-term, low level of IL-6 presents an inhibitory effect on liver regeneration (Tiberio et al., 2008). At the same time, STAT3 in the livers of 70% of healthy rats is activated within 30 min after partial resection of the liver and reaches a peak at 3 h after surgery, and the effect lasts for 46 h. Clinical trials have shown that the amount and activity of STAT3 protein in liver tissues of alcoholic cirrhosis and hepatitis cirrhosis are lower than those in normal liver (Horiguchi et al., 2007). The expression of IL-6 and TNF-α is delayed after PHx of the sclerotic liver mentioned earlier, which may be related to the upregulation of Pias3 protein and inhibits STAT3 activity in sclerotic liver (Stärkel et al., 2005). This partly explains the phenomenon that the regeneration of a sclerotic liver starts slowly. Studies have shown that liver fibrosis is not conducive

to the regeneration of residual liver after PHx, thus affecting the rapid stability of postoperative liver hemodynamics. Severe fibrosis is a high-risk factor for postoperative liver failure, intractable ascites, and even death of the donor (van den Broek et al., 2008). Early hemodynamic changes, infection, and inflammatory reactions after PHx often lead to acute liver damage. Acute liver injury is often accompanied by an increase in liver stiffness (Dechêne et al., 2010). After PHx, liver stiffness increases transiently in the first week, which might be related to changes in liver hemodynamics, active liver regeneration, and intrahepatic bile stasis (Inoue et al., 2009). Subsequently, liver stiffness gradually decreases and could recover to the preoperative normal level within 5 weeks after surgery.

5 Perspectives and conclusion

Liver regeneration after PHx is a sequential process from the beginning of hepatocyte proliferation to the recovery of liver tissue structure. As an abrupt and drastic change within the hepatic sinusoids, the functions and potentials of mechanical cues after PHx should be valued properly. They could serve as the initiating factors and driving forces in liver regeneration and subsequently cause variations in biochemical factors. Moreover, these mechanical loads are directly applied to hepatic cells within sinusoids, inducing fast responses compared to biochemical signals. To date, biomechanical mechanisms in the PHx-induced increase of portal vein pressure and other subsequent mechanical cues, as early signals for initiating liver regeneration, need a more comprehensive understanding. Early basic and clinical *in vivo* studies have shown that biomechanical changes, especially the hemodynamic cues after PHx, promote liver regeneration and propose a coupled pattern of these mechanical cues. In *in vitro* cases, however, hemodynamics in hepatic sinusoids can be decoupled into shear stress and mechanical stretch/pressure along the sinusoidal wall. Complete analysis of mechanical microenvironments based on *in vivo* data is one of the first critical steps to understanding their effects on liver regeneration.

Mechanics can directly manipulate LSECs and HSCs to secrete these liver regeneration-associated factors to promote the proliferation of hepatocytes, *i.e.*, mechanocrine. Different from existing hypotheses of "blood-flow theory" or "hormone theory", these biomechanical cues emphasize that mechanical signals can promote liver regeneration by modulating the release of biochemical signals. Therefore, biochemical factors and biomechanical cues combine to promote the progress of liver regeneration. More importantly, the patterns and parameters of magnitude, time, and frequency of mechanical loading can specify distinct cellular responses (Wang et al., 2014). It is essential to quantify those mechanical parameters within sinusoids *in vivo* before and after PHx. Meanwhile, *in vitro* coupled loading and cell co-culture can bridge the gap between *in vitro* variable-based mechanical decoupling and the *in vivo* complex mechanical niche. Elucidating these hemodynamic signals in the process of liver regeneration is of great significance for the treatment of liver tumors and liver transplantation related to PHx.

Author contributions

YW, DL, and ML conceived the outline of this manuscript; YW, NL, XS, WL, XZ, and DL retrieved the literature; YW and DL wrote the original draft; YW, NL, DL, and ML edited and revised the manuscript; YW, NL, XS, WL, XZ, DL, and ML approved the final version of this manuscript.

Funding

This work was supported by the National Key Research and Development Program of China grant 2021YFA0719302 and the National Natural Science Foundation of China (Grants 32130061 and 31870931).

Conflict of interest

The authors declare that the research was conducted in the absence of any commercial or financial relationships that could be construed as a potential conflict of interest.

Publisher's note

References

Abshagen, K., Eipel, C., Kalff, J. C., Menger, M. D., and Vollmar, B. (2008). Kupffer cells are mandatory for adequate liver regeneration by mediating hyperperfusion via modulation of vasoactive proteins. *Microcirculation* 15, 37–47. doi:10.1080/10739680701412989

Ahsan, T., and Nerem, R. M. (2010). Fluid shear stress promotes an endothelial-like phenotype during the early differentiation of embryonic stem cells. *Tissue Eng. Part. a.* 16, 3547–3553. doi:10.1089/ten.TEA.2010.0014

Anwar, M. A., Shalhoub, J., Lim, C. S., Gohel, M. S., and Davies, A. H. (2012). The effect of pressure-induced mechanical stretch on vascular wall differential gene expression. *J. Vasc. Res.* 49, 463–478. doi:10.1159/000339151

Balogh, N., Vajdovich, P., and Gaal, T. (2004). Gastrointestinal ischaemia-reperfusion - pathophysiological bases, therapeutic options. Literature reviews and own studies. *Magy. Allatorvosok Lapja* 126, 502–508.

Bismuth, H., and Houssin, D. (1984). Reduced-sized orthotopic liver graft in hepatic transplantation in children. *Surgery* 95, 367–370.

Braet, F., Shleper, M., Paizi, M., Brodsky, S., Spira, G., Resnick, N., et al. (2004). Liver sinusoidal endothelial cell modulation upon resection and shear stress *in vitro*. *Comp. Hepatol.* 3, 7. doi:10.1186/1476-5926-3-7

Campana, L., Esser, H., Huch, M., and Forbes, S. (2021). Liver regeneration and inflammation: From fundamental science to clinical applications. *Nat. Rev. Mol. Cell Biol.* 22, 608–624. doi:10.1038/s41580-021-00373-7

Cantre, D., Schuett, H., Hildebrandt, A., Dold, S., Menger, M. D., Vollmar, B., et al. (2008). Nitric oxide reduces organ injury and enhances regeneration of reduced-size livers by increasing hepatic arterial flow. *Br. J. Surg.* 95, 785–792. doi:10.1002/bjs.6139

Charras, G., and Yap, A. S. (2018). Tensile forces and mechanotransduction at cell-cell junctions. *Curr. Biol.* 28, R445–R457. doi:10.1016/j.cub.2018.02.003

Chembazhi, U. V., Bangru, S., Hernaez, M., and Kalsotra, A. (2021). Cellular plasticity balances the metabolic and proliferation dynamics of a regenerating liver. *Genome Res.* 31, 576–591. doi:10.1101/gr.267013.120

Chen, S. B., Zhu, J. C., Xue, J., Wang, X. L., Jing, P., Zhou, L. W., et al. (2022). Numerical simulation of flow characteristics in a permeable liver sinusoid with leukocytes. *Biophys. J.* 121, 4666–4678. doi:10.1016/j.bpj.2022.10.022

Chen, T., Oh, S., Gregory, S., Shen, X., and Diehl, A. M. (2020). Single-cell omics analysis reveals functional diversification of hepatocytes during liver regeneration. *JCI. Insight.* 5, E141024. doi:10.1172/jci.insight.141024

Chhabra, A., Song, H. H. G., Grzelak, K. A., Polacheck, W. J., Fleming, H. E., Chen, C. S., et al. (2022). A vascularized model of the human liver mimics regenerative responses. *Proc. Natl. Acad. Sci. U. S. A.* 119, e2115867119. doi:10.1073/pnas.2115867119

Christ, B., Collatz, M., Dahmen, U., Herrmann, K. H., Hoepfl, S., Koenig, M., et al. (2021). Hepatectomy-induced alterations in hepatic perfusion and function – toward multi-Scale computational modeling for a better prediction of post-hepatectomy liver function. *Front. Physiol.* 12, 733868. doi:10.3389/fphys.2021.733868

Cordero-Espinoza, L., and Huch, M. (2018). The balancing act of the liver: Tissue regeneration versus fibrosis. *J. Clin. Invest.* 128, 85–96. doi:10.1172/JCI93562

De Rudder, M., Dili, A., Staerkel, P., and Leclercq, I. A. (2021). Critical role of LSEC in post-hepatectomy liver regeneration and failure. *Int. J. Mol. Sci.* 22, 8053. doi:10.3390/ijms22158053

De Vries, R. J., Tessier, S. N., Banik, P. D., Nagpal, S., Cronin, S. E. J., Ozer, S., et al. (2019). Supercooling extends preservation time of human livers. *Nat. Biotechnol.* 37, 1131–1136. doi:10.1038/s41587-019-0223-y

Dechêne, A., Sowa, J. P., Gieseler, R. K., Jochum, C., Bechmann, L. P., El Fouly, A., et al. (2010). Acute liver failure is associated with elevated liver stiffness and hepatic stellate cell activation. *Hepatology* 52, 1008–1016. doi:10.1002/hep.23754

Deleve, L. D., Wang, X., and Guo, Y. (2008). Sinusoidal endothelial cells prevent rat stellate cell activation and promote reversion to quiescence. *Hepatology* 48, 920–930. doi:10.1002/hep.22351

Ding, B. S., Nolan, D. J., Butler, J. M., James, D., Babazadeh, A. O., Rosenwaks, Z., et al. (2010). Inductive angiocrine signals from sinusoidal endothelium are required for liver regeneration. *Nature* 468, 310–315. doi:10.1038/nature09493

Duan, J. L., Ruan, B., Song, P., Fang, Z. Q., Yue, Z.-S., Liu, J. J., et al. (2022). Shear stress-induced cellular senescence blunts liver regeneration through Notch-sirtuin 1-P21/P16 axis. *Hepatology* 75, 584–599. doi:10.1002/hep.32209

Eipel, C., Abshagen, K., and Vollmar, B. (2010). Regulation of hepatic blood flow: The hepatic arterial buffer response revisited. *World J. Gastroenterol.* 16, 6046–6057. doi:10.3748/wjg.v16.i48.6046

Everson, G. T., Hoefs, J. C., Niemann, C. U., Olthoff, K. M., Dupuis, R., Lauriski, S., et al. (2013). Functional elements associated with hepatic regeneration in living donors after right hepatic lobectomy. *Liver Transpl.* 19, 292–304. doi:10.1002/lt.23592

Fan, J., Chen, C. J., Wang, Y. C., Quan, W., Wang, J.-W., and Zhang, W. G. (2019). Hemodynamic changes in hepatic sinusoids of hepatic steatosis mice. *World J. Gastroenterol.* 25, 1355–1365. doi:10.3748/wjg.v25.i11.1355

Fausto, N., Campbell, J. S., and Riehle, K. J. (2006). Liver regeneration. *Hepatology* 43, S45–S53. doi:10.1002/hep.20969

Feng, A. C., Fan, H. L., Chen, T. W., and Hsieh, C. B. (2014). Hepatic hemodynamic changes during liver transplantation: A review. *World J. Gastroenterol.* 20, 11131–11141. doi:10.3748/wjg.v20.i32.11131

Fernandez, M. (2015). Molecular pathophysiology of portal hypertension. *Hepatology* 61, 1406–1415. doi:10.1002/hep.27343

Forbes, S. J., and Newsome, P. N. (2016). Liver regeneration - mechanisms and models to clinical application. *Nat. Rev. Gastroenterol. Hepatol.* 13, 473–485. doi:10.1038/nrgastro.2016.97

García-Valdecasas, J. C., Fuster, J., Charco, R., Bombuy, E., Fondevila, C., Ferrer, J., et al. (2003). Changes in portal vein flow after adult living-donor liver transplantation: Does it influence postoperative liver function? *Liver Transpl.* 9, 564–569. doi:10.1053/jlts.2003.50069

Giwa, S., Lewis, J. K., Alvarez, L., Langer, R., Roth, A. E., Church, G. M., et al. (2017). The promise of organ and tissue preservation to transform medicine. *Nat. Biotechnol.* 35, 530–542. doi:10.1038/nbt.3889

Gock, M., Eipel, C., Linnebacher, M., Klar, E., and Vollmar, B. (2011). Impact of portal branch ligation on tissue regeneration, microcirculatory response and microarchitecture in portal blood-deprived and undeprived liver tissue. *Microvasc. Res.* 81, 274–280. doi:10.1016/j.mvr.2011.03.005

Golse, N., Bucur, P. O., Adam, R., Castaing, D., Cunha, A. S., and Vibert, E. (2013). New paradigms in post-hepatectomy liver failure. *J. Gastrointest. Surg.* 17, 593–605. doi:10.1007/s11605-012-2048-6

Goto, T., Mikami, K. I., Miura, K., Ohshima, S., Yoneyama, K., Nakane, K., et al. (2004). Mechanical stretch induces matrix metalloproteinase 1 production in human hepatic stellate cells. *Pathophysiology* 11, 153–158. doi:10.1016/j.pathophys.2004.07.003

Gracia-Sancho, J., Russo, L., Garcia-Caldero, H., Carles Garcia-Pagan, J., Garcia-Cardena, G., and Bosch, J. (2011). Endothelial expression of transcription factor Kruppel-like factor 2 and its vasoprotective target genes in the normal and cirrhotic rat liver. *Gut* 60, 517–524. doi:10.1136/gut.2010.220913

Grosse-Segerath, L., and Lammert, E. (2021). Role of vasodilation in liver regeneration and health. *Biol. Chem.* 402, 1009–1019. doi:10.1515/hsz-2021-0155

Higgins, G. M., and Anderson, R. M. (1931). Experimental pathology of the liver I Restoration of the liver of the white rat following partial surgical removal. *Arch. Pathol.* 12, 186–202.

Hilscher, M. B., Sehrawat, T., Arab, J. P., Zeng, Z., Gao, J., Liu, M., et al. (2019). Mechanical stretch increases expression of CXCL1 in liver sinusoidal endothelial cells to recruit neutrophils, generate sinusoidal microthombi, and promote portal hypertension. *Gastroenterology* 157, 193–209.e9. doi:10.1053/j.gastro.2019.03.013

Hohmann, N., Weiwei, W., Dahmen, U., Dirsch, O., Deutsch, A., Voss-Böhme, A., et al. (2014). How does a single cell know when the liver has reached its correct size? *PLoS One* 9, e93207. doi:10.1371/journal.pone.0093207

Horiguchi, N., Ishac, E. J., and Gao, B. (2007). Liver regeneration is suppressed in alcoholic cirrhosis: Correlation with decreased STAT3 activation. *Alcohol* 41, 271–280. doi:10.1016/j.alcohol.2007.04.008

Hu, J. R., Lü, S. Q., Feng, S. L., and Long, M. (2017). Flow dynamics analyses of pathophysiological liver lobules using porous media theory. *Acta Mech. Sin.* 33, 823–832. doi:10.1007/s10409-017-0674-7

Hu, J., Srivastava, K., Wieland, M., Runge, A., Mogler, C., Besemfelder, E., et al. (2014). Endothelial cell-derived angiopoietin-2 controls liver regeneration as a spatiotemporal rheostat. *Science* 343, 416–419. doi:10.1126/science.1244880

Huang, W., Han, N., Du, L., Wang, M., Chen, L., and Tang, H. (2021). A narrative review of liver regeneration-from models to molecular basis. *Ann. Transl. Med.* 9, 1705. doi:10.21037/atm-21-5234

Illa, X., Vila, S., Yeste, J., Peralta, C., Gracia-Sancho, J., and Villa, R. (2014). A novel modular bioreactor to *in vitro* study the hepatic sinusoid. *Plos One* 9, e111864. doi:10.1371/journal.pone.0111864

Inoue, Y., Sugawara, Y., Tamura, S., Ohtsu, H., Taguri, M., Makuuchi, M., et al. (2009). Validity and feasibility of transient elastography for the transplanted liver in the peritransplantation period. *Transplantation* 88, 103–109. doi:10.1097/TP.0b013e3181aacb7f

Ishikawa, J., Takeo, M., Iwadate, A., Koya, J., Kihira, M., Oshima, M., et al. (2021). Mechanical homeostasis of liver sinusoid is involved in the initiation and termination of liver regeneration. *Commun. Biol.* 4, 409. doi:10.1038/s42003-021-01936-2

Janmey, P. A., and Miller, R. T. (2011). Mechanisms of mechanical signaling in development and disease. *J. Cell Sci.* 124, 9–18. doi:10.1242/jcs.071001

Kawai, M., Naruse, K., Komatsu, S., Kobayashi, S., Nagino, M., Nimura, Y., et al. (2002). Mechanical stress-dependent secretion of interleukin 6 by endothelial cells after portal vein embolization: Clinical and experimental studies. *J. Hepatol.* 37, 240–246. doi:10.1016/s0168-8278(02)00171-x

Kimura, M., Moteki, H., and Ogihara, M. (2023). Role of hepatocyte growth regulators in liver regeneration. *Cells* 12, 208. doi:10.3390/cells12020208

Klaas, M., Kangur, T., Viil, J., Maemets-Allas, K., Minajeva, A., Vadi, K., et al. (2016). The alterations in the extracellular matrix composition guide the repair of damaged liver tissue. *Sci. Rep.* 6, 27398. doi:10.1038/srep27398

Kobayashi, S., Nagino, M., Komatsu, S., Naruse, K., Nimura, Y., Nakanishi, M., et al. (2003). Stretch-induced IL-6 secretion from endothelial cells requires NF-κB activation. *Biochem. Biophys. Res. Commun.* 308, 306–312. doi:10.1016/s0006-291x(03)01362-7

Koch, K. S., and Leffert, H. L. (1979). Increased sodium ion influx is necessary to initiate rat hepatocyte proliferation. *Cell* 18, 153–163. doi:10.1016/0092-8674(79)90364-7

Kumar, A., Sharma, P., and Sarin, S. K. (2008). Hepatic venous pressure gradient measurement: Time to learn. *Indian J. Gastroenterol.* 27, 74–80.

Lalor, P. F., Lai, W. K., Curbishley, S. M., Shetty, S., and Adams, D. H. (2006). Human hepatic sinusoidal endothelial cells can be distinguished by expression of phenotypic markers related to their specialised functions *in vivo*. *World J. Gastroenterol.* 12, 5429–5439. doi:10.3748/wjg.v12.i34.5429

Lautt, W. W., and Greenway, C. V. (1987). Conceptual review of the hepatic vascular bed. *Hepatology* 7, 952–963. doi:10.1002/hep.1840070527

Li, N., Zhang, X. Y., Zhou, J., Li, W., Shu, X. Y., Wu, Y., et al. (2022). Multiscale biomechanics and mechanotransduction from liver fibrosis to cancer. *Adv. Drug Deliv. Rev.* 188, 114448. doi:10.1016/j.addr.2022.114448

Li, W. P., Li, L., and Hui, L. J. (2020). Cell plasticity in liver regeneration. *Trends Cell Biol.* 30, 329–338. doi:10.1016/j.tcb.2020.01.007

Lo, C. M., Fan, S. T., Liu, C. L., Wei, W. I., Lo, R. J., Lai, C. L., et al. (1997). Adult-to-adult living donor liver transplantation using extended right lobe grafts. *Ann. Surg.* 226, 261–270. doi:10.1097/00000658-199709000-00005

Long, Y., Niu, Y. D., Liang, K. N., and Du, Y. (2022). Mechanical communication in fibrosis progression. *Trends Cell Biol.* 32, 70–90. doi:10.1016/j.tcb.2021.10.002

Lorenz, L., Axnick, J., Buschmann, T., Henning, C., Urner, S., Fang, S., et al. (2018). Mechanosensing by β1 integrin induces angiocrine signals for liver growth and survival. *Nature* 562, 128–132. doi:10.1038/s41586-018-0522-3

Manavski, Y., Abel, T., Hu, J., Kleinltzum, D., Buchholz, C. J., Belz, C., et al. (2017). Endothelial transcription factor KLF2 negatively regulates liver regeneration via induction of activin A. *Proc. Natl. Acad. Sci. U. S. A.* 114, 3993–3998. doi:10.1073/pnas.1613392114

Marlini, M., Mabuchi, A., Mallard, B. L., Hairulhisyam, N., Akashi-Takamura, S., Harper, J. L., et al. (2016). Delayed liver regeneration in C3H/HeJ mice: Possible involvement of haemodynamic and structural changes in the hepatic microcirculation. *Exp. Physiol.* 101, 1492–1505. doi:10.1113/EP085727

Marrone, G., Russo, L., Rosado, E., Hide, D., Garcia-Cardena, G., Carlos Garcia-Pagan, J., et al. (2013). The transcription factor KLF2 mediates hepatic endothelial protection and paracrine endothelial-stellate cell deactivation induced by statins. *J. Hepatol.* 58, 98–103. doi:10.1016/j.jhep.2012.08.026

Marrone, G., Shah, V. H., and Gracia-Sancho, J. (2016). Sinusoidal communication in liver fibrosis and regeneration. *J. Hepatol.* 65, 608–617. doi:10.1016/j.jhep.2016.04.018

Marubashi, S., Sakon, M., Nagano, H., Gotoh, K., Hashimoto, K., Kubota, M., et al. (2004). Effect of portal hemodynamics on liver regeneration studied in a novel portohepatic shunt rat model. *Surgery* 136, 1028–1037. doi:10.1016/j.surg.2004.03.012

Mei, Y., and Thevananther, S. (2011). Endothelial nitric oxide synthase is a key mediator of hepatocyte proliferation in response to partial hepatectomy in mice. *Hepatology* 54, 1777–1789. doi:10.1002/hep.24560

Michalopoulos, G. K., and Bhushan, B. (2021). Liver regeneration: Biological and pathological mechanisms and implications. *Nat. Rev. Gastroenterol. Hepatol.* 18, 40–55. doi:10.1038/s41575-020-0342-4

Michalopoulos, G. K., and Defrances, M. C. (1997). Liver regeneration. *Science* 276, 60–66. doi:10.1126/science.276.5309.60

Michalopoulos, G. K. (2017). Hepatostat: Liver regeneration and normal liver tissue maintenance. *Hepatology* 65, 1384–1392. doi:10.1002/hep.28988

Michalopoulos, G. K. (2007). Liver regeneration. *J. Cell Physiol.* 213, 286–300. doi:10.1002/jcp.21172

Michalopoulos, G. K. (2011). "Liver regeneration," in *Molecular pathology of liver diseases*. Editor S. P. S. MONGA (Boston, MA: Springer US).

Michalopoulos, G. K. (2013). Principles of liver regeneration and growth homeostasis. *Compr. Physiol.* 3, 485–513. doi:10.1002/cphy.c120014

Mitchell, C., and Willenbring, H. (2008). A reproducible and well-tolerated method for 2/3 partial hepatectomy in mice. *Nat. Protoc.* 3, 1167–1170. doi:10.1038/nprot.2008.80

Morsiani, E., Aleotti, A., and Ricci, D. (1998). Haemodynamic and ultrastructural observations on the rat liver after two-thirds partial hepatectomy. *J. Anat.* 192, 507–515. doi:10.1046/j.1469-7580.1998.19240507.x

Mueller, L., Broering, D. C., Meyer, J., Vashist, Y., Goettsche, J., Wilms, C., et al. (2002). The induction of the immediate-early-genes Egr-1, PAI-1 and PRL-1 during liver regeneration in surgical models is related to increased portal flow. *J. Hepatol.* 37, 606–612. doi:10.1016/s0168-8278(02)00238-6

Niiya, T., Murakami, M., Aoki, T., Murai, N., Shimizu, Y., and Kusano, M. (1999). Immediate increase of portal pressure, reflecting sinusoidal shear stress, induced liver regeneration after partial hepatectomy. *J. Hepatobiliary Pancreat. Surg.* 6, 275–280. doi:10.1007/s005340050118

Nishii, K., Brodin, E., Renshaw, T., Weesner, R., Moran, E., Soker, S., et al. (2018). Shear stress upregulates regeneration-related immediate early genes in liver progenitors in 3D ECM-like microenvironments. *J. Cell Physiol.* 233, 4272–4281. doi:10.1002/jcp.26246

Pibiri, M., and Simbula, G. (2022). Role of the Hippo pathway in liver regeneration and repair: Recent advances. *Inflamm. Regen.* 42, 59. doi:10.1186/s41232-022-00235-5

Pichlmayr, R., Ringe, B., Gubernatis, G., Hauss, J., and Bunzendahl, H. (1988). Transplantation of a donor liver to 2 recipients (splitting transplantation)--a new method in the further development of segmental liver transplantation. *Langenbecks Arch. Chir.* 373, 127–130. doi:10.1007/BF01262776

Piscaglia, F., Zironi, G., Gaiani, S., Mazziotti, A., Cavallari, A., Gramantieri, L., et al. (1999). Systemic and splanchnic hemodynamic changes after liver transplantation for cirrhosis: A long-term prospective study. *Hepatology* 30, 58–64. doi:10.1002/hep.510300112

Poisson, J., Lemoinne, S., Boulanger, C., Durand, F., Moreau, R., Valla, D., et al. (2017). Liver sinusoidal endothelial cells: Physiology and role in liver diseases. *J. Hepatol.* 66, 212–227. doi:10.1016/j.jhep.2016.07.009

Powell, E. E., Wong, V. W. S., and Rinella, M. (2021). Non-alcoholic fatty liver disease. *Lancet* 397, 2212–2224. doi:10.1016/S0140-6736(20)32511-3

Rabbany, S. Y., and Rafii, S. (2018). Blood flow forces liver growth. *Nature* 562, 42–43. doi:10.1038/d41586-018-06741-2

Rai, R. M., Lee, F. Y. J., Rosen, A., Yang, S. Q., Lin, H. Z., Koteish, A., et al. (1998). Impaired liver regeneration in inducible nitric oxide synthasedeficient mice. *Proc. Natl. Acad. Sci. U. S. A.* 95, 13829–13834. doi:10.1073/pnas.95.23.13829

Raia, S., Nery, J. R., and Mies, S. (1989). Liver transplantation from live donors. *Lancet* 2, 497. doi:10.1016/s0140-6736(89)92101-6

Rohn, F., Kordes, C., Buschmann, T., Reichert, D., Wammers, M., Poschmann, G., et al. (2020). Impaired integrin α_5/β_1 -mediated hepatocyte growth factor release by stellate cells of the aged liver. *Aging Cell* 19, e13131. doi:10.1111/acel.13131

Sallberg, M., and Pasetto, A. (2020). Liver, tumor and viral hepatitis: Key players in the complex balance between tolerance and immune activation. *Front. Immunol.* 11, 552. doi:10.3389/fimmu.2020.00552

Sato, Y., Koyama, S., Tsukada, K., and Hatakeyama, K. (1997). Acute portal hypertension reflecting shear stress as a trigger of liver regeneration following partial hepatectomy. *Surg. Today.* 27, 518–526. doi:10.1007/BF02385805

Schoen, J. M., Wang, H. H., Minuk, G. Y., and Lautt, W. W. (2001). Shear stress-induced nitric oxide release triggers the liver regeneration cascade. *Nitric. Oxide* 5, 453–464. doi:10.1006/niox.2001.0373

Schrader, J., Gordon-Walker, T. T., Aucott, R. L., Van Deemter, M., Quaas, A., Walsh, S., et al. (2011). Matrix stiffness modulates proliferation, chemotherapeutic response, and dormancy in hepatocellular carcinoma cells. *Hepatology* 53, 1192–1205. doi:10.1002/hep.24108

Shah, V., Haddad, F. G., Garcia-Cardena, G., Frangos, J. A., Mennone, A., Groszmann, R. J., et al. (1997). Liver sinusoidal endothelial cells are responsible for nitric oxide modulation of resistance in the hepatic sinusoids. *J. Clin. Invest.* 100, 2923–2930. doi:10.1172/JCI119842

Shen, S., Luo, X., Gao, K., Sun, Y., Yao, D., and Zhu, L. (2019). Identification and integrative analysis of microRNAs and mRNAs involved in proliferation and invasion of pressure-treated human liver cancer cell lines. *Mol. Med. Rep.* 20, 375–387. doi:10.3892/mmr.2019.10223

Shu, W., Yang, M., Yang, J., Lin, S., Wei, X., and Xu, X. (2022). Cellular crosstalk during liver regeneration: Unity in diversity. *Cell Commun. Signal.* 20, 117. doi:10.1186/s12964-022-00918-z

Shu, X. Y., Li, N., Wu, Y., Li, W., Zhang, X. Y., Li, P. W., et al. (2021). Mechanotransduction of liver sinusoidal endothelial cells under varied mechanical stimuli. *Acta Mech. Sin.* 37, 201–217. doi:10.1007/s10409-021-01057-3

Simonetto, D. A., Yang, H.-Y., Yin, M., De Assuncao, T. M., Kwon, J. H., Hilscher, M., et al. (2015). Chronic passive venous congestion drives hepatic fibrogenesis via sinusoidal thrombosis and mechanical forces. *Hepatology* 61, 648–659. doi:10.1002/hep.27387

So, J., Kim, A., Lee, S. H., and Shin, D. (2020). Liver progenitor cell-driven liver regeneration. *Exp. Mol. Med.* 52, 1230–1238. doi:10.1038/s12276-020-0483-0

Song, Z. W., Gupta, K., Ng, I. C., Xing, J. W., Yang, Y. A., and Yu, H. (2017). Mechanosensing in liver regeneration. *Semin. Cell Dev. Biol.* 71, 153–167. doi:10.1016/j.semcdb.2017.07.041

Soydemir, S., Comella, O., Abdelmottaleb, D., and Pritchett, J. (2020). Does mechanocrine signaling by liver sinusoidal endothelial cells offer new opportunities for the development of anti-fibrotics? *Front. Med.* 6, 312. doi:10.3389/fmed.2019.00312

Stärkel, P., De Saeger, C., Leclercq, I., Strain, A., and Horsmans, Y. (2005). Deficient Stat3 DNA-binding is associated with high Pias3 expression and a positive anti-apoptotic balance in human end-stage alcoholic and hepatitis C cirrhosis. *J. Hepatol.* 43, 687–695. doi:10.1016/j.jhep.2005.03.024

Starzl, T. E., Brettschneider, L., Penn, I., Bell, P., Groth, C. G., Blanchard, H., et al. (1969). Orthotopic liver transplantation in man. *Transpl. Proc.* 1, 216–222.

Strong, R. W., Lynch, S. V., Ong, T. H., Matsunami, H., Koido, Y., and Balderson, G. A. (1990). Successful liver transplantation from a living donor to her son. *N. Engl. J. Med.* 322, 1505–1507. doi:10.1056/nejm199005243222106

Sugimoto, H., Hirota, M., Kure, S., Kanazumi, N., Nomoto, S., Inoue, S., et al. (2007). Normal hepatic hemodynamics during early postoperative period in recipients with adult live donor liver transplantation. *Transpl. Proc.* 39, 160–165. doi:10.1016/j.transproceed.2006.10.026

Tajik, A., Zhang, Y., Wei, F., Sun, J., Jia, Q., Zhou, W., et al. (2016). Transcription up regulation via force-induced direct stretching of chromatin. *Nat. Mat.* 15, 1287–1296. doi:10.1038/nmat4729

Tao, Y., Wang, M., Chen, E., and Tang, H. (2017). Liver regeneration: Analysis of the main relevant signaling molecules. *Mediat. Inflamm.* 2017, 1. 9. doi:10.1155/2017/4256352

Taub, R. (2004). Liver regeneration: From myth to mechanism. *Nat. Rev. Mol. Cell Biol.* 5, 836–847. doi:10.1038/nrm1489

Tiberio, G. A., Tiberio, L., Benetti, A., Cervi, E., Montani, N., Dreano, M., et al. (2008). IL-6 Promotes compensatory liver regeneration in cirrhotic rat after partial hepatectomy. *Cytokine* 42, 372–378. doi:10.1016/j.cyto.2008.03.012

Van Den Broek, M. A., Olde Damink, S. W., Dejong, C. H., Lang, H., Malagó, M., Jalan, R., et al. (2008). Liver failure after partial hepatic resection: Definition, pathophysiology, risk factors and treatment. *Liver Int.* 28, 767–780. doi:10.1111/j.1478-3231.2008.01777.x

Walesky, C. M., Kolb, K. E., Winston, C. L., Henderson, J., Kruft, B., Fleming, I., et al. (2020). Functional compensation precedes recovery of tissue mass following acute liver injury. *Nat. Commun.* 11, 5785. doi:10.1038/s41467-020-19558-3

Wang, H. H., and Lautt, W. W. (1998). Evidence of nitric oxide, a flow-dependent factor, being a trigger of liver regeneration in rats. *Can. J. Physiol. Pharmacol.* 76, 1072–1079. doi:10.1139/y98-128

Wang, T. H., Lü, S. Q., Hao, Y. J., Su, Z. N., Long, M., and Cui, Y. H. (2021). Influence of microflow on hepatic sinusoid blood flow and red blood cell deformation. *Biophys. J.* 120, 4859–4873. doi:10.1016/j.bpj.2021.09.020

Wang., J. W., Lü, D. Y., Mao, D. B., and Long, M. (2014). Mechanomics: An emerging field between biology and biomechanics. *Protein Cell.* 5, 518–531. doi:10.1007/s13238-014-0057-9

Wang., J. W., Wu, Y., Zhang, X., Zhang, F., Lü, D. Y., Shangguan, B., et al. (2019). Flow-enhanced priming of hESCs through H2B acetylation and chromatin decondensation. *Stem Cell Res. Ther.* 10, 349. doi:10.1186/s13287-019-1454-z

Wells, R. G. (2008). The role of matrix stiffness in regulating cell behavior. *Hepatology* 47, 1394–1400. doi:10.1002/hep.22193

Williams, M. J., Clouston, A. D., and Forbes, S. J. (2014). Links between hepatic fibrosis, ductular reaction, and progenitor cell expansion. *Gastroenterology* 146, 349–356. doi:10.1053/j.gastro.2013.11.034

Xue, Z. F., Wu, X. M., and Liu, M. (2013). Hepatic regeneration and the epithelial to mesenchymal transition. *World J. Gastroenterol.* 19, 1380–1386. doi:10.3748/wjg.v19.i9.1380

Yagi, S., Hirata, M., Miyachi, Y., and Uemoto, S. (2020). Liver regeneration after hepatectomy and partial liver transplantation. *Int. J. Mol. Sci.* 21, 8414. doi:10.3390/ijms21218414

Yee, A. G., and Revel, J. P. (1978). Loss and reappearance of gap junctions in regenerating liver. *J. Cell Biol.* 78, 554–564. doi:10.1083/jcb.78.2.554

Yi, S. H., Zhang, Y., Tang, D., and Zhu, L. (2015). Mechanical force and tensile strain activated hepatic stellate cells and inhibited retinol metabolism. *Biotechnol. Lett.* 37, 1141–1152. doi:10.1007/s10529-015-1785-5

You, Z. F., Zhou, L., Li, W. J., Huang, C. Y., and Du, Y. N. (2019). Mechanical microenvironment as a key cellular regulator in the liver. *Acta Mech. Sin.* 35, 289–298. doi:10.1007/s10409-019-00857-y

Zhang, F., Wang, J. W., Lü, D. Y., Zheng, L., Shangguan, B., Gao, Y. X., et al. (2021). Mechanomics analysis of hESCs under combined mechanical shear, stretch, and compression. *Biomech. Model. Mechanobiol.* 20, 205–222. doi:10.1007/s10237-020-01378-5

Zhu, C. Z., Dong, B. Z., Sun, L. Q., Wang, Y. X., and Chen, S. H. (2020). Cell sources and influencing factors of liver regeneration: A review. *Med. Sci. Monit.* 26, e929129. doi:10.12659/MSM.929129

Glossary

AFM	Atomic force microscopy
ALDLT	Adult to adult living donor liver transplantation
ECM	Extracellular matrix
EGF	Epidermal growth factor
EGFR	Epidermal growth factor receptor
eNOS	Endothelial nitric oxide synthase
GPCRs	G-protein-coupled receptors
HB-EGF	Heparin-binding EGF-like growth factor
HGF	Hepatocyte growth factor
HSCs	Hepatic stellate cells
IL-6	Interleukin-6
iNOS	Inducible nitric oxide synthase
KCs	Kupffer cells
KLF2	Kruppel-like factor 2
LDLT	Living donor liver transplantation
LPCs	Liver progenitor cells
LSECs	Liver sinusoidal endothelial cells
MMP-1	Metalloproteinase-1
NO	Nitric oxide
NPCs	Nonparenchymal cells
PHPL	PHx with partial portal ligation
PHS	Portohepatic shunt
PHx	Partial hepatectomy
PVE	Portal vein embolization
PVL	Portal vein branch ligation
RLT	Reduced size live transplantatio
SLT	Split liver transplantation
TGF-α	Transforming growth factor-α
TGF-β1	Transforming growth factor-β1
TIMP-1	Tissue inhibitor of metalloproteinases-1
TNF-α	Tumor necrosis factor-α
uPA	Urokinase plasminogen activator
VEGFR-2	Vascular endothelial cell growth factor receptor-2

Frontiers in
Bioengineering and Biotechnology

Accelerates the development of therapies, devices, and technologies to improve our lives

A multidisciplinary journal that accelerates the development of biological therapies, devices, processes and technologies to improve our lives by bridging the gap between discoveries and their application.

Discover the latest Research Topics

See more →

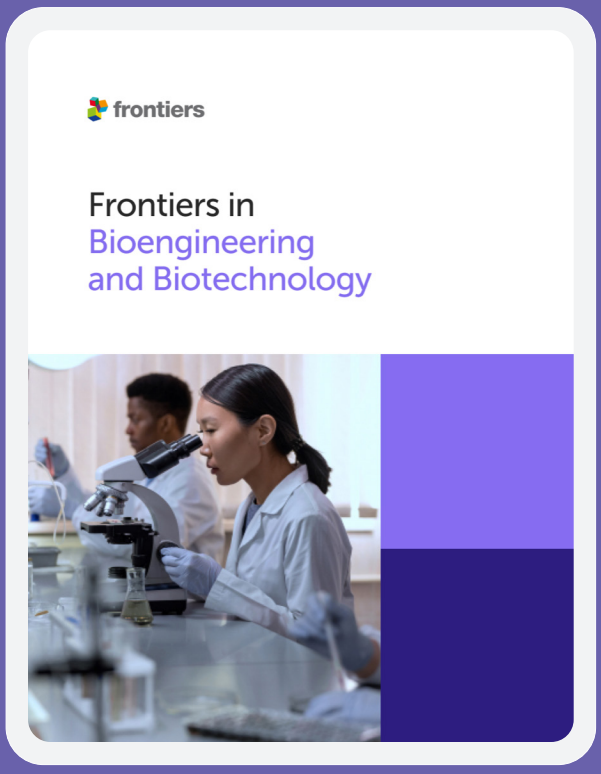

Frontiers

Avenue du Tribunal-Fédéral 34
1005 Lausanne, Switzerland
frontiersin.org

Contact us

+41 (0)21 510 17 00
frontiersin.org/about/contact